Dynamics of Immiscible Gravity Currents

Paul Andrew Allen

Submitted in accordance with the requirements for the degree of
Doctor of Philosophy

The University of Leeds

EPSRC Centre for Doctoral Training in Fluid Dynamics

School of Computing

September 2020

Dedicated to my parents, Lynette and Tony

Declaration

The candidate confirms that the work submitted is his own, except where work which has formed part of jointly authored publications has been included. The contribution of the candidate and the other authors to this work has been explicitly indicated below. The candidate confirms that appropriate credit has been given within the thesis where reference has been made to the work of others.

Chapters 1, 2 and 6 contain material from the jointly authored publication:

Allen, P. A., Dorrell, R. M., Harlen, O. G., Thomas, R. E. and McCaffrey, W. D. 2020. Pulse propagation in gravity currents. *Physics of fluids* 32(1), p.016603.

This paper was primarily authored by P. A. Allen who was responsible for all data collection, processing, analysis and writing. Contributions of all other authors were through advisory and editorial roles.

Acknowledgements

I would like to thank my supervisors Oliver Harlen, Rob Dorrell, Bill McCaffrey and Rob Thomas for their guidance, insight and support throughout my PhD. Without their expertise, it would have been impossible to complete this thesis. Thanks go to Gareth Keevil and Helena Brown for their invaluable support and advice in the experimental work conduct in the Sorby environmental fluids lab.

Thank you to my friends and family for the continual support throughout my time at the University of Leeds. I am grateful to my colleagues on the CDT for providing much needed fruitful discussions, much-needed breaks during the working day and in making the office an enjoyable place to work.

Finally, I want to thank my parents for their love, support, and encouragement and for providing the opportunity to pursue my education.

This work was supported by the Engineering and Physical Sciences Research Council (EPSRC) Centre for Doctoral Training in Fluid Dynamics at the University of Leeds under Grant No. EP/L01615X/1 and the sponsors of the Turbidites Research Group.

Abstract

Gravity currents are flows that are driven by a density difference and include pyroclastic flows, landslides and turbidity currents. Gravity currents can be a geohazard and have significant economic impact to connected industries. This thesis focuses on two important questions relating to gravity current dynamics: How do pulses or surges affect the flow dynamics? And, how does a viscosity contrast affect the mixing process between the current and its ambient?

Real-world gravity current flows rarely exist as a single discrete event, but are instead made up of multiple surges. These are studied by the sequential release of two lock gates. The first release creates a gravity current, while the second creates a pulse that eventually propagates to the head of the first current. A shallow-water model is used to analyse the flow structure in terms of two parameters: the densimetric Froude number at the head of the current, Fr, and a dimensionless time between releases, t_{re}. The pulse speed exhibits negative acceleration for a region of (Fr, t_{re})-space. Critically for sediment-laden gravity currents, pulsed flows may change from erosional to depositional further affecting their dynamics. Experimental modelling using glycerol/water mixtures reveals that the pulse can cause a rapid dilution of the current and transition to fully turbulent behaviour.

In a lock-exchange configuration, the effect of a viscosity contrast between the ambient and the current is studied using fully resolved direct numerical simulation of the Navier-Stokes equations. Viscosity acts to both dissipate energy in the bulk of the current and locally inhibit mixing at the interface. Energy lost to viscous heating is dominant when the viscosity contrast is large, i.e. ten times the ambient. However, when the viscosity contrast is small but non-zero, the reduced mixing of the current enables a more efficient transfer between kinetic and potential energy and the total energy lost to mixing and viscous dissipation is reduced when compared to an equal viscosity case.

Contents

List of Figures **xviii**

List of Tables **xx**

List of abbreviations **xxi**

1 Introduction **1**

1.1 Aims of the thesis 6
1.2 Studying gravity currents 7
1.2.1 Lock-exchange and lock-release problem 7
1.2.2 Navier-Stokes equations 9
1.2.3 Shallow-water and depth-averaged models 10
1.2.4 Froude number condition 13
1.2.5 Scaling arguments and similarity solutions 14
1.2.6 Two-layer shallow-water models 16
1.2.7 Entrainment 18
1.2.8 Depth-resolving models 19
1.3 Structure of the thesis 21

2 The phased lock-release problem **23**

2.1 Introduction 23
2.2 Theoretical modelling 24
2.2.1 Analysis of characteristics: single release case 26
2.2.2 Extension to double release 30
2.2.3 Verification 34
2.3 Results and Discussion 36
2.3.1 Shock Evolution 36
2.3.2 Classification of Solutions 38
2.3.3 Momentum of the Head 44
2.4 Conclusions and future work 46

3 Experimental study of pulses in gravity currents **49**

3.1 Introduction 49

3.2 Methodology 50
  3.2.1 Physical Setup 50
  3.2.2 Glycerol properties 53
  3.2.3 Procedure 56
  3.2.4 Cases 58
  3.2.5 Viscometry 59
3.3 Image processing 67
  3.3.1 Lens distortion 67
  3.3.2 Image processing 75
3.4 Surface tracking 77
  3.4.1 Single-release surface tracking 78
  3.4.2 Double-release surface tracking 81
3.5 Results and discussion 84
  3.5.1 Repeatability of the experiments 84
  3.5.2 Visualisation 84
  3.5.3 Validation of shallow-water model 90
3.6 Conclusions and further work 94

4 Direct numerical simulation of the lock-exchange problem 97

4.1 Introduction 97
  4.1.1 Lock-exchange problem 97
4.2 Methodology 99
  4.2.1 Solver and numerical details 104
  4.2.2 Analysis tools 111
  4.2.3 Resolution 121
4.3 Results and discussion 122
  4.3.1 Visualisations 125
  4.3.2 Depth averaging 131
  4.3.3 Mixing and energy distribution 132
4.4 Conclusions and future work 139

5 Two-layer model for the lock-exchange problem 141

5.1 Introduction 141
5.2 Methodology 142
  5.2.1 Numerical scheme 146
  5.2.2 Verification 161
5.3 Results and Discussion 163
5.4 Conclusions and future work 175

6 Conclusions and outlook 179

6.1 Implications 181
6.2 Outlook 183

References **183**

List of Figures

1.1 Pyroclastic flow produced by an eruption of the Soufriére hills volcano, Montserrat. Image published by Huppert (2006) and taken by R. S. J. Sparks. 2

1.2 Sandy debris flow produced in the laboratory. Image published in De Blasio et al. (2011). b - Laboratory scale turbidity current. Image published in Sequeiros et al. (2010) 3

1.3 (a) - Turbidite deposit consisting of a upwards-fining sandstone, a siltstone layer and a mudstone layer. (b) - Pebble-rich debrite deposit in the Paganzo Basin, south-western La Rioja Province, Argentina. Image published by Fallgatter et al. (2017). 3

1.4 Aerial photo of the tailings dam break out at Merriespruit, South Africa. Image published in Fourie et al. (2001). 5

1.5 Lock-release (right) and lock-exchange (left) configuration before release where the fluid is held in place by a vertical lock gate (top) and just after where the denser red fluid is driven to the right by (bottom). 8

1.6 Gravity current for low Reynolds numbers (left) and high Reynolds numbers (right). 9

1.7 Two-dimensional shallow water description of the flow with depth-averaged velocity $\bar{u}(x,t)$ and flow depth $h(x,t)$ 11

1.8 Schematic of the two-layer shallow-water model for the lock-exchange problem. Each layer has depth h_i, depth-averaged velocity, u_i and a Reynolds number Re_i. The total depth is fixed, so that $h_1 + h_2 = 1$. 17

2.1 Configuration of the single (left) and double (right) lock-release problems. Initial conditions (- -) and current depth, $h(x,t)$, (–) are displayed. 24

2.2 Characteristic diagrams shortly after the first release for a densimetric Froude number Fr less than 1. For $1 < Fr < 2$, x_{ref} has positive gradient until intersecting x_{fan} The head of the current x_N (–) moves at constant speed until $x_{\text{ref}}(\cdot -)$ collides with it. Positive (a) and negative (b) characteristics $(\cdots)$ are displayed for a small range of starting values. The boundary between the expansion fan and the constant region behind the head is $x_{\text{fan}}(\cdots -)$. 28

2.3 Characteristic diagram highlighting the two curves $x_{\text{ref}}(\cdot -)$ and $x_{\text{fan}}(\cdots -)$ and how the solution is partitioned into uniform (U), simple (S) and complex (C) regions shortly after the release (a) and at a later time (b). 28

2.4 Schematic showing an example structure of the characteristic space for a shock released into the U_2 region. Ahead of the shock, the regions are bounded by the two lines $x_{\text{ref}}(\cdot -)$ and $x_{\text{fan}}(\cdots -)$, the head of the current x_N (–) and the shock x_s (- -). At the point of release, an additional expansion fan is bounded between $x_{\text{fin}}(\cdots)$ and the slowest backwards travelling characteristic from the second release $(\cdot\cdot -)$. 32

2.5 Schematic showing an example structure of the characteristic space for a shock released into a C_3 region. Ahead of the shock, the regions are bounded by the two lines $x_{\text{ref}}(\cdot -)$ and $x_{\text{fan}}(\cdots -)$, the head of the current x_N (–) and the shock x_s (- -). At the point of release, an additional expansion fan is bounded between $x_{\text{fin}}(\cdots)$ and the slowest backwards travelling characteristic from the second release $(\cdot\cdot -)$. . . 33

2.6 (a) Depth and velocity profiles at $t = 1$ for a single release problem ($\Delta x = 0.0002$, $\Delta t = 10^{-5}$, $Fr = 1$). (b) Error in depth and velocity for fixed $\Delta t = 10^{-5}$ (left) and fixed $\Delta x = 0.005$ (right). Straight lines drawn between the end points have $E_h \sim \Delta t^{0.85}$, $E_u \sim \Delta t^{0.79}$, $E_h \sim \Delta x^{1.04}$ and $E_u \sim \Delta x^{1.04}$. 35

2.7 Comparison between the analytical expression and the numerically-computed x_{ref} between (1,1) and the point that it intersects the head. 36

2.8 Schematic showing examples of the three characteristic diagrams for the three distinct paths C_1 (a) and U_2 (b) shocks, x_s, (- -) can take through the single release solution, i,ii and iii. The shock intercepts x_{ref} and x_{fan} $(\cdots -)$ at $t_{\text{fan}}(\blacktriangledown)$ and $t_{\text{ref}}(\blacklozenge)$, respectively. The shock intercepts the front, $x_N(-)$, at $t = t_{\text{col}}(\blacksquare)$. Uniform ($U_i$), Simple ($S_i$) and complex ($C_i$) regions are indexed by the order in which they appear. 37

2.9 Example U_2N cases for: U_2Ni, (a) & (b) ($Fr = 0.4$ and $t_{\mathrm{re}} = 4.2$); U_2Nii, (c) & (d) ($Fr = 0.6$ and $t_{\mathrm{re}} = 5$); and U_2Niii, (e) & (f) ($Fr = 0.9$ and $t_{\mathrm{re}} = 5.8$): (a), (c), (e) Characteristic diagram displaying the flow boundaries (–), x_{ref} and x_{fan} ($\cdots -$), the shock x_s (- -) and $x_{\mathrm{fin}}(\cdot)$; (b), (d), (f) Shock velocity for $t > t_{\mathrm{re}}$. t_{fan}(▼), t_{ref}(◆), t_{col}(■) and t_{fin}(●) (a-f). The shock velocity is only constant in Uniform regions, §2.3.1. 39

2.10 Example U_2F cases for: U_2Fii, (c) & (d) ($Fr = 0.9$ and $t_{\mathrm{re}} = 10$); and U_2Fiii, (e) & (f) ($Fr = 1.1$ and $t_{\mathrm{re}} = 10$): (a), (c) Characteristic diagram displaying the flow boundaries (–), x_{ref} and x_{fan} ($\cdots -$), the shock x_s (- -) and $x_{\mathrm{fin}}(\cdot)$; (b), (d) Shock velocity for $t > t_{\mathrm{re}}$. t_{fan}(▼), t_{ref}(◆), t_{col}(■) and t_{fin}(●) (a-d). 40

2.11 Example C_3N cases for: C_3Ni, (a) & (b) ($Fr = 0.4$ and $t_{\mathrm{re}} = 10$); C_3Nii, (c) & (d) ($Fr = 0.6$ and $t_{\mathrm{re}} = 11.4$); and C_3Niii, (e) & (f) ($Fr = 0.7$ and $t_{\mathrm{re}} = 11$): (a), (c), (e) Characteristic diagram displaying the flow boundaries (–), x_{ref} and x_{fan} ($\cdots -$), the shock x_s (- -) and $x_{\mathrm{fin}}(\cdot)$; (b), (d), (f) Shock velocity for $t > t_{\mathrm{re}}$. t_{fan}(▼), t_{ref}(◆), t_{col}(■) and t_{fin}(●) (a-f). 41

2.12 Example C_3F cases for: C_3Fi, (a) & (b) ($Fr = 0.3$ and $t_{\mathrm{re}} = 20$); C_3Fii, (c) & (d) ($Fr = 0.8$ and $t_{\mathrm{re}} = 22$); and C_3Fiii, (e) & (f) ($Fr = 0.9$ and $t_{\mathrm{re}} = 20$): (a), (c), (e) Characteristic diagram displaying the flow boundaries (–), x_{ref} and x_{fan} ($\cdots -$), the shock x_s (- -) and $x_{\mathrm{fin}}(\cdot)$; (b), (d), (f) Shock velocity for $t > t_{\mathrm{re}}$. t_{fan}(▼), t_{ref}(◆), t_{col}(■) and t_{fin}(●) (a-f). 42

2.13 Structure of the (Fr, t_{re}) parameter space up to C_3 shocks. Numerically determined boundaries between regions (–), sub-regions ($\cdots$) and N/F (- -) are shown. 44

2.14 Depth $h(-\cdot)$ and velocity $u = m/h(\cdots)$ profiles at eight equally-spaced time steps until the shock reaches the head of the current for the following cases: U_2Ni (left) and C_2Ni (right). Positions of the curves x_{ref}(◆) and x_{ref}(▼) are displayed on the x-axis until they intersect the shock x_{s}(■). The position of x_{fin}(●) is also displayed on the x-axis. 45

2.15 Computed momentum at the head of the flow when the shock arrives, $m(x_N, t_{\mathrm{col}})$, for four Froude numbers $Fr = (0.5, 0.75, 1, 1.25)$ in increments of 2 pulse separation times t_{re} (–) against: (a) pulse separation time t_{re}; (b) displacement of the head at the time of collision, t_{col}. Momentum at the collision time, t_{col}, for a single release of twice the size $t_{\mathrm{re}} < 1$ ($\cdots$) is also shown. 46

3.1 Schematic of experimental design, based on Ho et al. (2018a,b) the first lock box is dyed red (lighter colour, in greyscale) and the second blue (darker) and are filled to a depth of 0.1 m. The ambient depth is 0.25 m . Pneumatically controlled gates release the first gate at $t = 0$ and the second at $t = t_{\mathrm{re}}$. The evolving flow is filmed with either a pair of rolling cameras or a fixed high-speed camera (not shown). Overspill boxes at either enable surface waves to dissipate and any excess ambient fluid to drain from the tank. Not to scale. 51

3.2 Stills from experimental videos demonstrating the mostly un-mixed and laminar transitional behaviour at the head of the current (left) and the fully mixed and turbulent behaviour after the pulse reaches the head (right). Ruler for scale in centimetres. 52

3.3 Snapshot of the lock-boxes just before the release of the lock gates. No mixing can be observed between the glycerol/water mixtures and the ambient. 57

3.4 The Ubbelohde or suspended level viscometer (Ubbelohde, 1936). The two bulbs are partially filled with the liquid to be measured through pipe a. Whilst pipe b is sealed, the liquid is drawn up pipe c, through suction, to above A. Pipe b is then released and the suction removed to allow the liquid to flow through the constriction below B. The time taken, t_{con}, to drain the fluid is proportional to the viscosity for large values of t_{con}. The device is kept vertical with clamps during the entire process. Not to scale. 60

3.5 Diagram of a parallel-plate rheometer. The plate separation, H, radius of the circular plate R and angular velocity Ω_{pp} are fixed. The viscosity is calculated by measuring the required torque M to maintain a fixed angular velocity, Ω_{pp}. In axisymmetric cylindrical coordinates (r, z). 63

3.6 Measured dynamic viscosity, μ ($\mathrm{kg{\cdot}m{\cdot}s}^{-s}$), from the rotary viscometer against the natural log of the target angular velocity, Ω_{pp} (s^{-1}), for different glycerol concentrations: 0.77 (sample 1); 0.84 (samples 2a, 2b and3); 0.90 (sample 4); and 0.995 (sample 5). Measurements were repeated over a range of temperatures to capture the range of temperatures observed during experiments. 65

3.7 Schematic of a pinhole camera. Light from an objects travels in straight lines through the aperture creating an inverted image on the image plane. The field of view is the angle between the the two extreme edges that are displayed on the image plane. 67

3.8 The affect on parallel rays of light from a convex (top) and concave (bottom) lens with focal lengths, Z_c and $-Z_c$, respectively. The convex lens bends light rays towards the central axis, whereas the concave lens bends light rays away. 68

3.9 The affect of different types of lens on the field of view in a camera. The convex lens has a narrow field of view, but increase the magnification and the amount of light entering from a more distance object. A concave lens has a negative focal length and any object outside of the camera will be out of focus. As such, the concave lens is not useful on its own, but is an essential part of a compound lens. 68

3.10 The virtual image plane is the observed space capture at distance of the focal length of the camera Z_c with plane co-ordinates (X_c, Y_c) centred about the principal axis (dashed line). 69

3.11 (a) A mesh grid with no distortion. Types of quadratic (b and c) and quartic (d and e) radial distortions: (a) barrel ($k_1 < 0, k_2 = 0$), (b) pincushion ($k_1 > 0, k_2 = 0$), (c) moustache ($k_1 < 0, k_2 > 0$) and (d) ($k_1 > 0, k_2 < 0$). The names are derived from common objects. The line appear to bulge in the centre of a barrel distortion resembling a barrel. The pincushion pinches at the corners. Lines near the centre curve upwards near the centre and then the other way in a moustache distortion. The final type does not appear in standard lens and, as such, has no name. 71

3.12 Still photos of the checkerboards taken in different orientations. The corners of the square detected using the detectCheckerboardPoints function in MATLAB are shown by red circles. Although not all of the corners are detected, a sufficient number are detected in order to the use the camera calibration. 73

3.13 Still photos of a front on checkerboard taken before camaera calibration (top) and afterwards(bottom). Straight red lines are drawn between the checkerboard corners to demonstrate the curvature that is removed by lens correction. 74

3.14 Downstream (case: RD90-3/8) image at dimensionless time $t = 9.0$ after release taken from the first camera. The cross-stream variation in head position can be observed. The variations cover the region between 1.84 and 1.85 m. The head position is taken to be the larger of these two values. 76

3.15 Downstream images (case: RD90-3/8) from the second camera, which tracks the head of the flow: (a) $t = 5.5$ and (b) $t = 10.4$ after initial release. Blurring is observed in (a), as a result of the shutter speed on the camera being too low. Parallax error may be observed in (b), because the camera is centred at 2.03 m. 76

3.16 Single-release (case: RS84) at t =2.4 (a & b) and t =12.8 (c & d): (a & c) - RGB colour channels and (b & d) - HSV colour channels. The RGB channels were normalised by three times the lightness, $3I = (R+G+B)$, before being converted to the HSV channels. Note that value, V, is the maximum value of the three RGB channels and, generally greater than the lightness, I. 79

3.17 R, S and H channels at $t = 2.4$ (a) and $t = 12.8$ (b) of a RS84 single-release flow. Regions of hue, H, greater than 0.65 and less than 0.1, regions of saturation, S, less than 0.1 and regions of red, R, less that 0.15 have been masked and excluded. 80

3.18 Images at $t = 2.4$ (a) and $t = 12.8$ (b) of a RS84 single-release flow. Coloured lines correspond to the highest vertical value with saturation, S, above: 0.4 (red); 0.6 (black); or 0.8 (green). The position of the current is significantly easier to identify by eye early in the experiments. 81

3.19 Colour channels for the double-release case: RD84-1/2 at $t = 3.4$ (a & b) and $t = 18.1$ (c & d). Corresponding channels are: RGB (a & c) and HSV (b & d). 82

3.20 Images for the double-release case RD84-1/2 for the camera tracking the pulse at $t = 3.4$ (a) and $t = 18.1$ (b). The black line indicates the boundary of the pixels that were excluded, the white line represents the points with the largest vertical gradient in hue H and the green line represents the largest vertical gradient in green. The excluded pixels are coloured grey. 83

3.21 Dimensionless head position, X_N (a-c) and speed $\dot{X}_N$ (d-f) for each of the three experiments conducted for each concentration: RS77 (a&d), RS84 (b&e) and RS90 (c&f). 85

3.22 Dimensionless position of the head, X_N, and pulse, X_s, (a-c) and speed of the head, $\dot{X}_N$, and pulse, $\dot{X}_s$, (d-f) for all of the experiments conducted for the following cases: RD77-1/2 (a&d), RD84-1/2 (b&e) and RD90-3/8 (c&f). Pulse separation times t_{re} are displayed on the t axis for each case: (a) 2.48, (b) 2.33 and (c) 3.36. 86

3.23 Snapshots from the RD90-1/8 case after $t_{\mathrm{re}} = 23.6$. Initially (top left), the pulse is predominantly in the second current (blue or darker fluid). The pulse gradually transitions into the first current (top right) and completely separates from the second current (bottom). Over time the pulse becomes wider and less pronounced. 87

3.24 Pulse arriving at the head for the RD77-1/2 case with release time $t_{\mathrm{re}} = 2.48$. The pulse arrives from the left and reaches the head of the current (top three images corresponding to $t = 10.67$, 12, 13.3). However, the current remains relatively dense until over 2 lock-lengths further downstream (bottom image at $t = 21$). Each image is approximately 35 cm wide. 88

3.25 Pulse arriving at the head for the RD84-1/8 case with release time $t_{\mathrm{re}} = 8.6$. The pulse arrives from the left and, but becomes indistinguishable from the current before it reaches the head (the three images correspond to $t = 24.1$, 27.5, 31). Each image is approximately 25 cm wide. 89

3.26 Pulse arriving at the head for the RD90-3/8 case with release time $t_{\mathrm{re}} = 3.36$. The pulse arrives from the left and, but becomes indistinguishable from the current before it reaches the head. (three images correspond to $t = 14.9$, 17.5, 20.2). Each image is approximately 25 cm wide. 90

3.27 (a) Head position against time and (b) head velocity against time for the single release experiments, x_N, and shallow-water simulations, X_N for concentration, 0.77, 0.84 and 0.90 and Froude numbers, Fr, 0.88, 0.83 and 0.80, respectively. Head position is plotted on the x-axis for comparison with the characteristic diagrams in chapter 2. 91

3.28 Shock position for the experiments, X_s, and the shallow-water model, x_s, at different gate release separation times, t_{re}: (a) concentration 0.84 ($Fr = 0.80$) and (b) concentration 0.90 ($Fr = 0.77$). 93

3.29 Shock velocity for the experiments, $\dot{X}_s$, and the shallow-water model, $\dot{x}_s$ at different gate release separation times, t_{re}: (a) concentration 0.84 ($Fr = 0.80$) and (b) concentration 0.90 ($Fr = 0.77$). 93

3.30 Comparison of the ratio of shock displacement from the front of the second lock box between experiments and the shallow-water model at concentrations 0.84 (–) and 0.90 ($\cdots$) for four different gate release separation times, t_{re}. 94

4.1 Diagram of the lock exchange problem. Initially denser (red) fluid and less dense (blue fluid) is held in place by a vertical gate in the centre of the domain (top). At $t = 0$ the gate is released with the density difference driving the flow outwards (bottom). 98

4.2 Geometry for the lock-exchange problem. A box length L, height H and width W in the x-, y-, and z-directions, respectively. The aspect ratios used in all simulations are $L/H = 2$ and $W/H = 1$. 100

4.3 the Legendre polynomials P_n up to degree 6. The Legendre polynomials are the unique polynomial solutions to the equation $\langle P_i, P_j \rangle = 2/(2i + 1)\delta_{ij}$. 106

4.4 The Legendre interpolation basis functions π_j based of the Legendre polynomial of degree $\mathcal{N} = 6$. At the GLL points ξ_k $\pi_j(\xi_k) = \delta_{jk}$. . . . 107

4.5 Example spectral element mesh on a $2 \times 1 \times 1$ domain with $32 \times 16 \times 16 = 2^{13}$ elements and $\mathcal{N} = 8$ (a). Close up highlighting the node structure within each element. The total number of nodes in the mesh is $2^{13} \times 8^3 \approx 4.2 \times 10^6$. 108

4.6 Concentration profiles ϕ for a one-dimensional pure diffusion problem at $t = 0$ and $t = 13.5$. The Péclet number Pe is fixed at 7000. 117

4.7 Distribution of concentration ϕ in the (x, y)-plane at $t = 0$ (a) and $t = 13.5$ (b) for the pure diffusion problem. 118

4.8 Normalised residual potential energy ($NRPE$, left) and Normalised θ ($N\theta$, right) over time for the pure diffusion problem. 119

4.9 Normalised residual potential energy $NRPE$ against time for different meshes: (a) - $\gamma = 0$, (b) - $\gamma = 0.1$, (c) - $\gamma = 1$, and (d) - $\gamma = 10$ . . . 123

4.10 Normalised volume fraction of mixed fluid $N\theta(t)$ against time for the four meshes A, B, C and D. The curves for B and C for $\gamma = 0$ and B, C, and D for $\gamma = 10$ are coincident. 123

4.11 Potential energy PE, Kinetic energy KE, Available potential energy APE and dissipated energy D for $\gamma = 10$ simulations with the meshes used. The curves for B, C, D and E are coincident. 124

4.12 Normalised residual potential energy $NRPE$ (a) and Normalised volume fraction of mixed fluid $N\theta$ (b) against time for mesh C and $\gamma = 0$ simulations at different Courant numbers 124

4.13 Potential energy PE, Kinetic energy KE, Available potential energy APE and dissipated energy D_v for $\gamma = 0$ on mesh C with Courant numbers of 0.1, 0.25 and 0.5. 125

4.14 Pseudo-colour plots of concentration ϕ on the centre plane $z = 1/2$ over $t = 0.5$ time steps for the $\gamma = 0$ ($Re_1 = Re_2 = 1000$). Deep red corresponds to the denser fluid 2 and deep blue corresponds to fluid 1. 127

4.15 Pseudo-colour plots of concentration ϕ on the centre plane $z = 1/2$ for three different cases: $\gamma = 0$ (left), $\gamma = 1$ (middle) and $\gamma = 10$ (right). These correspond to layer two Reynolds numbers $Re_2 = (1000, 500, 91)$, respectively. Deep red corresponds to the denser fluid 2 and deep blue corresponds to fluid 1. 128
4.16 Isosurface plots of concentration ϕ for $\gamma = 0$ (left) and $\gamma = 10$ (right). Each coloured surface corresponds to concentrations $\phi = (0.05, 0.25, 0.5, 0.75, 0.95)$ ranging from deep blue ($\phi = 0.05$) to deep red $\phi = 0.95$. 129
4.17 Isosurface plots of concentration ϕ for $\gamma = 0$ (left) and $\gamma = 10$ (right). Each coloured surface corresponds to concentrations $\phi = (0.05, 0.25, 0.5, 0.75, 0.95)$ ranging from deep blue ($\phi = 0.05$) to deep red $\phi = 0.95$. 130
4.18 Pseudo-colour plots of concentration for $\gamma = 0$ (left) and $\gamma = 10$ (right) overlaid with depth averaged profiles calculated on the centre plane $z = 1/2$: $h_{\text{int}}(x, z, t)$ (yellow); $h_{\max}(x, z, t)$ (red); $h_{\min}(x, z, t)$ (blue); and $h_{\text{ave}}(x, z, t) = (h_{\max}(x, z, t) + h_{\min}(x, z, t))/2$ (green). . . . 131
4.19 Centre-plane depth of the flow $h_{\text{ave}}(x, 1/2, t)$ for the cases $\gamma = 0, 0.1, 1, 10$.132
4.20 Pseudo-colour plots of u and v on the centre plane $z = 1/2$ for $\gamma = 0$. The lines overlaid are $h_{\text{ave}}(x, 1/2, t)$ (green). 133
4.21 Pseudo-colour plots of u and v on the centre plane $z = 1/2$ for $\gamma = 10$. The lines overlaid are $h_{\text{ave}}(x, 1/2, t)$ (green). 134
4.22 Normalised residual potential energy $NRPE$ (a) and normalised-θ $N\theta$ for the cases $\gamma = 0, 0.1, 1, 2, 4, 10$. 135
4.23 Energy distribution for the cases $\gamma = 0, 0.1, 1, 2, 4, 10$: potential energy PE (top-left), kinetic energy KE (top-right), available potential energy APE (bottom-left) and energy dissipated D (bottom-right). . 135
4.24 For the cases $\gamma = 0, 0.1, 1, 2, 410$: Gain in residual potential energy $D_m = RPE(t) - RPE(0)$ (top-left); energy lost to viscous dissipation D_v (top-right); rate of change of residual potential energy $\mathrm{d}D_m/\mathrm{d}t$ (bottom-left); and rate of change of viscous dissipation $\mathrm{d}D_v/\mathrm{d}t$ (bottom-right). 136
4.25 Isosurface plots of concentration ϕ for $\gamma = 0$ (top), $\gamma = 1$ (middle) and $\gamma = 10$ (right) cases and at times $t = 6$ (left) and $t = 9$ (right). Each coloured surface corresponds to concentrations $\phi = (0.05, 0.25, 0.5, 0.75, 0.95)$ ranging from deep blue ($\phi = 0.05$) to deep red $\phi = 0.95$. 137
4.26 Surface area of the 0.5 isosurface $A_{0.5}$ against time for the cases $\gamma = 0, 0.1, 1, 2, 4, 10$ 139

5.1 Schematic of the two-layer shallow-water model for the lock-exchange problem. Each layer has depth h_i, depth-averaged velocity u_i and Reynolds number $Re_i = \sqrt{g'H^3/2\nu_i^2}$, where ν_i is the kinematic viscosity of layer i and $g' = g(\rho_1 - \rho_2)/\rho_2)$ is the reduced gravity. The total depth is fixed, so that $h_1 + h_2 = H$ 142

5.2 Regions in (h, m)-space (a) and (h, u)-space (b), where the system of equations are hyperbolic, shown in yellow. Outside of these ranges, shown in purple, the finite-volume schemes cannot be applied. Critically, as $h \to 1$, the equations become elliptic for all finite values of the velocity u. Thus an arbitrarily thin wetting layer in the overlying fluid is not compatible with a finite-volume scheme. 147

5.3 The five possible solutions to a linearised scalar conservation equation for the Riemann problem. Solid lines represent shocks (a and b) in the Riemann solution or expansion fan regions (c,d and e). Dotted lines represent characteristic curves. They are characterised by the values of the eigenvalues to the left $(\lambda_l^p$ and right $(\lambda_r^p$ of the cell interface located at the position of the t axis: (a) $(\lambda_r^p < \lambda_l^p < 0)$ - left going shock, (b) $(0 < \lambda_r^p < \lambda_l^p$ - right going shock, (c) $(\lambda_l^p < \lambda_r^p < 0)$ left going rarefaction wave, (d) $(0 < \lambda_l^p < \lambda_r^p)$ - right going rarefaction wave and (e) $(\lambda_l^p < 0 < \lambda_r^p)$ transonic rarefaction wave. 153

5.4 Stability of linearly perturbed solution in: (a) (h_0, m_0)-space and (b) (h_0, u_0)-space. Dark blue represents the region that is linearly unstable for $Re_1/Re_2 = 1$. Each subsequent colour (up to yellow, where $Re_1/Re_2 = 100$) represents the additional region that becomes unstable as the Reynolds number ratio is increased. The region coloured white is stable for all Reynolds number ratios considered. As discussed in the text, the stability is independent on magnitude of the Reynolds numbers (only their relative magnitude) and the wavenumber k. 160

5.5 Evolution of the depth, h, and momentum over time with the following parameters: $N_x = 1600, Cr = 0.02, D_1 = 10^{-3}, Re_1 = 1000, Re_2 = 1000$. 162

5.6 Depth h (top) and momentum m (bottom) profiles at $t = 12.5$ for various values of N_x. Other parameters are: $Cr = 0.02, D_1 = 0, Re_1 = 1000, Re_2 = 1000$. As N_x increases, the profiles converge towards a value. For low values of N_x significant numerical diffusion can be observed. 164

5.7 ℓ_1-error for depth E_h and momentum E_m at: (a) fixed Courant number $Cr = 0.02$ (a) and $N_x = (100, 200, 400, 800, 1600, 3200)$ and (b) fixed $N_x = 1600$ and $Cr = (0.5, 0.25, 0.1, 0.05, 0.02, 0.005)$. Other parameters for these graphs are $D_1 = 1/1000$, $Re_1 = 1000$ and $Re_2 = 1000$. The gradient of the lines (computed using the end points) provide the convergence rate of the scheme. $E_h \sim \Delta x^{0.93}$, $E_m \sim \Delta x^{1.06}$, $E_h \sim \Delta t^{1.01}$, $E_m \sim \Delta t^{0.99}$. 165

5.8 Depth h (top) and momentum m (bottom) profiles at $t = 12.5$ for four different values of D_1. Other parameters are: $N_x = 1600, Cr = 0.02, Re_1 = 1000, Re_2 = 1000$. 166

5.9 Depth (top of each pair) and momentum (bottom of each pair) profiles for the lock exchange problem with both layers having the same Reynolds number compared to the inviscid case $Re = \infty$. Profiles are at times: (a) 0.5, (b) 2.5, (c) 8.5 and (d) 12. 168

5.10 Depth (top of each pair) and momentum (bottom of each pair) profiles for the lock exchange problem with both layers having the same Reynolds number compared to the inviscid case $Re = \infty$. Profiles are at times: (a) 0.5, (b) 2.5, (c) 3.5 and (d) 12. Inset in (a) shows the head of the left propagation wavefront. 169

5.11 Velocity profiles for the top (a&c) and bottom (b&d) at $t = 0.5$. The top two graphs (a&b) vary the Reynolds number in both layers, whereas the bottom two graphs (c&d) fix the top layer Reynolds number ($Re_1 = 1000$) and vary the basal layers Reynolds number Re_2. Top layer velocity is computed $u_1 = -m/(1-h)$ and basal layer $u_2 = m/h$. 170

5.12 Total viscous diffusion ψ ($--$) and the contribution from each layer $h(1-h)\psi_1/Re_1$ ($-\cdot$) and $h(1-h)\psi_2/Re_2$ ($\cdots$) at $t = 0.5$ for the left-travelling wavefront, when the viscosity in both layers are equal. (a), (b), and (c) corresponds to the Reynolds number in both layers being 200, 50, and 25, respectively. (d) compares the total viscous diffusion for these three cases. Co-ordinates in the frame of the left travelling wavefront ξ_L are used. 171

5.13 Total viscous diffusion ψ ($--$) and the contribution from each layer $h(1-h)\psi_1/Re_1$ ($-\cdot$) and $h(1-h)\psi_2/Re_2$ ($\cdots$) at $t = 0.5$ for the right-travelling wavefront, when the viscosity in the top layer is fixed at $Re_1 = 1000$. (a), (b) and (c) corresponds to the Reynolds number in the basal layers being 1000, 167 and 24, respectively. (d) compares the total viscous diffusion for these three cases. Co-ordinates in the frame of the right travelling wavefront ξ_R are used. 173

5.14 Total viscous diffusion ψ $(--)$ and the contribution from each layer $h(1-h)\psi_1/Re_1$ $(-\cdot)$ and $h(1-h)\psi_2/Re_2$ $(\cdots)$ at $t = 0.5$ for the left-travelling wavefront, when the viscosity in the top layer is fixed at $Re_1 = 1000$. (a), (b) and (c) corresponds to the Reynolds number in the basal layers being 1000, 167 and 24, respectively. (d) compares the total viscous diffusion for these three cases. Co-ordinates in the frame of the left travelling wavefront ξ_L are used. 174

5.15 Depth-averaged concentration h_{ave} and fluid 2 momentum m_{ave} from the DNS and fluid 2 depth h and momentum m from the two-layer shallow model at five different times. The two-layer shallow water model uses the profiles of h_{ave} and m_{ave} at $t = 0.5$ as initial conditions. 176

List of Tables

3.1 Properties of pure glycerol at room temperature (20 °C) (Christoph et al., 2006). 54

3.2 Temperature (T,° C) and concentration ranges considered by the three studies from which the empirical model of Cheng (2008) for the dynamic viscosity μ of glycerol-water mixtures is constructed. Also included is the maximum and mean error between the model fit and the data points in each of three works calculated by Cheng (2008). The percentage error is calculated $|\mu_{\text{predicted}} - \mu_{\text{actual}}|/\mu_{\text{actual}} \times 100\%$. 56

3.3 Table of experimental parameters. Key: R - rolling cameras, HS - high speed camera, S - single release, D - double release; glycerol concentration, α_g, by volume (0.77,0.84 or 0.90); and fraction of remaining fluid in the first lock at $t = t_{\text{re}}$ $(1/2, 3/8, 1/4, 1/8)$. The kinematic viscosity of the current and the Reynolds number $Re = \sqrt{g' h_{\text{lock}}^3}/2\nu$ Note that at 0.90 concentration, the time to reach a remaining fraction of 1/8 was of the order of minutes and a t_{re}-value of 23.5 was chosen instead. 61

3.4 Temperature measurements taken from the ambient, first and second lock-boxes. The corresponding sample or batch number is given for each case. For the cases measured, the temperature of the mixture before the u-tube viscometer used, the time for the liquid to drain and the corresponding kinematic viscosity calculated from the u-tube viscometer also given. Finally, the Reynolds number calculated from $Re_{\text{act}} = \sqrt{h_{\text{lock}}^3 g'}/2\nu$ is given. 62

3.5 Table of the measured dynamic viscosities from the rotary rheometer for the six different samples at glycerol concentration α_g. The target dynamic viscosity and the current density, ρ_c, is calculated using the empirical model of Cheng (2008). The viscosity discrepancy is calculated as $|\mu_{\text{measured}} - \mu_{\text{target}}|/\mu_{\text{target}}$. The corresponding Reynolds numbers from the measured viscosity, $Re_{\text{act}} = \sqrt{g' h_{\text{lock}}^3} \rho_c / 2\mu$, are given. The measured dynamic viscosity is calculated from the mean value over possible angular velocities, Ω_{pp}, from the data presented in figure 3.5 with the exception of sample three, where the values $\Omega_{pp} \leq 0.1$ ($\log(\Omega_{pp}) \leq -2.3$) are excluded before averaging. 66

3.6 Table of parameters and errors from the camera calibration. Errors for the radial diffusion coefficients, k_i are one standard deviation of the data. The camera co-ordinates of the top right corner of the image is $(x_{\max}, y_{\max})$ and has corresponding distance $r_{\max}$ from the principal point. This is approximately equivalent for all four corners of the image. The correction is calculated at the extreme points. Also given is the smallest and largest corrections at one standard deviation from the mean. 72

4.1 Fluid 2 (current) Re_2 and fluid 1 (ambient) Re_1 Reynolds numbers, Schmidt numbers Sc and Péclet numbers Pe corresponding to the cases studied in this chapter. 105

4.2 Coefficients for the k-th order backwards difference scheme (a_i) and the extrapolation scheme (b_i) for $k = 1, 2, 3$. 109

4.3 Characteristics of the meshes presented in this chapter. The number of elements in each spatial direction (x, y, z) is (N_x, N_y, N_z). The total number of elements in the domain is $\mathcal{E} = N_x N_y N_z$. Each element contains $\mathcal{N}$ GLL points in each spatial direction giving the total number of nodes $n = \mathcal{E}\mathcal{N}^3$. 121

4.4 Computational time in core hours (number of computational cores times the clock time) for each case and mesh. The number of cores used for each simulation is shown in brackets. Dashed indicate that a lower resolution mesh was deemed sufficiently resolved and hence not conducted. 121

List of abbreviations

Abbreviations

APE	Available Potential Energy
KE	Kinetic Energy
$NRPE$	Normalised Residual Potential Energy
PE	Potential Energy
RPE	Residual Potential Energy
BDF	Backwards Difference
DNS	Direct Numerical Simulation
EXT	Extrapolation
FEM	Finite Element Methods
GLL	Gauss-Lobatto-Legendre
HSV	Hue, Saturation and Value
LES	Large Eddy Simulation
ODE	Ordinary Differential Equation
PDE	Partial Differential Equation
RANS	Reynolds-Averaged Navier-Stokes
RGB	Red, Green and Blue
SEM	Spectral Element Methods
SGS	Sub-Grid Scale

Chapter 1

Introduction

Gravity currents are flows driven by pressure gradients resulting from density differences. These may be the result of temperature, suspended sediment or salinity differences. Gravity currents form significant geophysical flows in atmospheric, terrestrial and subaqueous environments. Examples include landslides, avalanches, turbidity currents, pyroclastic currents and lahars (Simpson, 1997). A pyroclastic current produced by an eruption of the Soufriére hills volcano, Montserrat is displayed in figure 1.1. Pyroclastic currents are comprised of a hot gas with a suspension of particles which creates an excess density to the surrounding air (Doyle et al., 2010). They can attain speeds of hundreds of metres per second (Doyle et al., 2010), travel for greater than 100 km and transport blocks of nearly a metre in diameter (Roche et al., 2016). The majority of fatalities from volcanic eruptions are associated with pyroclastic currents (Breard and Lube, 2017). Generally, gravity currents are restricted to the study of flows along (nearly) horizontal boundaries and closely related problems, such as a liquid protruding in between a less dense and a more dense layer, or a stratified density gradient are classed as intrusions (Ungarish, 2009). When the pressure gradients drive the flow vertically, flows are often classed as plumes (Turner, 1979; Woods, 2010). Although the driving forces are the same, differing flow dynamics are observed.

Two significant types of underwater gravity currents are sub-aqueous debris flows and turbidity currents, figure 1.2. Both have a density difference with the surrounding water caused by the presence of suspended sediment and are the dominant process for transporting sediment from shallow to deep water environments (Meiburg and Kneller, 2010). One mechanism of initiation for sub-aqueous debris flows is the geotechnical failure of the sea-floor. The resulting sea-floor landslide suspends a large amount of sediment, causing a pressure differential driving the cur-

Figure 1.1: Pyroclastic flow produced by an eruption of the Soufriére hills volcano, Montserrat. Image published by Huppert (2006) and taken by R. S. J. Sparks.

rent down the slope. A single flow can transport 100 km^3 (Piper et al., 1999), which is roughly ten years worth of sediment transported by all the world's rivers (Milliman and Syvitski, 1992). Sub-aqueous debris flows have their sediment supported by matrix strength (particle-particle interaction), exhibit laminar flow characteristics and non-Newtonian behaviour such as yield strength and shear-thinning or shear-thickening (Talling et al., 2012). Further, a wide range of particle sizes can be observed ranging from silts to sands and even cobbles and boulders (De Blasio et al., 2011). Turbidity currents produce graded deposits (turbidites) by the preferential settling of larger grains, figure 1.3. Debris flow deposits (debrites) are associated with en masse settling, where the entire flow, or parts of it, arrest almost instantaneously (Amy and Talling, 2006).

Sub-aqueous debris flows can transition into turbidity currents through a variety of mechanisms discussed by Felix and Peakall (2006):

- Instant or gradual liquefaction of part or the entire initial sediment mass (Kuenen and Migliorini, 1950);
- Ingestion of water underneath the head of the debris flow (Allen, 1971);
- Progressive disintegration, i.e. the continual break up into smaller parts (Schwarz, 1982);

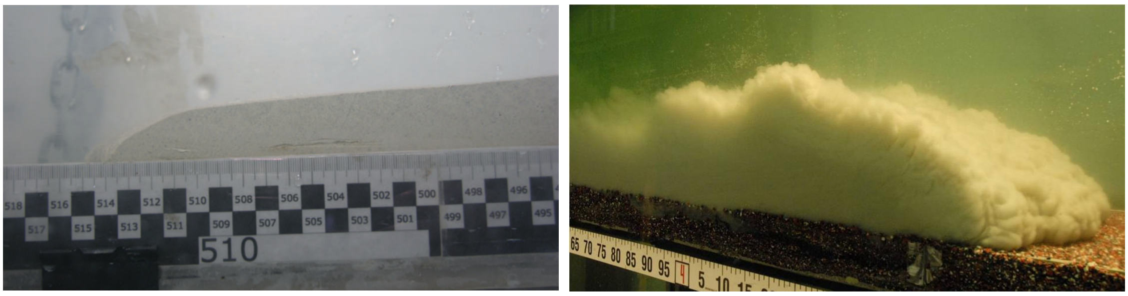

(a) (b)

Figure 1.2: Sandy debris flow produced in the laboratory. Image published in De Blasio et al. (2011). b - Laboratory scale turbidity current. Image published in Sequeiros et al. (2010)

- Dilution through a hydraulic jump (van Andel and Komar, 1969);
- Erosion of material by shear at the head (Hampton, 1972); and
- Turbulent mixing with the overlying layer of water as a result of the waves and instabilities (Morgenstern, 1967).

(a) (b)

Figure 1.3: (a) - Turbidite deposit consisting of a upwards-fining sandstone, a siltstone layer and a mudstone layer. (b) - Pebble-rich debrite deposit in the Paganzo Basin, south-western La Rioja Province, Argentina. Image published by Fallgatter et al. (2017).

Critically, the turbidity currents predicted by all these methods are dilute and usually contain only a limited amount of the initial mass contained in the underwater landslide, i.e. they are inefficient. Further, the transition takes place over long time and length scales. Turbidity current deposits indicate the transition can not only occur rapidly but also suspend more of the initial mass (Talling et al., 2002).

Some events may remain as debris flows for their entire flow distance (up to thousands of kilometres (Embley, 1976)) with only slight changes in rheology. Whereas others may fully transform into turbidity currents before reaching the continental slope boundary (Talling et al., 2002). Sub-aqueous debris flow are more likely to transform than their sub-aerial counter-parts because of the increased resistance from the ambient (Norem et al., 1990) and the lack of surface tension from interstitial water (Mulder and Alexander, 2001).

Moreover, there is uncertainty regarding the driving mechanisms, for example, does the rheology control the transition to turbulent flow? Is the change in rheology driven by sediment deposition and suspension, or by mixing, or both? An increased understanding in these critical areas will lead to more accurate predictions of the attributes of turbidity currents created by sea-floor landslides. Knowledge of run-out lengths and sediment deposition patterns are critical, not only for predicting the location of turbidite deposits but for identifying regions with risk of damage from these currents.

The inherent pulsing nature of debris flows (Hungr, 2000) may also cause parts of the debris flow to transform through different mechanisms (Felix et al., 2009). Deposits of seismically generated turbidity currents at the Cascadia margin, Washington USA record multiple currents that combined downstream at as many as seven confluences (Goldfinger et al., 2017). The separation time between the flows can be negligible or of the order a few hours. Further, experimental modelling has demonstrated that the signature of individual turbidity currents can be destroyed after the different events interact (Ho et al., 2018b).

Turbidity currents have significant economic impact; they can travel with head speeds as high as 19 ms^{-1} on slopes less than $0.25°$ (Piper et al., 1999) and can cause significant damage to sea-floor equipment, including pipelines, oil rig moorings (Gonzalez-Juez et al., 2009; Barley, 1999) and seafloor telecommunication cables (Dengler et al., 1984; Heezen and Ewing, 1952) (which accounts for over 95% of trans-oceanic data transfer (Carter et al., 2009)). Turbidity currents are a key mechanism of sediment distribution from shallow to the deep marine environment throughout the oceans and lead to the creation of sedimentary rocks (turbidites) which are linked to gold deposits (Keppie et al., 1986), banded iron-formations (Lascelles, 2007) and host some of the largest hydrocarbon reservoirs (Weimer et al., 2007).

Pulses are a common feature in gravity currents and may result from flow instabilities, variable supply of dense material (Mulder and Alexander, 2001), combining of flows from different sources (Goldfinger et al., 2017), flow splitting and recombining (Nakajima and Kanai, 2000), or flow interactions with topography (Haughton, 1994). For example, failure mechanisms for landslides and similar events are varied (Wang et al., 2016) and can result in pulsed flows: an initial failure of an embankment or dam can create a steep main scarp as the supporting material slides away, which, in turn, can lead to a further 'retrogressive' failure. The process may repeat creating a significantly larger event comprised of many smaller pulses. Surges and pulses internal to gravity currents can have a significant impact on the hazards associated and flow properties when compared to a single release of the same volume. This is particularly significant for compositional gravity currents where the variations in velocity affect the deposition or erosion that can occur (Dorrell et al., 2018).

Figure 1.4: Aerial photo of the tailings dam break out at Merriespruit, South Africa. Image published in Fourie et al. (2001).

After 50 mm of heavy rain the gold mine tailings dam at Merriespruit, South Africa failed retrogressively (Wagener et al., 1998). The breakout led to the deaths of 17 people and widespread damage in the village of Merriespruit (Fourie et al., 2001), figure 1.4. After the dam had breached the tailings liquefied retrogressively creating a multi-pulsed flow over a period of a few minutes (Blight and Fourie, 2003). New Zealand's worst volcanic disaster occurred in 1953 at Mount Ruapehu when the tephra (rock fragments and particles ejected during a volcanic eruption) dam over the outlet of Crater Lake failed creating a lahar and the subsequent destruction of a rail bridge leading to the loss of 151 lives (O'Shea, 1954; Manville, 2004). A new tephra dam was formed following the 1995-96 eruption sequence that failed retrogressively 11 years later on the 18th March 2007 (Massey et al., 2010). Heavy rains in 1999 remobilised large tephra deposits deposited during the 1995-96 sequence. Hodgson and Manville (1999) observed deposits that showed between one and three depositional units signifying a pulsed flow.

Pyroclastic flows are a suspension of particles in hot gas that capable of travelling hundreds of metres per second (Doyle et al., 2010) and are formed from a collapsing eruption column (Wilson, 1976). A pyroclastic flow generated by the 1997 eruption of the Soufriére hills volcano contained three distinct major flow surges over its 25-minute duration (Loughlin et al., 2002). Deposits from the first two major surges partially filled the main drainage channel which the pyroclastic flow flowed along. This caused the third to overspill and travel into a region considered to be at low risk. The release dynamics of these gravity currents and potential evolution downstream in multiple surges impacts the dynamics of the flow. The deposits left by previous surges, and information they contain, can be destroyed by subsequent surges making flow dynamics difficult to identify. Further, run-out length, inundation zones and hazards are affected by the internal dynamics.

1.1 Aims of the thesis

Many geophysical gravity currents flows are modelled as single discrete events even though they arise from the combining of initially distinct flow events or separate into pulses and recombine further downstream. Pulses in gravity currents are studied in a double lock-release configuration in this thesis, where the denser fluid is held behind two lock gates that are released sequentially. The density difference drives the fluid out of the first lock-box as a gravity current. The second release creates a pulse that propagates towards the head of the current. The time between releases t_{re} and the dimensionless speed of the current are varied to study the range of possible dynamics. The equations are solved using the Lax-Wendroff finite-difference scheme employed by Bonnecaze et al. (1993). Experiments based on the setup of Ho et al. (2018a,b, 2019), but at a lower viscosity, are conducted. Further, a theoretical shallow-water model is used to analyse the flow dynamics. Preliminary, but unpublished, experiments of Ho et al. (2018a,b, 2019) indicate that a rapid transition from transitional or laminar behaviour to fully turbulent when the pulse reaches the head of the gravity current and a significant increase in the rate of mixing is observed. The experiments provide a source of validation to the shallow-water model and this transition from transitional or laminar behaviour to fully turbulent is studied further.

The effect of viscosity on mixing dynamics in a gravity-driven flow is then studied using the lock-exchange problem, where the lock-box occupies one-half of the domain. Direct numerical simulations, which fully resolve the flow dynamics are conducted in which the viscosity of the current is varied. The aim of this is to characterise the impact of a viscosity contrast between the ambient and the current on the flow dynamics and on the mixing that occurs. The results from the direct numerical simulations are then compared to a theoretical two-layer shallow-water model, which has significantly reduced computational time.

1.2 Studying gravity currents

1.2.1 Lock-exchange and lock-release problem

Gravity currents have been extensively studied by theoretical and experimental approaches, often based around the idealized lock-release or lock-exchange problem, where dense fluid is released by the rapid removal of a gate, providing a well-controlled initial condition, figure 1.5. The lock-box length is l and the depth of the locked fluid is h_{lock}. This method provides a suitable means to create repeatable fixed-volume currents that allow meaningful comparison to theoretical models (Hoult, 1972; Huppert and Simpson, 1980; Huppert, 1982; Shin et al., 2004; Lowe et al., 2005). Specifically in this thesis the lock-exchange problem will refer to a configuration where the locked dense fluid will occupy one half of the domain. Although these two problems are similar, quantitative differences between the two flows can be observed when the ratio between the locked fluid depth h_{lock} and the ambient depth H is less than two (Ungarish, 2009). This is discussed further in section 1.2.6. Recently, surge effects have been studied in the laboratory for turbulent saline flows using multiple lock-releases, in which a series of lock-boxes positioned behind the first were released at set times after the initial release (Ho et al., 2018a,b, 2019). The second current intruded into the first release and propagated towards the head of the current.

The lock-exchange and lock-release are examples of constant-volume grav-

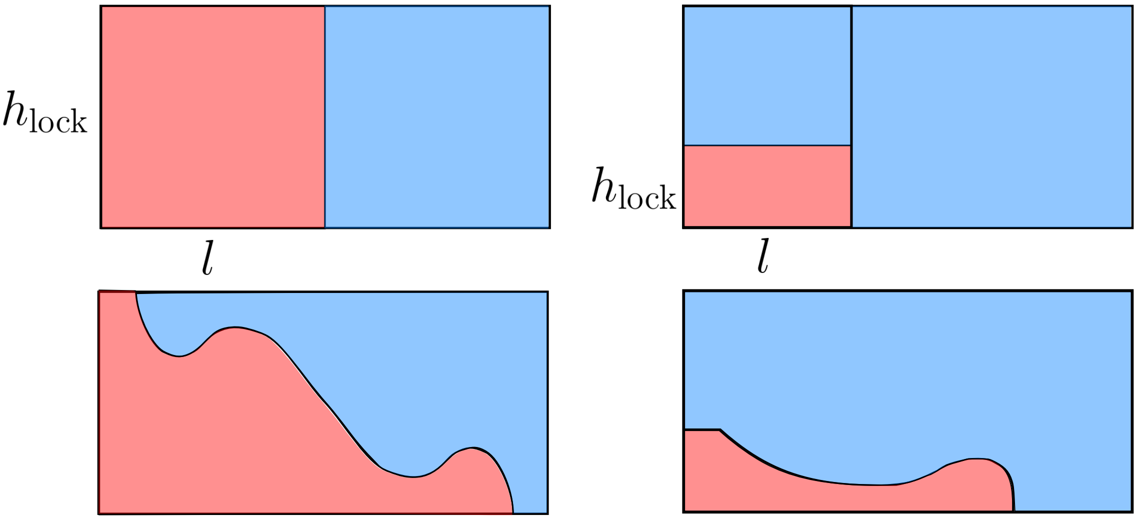

Figure 1.5: Lock-release (right) and lock-exchange (left) configuration before release where the fluid is held in place by a vertical lock gate (top) and just after where the denser red fluid is driven to the right by (bottom).

ity currents. I.e. the total volume per unit width $q_{\text{vol}} = h_{\text{lock}}l$ of dense material remains constant throughout. In theory, the material can be supplied at any variable rate, but the two most commonly studied are the constant-volume gravity current, where q_{vol} is constant, and the constant-flux, where the rate of supply of material $\mathrm{d}q_{\text{vol}}/\mathrm{d}t$ is constant (for example, Didden and Maxworthy (1982); Britter (1979); Hallworth et al. (1996) and many others).

The form of a gravity current is characterised by the Reynolds number of the flow $Re = \rho UL/\mu$, where ρ is the density, μ is the dynamic viscosity, and U and L are a suitable velocity and length scales for the current, indicates the dominant force that opposes buoyancy. When the Reynolds number of the current is small and the viscosity of the current is large compared to the ambient, $Re \ll 1$, the current propagates the balance is between viscous forces and buoyancy. In the viscous regime a better estimate for the size of viscous forces is the effective or reduced Reynold numbers $Re_\delta = \delta\rho UH/\mu$, where H is a depth scale for the flow and $\delta = H/L$ is the depth aspect ratio (Ungarish, 2009). However, when $Re \gg 1$, the balance is between buoyancy and inertial forces. For viscously dominated flows, like the spreading of honey, the depth decreases monotonically to zero in the direction of propagation and a parabolic velocity profile can be observed over the height of the current, figure 1.6. Whereas, when the Reynolds number is high and viscous forces are negligible a head is formed that rises up from the bed and a turbulent wake behind it is often observed, where mixing can occur, figure 1.6. A uniform mean velocity profile can be observed within the body of the current, but small-scale turbulent structures will be present throughout (Cantero et al., 2008)

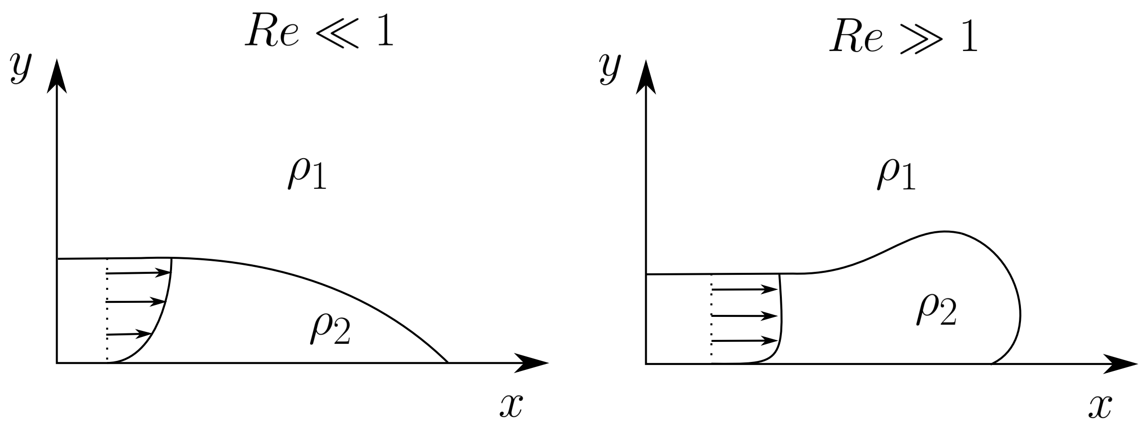

Figure 1.6: Gravity current for low Reynolds numbers (left) and high Reynolds numbers (right).

Initially an inertial gravity current of constant volume evolves at a constant propagation speed on a horizontal bed during the "slumping phase." When the lock-depth h_{lock} is less than half that of the ambient a backwards-travelling rarefaction wave is observed within the lock-box as the fluid drains out (Hogg, 2006). This disturbance reflects off the back of the lock-box and towards the head of the current and signifies the region of the flow affected by the finite supply of material. Upon reaching the head, the current enters a self-similar phase and the head propagates at a speed proportional to $t^{2/3}$ (Rottman and Simpson, 1983; Hogg, 2006). For viscously dominated lock-release gravity currents, a self-similar phase exists in which the current propagates at a speed proportional to $t^{1/5}$.

1.2.2 Navier-Stokes equations

For a general fluid-flow problem in orthogonal co-ordinates $\mathbf{x} = (x, y, z)$ with horizontal direction x, vertical direction y, cross-stream direction z, and corresponding velocity components $\mathbf{u} = \mathbf{u}(\mathbf{x}, t) = (u, v, w)$, the equations for mass and momentum conservation are (Tritton, 2012):

$$\rho \left(\frac{\partial \mathbf{u}}{\partial t} + (\mathbf{u} \cdot \nabla) \mathbf{u} \right) = - \nabla p + \nabla \cdot \boldsymbol{\tau} + \rho \mathbf{g}, \tag{1.1}$$

$$\frac{\partial \rho}{\partial t} + \nabla \cdot (\rho \mathbf{u}) = 0, \tag{1.2}$$

where $\rho = \rho(\mathbf{x}, t)$ is the density, $p = p(\mathbf{x}, t)$ is the pressure, $\mathbf{g} = (0, -g, 0)$ is the body force, g is acceleration due to gravity and $\boldsymbol{\tau}$ is the deviatoric stress tensor. For a viscous Newtonian fluid the deviatoric stress tensor $\boldsymbol{\tau}$ is

$$\boldsymbol{\tau} = \mu \left(\nabla \mathbf{u} + \nabla \mathbf{u}^T \right), \tag{1.3}$$

where μ is the dynamic viscosity of the liquid. Further, if the flow is assumed to be incompressible, i.e. $D\rho/Dt \equiv \partial\,\rho/\,\partial\,t + \mathbf{u}\cdot\nabla\rho = 0$, then the equations reduce to the incompressible Navier-Stokes equations

$$\begin{aligned}\rho\left(\frac{\partial\,\mathbf{u}}{\partial\,t} + (\mathbf{u}\cdot\nabla)\,\mathbf{u}\right) =& -\nabla p + \mu\nabla^2\mathbf{u} + \rho\mathbf{g} && (1.4)\\ \nabla\cdot\mathbf{u} =& 0. && (1.5)\end{aligned}$$

When the ambient density and viscosity are small relative to that of the current $\rho_2 \gg \rho_1$, $\mu_2 \gg \mu_1$ the flow in the ambient can be neglected (for example, Stansby et al. (1998)) and replaced with a free-surface boundary condition. If the current and ambient have similar densities $\rho_2/\rho_1 \sim 1$, then the Boussinesq approximation can be applied. The Boussinesq approximation neglects density variations in the governing equations except in the gravitational forcing term and enables a simplified momentum equation for the current to be posed in this case

$$\left(\frac{\partial\,\mathbf{u}}{\partial\,t} + (\mathbf{u}\cdot\nabla)\,\mathbf{u}\right) = -\frac{1}{\rho_2}\nabla p + \nu_2\nabla^2\mathbf{u} + g'(0,-1,0), \qquad (1.6)$$

where $\nu_2 = \mu_2/\rho_2$ in the kinematic viscosity of the current and $g' = g(\rho_2 - \rho_1)/\rho_2$ is the reduced gravity. The Boussinesq approximation remains valid for density variations of up to 20% and the transition to non-Boussinesq flow dynamics is not dramatic (Ungarish, 2007, 2009).

1.2.3 Shallow-water and depth-averaged models

The shallow-water equations are a system of equations that have been extensively used in the study of high Reynolds number gravity currents (Huppert, 2006) and are obtained by exploiting the long and thin nature of a flow (Whitham, 2011), where $\mathcal{H}$ a depth scale for the flow is small compared to $\mathcal{L}$ a length scale for the flow in the flow direction so that $\delta = \mathcal{H}/\mathcal{L} \ll 1$. In the limit of small δ, the flow is effectively uni-direction and vertical variations in velocity can be neglected to obtain a system of equations for the depth-averaged velocity $\bar{u} = \bar{u}(x,t)$ and flow depth $h = h(x,t)$.

Consider the flow an incompressible fluid with constant density ρ and no cross-stream variation, so that the flow can be described in two dimensions (x, y). The effects on entrainment are neglected and the fluid is confined between a rigid base at $y = 0$ and a free surface at $y = h(x,t)$, figure 1.7. Further, it is assumed the viscosity is negligible and that the vertical scales of the flow are small when compared

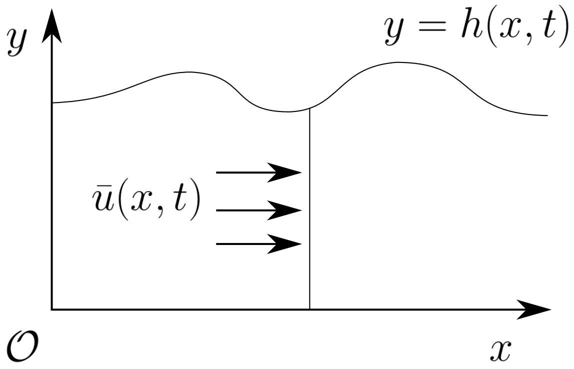

Figure 1.7: Two-dimensional shallow water description of the flow with depth-averaged velocity $\bar{u}(x,t)$ and flow depth $h(x,t)$

the horizontal. i.e. the length of the flow $\mathcal{L} \gg h(x,t)$ and $|u(x,y,t)| \gg |v(x,y,t)|$.

At the free surface atmospheric pressure p_a is imposed $p(x,y,t) = p_a$. Additionally the kinematic condition at both flow boundaries are

$$v(x,0,t) = 0, \tag{1.7}$$

$$v(x,h(x,t),t) = \frac{\partial h}{\partial t} + \frac{\partial h}{\partial x} u(x,h(x,t),t). \tag{1.8}$$

With these assumptions the Navier-Stokes equations (1.1-1.2) reduce to the two-dimensional Euler equations

$$\rho\left(\frac{\partial u}{\partial t} + u\frac{\partial u}{\partial x} + v\frac{\partial u}{\partial y}\right) = -\frac{\partial p}{\partial x}, \tag{1.9}$$

$$\rho\left(\frac{\partial v}{\partial t} + u\frac{\partial v}{\partial x} + v\frac{\partial v}{\partial y}\right) = -\frac{\partial p}{\partial y} - \rho g, \tag{1.10}$$

with the incompressibility condition

$$\frac{\partial u}{\partial x} + \frac{\partial v}{\partial y} = 0. \tag{1.11}$$

By integrating the incompressibility condition (1.11) over the depth of the current yields

$$\int_0^h \frac{\partial u}{\partial x} + \frac{\partial v}{\partial y}\,\mathrm{d}y = 0 \quad \Longrightarrow \quad \frac{\partial h}{\partial t} + \frac{\partial}{\partial x}\left(h\bar{u}\right) = 0, \tag{1.12}$$

where

$$\bar{u} = \frac{1}{h}\int_0^h u\,\mathrm{d}y \tag{1.13}$$

is the depth-averaged velocity. Given that the vertical velocity v is negligible compared to the u, the left hand side of the y-momentum equation (1.10) can be neglected. Thus, the pressure is purely hydrostatic

$$p = p_a + \rho g(h - y). \tag{1.14}$$

With the hydrostatic pressure and neglected v components of velocity, the depth-integrated horizontal momentum equation is

$$\rho \frac{\partial}{\partial t}\left(\int_0^h u \, \mathrm{d}y\right) + \rho \frac{\partial}{\partial x}\left(\int_0^h u^2 \, \mathrm{d}y\right) + \frac{\partial}{\partial x}\left(\int_0^h \rho g(h - y) \, \mathrm{d}y\right) = 0, \tag{1.15}$$

which can be simplified to

$$\frac{\partial}{\partial t}(h\bar{u}) + \frac{\partial}{\partial x}\left(\beta_u h\bar{u}^2 + g\frac{h^2}{2}\right) = 0, \tag{1.16}$$

where

$$\beta_u h\bar{u}^2 = \int\limits_0^h u^2 \, \mathrm{d}y. \tag{1.17}$$

The coefficient $\beta_u \geq 1$ allows for variations in the horizontal velocity profile over the depth and is known as a shape factor. When $\beta_u = 1$, there is no depth variation in the horizontal velocity and thus $\bar{u} = u$. For a value of $\beta_u > 1$ there is shear in the horizontal velocity profile, which may depend on the Reynolds number and the boundary roughness (Piau, 1996; Hogg and Pritchard, 2004). For high Reynolds number flows β_u is typically set equal to one (Iverson, 1997; Iverson and Denlinger, 2001; Ancey, 2001). However, when the density difference arises from suspended sediment or particles, such as a turbidity current, both velocity and density profiles are stratified over the depth of the flow (Islam and Imran, 2010; Sequeiros et al., 2010; Abad et al., 2011; Dorrell et al., 2019). Neglecting this stratification, by assuming $\beta_u = 1$ (Castro-Díaz et al., 2013; Hu et al., 2012; Parsons et al., 2009), produces different predictions for run-out lengths and flow entrainment/deposition rates (Dorrell et al., 2014). In this thesis the shape-factor β_u is assumed to be unity and thus the shallow-water equations, written in terms of the discharge $m = hu$ are given by

$$\frac{\partial h}{\partial t} + \frac{\partial m}{\partial x} = 0, \tag{1.18}$$

$$\frac{\partial m}{\partial t} + \frac{\partial}{\partial x}\left(\frac{m^2}{h} + g\frac{h^2}{2}\right) = 0. \tag{1.19}$$

When the current and ambient have similar densities, the Boussinesq approximation can be applied and the gravitational acceleration in (1.19) is replaced by the reduced gravity g'. If the mixing or entrainment occurs within the flow, so that a sharp interface at $y = h(x,t)$ does not exist, then an alternative definition posed by Ellison and Turner (1959) can be used. By defining

$$\bar{u}h = \int_0^\infty u(x,y,t)\,\mathrm{d}y, \tag{1.20}$$

$$\bar{u}^2 h = \int_0^\infty u^2(x,y,t)\,\mathrm{d}y, \tag{1.21}$$

the depth h and depth-averaged velocity of the flow $\bar{u}$ can be calculated

$$\bar{u} = \frac{1}{h}\int_0^\infty u\,\mathrm{d}y \tag{1.22}$$

$$h = \frac{(\bar{u}h)^2}{\bar{u}^2 h} = \frac{\left(\int_0^\infty u(x,y,t)\,\mathrm{d}y\right)^2}{\int_0^\infty u^2(x,y,t)\,\mathrm{d}y}. \tag{1.23}$$

However, this integral depth is an underestimate of height of the flow where the velocity goes to zero (Dorrell et al., 2014).

In the opposite limit when the viscosity of the current is large, so that the Reynolds number is small $Re \ll 1$, a parabolic horizontal velocity profile can be obtained by balancing viscous forces to the buoyancy. This simplifies the system of equations to a single equation for the depth of the flow (Didden and Maxworthy, 1982; Rottman and Simpson, 1983; Ungarish, 2009):

$$\frac{\partial h}{\partial t} - \frac{1}{3}\frac{g'}{\nu}\frac{\partial}{\partial x}\left(h^3\frac{\partial h}{\partial x}\right) = 0. \tag{1.24}$$

1.2.4 Froude number condition

The shallow-water model neglects vertical gradients, but these become significant at the head of the flow where turbulent drag and three-dimensional flow structures dissipate momentum. To capture this dissipation, shallow-water and other theoretical models are supplemented with an imposed flow velocity at the head $x = x_N(t)$ via a densimetric Froude number condition (Abbott, 1961). The densimetric Froude number is a dimensionless velocity of the current $Fr = u_N/\sqrt{g'h_N}$, where subscript

N indicate values at the head, and is ratio between flow speed and infinitesimal long surface waves on the gravity current (Hogg, 2006). Theoretical values of the Froude number can be determined through application of Bernoulli's theorem and a momentum balance far upstream and far downstream of the head of the current in rectangular channels (von Kármán, 1940; Benjamin, 1968). Von Kármán (1940) incorrectly applied Bernoulli's theorem along a contour through a turbulent region of the flow. This was corrected by Benjamin (1968) who arrived at the same result. The Froude number calculated by Benjamin Fr_B is a function of the fractional depth of the current $a = h_N/H$ and is given

$$Fr_B \equiv Fr_B(a) = \sqrt{\frac{(2-a)(1-a)}{1+a}}. \tag{1.25}$$

Note that in the limit of an infinitely deep ambient the Froude number tends to $\sqrt{2}$. Further expressions can be obtained with a vorticity balance without the requirement of an explicit dissipation assumption for Boussinesq flows (Borden and Meiburg, 2013; Konopliv et al., 2016). These differing approaches have been demonstrated to differ only by an assumption about the dissipation and can be reconciled within the same framework (Ungarish and Hogg, 2018).

In addition, densimetric Froude number conditions have been calculated for a stratified ambient (Ungarish, 2005) and non-rectangular cross-sections (Ungarish, 2012). The densimetric Froude number condition has also be determined experimentally to be 1.2 for deep currents (Huppert and Simpson, 1980; Simpson and Britter, 1979), which is similar to the theoretical value of $\sqrt{2}$ obtained using the two-dimensional theory of Benjamin (1968). For non-Boussinesq flows, where the density difference between the current and the ambient is large, the Froude number can be large and tends to infinity as the density ratio becomes large. For example, water propagating into an air ambient. This corresponds to the depth of the flow front tending to zero (Whitham, 2011).

1.2.5 Scaling arguments and similarity solutions

Dimensional arguments and simple integral models are able to predict the position of the head x_N as a function of the initial conditions by assuming a dominant balance between buoyancy and either inertial or viscous forces (Fay, 1971; Hoult, 1972; Huppert and Simpson, 1980; Huppert, 1982; Hogg et al., 2005). After an initial transience, the flows generally enter a self-similar phase where the solution is similar to itself when the independent and dependent variables are appropriately scaled. These similarity solutions capture some of the horizontal features of the flow. However, similarity solutions do not always exist. For example, in the axisymmetric spreading of a compositional gravity current, the tail of the current is self-similar but the head is time-dependent (Johnson et al., 2015). Further, particle-laden gravity currents which can be modelled by the depth-averaged equations with an additional particle-advection equation and variable buoyancy depending on particle concentrations, for example Bonnecaze et al. (1993); Dade and Huppert (1995), do not yield similarity solutions in general.

When viscous forces are dominant from the outset ($Re \ll 1$) a similarity solution exists for the mass and momentum conservation equations (1.24) (Huppert, 1982, 1986). These similarity solutions capture some of the vertical structure of the flow and the head propagation speed and have been shown to provide excellent agreement to available experiments (Huppert, 1982, 1986).

Provided, the initial Reynolds number is large the current propagates under a balance between inertia and buoyancy forces and the standard shallow-water theory presented in the section 1.2.3 can be applied. In addition, the simple box model, which assumes that the slumping motion of the current maintains a rectangular cross-section throughout, introduced by Huppert and Simpson (1980) can be used with the supplement of a Froude number condition. However, as the current thins, viscous forces become more important over time and at a critical time, t_c, viscous and inertia forces become equal in magnitude. For $t \gg t_c$ viscous forces provide the dominant resistance to buoyancy and the current propagates under the viscous buoyancy balance. For a lock-release (constant volume) gravity current, the critical time in which viscous, inertial and buoyancy forces are in balance is

$$t_c \sim (l^4 h_{\mathrm{lock}}^4/(\nu^3 g'^2))^{1/7}, \tag{1.26}$$

where l is the length of the lock-box, h_{lock} in the depth of the locked fluid and ν is the kinematic viscosity of the current.

A near plug-like flow is observed when the current propagates in a balance between inertia and buoyancy. However, deviation from this constant velocity profile is observed in a thin boundary layer near the base of the flow where viscous effects become significant and act as a drag force on the gravity current. Further, when the viscosities of the ambient and current are similar a boundary layer occurs near the fluid interface. Hogg and Woods (2001) study the transition from inertia to bottom-drag dominated gravity currents when viscous effects in the bulk of the current are negligible.

1.2.6 Two-layer shallow-water models

The single-layer or single-fluid shallow-water model introduced above is applicable when the depth of the ambient is large relative to that of the current or the ambient fluid has negligible density. For example, the lock-release problem figure 1.8. When the densities of the fluids are similar (so that momentum is not negligible) qualitatively different flow behaviour is observed when the depth ratio between the lock fluid and the ambient is less than two (Ungarish, 2009). The backwards travelling rarefaction wave observed during the slumping phase is replaced by a shock, which is similar to the current head when the depth ratio is unity (the lock-exchange configuration, figure 1.8). Further, the slumping time is considerably longer. These qualitative differences arise because of the momentum required to drive the ambient fluid back into the lock box inhibits the propagation of the current. When the depth ratio between the locked fluid and the ambient is greater than two, the flow dynamics are qualitatively similar to an infinite depth ambient, but quantitative differences are still observed that decrease with increase lock depth to ambient ratio.

Thus, when the depth ratio between the locked fluid and the ambient is less than two, the flow in the ambient cannot be neglected. To incorporate this into a depth-averaged model, the flow is split into two layers each with depth-averaged velocity u_i and thickness h_i, so that the total depth of the flow is given $H(x,t) = h_1(x,t) + h_2(x,t)$, figure 1.8. The denser layer or current is labelled layer 2 and the less dense or ambient layer 1. In this thesis the total depth of the flow is considered fixed, i.e. H is a constant and a rigid boundary is placed at $y = H$.

In terms of the interface pressure P_i at $y = h_1(x,t)$ the two-layer shallow-water equations are in (Hogg et al., 2000):

$$\frac{\partial h_1}{\partial t} + \frac{\partial}{\partial x}(h_1 u_1) = 0, \tag{1.27}$$

$$\frac{\partial}{\partial t}(h_1 u_1) + \frac{\partial}{\partial x}\left(h_1 {u_1}^2\right) + h_1 \frac{\partial P_i}{\partial x} = 0 \tag{1.28}$$

$$\frac{\partial h_2}{\partial t} + \frac{\partial}{\partial x}(h_2 u_2) = 0, \tag{1.29}$$

$$\frac{\partial}{\partial t}(h_2 u_2) + \frac{\partial}{\partial x}\left(h_2 {u_2}^2 + g'\frac{h_2^2}{2}\right) + h_2 \frac{\partial P_i}{\partial x} = 0, \tag{1.30}$$

As the flow is confined between the depths of $y = 0$ and $y = H$ the mass conservation

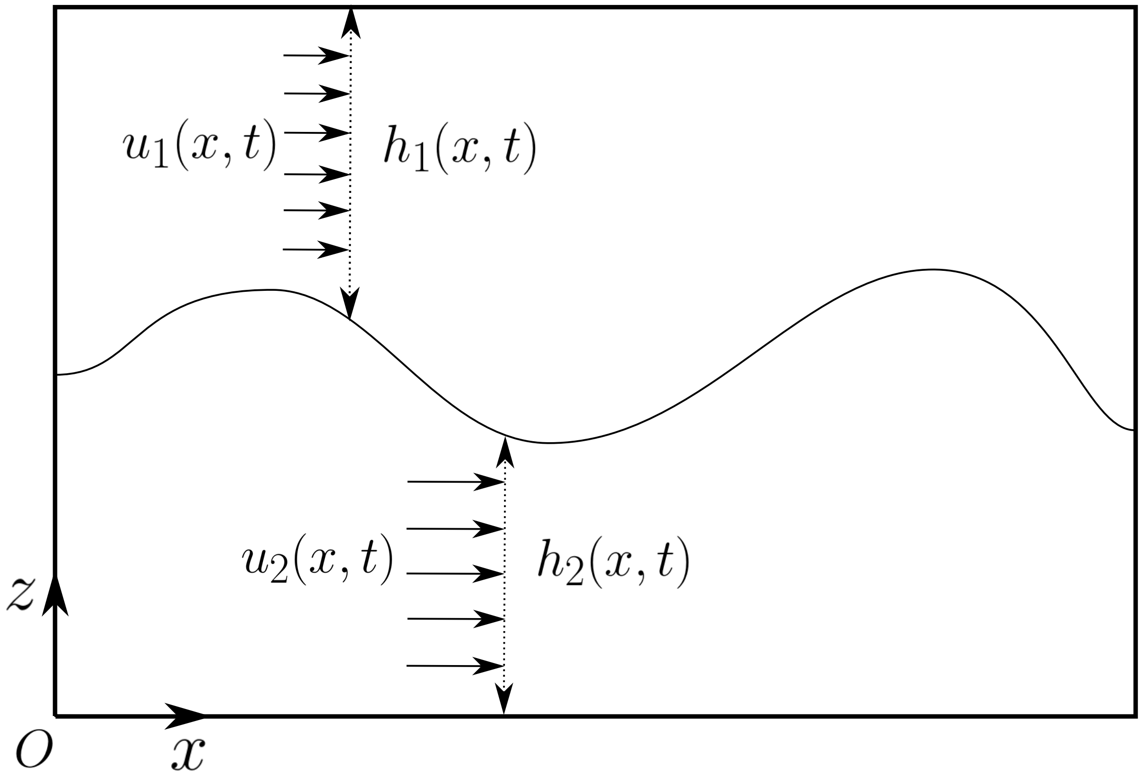

Figure 1.8: Schematic of the two-layer shallow-water model for the lock-exchange problem. Each layer has depth h_i, depth-averaged velocity, u_i and a Reynolds number Re_i. The total depth is fixed, so that $h_1 + h_2 = 1$

for the system forces the discharge of each layer to be equal and opposite

$$u_1 h_1 + u_2 h_2 = 0, \tag{1.31}$$

and thus using $h_1 = H - h_2$ and $u_1 = -u_2 h_2/(H - h_2)$, the system can be reduced to two equations for the mass and momentum conservation equation for layer two (Hogg et al., 2000):

$$\frac{\partial h_2}{\partial t} + \frac{\partial}{\partial x}(h_2 u_2) = 0 \tag{1.32}$$

$$\frac{\partial}{\partial t}(h_2 u_2) + \left(1 - \frac{h_2}{H}\right)\frac{\partial}{\partial x}\left(h_2 u_2^2 + g'\frac{h_2^2}{2}\right) - \frac{h_2}{H^2}\frac{\partial}{\partial x}\left(\frac{h_2^2 u_2^2}{1 - \frac{h_2}{H}}\right) = 0. \tag{1.33}$$

The terms in this second equation are change in momentum over time, gain of momentum in fluid 2 from convection and hydrostatic pressure, and momentum lost accelerating fluid 1. In the limit of the current being thin compared to the total flow depth $h_2 \ll H$, the equations for the single-layer shallow-model are recovered.

1.2.7 Entrainment

As a turbulent gravity current propagates, mixing occurs resulting in entraining of ambient fluid into the current (Hallworth et al., 1993, 1996; Marino et al., 2005; Sher and Woods, 2015). Prandtl (1952) first proposed that mixing between the ambient and the head of a gravity current would lead to the body of the current travelling faster than the head. For a turbulent lock-release problem mixing increases the volume of the current by a factor roughly 3-4 over 8-10 lock lengths from release and by 7-10 lock lengths all the current had entrained at least some ambient (Sher and Woods, 2015). This entrainment reduces the buoyancy and leads to stratification within the current affecting the driving force of the current, and hence its dynamics. The majority of box models and self-similar shallow-water theory models neglect entrainment within the flow (Sher and Woods, 2015) and therefore variations in buoyancy.

For large scale flows, the Péclet number $Pe = HU/D$ is large, where D is the mass diffusivity and is the ratio between momentum and mass diffusivities. Large values of the Péclet number $Pe = HU/D$ indicate that molecular diffusivity is negligible and mixing only occurs through turbulent processes (Johnson and Hogg, 2013). Mixing and entrainment in gravity currents has extensively been studied both experimentally and theoretically by numerous studies (For example, Hallworth et al. (1993, 1996); Hacker et al. (1996); Marino et al. (2005); Fragoso et al. (2013); Johnson and Hogg (2013); Sher and Woods (2015)). Hallworth et al. (1993, 1996) investigated the entrainment of ambient fluid both experimentally and theoretically. They conclude from many experiments that the majority of mixing occurs almost entirely at the head arising from the shear instability of the interface and the overriding of the head of the current. Hacker et al. (1996) however, report that a significant amount of mixing arises during the early stages of flow. This led to studies using direct numerical simulation to try and interpret the controls on mixing (Härtel et al., 2000).

The rate of entrainment (defined as the rate of volume flux over surface area) as a result of turbulence in a shear flow can be modelled using an empirical relationship, in which the rate of entrainment is proportional to the velocity between the two layers by dimensional arguments (Morton et al., 1956; Turner, 1986). I.e., the rate of entrainment $w_e = E|u_1 - u_2|$, where the dimensionless parameter E is in general a function of all dimensionless groups relevant to the flow and in particular, the Reynolds number Re, the density ratio ρ_2/ρ_1 of the two layers, the bulk Richardson number $Ri = g'H/U^2$, which is the ratio of stabilising effect of the density difference to the destabilising velocity shear and the Péclet number $Pe = HU/D$. However in the regime of gravity currents satisfying the Boussinesq approximation ($\rho_2/\rho_1 \approx 1$) and where Re and Pe are both large, the entrainment constant E reduces to a function of the bulk Richardson number Ri and has the asymptotic behaviour $E = 0.075$, when $Ri \ll 1$ and $E \sim 1/Ri$, when $Ri \gg 1$.

Johnson and Hogg (2013) use an empirical relationship for the rate of entrainment in a shallow-water model, which incorporates variable buoyancy along the current. They predict that a third regime can exist between the inertial-buoyancy and viscous-buoyancy regimes in which the head of the current evolves $x_N \sim t^{0.447}$. This regime will only occur if the current is initially large enough so that entrainment becomes important before viscous forces set in. Thus, laboratory-scale experiments may not exhibit this regime.

The depth-averaged assumption assumes that the entrained fluid is distributed evenly over the depth of the current. However, the experiments of Sher and Woods (2015); Marino et al. (2005) demonstrate that the reduced gravity maximum occurs at the head of the current for up to 25 lock lengths and decreases upstream from the head.

1.2.8 Depth-resolving models

With the increase of computational power depth-resolved models have been increasingly used to study turbulent gravity currents over the past 20 years (Meiburg and Kneller, 2010). These models fall into three categories Reynolds-averaged Navier-Stokes (RANS) equations, large eddy simulations (LES) and direct numerical simulations (DNS),

The RANS equations are time-averaged fluid flow equations for the time-averaged velocity. They solve for the large scale three-dimensional structure of the flow, but require supplementation with empirical models for the additional dissipation arising from the fluctuating (time-dependent) components of velocity. These closure models are commonly used in oceanographic examples (Mellor and Yamada, 1982; Ilıcak et al., 2008). Numerous studies have been conducted with some of the available second-order closure models, for example, two-equations RANS models such as k–ε (Kassem and Imran, 2004; Imran et al., 2004) or k–ω (Burchard et al., 2009). Ilıcak et al. (2008) test a variety of available two-equation models and produce salinity profiles within 20% of observations of gravity currents in the Red Sea.

Large eddy simulations (LES) resolve more of the flow structure than RANS models and only parametrise the small scale turbulent motions below a cut-off length scale (Sagaut, 2006). The governing equations are filtered to remove this small scale motion, the effects of which are then included with a sub-grid-scale (SGS) model. A variety of choices of sub-grid scale models exist and Özgökmen et al. (2009b) demonstrate that they all produce different rates of mixing in the lock-exchange problem, with the optimal model varying with Reynolds number.

Direct numerical simulations require no empirical modelling and numerically solve the Navier-Stokes equations directly. Thus, the scales of motion needs to be resolved down to the Kolmogorov scale (Kolmogorov, 1941), which is an eddy length scale at which viscous and inertial forces are equal in magnitude. These high-resolution numerical models are used to develop and validate parameterisations discussed in Ilıcak et al. (2009). Resolving all scales of the flow down to viscosity requires significant computation power, with simulations of the order 10^3 times longer for DNS when compared to LES for stratified mixing in turbulent flows (Özgökmen et al., 2009a). This limits the range of Reynolds numbers that can be studied.

Two-dimensional simulations can greatly reduce the computational cost by neglecting all variations in the cross-stream direction (for example, Özgökmen et al. (2004); Cantero et al. (2007); Kneller et al. (2016)). However, Özgökmen et al. (2004) demonstrate that the head propagation speed is 20% lower for two-dimensional rather than three-dimensional simulations, and the work of Cantero et al. (2007) reveals a strong three-dimensional structure in the body of the current. Espath et al. (2014) conducted two- and three-dimensional simulations of a mono-dispersed particulate gravity current produced by a lock-release and conclude that, with the exception of the sedimentation rate, two-dimensional simulations are not able to reproduce the results obtained in three-dimensional simulations. This conclusion was also found for bi-dispersed particulate gravity currents (Francisco et al., 2017).

A variety of different numerical schemes exist for conducting DNS. Härtel et al. (2000) produced some of the first direct numerical simulation of a gravity current in the lock exchange configuration. The Navier-Stokes equations were solved using a mixed spectral/spectral-element method discussed and validated in Härtel et al. (1997). Nasr-Azadani and Meiburg (2011) use the finite-difference based spatial discretisation of Chorin (1968). For a particle driven flow Necker et al. (2002, 2005) used the method of Härtel et al. (1997, 2000). The spectral element code NEK5000 (Fischer et al., 2008) has been used extensively to study lock-exchange flow (Özgökmen and Chassignet, 2002) and extended to complex geometry (Özgökmen et al., 2004) and ambient stratification (Özgökmen et al., 2006).

1.3 Structure of the thesis

This thesis is structured as follows: In chapter 2 a shallow-water model is employed that extends the analysis of the single-release case presented by Hogg (2006) to a double-lock release; Next in chapter 3 the double lock-release experimental configuration studied by Ho et al. (2018a,b, 2019) is extended to higher viscosity glycerol/water gravity currents; Then in chapter 4 the lock-exchange problem with a viscosity contrast between the two fluids is studied with direct numerical simulation of the Navier-Stokes equations; This problem is then considered with a shallow-water type model in chapter 5; finally concluding remarks are discussed in chapter 6.

Chapter 2

The phased lock-release problem

2.1 Introduction

In chapter 1 numerous examples of pulsed gravity current were discussed. A pulsed flow can either arise from flow instabilities, variation in the supply of material (Mulder and Alexander, 2001), combining of flows from different sources (Goldfinger et al., 2017), flow splitting and recombining (Nakajima and Kanai, 2000). Although the lock-release problem has been extensively studied, it assumes that all the material is released instantaneously and thus the dynamics of pulse-prone gravity currents or the combining of separate events may be poorly captured. The goal of this chapter is to extend the lock-release problem for the shallow-water equations to a double-release case, where a second equally sized lock-box is released subsequently. The second release will create a shock that will propagate through towards the head current.

Hogg (2006) employed the method of characteristics to solve the problem of a single-lock release flow. The shallow-water equations yield two families of characteristic curves along which the Riemann invariants $\alpha = u + 2\sqrt{g'h}$ and $\beta = u - 2\sqrt{g'h}$ are conserved. Hogg (2006) showed that the structure of the solution depended qualitatively on the densimetric Froude number, Fr. For $Fr \geq 2$, characteristics leaving the back of the head never reached the back of the lock-box and an internal shock formed for $Fr > 2$. For $Fr < 2$, a structured solution exists in which the characteristic (x, t)-space is split into regions where both, one or neither of the two characteristics variables are constant. Hogg (2006) analytically determined the boundary between these regions and the solution when at least one of the characteristic variables is constant. These models have not been extended to the multiple

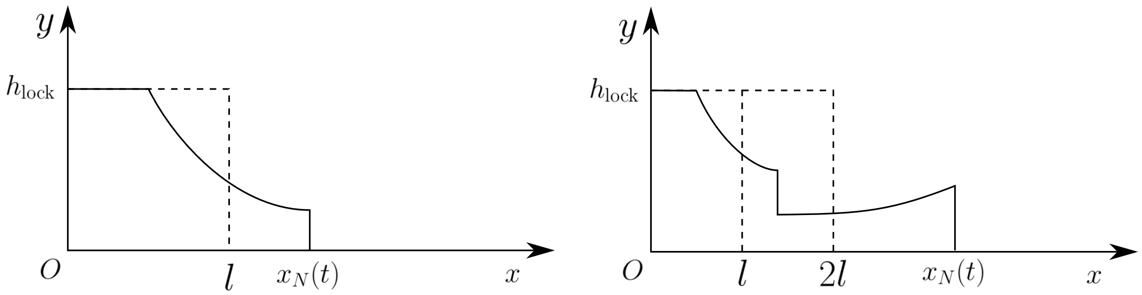

Figure 2.1: Configuration of the single (left) and double (right) lock-release problems. Initial conditions (- -) and current depth, $h(x,t)$, (–) are displayed.

release case.

A Lax-Wendroff finite-difference scheme based on the implementation of Bonnecaze et al. (1993) is employed to solve the governing shallow-water equations. The characteristics are then computed from this solution afterwards, in order to describe the form of the solution in (x,t) space. For a double-release problem with identical lock-boxes, there is an additional parameter as well as the densimetric Froude number: the dimensionless release time $t^*_{\rm re} = t_{\rm re}\sqrt{g' h_{\rm lock}}/l$, where $t_{\rm re}$ is the gate separation time, $h_{\rm lock}$ is the lock depth and l is the lock length. The work presented here explores the $(Fr, t_{\rm re})$ parameter space for $Fr < 2$. Simulations of the single-release case are compared to the analytical solution of Hogg (2006) for validation. The double-release simulations reveal a variety of distinct regions in the $(Fr, t_{\rm re})$ parameter space with qualitatively different behaviour in the shock velocity. For $t_{\rm re} \to \infty$, the two releases behave as two non-interacting events, whereas for $t_{\rm re} \leq 1$ the flow is effectively a single discrete event of twice the volume. However, the two events interact, affecting pulse propagation, for intermediate $t_{\rm re}$-values and a range of qualitatively different solutions are obtained. Regions are separated by three key characteristic curves, which corresponds to whether or not they are affected by the amount of material in the second lock-box and the path through the single release solution structure. The velocity of the shock has implications for the dynamics of the pulsed gravity currents flows discussed in chapter 1 and the assessment of their hazards.

2.2 Theoretical modelling

Consider a constant volume gravity current propagating over a fixed horizontal rigid surface in two spatial dimensions (x,y), where x and y are the horizontal and vertical co-ordinates, respectively, with the time from the first release defined as t, figure

2.1. The current has density ρ_2 and the deep ambient has density ρ_1. Thus, the buoyancy-adjusted gravity for the current may be expressed as $g' = (\rho_2 - \rho_1)g/\rho_2$, where $g = 9.81$ ms^{-2}. In the lock-gate configuration, the flow quickly reaches a state where the height $h(x,t)$ is much smaller than the length of the current $x_N(t)$. Therefore, in considering the horizontal momentum of the flow we can average over the depth and assume purely hydrostatic pressure. Further, the flows are assumed inviscid (with no basal drag), entrainment is negligible, and the ambient is quiescent and infinitely deep. These assumptions allow us to apply the simplified depth-averaged shallow-water equations as discussed in the chapter 1

$$\frac{\partial h}{\partial t} + \frac{\partial m}{\partial x} = 0, \tag{2.1}$$

$$\frac{\partial m}{\partial t} + \frac{\partial}{\partial x}\left(\frac{m^2}{h} + g'\frac{h^2}{2}\right) = 0, \tag{2.2}$$

where h and m are respectively the depth and the discharge of the flow. The shallow water equations are first order approximations in terms of the aspect ratio between the depth and length of the current δ and contain no source terms, i.e. drag and entrainment. However, at the head of the current $x = x_N(t)$ the dissipation is accounted for via a densimetric Froude number condition (Benjamin, 1968), which is imposed as a dynamic boundary condition at the head

$$\frac{\mathrm{d}x_N}{\mathrm{d}t} \equiv \dot{x}_N = \frac{m(x_N,t)}{h(x_N,t)} = \sqrt{\frac{\rho_2}{\rho_1}}\sqrt{g'h(x_N,t)}Fr_B(a) = \sqrt{g'h(x_N,t)}Fr, \tag{2.3}$$

where $Fr = \sqrt{\rho_2/\rho_1}Fr_B$ is a constant, subscript N denotes a value at the head and $a = h_N/H \leq 1/2$. The factor of $\sqrt{\rho_2/\rho_1}$ arises because the speed of the front, as calculated by Benjamin (1968) is proportional to $(\rho_2 - \rho_1)/\rho_1$ and the intrinsic speed of the current is proportional to $(\rho_2 - \rho_1)/\rho_2$. Critically, the Boussinesq approximation is not required and so large density differences can be considered and we refer to Ungarish (2009) for further details. For an infinitely deep ambient ($a \to 0$), $Fr_B(a) \to \sqrt{2}$ and thus the dimensionless head speed imposed is proportional to $\sqrt{\rho_2/\rho_1}$. This analysis assumes that $\rho_2 > \rho_1$. If a top surface current is considered, i.e. a current in the fluid of density ρ_1 propagating into a infinitely deep quiescent ambient of density ρ_2. Then the head speed is proportional to $\sqrt{\rho_1/\rho_2}$. Thus, all possible values of Fr can be obtained. Recall, as motivated earlier, that this chapter limits the range of study to $Fr < 2$ and therefore fluids with $\sqrt{\rho_2/\rho_1} \geq \sqrt{2}$ can produce flows outside of this range. Note that this condition is less restrictive than the Boussinesq approximation.

Both lock-boxes are assumed to be of the same length l and filled to a depth of h_{lock}. Initially, no flux boundary conditions are imposed at the back of both lock-boxes $x = 0, l$. After the second gate is released at $t = t_{\text{re}}$, the no flux condition at $x = l$ is removed. From the momentum equation (2.2), no flux is equivalent to $\partial h / \partial x = 0$ and so

$$\frac{\partial h}{\partial x}(x_0, t) = 0 \quad \text{for} \quad \begin{cases} x_0 = 0, l & \text{if} \quad t \le t_{\text{re}}, \\ x_0 = 0 & \text{if} \quad t > t_{\text{re}}. \end{cases} \tag{2.4}$$

Similarly, the initial conditions, figure 2.1, are defined as

$$h(x, 0) = \begin{cases} h_{\text{lock}} & \text{if} \quad x \in [0, 2l], \\ 0 & \text{otherwise.} \end{cases} \tag{2.5}$$

The mass and momentum conservation equations (2.1) & (2.2) are non-dimensionalised using l as the horizontal length scale, h_{lock} as the depth scale, $\sqrt{g' h_{\text{lock}}^3}$ as the momentum scale and $l / \sqrt{g' h_{\text{lock}}}$ as the convective time-scale:

$$\frac{\partial h^*}{\partial t^*} + \frac{\partial m^*}{\partial x^*} = 0, \tag{2.6}$$

$$\frac{\partial m^*}{\partial t^*} + \frac{\partial}{\partial x^*}\left(\frac{m^{*2}}{h^*} + \frac{h^{*2}}{2}\right) = 0, \tag{2.7}$$

where * denotes a dimensionless variable. Similarly, the dimensionless boundary conditions (2.4) and (2.3) are:

$$\frac{\partial h^*}{\partial x^*}(x_0^*, t^*) = 0 \quad \text{for} \quad \begin{cases} x_0^* = 0, 1 & \text{if} \quad 0 \le t^* \le t_{\text{re}}^*, \\ x_0^* = 0 & \text{if} \quad t^* > t_{\text{re}}^*, \end{cases} \tag{2.8}$$

$$\frac{\mathrm{d}x_N^*}{\mathrm{d}t^*} = \frac{m_N^*}{h_N^*} = Fr\sqrt{h_N^*} \tag{2.9}$$

and initial conditions (2.5) become

$$h^*(x^*, t^*) = \begin{cases} 1 & \text{if} \quad x^* \in [0, 2], \\ 0 & \text{otherwise.} \end{cases} \tag{2.10}$$

2.2.1 Analysis of characteristics: single release case

This section will discuss the behaviour of the flow for $t < t_{\text{re}}$, which is equivalent to the single release solution of Hogg (2006). From this point the * are neglected from the dimensionless variables for brevity, unless stated otherwise. The system of equations (2.6-2.7) can be transformed into its characteristic form (Whitham, 2011) by changing to characteristic variables

$$\alpha = u + 2c, \quad \beta = u - 2c, \tag{2.11}$$

where $u = m^*/h^*$ and $c = \sqrt{h^*}$ to obtain

$$\frac{\mathrm{d}\alpha}{\mathrm{d}t} = 0 \quad \text{on} \quad \frac{\mathrm{d}x}{\mathrm{d}t} = u + c, \tag{2.12}$$

$$\frac{\mathrm{d}\beta}{\mathrm{d}t} = 0 \quad \text{on} \quad \frac{\mathrm{d}x}{\mathrm{d}t} = u - c. \tag{2.13}$$

Thus, α and β, the Riemann invariants, are constant along characteristics curves with gradients in (x, t)-space of $u+c$ and $u-c$, respectively. The gradients $u \pm c$ are the eigenvalues of the system of equations (2.6) & (2.7) and, provided the flow depth is non-zero, are real and distinct everywhere. Thus, the system is hyperbolic and the method of characteristics may be applied. The values of the characteristic variables can be determined from boundary or initial conditions that the characteristics pass through.

Initially, $\alpha = 2$ and $\beta = -2$ on all positive and negative characteristics that originate from $0 < x < 2$, $t = 0$, see figure 2.2. Thus, with the imposed densimetric Froude number condition $u_N = Frc_N$, positive characteristics collide with the head at a finite time provided $Fr \not\to \infty$ (in the limit $Fr \to \infty$, the head corresponds to the leading characteristic). While positive characteristics arrive at the head with $\alpha = 2$, the velocity and wave speed at the head are constant and take value

$$u_N = Frc_N \quad \text{and} \quad c_N = \frac{2}{Fr + 2}. \tag{2.14}$$

Thus, negative characteristics emanating from the back of head have constant

$$\beta = \beta_m \equiv 2(Fr - 2)/(Fr + 2) \geq -2. \tag{2.15}$$

An expansion fan of negative characteristics emanates from (2,0) and connects the two regions where β is constant, see figure 2.2b. These negative characteristics correspond to straight lines through the origin and satisfy

$$x = 1 + (4 + 6\beta)(2 - \beta)^{-\frac{3}{2}} t \quad \text{for} \quad \beta \in [-2, \beta_m]. \tag{2.16}$$

The negative characteristics with $\beta = \beta_m$ and $\beta = -2$, and their subsequent reflections are denoted $x_{\text{fan}}(t)$ and $x_{\text{ref}}(t)$, respectively, and form the boundaries between uniform (U) and simple (S) wave regions in which either β is constant or β varies. The fastest backwards travelling negative characteristic, $x_{\text{ref}}(t)$, originates

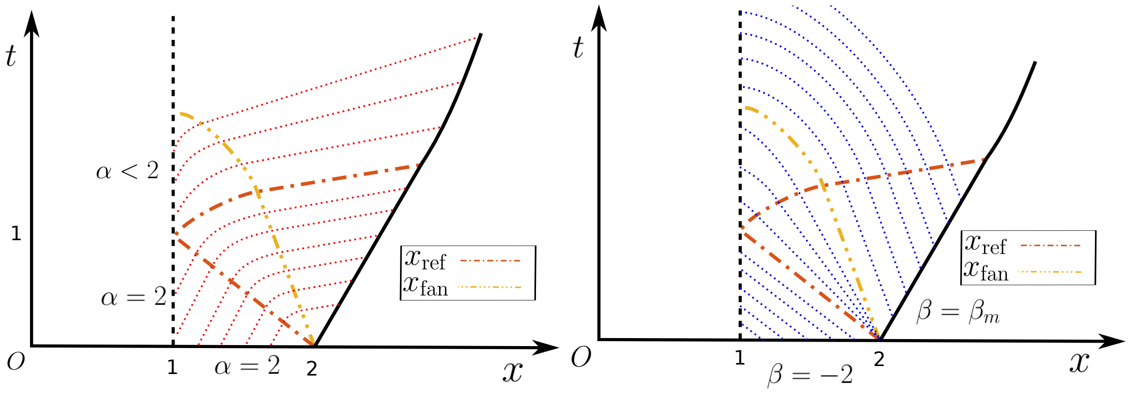

(a) (b)

Figure 2.2: Characteristic diagrams shortly after the first release for a densimetric Froude number Fr less than 1. For $1 < Fr < 2$, x_{ref} has positive gradient until intersecting x_{fan} The head of the current x_N (–) moves at constant speed until $x_{\mathrm{ref}}(\cdot -)$ collides with it. Positive (a) and negative (b) characteristics $(\cdots)$ are displayed for a small range of starting values. The boundary between the expansion fan and the constant region behind the head is $x_{\mathrm{fan}}(\cdots -)$.

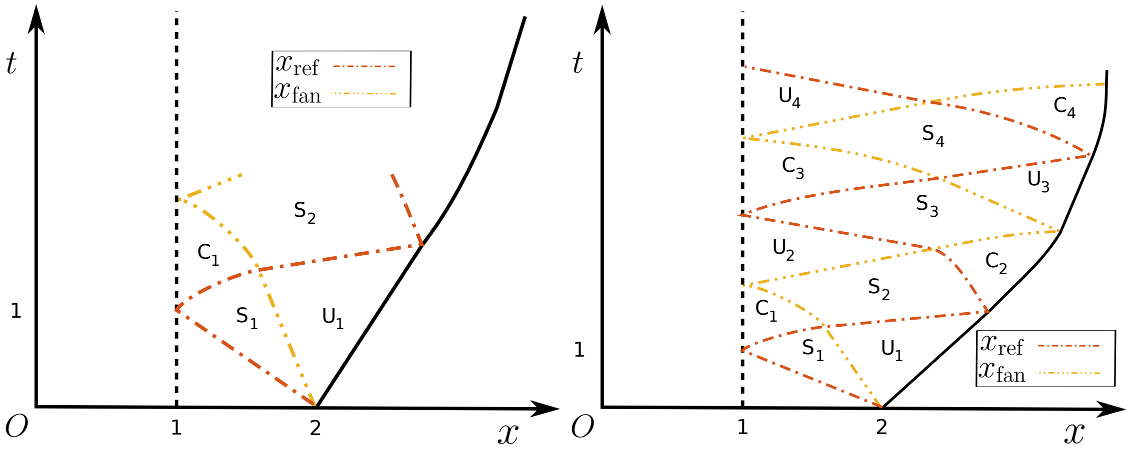

(a) (b)

Figure 2.3: Characteristic diagram highlighting the two curves $x_{\mathrm{ref}}(\cdot -)$ and $x_{\mathrm{fan}}(\cdots -)$ and how the solution is partitioned into uniform (U), simple (S) and complex (C) regions shortly after the release (a) and at a later time (b).

from the initial release at $x = 2$ and represents the furthest part of the lock that is affected by the initial release. For clarity, the curves x_{ref} and x_{fan} represent different characteristics with different values of the conserved quantities after each reflection. They alternate between positive and negative characteristics between each branch. All positive characteristics intersecting the first branch of x_{ref} arrive from unperturbed fluid and so have $\alpha = 2$, yielding $\mathrm{d}x/\mathrm{d}t = -1$ and thus $x_{\mathrm{ref}}(1) = 1$. The positive characteristics emanating from $t > 1$ have $\alpha < 2$, because $h < 1$ and $u = 0$. The last characteristic with $\alpha = 2$ signifies the boundary of the region of the flow that is affected by the finite length of the first lock-box. For $t > 1$, x_{ref} defines the last characteristic with $\alpha = 2$. The curves x_{ref} and x_{fan} collide at $t = (2 + Fr)^{3/2}/\sqrt{8}$. Beyond this point, x_{fan} enters a region of varying α and therefore has a non-constant gradient. In contrast, x_{ref} enters a region of constant β and thus has constant gradient until reaching the head. Hogg (2006) gives the x_{ref} characteristic between the back wall and the head as

$$x_{\mathrm{ref}}(t) = \begin{cases} 2 + 2t - 3t^{\frac{1}{3}} & \text{if} \quad t \in \left[1, \frac{(2+Fr)^{\frac{3}{2}}}{\sqrt{8}}\right], \\ 2 - \sqrt{2(2+Fr)} + 2\frac{Fr+1}{Fr+2}t & \text{if} \quad t \in \left[\frac{(2+Fr)^{\frac{3}{2}}}{\sqrt{8}}, \frac{(2+Fr)^{\frac{3}{2}}}{\sqrt{2}}\right]. \end{cases} \tag{2.17}$$

At times beyond this characteristic, complex (C) or simple (S) wave regions exist, where both or one characteristic varies in time, respectively. The lines x_{fan} and x_{ref} are continually defined through reflections as, respectively, the first or last characteristic upon which either α or β are locally constant. For $Fr < 2$ they reflect between the head and the rear lock-box and divide the solution space into uniform (U), simple (S) and complex (C) wave regions, figure 2.3. Constant negative characteristics in regions U_1, S_2 and U_2 have $\beta = \beta_m$ (2.15) and thus, at the back of the first lock-box where, from the boundary condition (2.8), $u = 0$ and hence $\alpha = -\beta = 2c = -\beta_m$, new positive characteristics in the regions U_2, S_3 and U_3 take the value $\alpha = -\beta_m$.

The densimetric Froude number condition (2.9) implies negative characteristics have $\beta = \beta_m(Fr - 2)/(Fr + 2)$ when positive characteristics with the constant value $\alpha = -\beta_m$ arrive at the head. This holds in regions U_3, S_4 and U_4. These boundary conditions continually create regions in the flow where the characteristics variables α or β are constant. The values of α or β may be calculated in any region in which they are constant (Hogg, 2006). For $n \in \mathbb{N}$ regions U_{2n}, S_{2n+1} and U_{2n+1} have

$$\alpha = 2\left[\frac{2 - Fr}{2 + Fr}\right]^n \equiv 2\lambda^n, \tag{2.18}$$

because of the no flux boundary condition (2.8), while in regions U_{2n+1}, S_{2n+2} and U_{2n+2}

$$\beta = -2\left[\frac{2-Fr}{2+Fr}\right]^{n+1} = -2\lambda^{n+1,} \tag{2.19}$$

because of the densimetric Froude number condition (2.9). As $n \to \infty$, $\alpha \to 0$, and $\beta \to 0$, and thus $u \to 0$ and $c \to 0$. When $Fr \sim 0$, $\lambda \sim 1$ and therefore the flows will interact for a large number of reflections and hence longer release times. For $Fr \lesssim 2$ there is minimal interaction between the events. Critically, x_{ref} and x_{fan} partition the single-release solution into three distinct regions for any fixed t where the behaviour of α and β are qualitatively different.

2.2.2 Extension to double release

From the structure described in section 2.2.1 we can determine the nature of the solution when the second gate is released at $t = t_{\text{re}}$. If $t_{\text{re}} \leq 1$ then trivially the solution behaves identically to a single-release of lock-box length 2, because the backwards travelling disturbance has insufficient time to reach $x = 1$. For $t_{\text{re}} > 1$, a shock is created where positive characteristics in $x < 1$, having $\alpha = 2$, collide with positive characteristics from $x \geq 1$ having $\alpha < 2$. Depending on the release time, t_{re}, the shock is released into a region of constant depth (uniform region) or varying depth and velocity (complex region) and so the relative position of the two curves, x_{ref} and x_{fan}, determine the initial motion of the shock. Imposing that mass and momentum fluxes are conserved across the shock, the shock velocity $\dot{x}_{\text{s}}$ can be obtained from the Rankine-Hugoniot conditions of the shallow water equations, because they are in a conservative form. In terms of the characteristic variables ahead of and behind the shock, $\alpha^+, \beta^+, \alpha^-, \beta^-$, respectively, the shock velocity $\dot{x}_s$ is

$$\dot{x}_{\text{s}} = \frac{1}{2}\frac{\left(\alpha^+ + \beta^+\right)\left(\alpha^+ - \beta^+\right)^2 - \left(\alpha^- + \beta^-\right)\left(\alpha^- - \beta^-\right)^2}{\left(\alpha^+ - \beta^+\right)^2 - \left(\alpha^- - \beta^-\right)^2}, \tag{2.20}$$

from mass conservation (2.6) and

$$\dot{x}_{\text{s}} = \frac{1}{16}\frac{8\left(\alpha^+ - \beta^+\right)^2\left(\alpha^+ + \beta^+\right)^2 - 8\left(\alpha^- - \beta^-\right)^2\left(\alpha^- + \beta^-\right)^2 + \left(\alpha^+ - \beta^+\right)^4 - \left(\alpha^- - \beta^-\right)^4}{\left(\alpha^+ + \beta^+\right)\left(\alpha^+ - \beta^+\right)^2 - \left(\alpha^- + \beta^-\right)\left(\alpha^- - \beta^-\right)^2} \tag{2.21}$$

from momentum conservation (2.7). Initially $\alpha^- = 2$ as the positive characteristics come from unperturbed fluid. Shocks that propagate into a uniform region have both α^+ and β^+ constant and thus, by the Rankine-Hugoniot conditions (2.20) & (2.21), both $\dot{x}_{\text{s}}$ and β^- are also constant. In simple and complex regions, the shock will accelerate or decelerate and values of β^- will vary.

In uniform regions adjacent to $x = 1$, the boundary condition $u(1) = 0$ (2.8) implies that $u(x) = 0$ throughout the uniform region. Thus, and whilst $\alpha^- = 2$, the problem replicates the wet dam break (Whitham, 2011) and the shock velocity can be calculated explicitly throughout the uniform region. The Rankine-Hugoniot conditions (2.20) & (2.21) provide an implicit relation for the constant shock velocity, $\dot{x}_\mathrm{s}$, for uniform regions adjacent to the head. For a shock of positive velocity, $\dot{x}_\mathrm{s}$, causality implies that positive characteristics cannot be emitted by the shock. Thus, the shock represents the furthest point in the domain that has been affected by the release of the second gate.

Similar to the line $x_\mathrm{ref}(t)$, an additional line $x_\mathrm{fin}(t)$ is introduced for the second release. The first branch tracks the backwards propagating disturbance of the second release, i.e. the fastest negative characteristic from $(1, t_\mathrm{re})$. On this characteristic $\beta = -2$, and positive characteristics intersecting it arrive from unperturbed fluid and therefore $\alpha = 2$. Thus

$$\frac{\mathrm{d}x_\mathrm{fin}}{\mathrm{d}t} = -c = -1 \tag{2.22}$$

and so

$$x_\mathrm{fin}(t) = 1 - (t - t_\mathrm{re}) \quad \text{for} \quad t \in [t_\mathrm{re}, t_\mathrm{re} + 1]. \tag{2.23}$$

At $t = t_\mathrm{re} + 1$, the fluid at the back of the second lock starts to be affected by the gate release and beyond this time $\alpha < 2$ at $x = 0$. The last $\alpha = 2$ characteristic leaves $x = 0$ at $t = t_\mathrm{re} + 1$, which is denoted as the continuation of the line x_fin. The second branch of the curve x_fin defines the part of the solution affected by the finite length of the second lock-box. If this characteristic intersects the shock, then $\alpha^- < 2$ thereafter.

Both β^- and the shock velocity $\dot{x}_\mathrm{s}$ are constant when the shock propagates through a uniform region. Thus, for a shock propagating in a uniform region, a region of constant β is created, which in turn creates another region of constant $\alpha < 2$ upon reaching the back of the lock-box. The structure of the characteristic space is displayed for a shock released into a uniform region, figure 2.4, and a complex region, figure 2.5 . For shocks released into either uniform or complex regions negative characteristics will have gradients greater than -1 (2.13) and another expansion fan of negative characteristics must exist at $(1, t_\mathrm{re})$. A shock released into a uniform region will initially travel at a constant speed. Further, the flow depth and velocity will be constant either side of the shock. This will hold until the shock intersects one of the three curves x_ref, x_fan, or x_fin, with each possibility leading to a different structure behind the shock. The example drawn in figure 2.4 has the shock

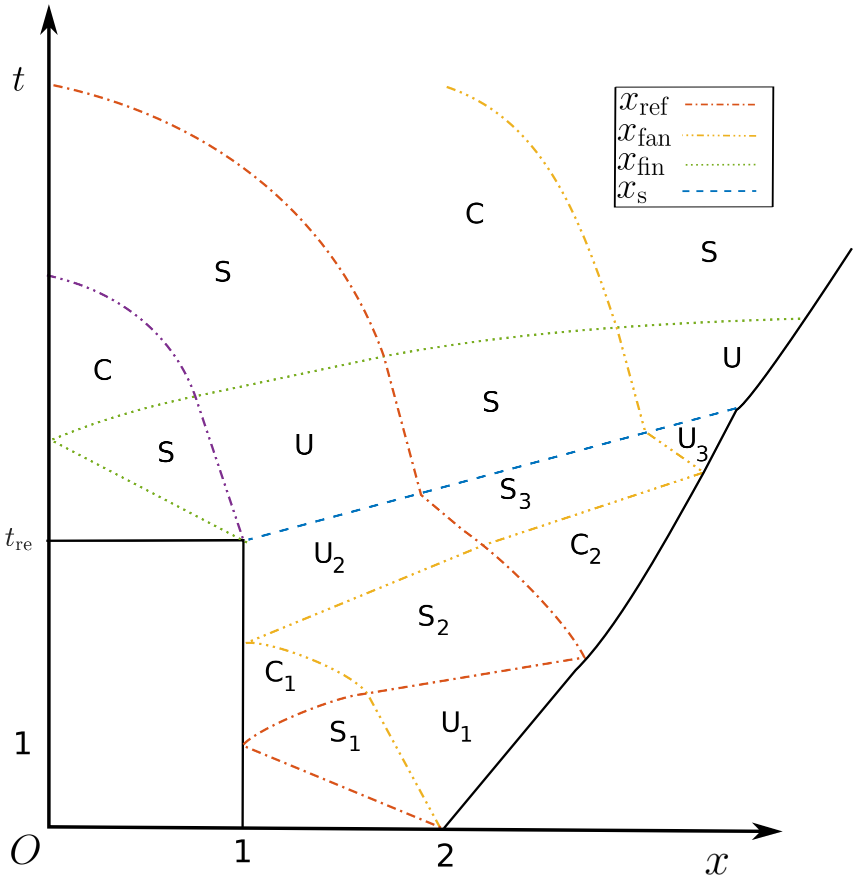

Figure 2.4: Schematic showing an example structure of the characteristic space for a shock released into the U_2 region. Ahead of the shock, the regions are bounded by the two lines $x_{\text{ref}}(\cdot -)$ and $x_{\text{fan}}(\cdots -)$, the head of the current x_N $(-)$ and the shock x_s (- -). At the point of release, an additional expansion fan is bounded between $x_{\text{fin}}(\cdots)$ and the slowest backwards travelling characteristic from the second release $(\cdot\cdot -)$.

intersecting x_{ref} initially. For complex shocks, figure 2.5, the shock speed accelerates from the outset, because the values of α^+ and β^+ are decreasing. The shock may exhibit a region of constant velocity, but only once it has intersected both x_{ref} and x_{fan}. The three curves x_{ref}, x_{fan} and x_{fin} bound critical regions where characteristic variables α and β change from either being constant or varying. The single release solution space is partitioned by x_{ref} and x_{fan} into regions with varying or constant α and β. Therefore, their position relative to the shock when it is released influences the initial shock velocity. The dynamics of the shock change when it collides with x_{ref} or x_{fan}, which in turn affects the negative characteristics behind it. Further, when x_{fin} intersects the shock, an additional change in dynamics occurs. The order in which these effects occur creates a range of different shock velocities.

The shallow-water equations (2.6) & (2.7) coupled with boundary (2.8) & (2.9) and initial (2.10) conditions are solved using the method of Bonnecaze et al.

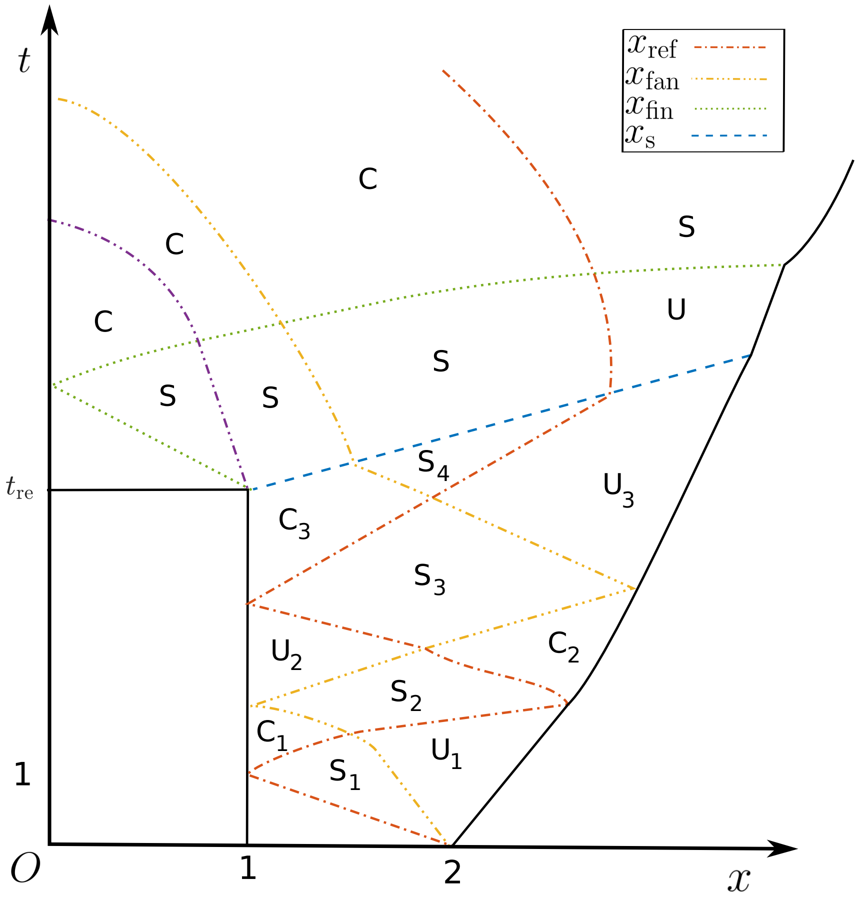

Figure 2.5: Schematic showing an example structure of the characteristic space for a shock released into a C_3 region. Ahead of the shock, the regions are bounded by the two lines $x_{\rm ref}(\cdot -)$ and $x_{\rm fan}(\cdots -)$, the head of the current x_N (–) and the shock x_s (- -). At the point of release, an additional expansion fan is bounded between $x_{\rm fin}(\cdots)$ and the slowest backwards travelling characteristic from the second release $(\cdot\cdot -)$.

(1993). For stability the initial depth, h_N, and velocity, u_N, at the head were set to slumping phase values;

$$u_N = \frac{2Fr}{2+Fr} \quad \text{and} \quad h_N = \left(\frac{2}{Fr+2}\right)^2. \tag{2.24}$$

Further, the shock initiates at $(x, t) = (1, t_{\mathrm{re}})$, where $u = 0$, and thus the positive and negative characteristics ahead of the shock takes values

$$\alpha^+ = 2\sqrt{h(1, t_{\mathrm{re}})} \quad \text{and} \quad \beta^+ = -2\sqrt{h(1, t_{\mathrm{re}})}. \tag{2.25}$$

Together with $\alpha^- = 2$, the Rankine-Hugoniot conditions (2.20) & (2.21) were used to determine the initial shock velocity and depth, $\dot{x}_s(t_{\mathrm{re}})$, and these were imposed at the node coinciding with the shock for the first time step after release. The position of the shock is determined

The shallow-water equations are remapped to the unit interval using the change of variables $(\zeta, \tau) = x/x_N(t), t)$. This removes the moving boundary condition simplifying the application of the Froude number condition. For full details see appendix A of Bonnecaze et al. (1993). The transformed equations are solved using a Lax-Wendroff finite-different scheme. The dynamics of the shock are resolved directly from the numerical integration of the governing equations and do not require use of the Rankine-Hugoniot conditions. The position, and from it the velocity, of the shock presented in the results and discussion section is calculated from the largest jump in depth behind the head of the flow. Numerical integration with a upwind finite-difference scheme is used to determine the positive characteristic that arrives at the head, $\zeta = 1$, at the next time step and provide, together with the Froude number condition, a second equation for u and c at the head. This enabled us to determine suitable values used as boundary conditions at the head for the next time step.

2.2.3 Verification

Model verification is performed by comparing the numerical solution at $t = 1$ and the curve $x_{\mathrm{ref}}(t)$ with the exact solution given by Hogg (2006). This was chosen, because of the significance of the three lines $x_{\mathrm{ref}}(t)$, $x_{\mathrm{fan}}(t)$ and $x_{\mathrm{fin}}(t)$ to assess the ability of the simulations to capture the distinct regions where behaviour changes. Depth and velocity profiles at $t = 1$ are compared for fixed Δt and varying Δx and vice versa, figure 2.6. The error of the variable E_f is calculated via the ℓ_1-norm of

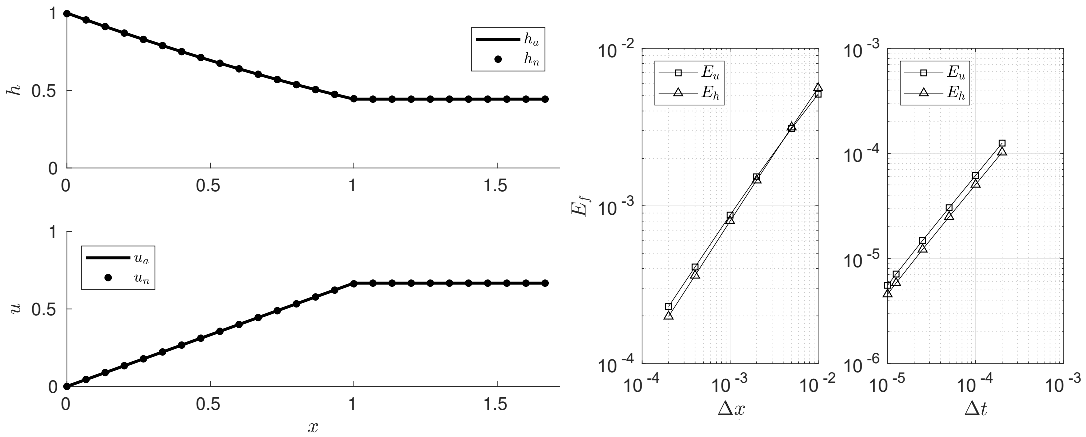

(a)

(b)

Figure 2.6: (a) Depth and velocity profiles at $t = 1$ for a single release problem ($\Delta x = 0.0002$, $\Delta t = 10^{-5}$, $Fr = 1$). (b) Error in depth and velocity for fixed $\Delta t = 10^{-5}$ (left) and fixed $\Delta x = 0.005$ (right). Straight lines drawn between the end points have $E_h \sim \Delta t^{0.85}$, $E_u \sim \Delta t^{0.79}$, $E_h \sim \Delta x^{1.04}$ and $E_u \sim \Delta x^{1.04}$.

the variable

$$E_f = \frac{\ell_1(f_a - f_n)}{N_{\text{int}}} = \frac{1}{N_{\text{int}}} \sum_{k=1}^{N_{\text{int}}} |f_a - f_n|, \tag{2.26}$$

where $f = h$ or $f = u \equiv m/h$ and N_{int} is the number of nodes over the averaging interval. The numerical, subscript n, and analytical, subscript a, solutions are interpolated onto an equally spaced grid with $N_{\text{int}} = 10^4$. For fixed Δx the error quickly converges to the spatial error and therefore a numerical solution $\Delta t = 10^{-6}$ and $\Delta x = 0.005$ is used instead of the analytical solution for comparison. A fixed time step is used throughout the simulations, which was chosen conservatively to ensure that the CFL condition was satisfied. After $t = 1$, complex regions start appearing in the characteristic space and a depth and velocity profile across the length of the current cannot be explicitly written down everywhere. However, the curve x_{ref} has been expressed in closed form in equation (2.17) and this expression is compared to a positive characteristic emanating from (1,1) calculated from the numerical solution. An excellent agreement between the analytical and numerical expression for x_{ref} is observed, figure 2.7. Although the Lax-Wendroff finite-difference scheme is formally second order accurate, the model verification suggests that it is first order accurate in both time and space. This is to be expected as the analytic solution of the dam break does not have a continuous derivative everywhere. Although not displayed here, for lower resolutions the contribution to the error is largest at $x = 0$ and $x = 1$.

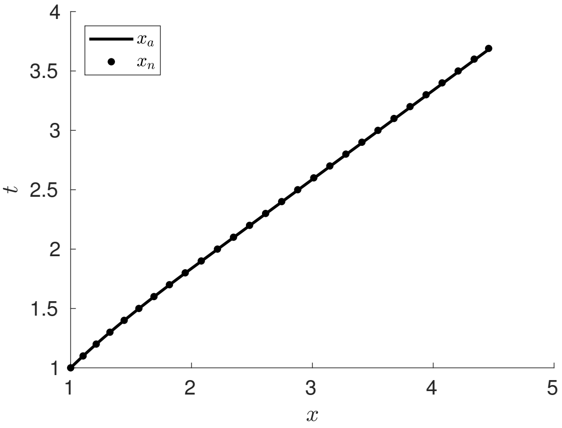

Figure 2.7: Comparison between the analytical expression and the numerically-computed x_{ref} between (1,1) and the point that it intersects the head.

2.3 Results and Discussion

In this section, the range of possible solutions from the shallow-water model are classified in terms of qualitative differences in the shock velocity throughout its motion towards the head of the current. The generic structure of the (Fr, t_{re}) phase space is presented from a parametric study, and the solution types are presented.

2.3.1 Shock Evolution

The numerical solutions are first distinguished by the region the shock is released within, C_1, U_2, C_3 etc. If the shock at $x_{\text{s}}(t)$ is released into a uniform region, the shock velocity remains constant until it enters the simple wave region. If the shock is released into a complex region, its velocity varies from the outset. The characteristics that bound the region of varying or constant α and β, $x_{\text{fan}}(t)$ and $x_{\text{ref}}(t)$, are bounded by the flow front and must collide with the shock before it reaches the front. The intersection times, t_{fan} and t_{ref}, i.e. $x_{\text{fan}}(t_{\text{fan}}) = x_{\text{s}}(t_{\text{fan}})$ and $x_{\text{ref}}(t_{\text{ref}}) = x_{\text{s}}(t_{\text{ref}})$, signify changes in behaviour in front of the shock.

If the shock is released into a complex region, three distinct paths through (x, t)-space may occur: i) The shock first intersects x_{fan} and enters a simple wave region in which β is constant. The shock then intersects x_{ref} after it has reflected off the front, entering another complex region; ii) The shock intersects x_{fan} first, but intersects x_{ref} before it has reflected off the head. Thus, the shock enters a uniform region until colliding with the head; iii) The shock intersects x_{ref}, entering a simple region within which α is constant. It then intersects x_{fan}, entering a uniform region. The three possibilities for C_1 are displayed in figure 2.8a. A similar distinction is

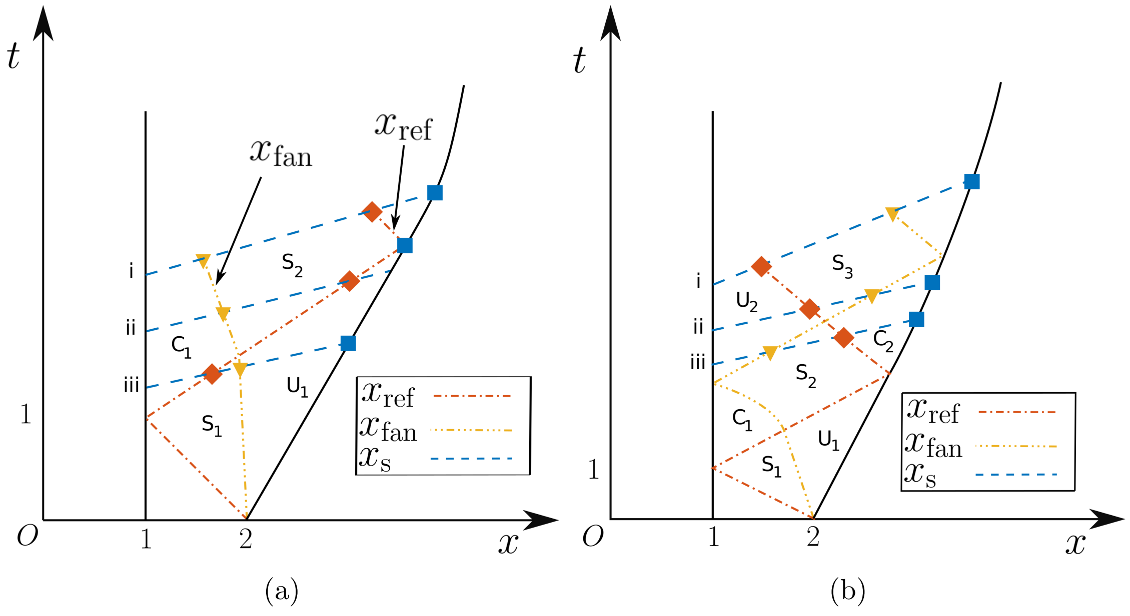

Figure 2.8: Schematic showing examples of the three characteristic diagrams for the three distinct paths C$_1$ (a) and U$_2$ (b) shocks, x_s, (- -) can take through the single release solution, i,ii and iii. The shock intercepts x_{ref} and x_{fan} $(\cdots -)$ at $t_{\text{fan}}(\blacktriangledown)$ and $t_{\text{ref}}(\blacklozenge)$, respectively. The shock intercepts the front, $x_N(-)$, at $t = t_{\text{col}}(\blacksquare)$. Uniform (U$_i$), Simple (S$_i$) and complex (C$_i$) regions are indexed by the order in which they appear.

drawn for the uniform cases, for example U$_2$ in figure 2.8b: i) β varies within the simple wave region before becoming constant again; ii) β starts varying first followed by α; iii) α starts varying followed by β. Further, if the shock is affected by the finite length of the domain lock-box, i.e. x_{fin} intersects with the shock before it reaches the head of the flow, then this is equivalent to $\alpha^- < 2$ beyond this point. The first time the shock and x_{fin} coincide is defined as t_{fin}, such that $x_{\text{fin}}(t_{\text{fin}}) = x_s(t_{\text{fin}})$. If the shock is affected by the finite length of the lock-box, the case is labelled ‘F’, otherwise ‘N’. For example U$_2$Fi is a shock that is released into the U$_2$ region of type i that is affected by the finite length of the lock-box.

Numerical solutions for the U$_2$N shocks are displayed in figure 2.9. For case i, figure 2.9a&b, β varies upon entering the S$_3$ region and the shock accelerates at approximately a constant rate until entering U$_3$, where it returns to a constant but higher velocity until colliding with the head of the current. In contrast the shock velocity increases throughout in cases ii, figure 2.9c&d, and iii, figure 2.9e&f, as first one characteristic starts varying and then the other (β first for case ii and α first for case iii). The shock velocity at t_{fin} is largest for case iii, with case i being the slowest.

For larger densimetric Froude numbers, the shock has further to travel before reaching the front and therefore is more likely to be affected by the finite length of the lock-box. The U_2F shocks are qualitatively similar to the U_2N cases, figure 2.10, until x_{fin} collides with the shock at $t = t_{\text{fin}}$, after which the velocity decreases and the maximum shock velocity occurs before the head. Case U_2Fi does not exist. i.e., the shock can only be affected by the finite length of the lock-box if it enters a region where α is varying. Further, our simulations reveal that this case U_4Fi does not exist. Shocks released into complex regions immediately increase in velocity as both α^+ is decreasing and β^+ is increasing. Example C_3N cases are presented in figure 2.11. As expected, the acceleration of the shock decreases after t_{fan} for case i, because β takes a constant value until t_{ref}, after which β starts decreasing again and the acceleration of the shock increases. For cases ii and iii, the acceleration of the shock decreases when it enters the S_3 region before becoming zero when entering U_3 until reaching the head of the current. For C_3 and subsequent complex and uniform cases, the shock may feel the affect of the finite length of the lock-box before colliding with x_{ref} or x_{fan}. The acceleration of the shock still decreases after it is affected by the finite length of the domain, but the range of possibilities becomes more complex, figure 2.12.

2.3.2 Classification of Solutions

A large number of numerical simulations were run in the range of values $(Fr, t_{\text{re}}) \in [0, 2) \times (1, 21]$ and from the three curves, $x_{\text{ref}}, x_{\text{fan}} \& x_{\text{fin}}$, and the shock, x_s, the corresponding case was determined. For each Fr, the boundaries between regions were chosen at t_{re} values between the simulations of different cases. In an iterative process, further simulations were run at these parameter values in order to resolve the parameter space accurately. The distinct regions of the parameter space are presented in figure 2.13, with the i, ii, and iii distinctions only shown for cases C_1, U_2 and C_3. As $Fr \to 0$, the boundaries collapse onto odd integers and the regions of complex shocks tend to zero. This is to be expected, as x_{ref} and x_{fan} coincide for $Fr = 0$, and, in fact, $u = 0$ everywhere so positive and negative characteristics have gradient 1 or -1, respectively. Cases C_1ii and C_1iii are the only two possible cases where the shock collides with x_{ref} with $\alpha = 2$. Our simulations reveal that neither of these cases exist.

The classification of each case determines exactly which three regions the shock travels through. The Rankine-Hugoniot conditions (2.20) & (2.21) ensure that the shock velocity is constant in uniform regions where the shock is not affected by the finite length of the lock-box $\alpha^- = 2$. For shocks in simple wave regions, one of

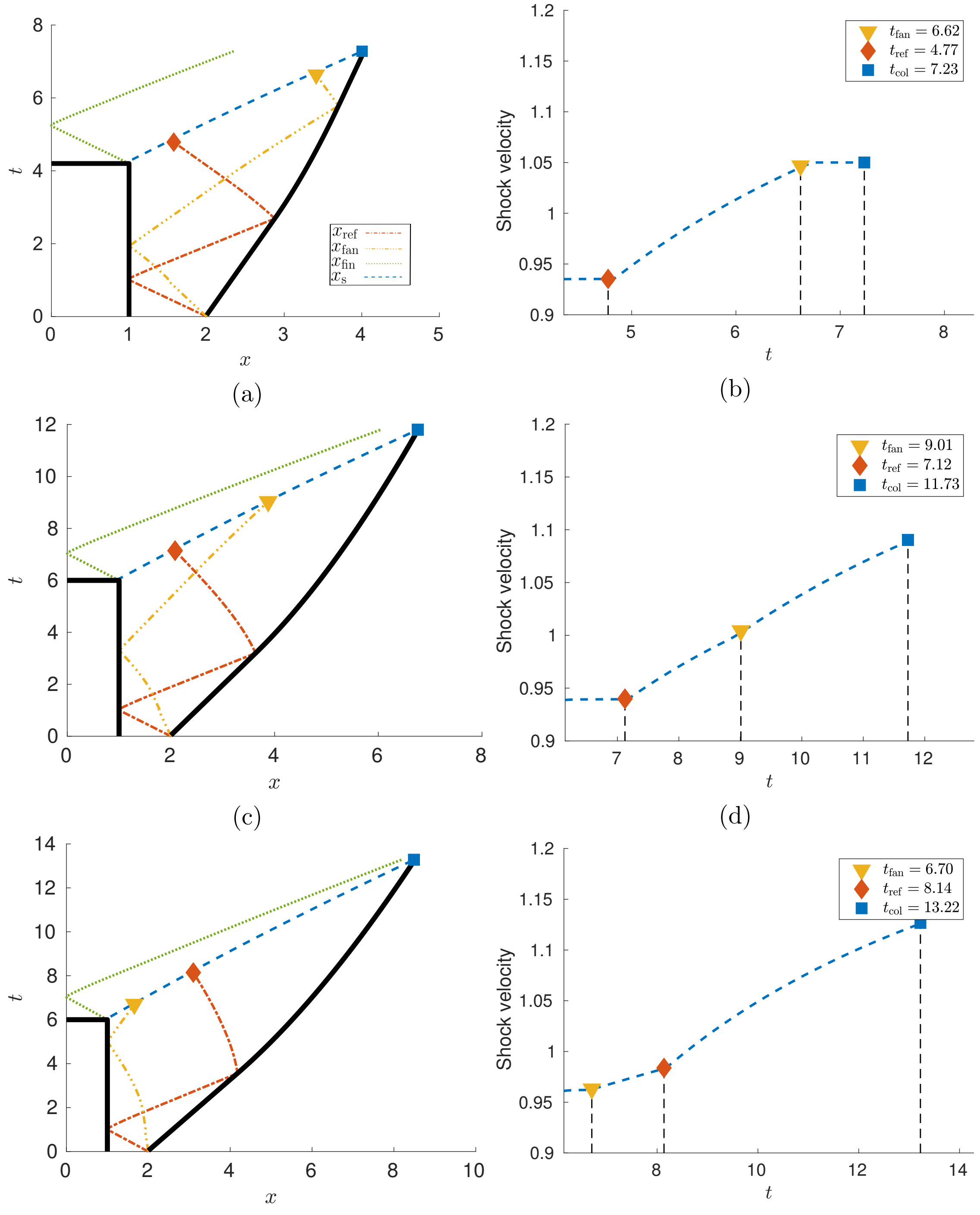

(a) (b)

(c) (d)

(e) (f)

Figure 2.9: Example U$_2$N cases for: U$_2$Ni, (a) & (b) ($Fr = 0.4$ and $t_{\rm re} = 4.2$); U$_2$Nii, (c) & (d) ($Fr = 0.6$ and $t_{\rm re} = 5$); and U$_2$Niii, (e) & (f) ($Fr = 0.9$ and $t_{\rm re} = 5.8$): (a), (c), (e) Characteristic diagram displaying the flow boundaries (–), $x_{\rm ref}$ and $x_{\rm fan}$ ($\cdots -$), the shock x_s (- -) and $x_{\rm fin}(\cdot)$; (b), (d), (f) Shock velocity for $t > t_{\rm re}$. $t_{\rm fan}$(▼), $t_{\rm ref}$(♦), $t_{\rm col}$(■) and $t_{\rm fin}$(●) (a-f). The shock velocity is only constant in Uniform regions, §2.3.1.

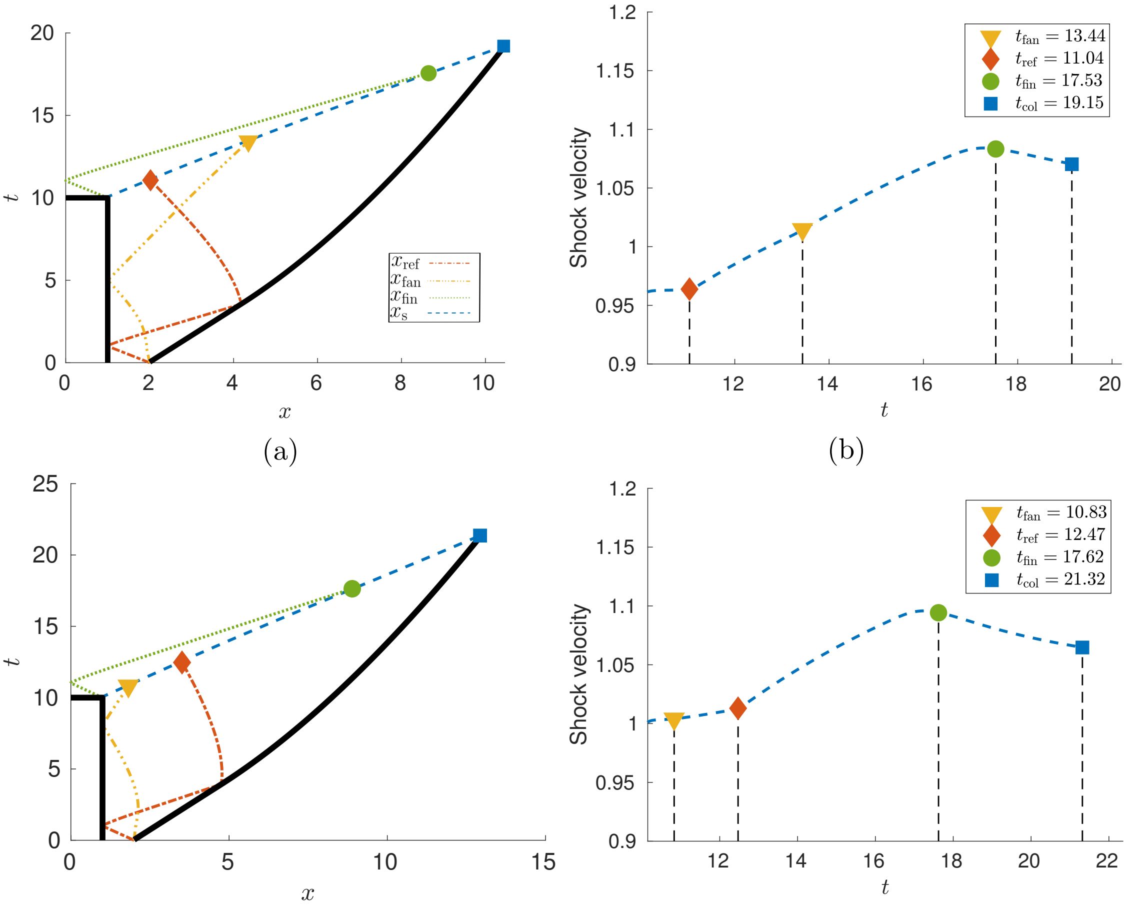

(a) (b)

(c) (d)

Figure 2.10: Example U$_2$F cases for: U$_2$Fii, (c) & (d) ($Fr = 0.9$ and $t_{\mathrm{re}} = 10$); and U$_2$Fiii, (e) & (f) ($Fr = 1.1$ and $t_{\mathrm{re}} = 10$): (a), (c) Characteristic diagram displaying the flow boundaries (–), x_{ref} and x_{fan} ($\cdots -$), the shock x_s (- -) and $x_{\mathrm{fin}}(\cdot)$; (b), (d) Shock velocity for $t > t_{\mathrm{re}}$. $t_{\mathrm{fan}}(\blacktriangledown)$, $t_{\mathrm{ref}}(\blacklozenge)$, $t_{\mathrm{col}}(\blacksquare)$ and $t_{\mathrm{fin}}(\bullet)$ (a-d).

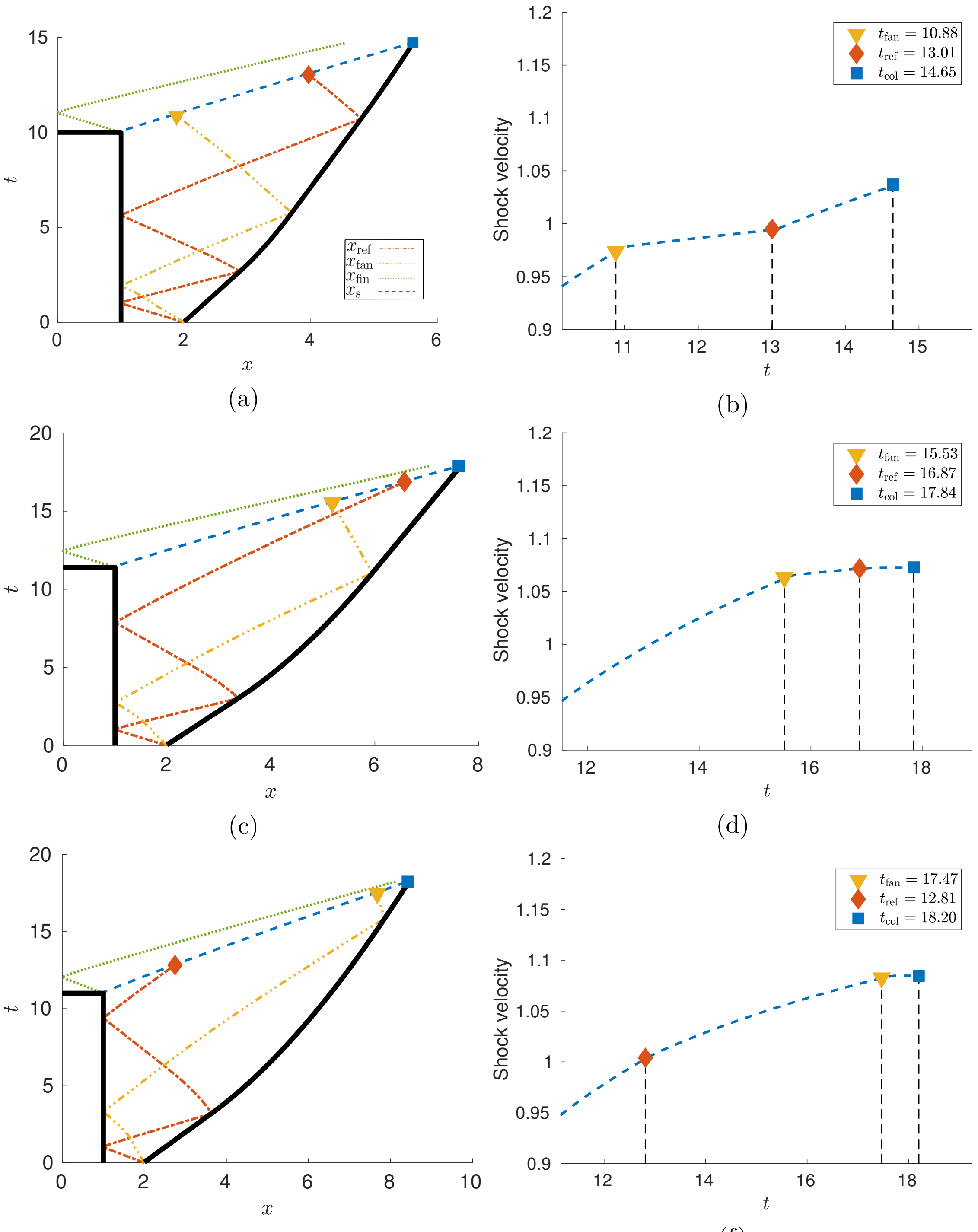

(a) (b)

(c) (d)

(e) (f)

Figure 2.11: Example C_3N cases for: C_3Ni, (a) & (b) ($Fr = 0.4$ and $t_{\mathrm{re}} = 10$); C_3Nii, (c) & (d) ($Fr = 0.6$ and $t_{\mathrm{re}} = 11.4$); and C_3Niii, (e) & (f) ($Fr = 0.7$ and $t_{\mathrm{re}} = 11$): (a), (c), (e) Characteristic diagram displaying the flow boundaries (–), x_{ref} and x_{fan} ($\cdots -$), the shock x_s (- -) and $x_{\mathrm{fin}}(\cdot)$; (b), (d), (f) Shock velocity for $t > t_{\mathrm{re}}$. $t_{\mathrm{fan}}(\blacktriangledown)$, $t_{\mathrm{ref}}(\blacklozenge)$, $t_{\mathrm{col}}(\blacksquare)$ and $t_{\mathrm{fin}}(\bullet)$ (a-f).

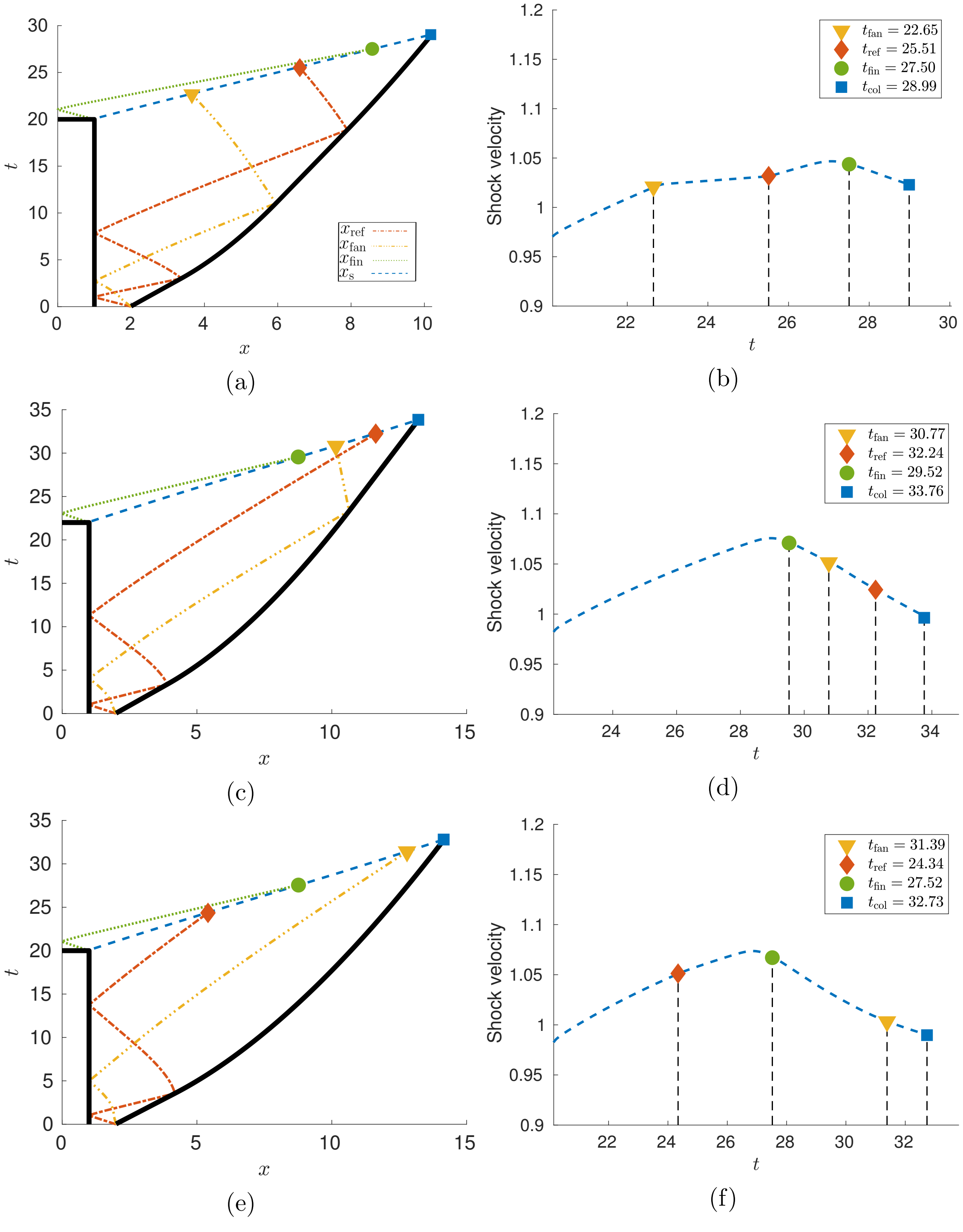

(a) (b)

(c) (d)

(e) (f)

Figure 2.12: Example C$_3$F cases for: C$_3$Fi, (a) & (b) ($Fr = 0.3$ and $t_{\rm re} = 20$); C$_3$Fii, (c) & (d) ($Fr = 0.8$ and $t_{\rm re} = 22$); and C$_3$Fiii, (e) & (f) ($Fr = 0.9$ and $t_{\rm re} = 20$): (a), (c), (e) Characteristic diagram displaying the flow boundaries (–), $x_{\rm ref}$ and $x_{\rm fan}$ ($\cdots$ –), the shock x_s (- -) and $x_{\rm fin}(\cdot)$; (b), (d), (f) Shock velocity for $t > t_{\rm re}$. $t_{\rm fan}(\blacktriangledown)$, $t_{\rm ref}(\blacklozenge)$, $t_{\rm col}(\blacksquare)$ and $t_{\rm fin}(\bullet)$ (a-f).

α^+ or β^+ will take constant value given in equation (2.18) or (2.19), respectively, while the other will vary monotonically between two constant values dependent on Fr (from the neighbouring uniform regions). In a complex region, the values of α^+ and β^+ both vary between the constant values given in equations (2.18) & (2.19).

Solving the Rankine-Hugoniot conditions (2.20) & (2.21) numerically for a fixed $\alpha^- = 2$ and varying Fr, α^+ and β^+ enables us to explore the regions of the flow where the shock $\dot{x}_{\mathrm{s}}$ may accelerating or decelerating. Studying the regions up to S_7 and C_6 revealed that the shock accelerates for all possible parameter values in regions of fixed α^+ (S_3, S_5 and S_7) and for all values of α^+ above a critical value of the densimetric Froude number Fr_c in regions of fixed β^+ (S_2, S_4 and S_6). Similarly one variable was fixed and the other varied to determine Fr_c-values for complex regions. This analysis revealed that apart from case C_3Ni in the C_4 region and C_3Niii in the C_3 region, all the Fr_c-values lie in the F region of the parameter space and therefore, all shocks in the N region up to case U_6 have non-decreasing velocities, $\dot{x}_{\mathrm{s}}$. Sampling the C_3Niii case did not reveal any decelerating shocks. Decelerating shocks were found in C_3Ni near the N-F boundary and just before the shock reaches the head. However, these were also observed for other cases near the N-F boundary. As the numerical method is not exact, the maximum shock velocity may arise just before the reflection of the backwards travelling disturbance x_{fin} reaches the shock, figure 2.12b,d&f. The velocity maximum occurs just before t_{fin}. This is believed to be a numerical artefact from the dissipative nature of the Lax-Wendroff scheme and that N shock do not necessarily decelerate.

The velocity of the flow behind the shock $u^- = (\alpha^- + \beta^-)/2$ is related to the velocity of the shock through the Rankine-Hugoniot conditions (2.20) & (2.21). The simulations reveal that the acceleration of the flow behind the shock has the same sign as the shock acceleration, except when the shock is propagating through S_{2n} regions of the flow, i.e. regions where β^+ takes a constant value. In these regions the acceleration has the opposite polarity. Critically, this means that an increasing shock speed is equivalent to an increasing fluid velocity behind the shock for all other regions in the single release flow.

Depth h and velocity $u = m/h$ are compared for cases U_2Ni and C_3Ni in figure 2.14. The position of the curves $x_{\mathrm{ref}}(\blacklozenge)$ and $x_{\mathrm{fan}}(\blacktriangledown)$ are displayed along the x-axis to highlight the boundaries between uniform, simple, and complex regions. After the second release the position of the shock ($\blacksquare$) and $x_{\mathrm{ref}}(\bullet)$ are also shown. Both cases are for the same Fr, so the initial dynamics are identical. After the second release, the flow depth is deeper, but slower, behind the shock for the U_2Na case when compared with the C_3Ni case. When the shock reaches the head of

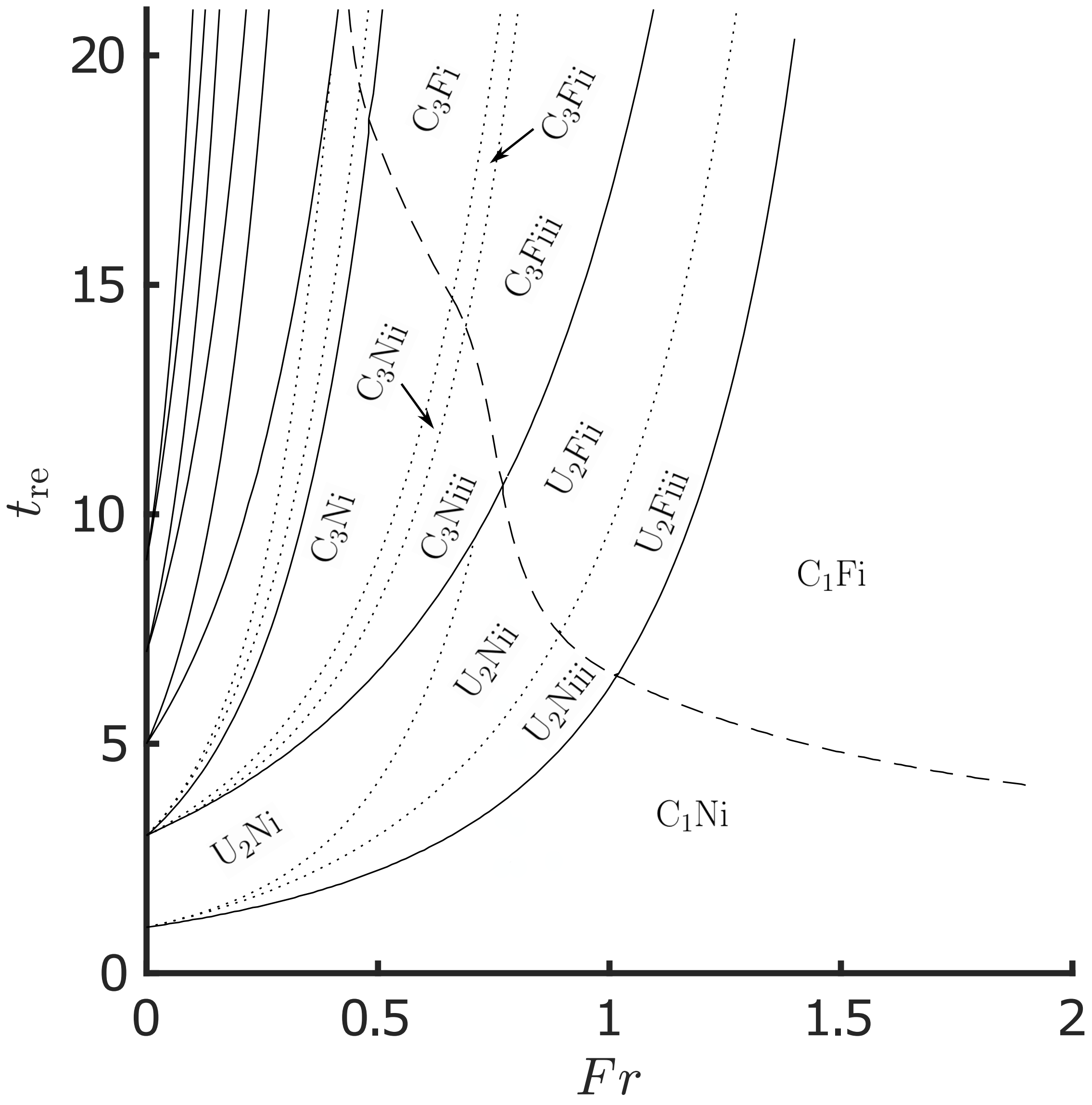

Figure 2.13: Structure of the (Fr, t_{re}) parameter space up to $\mathrm{C_3}$ shocks. Numerically determined boundaries between regions (–), sub-regions ($\cdots$) and N/F (- -) are shown.

the flow the expected constant depth and velocity is observed for the $\mathrm{U_2Na}$ case. Whereas for the $\mathrm{C_3Ni}$ case, the velocity increases to a maximum at the head of the flow. This maximum is larger than the maximum velocity for the $\mathrm{U_2Na}$ case.

2.3.3 Momentum of the Head

Both the destructive potential, i.e. the amount of damage it can cause, of the gravity current and its run-out length can be affected by the fluid momentum at the head of the current $m(x_N, t)$. In figure 2.15 we compare the momentum at the time when the shock collides with the head at the same time, $m(x_N, t_{\mathrm{col}})$, for

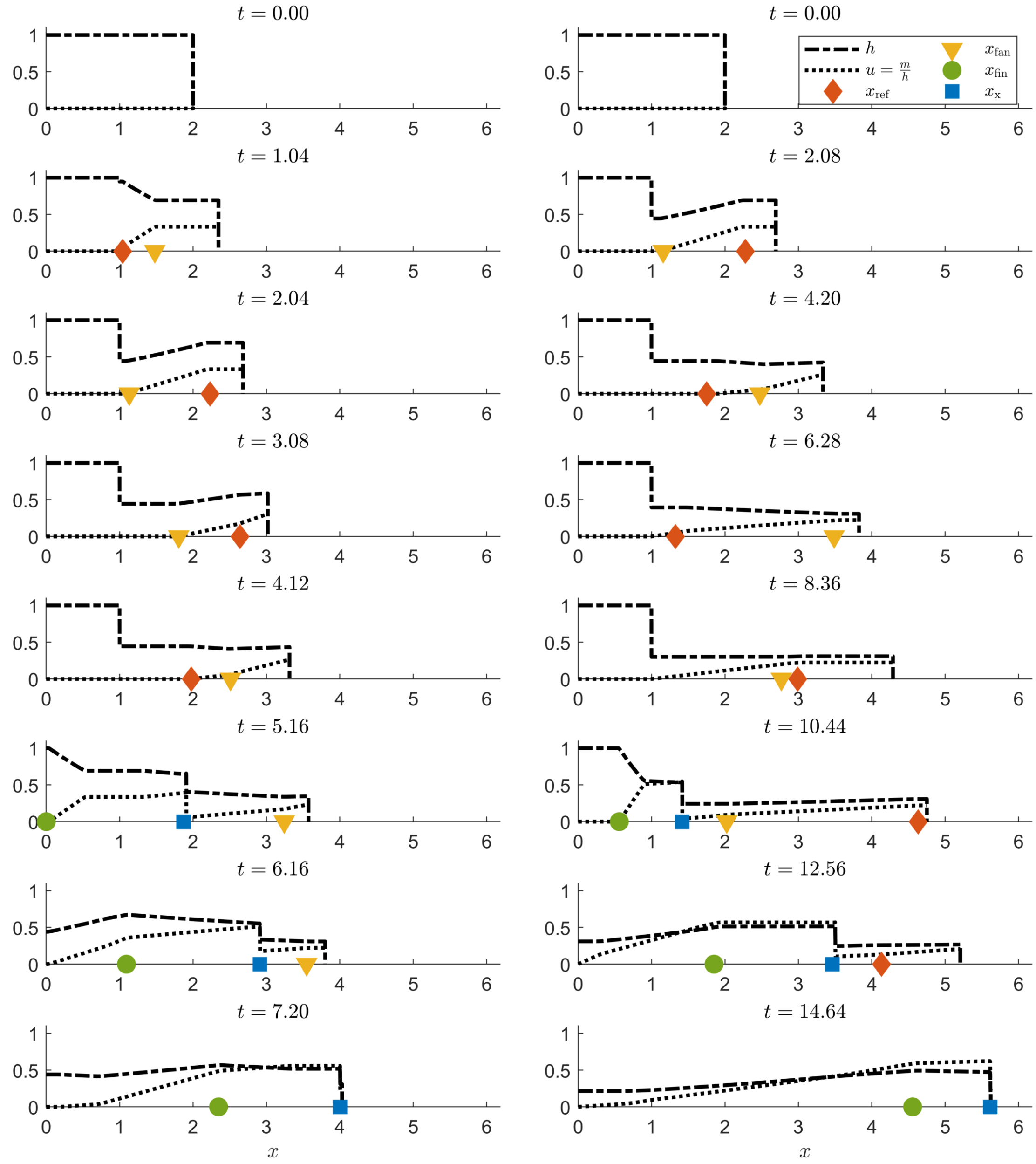

Figure 2.14: Depth $h(-\cdot)$ and velocity $u = m/h(\cdots)$ profiles at eight equally-spaced time steps until the shock reaches the head of the current for the following cases: U$_2$Ni (left) and C$_2$Ni (right). Positions of the curves x_{ref}(♦) and x_{ref}(▼) are displayed on the x-axis until they intersect the shock x_{s}(■). The position of x_{fin}(●) is also displayed on the x-axis.

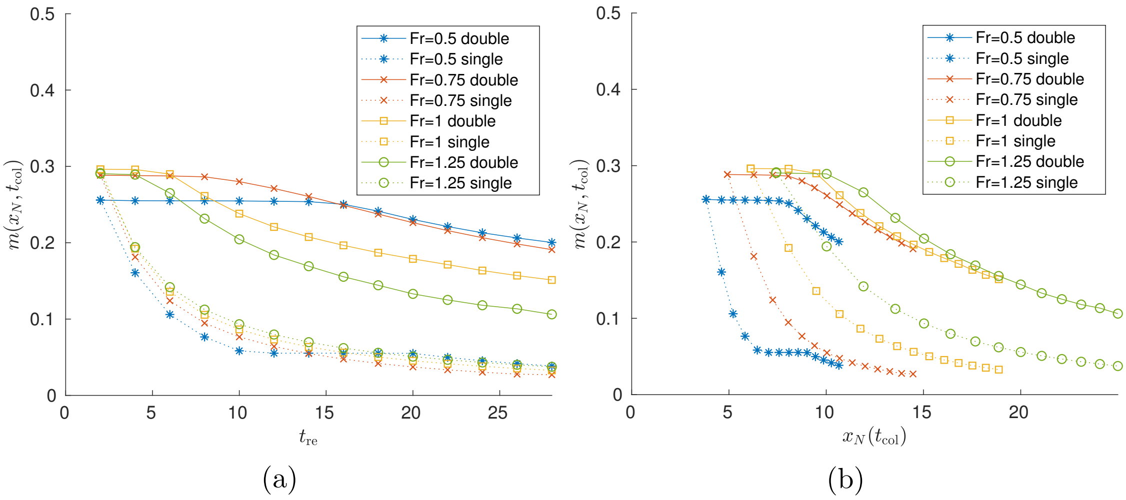

(a) (b)

Figure 2.15: Computed momentum at the head of the flow when the shock arrives, $m(x_N, t_{\mathrm{col}})$, for four Froude numbers $Fr = (0.5, 0.75, 1, 1.25)$ in increments of 2 pulse separation times t_{re} (–) against: (a) pulse separation time t_{re}; (b) displacement of the head at the time of collision, t_{col}. Momentum at the collision time, t_{col}, for a single release of twice the size $t_{\mathrm{re}} < 1$ $(\cdots)$ is also shown.

four different Froude numbers Fr against pulse separation times t_{re}. Also shown on this plot is the corresponding momentum for a single release of twice the size at $(x, t) = (x_N, t_{\mathrm{col}})$. For a fixed Fr, the momentum is significantly lower for a single release than the corresponding double release. Although both cases contain the same amount of material, the depth at the head of the flow starts decreasing later for the single release and therefore the dissipation is larger. Further, the dissipation is significantly larger at the head of the flow than at the shock.

In contrast to the single release, where increasing the densimetric Froude number decreases the dissipation at the head, plotted against separation time the momentum in the corresponding double release is lower for higher densimetric Froude numbers. This is a consequence of the head moving faster for higher Froude numbers. If instead the momentum at $t = t_{\mathrm{col}}$ is plotted against the position of the head $x_N(t_{\mathrm{col}})$, figure 2.15b the expected trend is observed with higher Froude numbers being less dissipative. Critically, although the distinction is less with larger Froude numbers Fr, a single release event is more dissipative than a double release.

2.4 Conclusions and future work

We have explored the effect of pulses on gravity current propagation using an extension of the shallow-water model for the single lock-release case studied by Hogg (2006). The range of solutions are classified in terms of two parameters: the Froude number at the head of the current, Fr, and a dimensionless pulse separation time, t_{re}. For $t_{\mathrm{re}} \leq 1$ the problem is identical to a single release, whilst the limits $t_{\mathrm{re}} \to \infty$ and $t_{\mathrm{re}} \to 1^+$ correspond to two independent events and a single event of twice the volume, respectively. For intermediate values of t_{re} the order the pulse intersects three curves x_{ref}, x_{fan} and x_{fin}, qualitatively determine its propagation velocity. Critically, the pulse has non-negative acceleration before it intersects x_{fin} and negative acceleration thereafter. For small values of t_{re} and/or small values of the Froude number, Fr, x_{fin} does not intersect the pulse before it reaches the front, figure 2.13.

Variations in pulse velocity affect the rate of energy dissipation, and thus of the energy transferred through to the head of the current, which may enable the flow to transition from laminar to turbulent behaviour. For pulse-prone, compositional flows such as pyroclastic flows, the dynamics of the flow depend on dynamics of the release and the changes in flow velocity may have implications for hazard prediction models, which sometimes neglect the release dynamics and the subsequent pulses created.

The parameter space considered in this chapter is limited to $t_{\mathrm{re}} \in (1, 21]$ and $Fr \in (0, 2)$. Hogg (2006) considered the single-release problem for $Fr \in (0, \infty)$. However, qualitative differences in the solution are observed for $Fr \geq 2$. When $Fr \geq 2$ and finite the characteristic x_{ref} reflects once off the back of the lock-box and then off the head, but the propagates forwards in time and space, but at a slower rate than the head. Further, the x_{fan} characteristic propagates forwards from release and never intersects the head or the back of the lock-box. Further, an internal shock occurs within the solution in finite time for $Fr > 2$. As $Fr \to \infty$ this shock does not occur, x_{ref} only reflects off the back wall and x_{fan} is coincident with the head of the flow x_N. This shock may form before the pulse reaches it and the pulse may affect the formation of the shock. Thus, a considerably different structure would be observed in the (Fr, t_{re})-parameter space for $Fr \geq 2$. Studying a larger region of t_{re} would be less insightful as the distinctions between the cases reduce as t_{re} increases and the releases appear more like independent events. This chapter is restricted to equally sized lock-boxes. Further extensions to this could explore varying the depth or length of one of the lock-boxes. Further, entrainment, basal-drag and bed slope are neglected and their effects could be incorporated. Finally, a sediment-bearing flow could be studied in the double-lock configuration by employing the full equations studied by Bonnecaze et al. (1993).

Chapter 3

Experimental study of pulses in gravity currents

3.1 Introduction

In this chapter the double lock-release problem considered in the previous chapter will be studied using idealised experiments in a similar configuration to Ho et al. (2018a,b, 2019). Ho et al. (2018a,b) investigated the phased release of turbulent saline gravity currents, where two lock boxes of equal volume of locked fluid were released sequentially into a quiescent ambient. Their flows quickly entrained ambient water creating a density stratification after the first release. For a short delay time between releases, the fluid from the second lock-box propagated through the body of the first at the bottom of the mixing zone. The velocity and density maximum occurs just behind the head of the current (Sher and Woods, 2015; Hughes, 2016) and Ho et al. (2018b) argue that this results in the intrusion catching up with the head of the current. Whereas for long delay times, a pulse was created that propagated similar to the first release and mixed with both the first current and the ambient diluting it. The thin basal layer of the remnants of the first pulse reduced the drag of the flow and led to the pulse catching up with the head. The complex dynamics, that arise from the density stratification, would be poorly captured by the depth-averaged shallow-water presented in the previous chapter.

A preliminary, unpublished, experiment conducted by Ho et al. (2018a,b) used a higher viscosity 0.8 glycerol/water mixture (80% glycerol) for the current and a water ambient, which produced a laminar-transitional gravity current. Laminar-transitional is identified as plug-like flow in the body with only a small region of velocity fluctuations localised at the head. However, the Reynolds number defined in chapter 1 $Re \gg 1$. A small region behind the head was mixed, but the bulk of the release remained unmixed, signified by the interface remaining sharp. The second release displaced the remnants of the first release and created a bore that transitioned into the tail of the first current and towards the head of the current. This is in contrast to the turbulent saline releases of Ho et al. (2018a,b, 2019), where the second release propagates through the body of the first release and transfers material to the head.

Intriguingly, the pulse caused a rapid transition to turbulent behaviour upon arriving at the head of the flow, which coincided with a rapid dilution of the head brought on by a cascade of mixing, figure 3.2. I.e., increased energy resulted in the onset of turbulence and more mixing, which is turn reduced the viscosity and promoted further mixing. This was enhanced by the highly non-linear dependency of viscosity on the concentration for glycerol/water mixtures (Cheng, 2008). This can be observed behind the head in figure 3.2 by the significant amount of mixing, whilst the mixed fluid and the current maintain a well defined boundary. In addition to exploring the behaviour of pulsed flows at a higher viscosity, this work investigates the laminar-transitional to turbulent transition observed in this preliminary experiment. Further, a comparison between the shallow-water model presented in chapter 2 is presented.

3.2 Methodology

3.2.1 Physical Setup

Pulsed gravity currents were created in a horizontal Perspex® tank of length 5 m, width 0.2 m and depth 0.3 m by releasing glycerol/water mixtures into a water ambient, figure 3.1. The configuration of the tank was identical to the work of Ho et al. (2018a,b). Two lock gates encapsulating the dense fluid were spaced at 0.25 m intervals from the end of tank. 0.25 m deep Perspex® sheets were placed 0.1 m from either end of the tank to create overspill boxes, which enabled surface waves to dissipate.

In the first series of experiments, the evolving flow was recorded by two rolling cameras capable of recording high-definition video at 24 Hz. Each camera frame had a resolution of 1920 by 1080 pixels with each pixel representing 3.0×10^{-4} m at the nearside of the tank. The cameras were moved by hand along fixed rollers

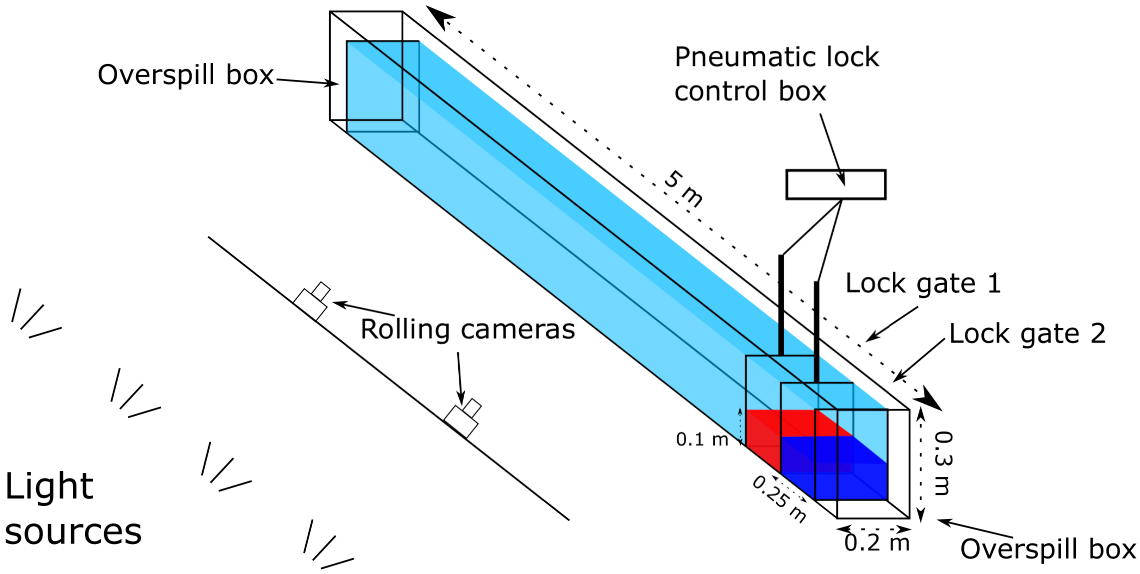

Figure 3.1: Schematic of experimental design, based on Ho et al. (2018a,b) the first lock box is dyed red (lighter colour, in greyscale) and the second blue (darker) and are filled to a depth of 0.1 m. The ambient depth is 0.25 m . Pneumatically controlled gates release the first gate at $t = 0$ and the second at $t = t_{\mathrm{re}}$. The evolving flow is filmed with either a pair of rolling cameras or a fixed high-speed camera (not shown). Overspill boxes at either enable surface waves to dissipate and any excess ambient fluid to drain from the tank. Not to scale.

to keep them steady. A measuring tape was placed just below the tank on the nearside face, to enable the extraction of the distance from the videos afterwards. The first camera tracked the head and the second tracked the pulse from initiation during the double release experiments. The cameras were refocused before each experiment. Sliding cameras were used so that the entire flow could be captured at relatively high resolution over the run-out length, which was approximately 2-3 m. Beyond this distance, the flows became viscously dominated and propagated very slowly. In, a second series a high-speed camera was installed in a fixed position and focused a location capturing the pulse transition region (0.15-0.75 m downstream of the front of the first lock gate). The high-speed camera recorded at high-definition (1920 by 1200 pixels) video at 200 Hz for a period of 18 s, which was sufficient to capture both the head and the pulse for the range of t_{re} values considered. With all cameras, photographs of a chequerboard were taken before each experiment and the inherent lens distortion was removed from the videos subsequently using the Camera Calibration toolbox in MATLAB (Bouguet, 2004). During the early stages of the flow, when the current was moving at its fastest, some of the videos were slightly blurred, likely a result of the shutter speed being insufficient. Every effort was made to move the cameras smoothly to account for this, but removing the all blurriness proved impossible.

The depth of the mixture within the lock-gate, h_{lock}, was 0.1 m and the ambient 0.25 m. Therefore, the depth ratio between the ambient and lock was 2.5. For depth ratios less than 2, single-layer shallow-water models (equivalent to an infinite ambient depth) are not suitable for capturing the dynamics of a lock release, because the initially smooth rarefaction wave develops a shock, which is subsequently reflected off the back of the lock-box and travels towards the head of the currents (Ungarish, 2009). Further, the slumping distance (region of constant head speed, $\dot{x}_n$) of the motion is larger and the shape of the interface is changed. These differences will still be present for a ratio of 2.5. However, they are less significant. Having a ratio larger than 2.5 would be more desirable in this regard, but with a fixed tank size, the only way to increase this would be by decreasing the depth of the locked fluid. However, the depth of the resulting current would also be reduced, decreasing the resolution at which the current can be observed. Therefore, the ratio of 2.5 was chosen as a balance between the resolution and the agreement with the single layer shallow water model.

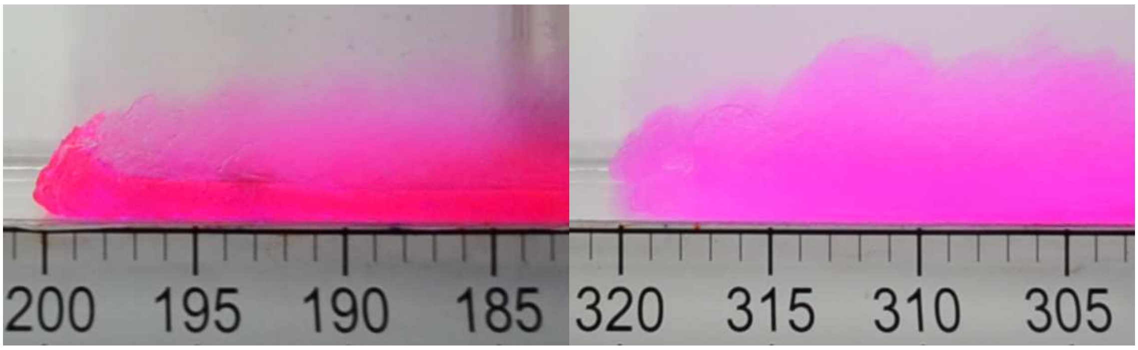

Figure 3.2: Stills from experimental videos demonstrating the mostly un-mixed and laminar transitional behaviour at the head of the current (left) and the fully mixed and turbulent behaviour after the pulse reaches the head (right). Ruler for scale in centimetres.

Lock-release flows are often used to model large-scale geophysical flow that may be unconfined or only partially confined. The design and withdrawal mechanisms of the lock gate can have an impact on the resulting experiment. Two-dimensional simulations that resolved the motion of the lock-gate have been conducted to assess the impact on the withdrawal on the flow (Giorgio Serchi et al., 2011). The withdrawal of a lock gate causes disturbance in six main ways: i) spontaneous rotation of the current ambient interface; ii) reduction in free surface height inside the lock-box as the current starts to flow; iii) tangential shear on the withdrawing lock-gate; iv) Variations in free surface height; v) Wake vorticity of the lock-gate and replacing the void left by withdrawal; vi) difference in timescales between the flow and the triggering mechanism. Although these are argued to be more significant to compositional gravity currents, Giorgio Serchi et al. (2011) conclude that to minimise these affects the lock-gate should be as feasibly thin as possible and withdrawn mechanically as quickly as possible without inducing shaking.

A pneumatic lock-control box controlled the withdrawal of the lock-gates to ensure they were raised smoothly and consistently. The lock-gate were set into groves cut into the side of the Perspex® tank. The groves created a tight seal to stop leakage and prevented the gates from shaking. Upon release of the first lock-gate, the lateral pressure gradient drove the flow out as a gravity current. The time between withdrawal, t_{re}, was specified for double-release flows. The release of the second current created a pulse, which transitioned from the second current into the first and propagated towards the head of the flow.

Giorgio Serchi et al. (2011) recommended that the lock gate be withdrawn as quickly as possible, whilst not shaking the gate, and that the gate is as thin as possible. However, the flows considered in their simulations were of a significantly higher lock-gate Reynolds number, defined as $Re_{\mathrm{gate}} = U_{\mathrm{gate}} d_{\mathrm{gate}}/\nu$, where U_{gate} is the gate withdrawal speed, d_{gate} is the width of the lock box and ν is the kinematic viscosity, which was constant in their simulations. Their lock-gate Reynolds numbers were 1500 or 3000 and within the fully turbulent regime. Using the viscosity of the glycerol/water mixtures, a lock-width of 0.005 m and withdrawal speed of $1\,\mathrm{ms}^{-1}$ yields Re_{gate}-values of 20, 43 and 90, which are laminar-transitional. Although the gates could have been withdrawn faster than $1\,\mathrm{ms}^{-1}$, this would increase the turbulent mixing of the flow. This was highlighted by the increased amount of mixing in the cases with lower glycerol concentration.

3.2.2 Glycerol properties

Glycerol ($CH_2(OH)CH(OH)CH_2(OH)$), for a more complete description see Christoph et al. (2006), is a colourless, odourless, viscous liquid that is a simple polyol compound. It has extensive uses in the food and pharmaceutical industries. The three hydroxyl (OH^-) groups result in its water solubility and its hygroscopic (attracting and holding water molecules) nature. Pure glycerol can be synthesised, but it is an expensive process to do so Christoph et al. (2006). The glycerol used in the experiments had been purified and was quoted to be at least 99.5% pure. Glycerol behaves like a Newtonian fluid and its mixtures with water vary in viscosity by three orders of magnitude (from pure water to pure glycerol), making it highly suitable for a wide range of experiments. Furthermore, as discussed later in this section, empirical relationships for the viscosity exist and are accurate to within a few percent over all possible concentrations and the temperatures experienced in the

Table 3.1: Properties of pure glycerol at room temperature (20 °C) (Christoph et al., 2006).

Density (ρ_g, kgm^{-3})	Dynamic Viscosity (μ_g, Nsm^{-2})	Kinematic Viscosity (ν_g, m^{2}s^{-1})	Molar Mass (M_g, gmol^{-1})
1261	1.412	0.00112	92.094

experiments. Relevant properties of pure glycerol are given in table 3.1.

The concentrations studied in the experiments were chosen to provide Reynolds numbers, Re_t, within the laminar-transitional regime. These Reynolds numbers were determined using the half lock height, $h_{\text{lock}}/2$ as the length scale and a balance between kinetic and potential energy for the velocity scale, $U \sim \sqrt{g' h_{\text{lock}}}$,

$$Re_t = \sqrt{g' h_{\text{lock}}^3}/2\nu, \tag{3.1}$$

where $\nu = \mu/\rho$ is the kinematic viscosity. For $Re_t = 90$, 180 and 360, the viscosity and density parametrisation of glycerol/water mixtures by Cheng (2008) was used to determine the required glycerol concentration, α_g, (correct to two s.f.) by volume, at room temperature (20 °C) of $\alpha_g = 0.90, 0.84$ and 0.77, respectively. Selection of these Reynolds numbers minimised turbulent mixing and entrainment in the current and thus ensured that the glycerol concentration in the current remained relatively constant throughout. In addition these Reynolds numbers ensured that the flow was not dominated by viscous drag and kept the gravity current in the inertial-buoyancy regime for long enough to enable comparison with the shallow-water model. The finite supply of material implies that the current would slow down and become thinner after the initial slumping phase, resulting in an increased effect from viscous drag over time. Thus, the inviscid assumption required for our shallow-water model becomes invalid at long time-scales. The time-scale when viscous, inertial and buoyancy forces are are all equal can be estimated by a simple dimensional argument

$$t_{\text{c}} \sim \left[\frac{(h_{\text{lock}} l)^4}{g'^2 \nu^3}\right]^{\frac{1}{7}}, \tag{3.2}$$

Huppert (1982). This produced non-dimensional transition times for the three concentrations, $\alpha_g = 0.77, 0.84, 0.90$, of 11.5, 8.5 and 6.2, respectively. For values of t larger than this, the viscous forces will become larger and the current would propagate with a dominant balance between viscous and buoyancy forces.

The dynamic viscosity, μ, and density, ρ, of the pure glycerol (subscript g)

and water (subscript w) are given by Cheng (2008):

$$\mu_w = 0.00179 \exp\left(\frac{-(1230+T)T}{36100+360T}\right), \tag{3.3}$$

$$\mu_g = 12.1 \exp\left(\frac{(T-1233)T}{9900+70T}\right), \tag{3.4}$$

$$\rho_w = 1000\left(1 - \left|\frac{T-4}{622}\right|^{\frac{17}{10}}\right), \tag{3.5}$$

$$\rho_g = 1277 - 0.654T. \tag{3.6}$$

and the mass fraction of glycerol C_m

$$C_m = \frac{\alpha_g \rho_g}{\alpha_g \rho_g + (\alpha_w)\rho_w}, \tag{3.7}$$

where $\alpha_w = 1 - \alpha_g$ is the water concentration and $T \in [0, 100]$ is the temperature in Celsius. Cheng (2008) used a mixing power law for the dynamic viscosity and a volume weighted density

$$\mu = \mu_w^{\iota} \mu_g^{1-\iota}, \tag{3.8}$$

$$\rho = \alpha_g \rho_g + (1 - \alpha_w)\rho_w, \tag{3.9}$$

where the parameter ι is given in terms of C_m and two parameters a and b

$$\iota = 1 - C_m + abC_m \frac{1 - C_m}{aC_m + b(1 - C_m)}, \tag{3.10}$$

$$a = 0.705 - 0.0017T, \tag{3.11}$$

$$b = (4.9 + 0.036T)a^{\frac{5}{2}}. \tag{3.12}$$

The empirical model derived by Cheng (2008) is based on three studies (Segur and Oberstar, 1951; Shankar and Kumar, 1994; Chenlo et al., 2004) into the viscosity of water/glycerol mixtures and is able to predict the dynamic viscosity, μ within a few percent, table 3.2. Crucially, the temperature (approximately 20 °C) and the glycerol concentration (0.77 to 0.90) lies within the ranges considered by the empirical model of Cheng (2008). However, at high concentration ranges, the viscosity of the mixture can vary by as much as 10% for a change of 1 °C or 0.01 concentration and thus, care must be taken to ensure that temperature and concentration fluctuations do not contribute a major source of error. Like most mixtures, there is a volume contraction when glycerol and water mix. At 20 °C, the largest contraction is approximately 1.1% (Volk and Kähler, 2018) and occurs at a glycerol concentration of 0.6. This is an upper bound on the error of the volume-weighted

Table 3.2: Temperature (T,° C) and concentration ranges considered by the three studies from which the empirical model of Cheng (2008) for the dynamic viscosity μ of glycerol-water mixtures is constructed. Also included is the maximum and mean error between the model fit and the data points in each of three works calculated by Cheng (2008). The percentage error is calculated $|\mu_{\text{predicted}} - \mu_{\text{actual}}|/\mu_{\text{actual}} \times 100\%$

Reference	Temperature range (°C)	range of glycerol mass concentration (C_m)	Maximum error (%)	Mean error (%)
Chenlo et al. (2004)	20-50	0-0.315	2.2	0.7
Segur and Oberstar (1951)	0-100	0-1	3.5	1.3
Shankar and Kumar (1994)	10-50	0-1	8.5	2.3

mixture density and less than the error in dynamic viscosity.

3.2.3 Procedure

On the Friday of the week proceeding any experimental work, two large storage tanks (each with volume 1.8 m^3) were filled with domestic water and left over the weekend to equilibrate to lab temperature. This removed variations in the ambient temperature and provided enough water to run 14 experiments (each of volume 0.25 m^3) The temperature of the laboratory area was thermostatically controlled 24 hours a day.

The glycerol/water mixtures were premixed at least a day prior to experimentation in a 0.2 m^3 mixing tank at the desired concentration for a series of experiments. Mixing was preformed with an electric motor-driven vertical impeller with four blades inclined at 30°. A minimum of 45 l of liquid was required to submerge the impeller blades, but larger volumes reduced the amount of air that was entrained during mixing. Post mixing, the mixture was left to rest for a few hours so that most of the air could escape. A pump was then used to extract the mixture from the bottom of the mixing tank and fill 5 l containers (corresponding to the required volume of locked fluid, $0.1 \times 0.25 \times 0.2$ m^3). Each container contained a small amount of either red or blue dye and was shaken to mix the dye in. The containers were then left overnight to allow remaining air bubbles to escape. A total of four batches were mixed and samples of the mixture, labelled in order, were kept and later used to measure the viscosity in a rotary rheometer. The second batch, with concentration 0.84, was sampled twice and labelled 2a and 2b.

Both the mixing process and the pumping raised the temperature by a few degrees each, but this had dissipated by the following morning. Over the period the experiments were conducted, the stored water temperature varied by at most 1.5 °C during the first phase of experiments. Fluctuations were the result of variable lab temperature caused by other work being conducted in the lab area that affected the temperature near the thermostat. and were beyond our control. During the second phase of experiment, the temperature was lower by as much as 3 °C. as a result of temperature gradients throughout the lab area and seasonal temperature variations.

The temperature-normalised domestic water was pumped into the perspex tank to the desired depth of the ambient (0.25 m) prior to each experiment. The lock-gates were then lowered and a 0.25 m high perspex panel was placed 5 m downstream to create the overspill box at the far end. This panel and the lock-gates sat inside groves cut into the side of the Perspex® to create a seal and prevent seepage. Silicon grease was applied to the seals when necessary to keep them watertight. The drain was then opened to release some of the water in this overspill box. Various concentrations, table 3.3, of dyed blue glycerol/water mixture were partially filled into the back lock box with a peristaltic pump to a depth $h_{\text{lock}} = 0.1$ m. Two holes of radius 0.01 m had been carefully drilled into each lock gate centred 0.01 m above the ambient depth 0.25 m. Filling the lock boxes displaced the ambient water into the overspill boxes, which kept the ambient at the required depth of 0.25 m.

The filling rate was initially slow in order to minimise mixing with the ambient water. The filling rate was increased after there was sufficient glycerol/water mixture to fully submerge the outlet of the pipe. The pipe was clamped in place prevent it from moving during the filling process. The filling process took roughly 20-25 minutes, which was limited by the maximum speed of the pump, and unavoidably increased the temperature of the mixture by approximately 2 °C, because of the work done forcing the highly viscous mixture though the pipe. For double-release experiments, the same procedure was followed to fill the front lock-box with red-dyed mixture, figure 3.3.

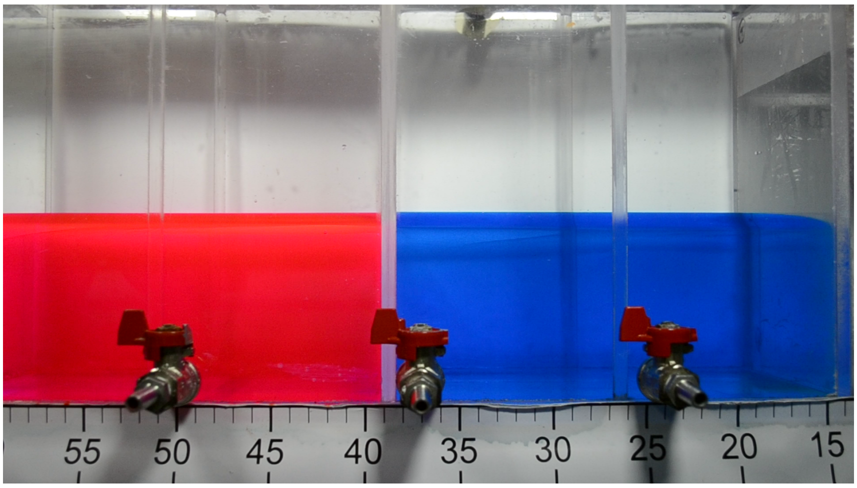

Figure 3.3: Snapshot of the lock-boxes just before the release of the lock gates. No mixing can be observed between the glycerol/water mixtures and the ambient.

Following this procedure resulted in no observable mixing at the free surface. Further, there was no noticeable diffusion of the interface between the mixture and ambient water. This, however, does not mean that no mixing took place, since glycerol is hygroscopic and there could have been a mass exchange dominated in the direction into the current. For this reason, and to save considerable time, the experiment was conducted at the conclusion of filling rather than allowing the glycerol/water mixture to reach the same temperature as the ambient water.

Before each experiment commenced, the ambient and glycerol/water mixtures temperatures were measured with a digital thermometer. A small amount of glycerol remained in the pipes of the peristaltic pump and this was used to measure the viscosity using a British standard u-tube viscometer, as discussed later. Further, the temperature of the mixture was taken before being used in the u-tube viscometer.

After each experiment, the tank was refilled with domestic tap water and a squeegee was used to mix any deposited glycerol/water mixture with this water before being drained. The lock-boxes were refilled at least three times, again with domestic tap water, and released into an air ambient before being drained. This ensured that all glycerol from the previous experiment had been removed. The hygroscopic nature of glycerol made this cleaning process relatively straightforward. Further, although transparent, glycerol has a significantly different refractive index than water (Haynes, 2014), facilitating detection of unmixed patches.

Glycerol is a simple sugar alcohol and therefore is an ideal medium for bacterial growth. Care was taken to minimise and to clean any spillages throughout the experimental work. Further, the glycerol used in each experiment was inspected beforehand to ensure that it had not been contaminated. Glycerol was mixed in batches to accommodate this and used within a few days.

3.2.4 Cases

The single-release experiments were conducted to determine appropriate release times of the second gate, t_{re}. For the single-release experiments, the second gate was held stationary to record the depth of fluid remaining within the lock-box. The release times, t_{re}, were chosen in terms of fractions $(1/2, 3/8, 1/4$ and $1/8)$ of remaining fluid within the first lock box. A piece-wise linear interpolation of the depth inside the lock box, using each end of the box and the mid-point as the three stencil points, was used to determine this remaining fraction. All experimental cases are presented in table 3.3. Initially, multiple runs of each case was conducted to assess repeatability, table 3.4, which is discussed in section 3.5.1. Note that for the RD90-1/8 case, the time scale to reach 1/8 depth was of the order of minutes and a more appropriate non-dimensional time of 23.5 was chosen.

The range of Reynolds numbers was selected, because a suitable glycerol concentration to inhibit mixing with the ambient, whilst maintaining the inertia-buoyancy balance could not be known a priori. Further, the range was selected around that of the preliminary experiment to attempt to reproduce the laminar-transitional to fully turbulent behaviour observed in the preliminary experiment of Ho et al. (2018a,b), for similar Reynolds number values. Release times were chosen to be similar across the experiments. Further, fractions of greater than 1/2 were not considered, because the pulse would become increasingly smaller and difficult to detect. Non-dimensional release times of less than 1 would yield meaningless comparisons to the theoretical shallow water model, because this is the time for the backwards travelling disturbance to reach the back of the lock-box.

After the series of experiments with the rolling cameras, it became obvious that there was still a noticeable amount of mixing with the ambient and dilution at the head for the higher two concentrations. As a result of this, and further, to keep costs down, only the highest concentration was used with the high-speed camera.

3.2.5 Viscometry

The section details the two methods used to measure post experiment the glycerol/water mixture viscosity: the Ubbelohde u-tube viscometer and the parallel-plate rotary rheometer. Both utilise Stokes' flow and are suitable for measuring high viscosity liquids, like oils. The rotary rheometer may also be used for non-Newtonian fluids.

The Ubbelohde, or suspended level, viscometer, figure 3.4, is a type of u-tube or capillary viscometer invented by Dr. Leo Ubbelohde to measure the viscosity of viscous liquids, (Ubbelohde, 1936). Liquid is filled through the top pipe until the bottom two bulbs are half full. Then, by closing pipe b and providing suction to the top of pipe c, liquid is drawn up the pipe and through a constriction of known diameter, R, and length, $\mathcal{L}_u$, to a level above line A. Pipe b is then released to allow the fluid to return to equilibrium in the bottom of the viscometer. The previously used Ostwald viscometer did not have this pipe and as such, the variations of total fluid in the device affected the hydrostatic pressure between a and c. By assuming

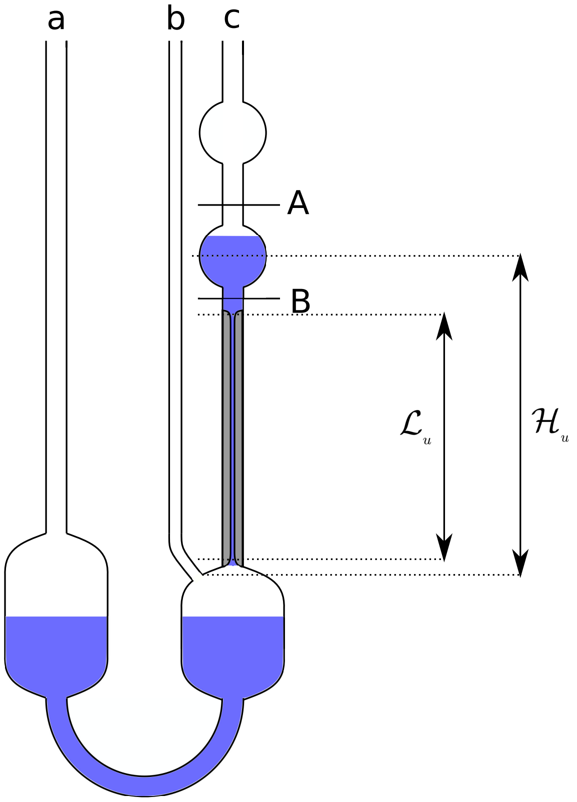

Figure 3.4: The Ubbelohde or suspended level viscometer (Ubbelohde, 1936). The two bulbs are partially filled with the liquid to be measured through pipe a. Whilst pipe b is sealed, the liquid is drawn up pipe c, through suction, to above A. Pipe b is then released and the suction removed to allow the liquid to flow through the constriction below B. The time taken, t_{con}, to drain the fluid is proportional to the viscosity for large values of t_{con}. The device is kept vertical with clamps during the entire process. Not to scale.

Table 3.3: Table of experimental parameters. Key: R - rolling cameras, HS - high speed camera, S - single release, D - double release; glycerol concentration, α_g, by volume (0.77,0.84 or 0.90); and fraction of remaining fluid in the first lock at $t = t_{\mathrm{re}}$ $(1/2, 3/8, 1/4, 1/8)$. The kinematic viscosity of the current and the Reynolds number $Re = \sqrt{g' h_{\mathrm{lock}}^3}/2\nu$ Note that at 0.90 concentration, the time to reach a remaining fraction of 1/8 was of the order of minutes and a t_{re}-value of 23.5 was chosen instead.

Case name	Single/ Double	(α_g)	Remaining fraction	t_{re}	Current density (ρ_c, kg·m^{-3})	Kinematic viscosity (ν, $\times 10^{-5}$m^2·s^{-1})	Reynolds number Re
RS77	S	0.77	-	-	1210	5.54	374
RS84	S	0.84	-	-	1227	11.6	184
RS90	S	0.90	-	-	1240	24.4	90
RD77-1/2	D	0.77	1/2	2.48	1210.3	5.54	374
RD84-1/2	D	0.84	1/2	2.33	1227	11.6	184
RD84-3/8	D	0.84	3/8	3.19	1227	11.6	184
RD84-1/4	D	0.84	1/4	4.9	1227	11.6	184
RD84-1/8	D	0.84	1/8	8.6	1227	11.6	184
RD90-1/2	D	0.90	1/2	2.3	1240	24.4	90
RD90-3/8	D	0.90	3/8	3.36	1240	24.4	90
RD90-1/4	D	0.90	1/4	5.84	1240	24.4	90
RD90-1/8	D	0.90	-	23.5	1240	24.4	90
HSD90-1/2	D	0.90	1/2	2.3	1240	24.4	90
HSD90-3/8	D	0.90	3/8	3.36	1240	24.4	90
HSD90-1/4	D	0.90	1/4	5.84	1240	24.4	90

Poiseuille flow within the constriction, the rate of change of volume, V, can be calculated

$$\frac{\mathrm{d}V}{\mathrm{d}t} = v_{\mathrm{con}} \pi R^2 = \frac{\pi R^4}{8\mu} \left(\frac{\Delta P}{\mathcal{L}_u} \right), \tag{3.13}$$

where v_{con} is the velocity of the liquid in the constriction and ΔP is the pressure difference between the top of the free surface and the bottom of the constriction. The difference between measurement points A and B is significantly less than the length of the constriction $\mathcal{L}_u$ and so constant pressure may be assumed, i.e. $\Delta P = \rho g \mathcal{H}_u$. For a known volume, V_0, between the lines A and B the volume flux equation (3.13) may be integrated with respect to time to yield

$$V = \frac{\pi R^4}{8\mu} \frac{\rho g \mathcal{H}}{\mathcal{L}_u} t_{\mathrm{con}} \qquad \Longrightarrow \qquad \nu = \frac{\mu}{\rho} = \frac{\pi R^4 g \mathcal{H}_u}{8 \mathcal{L} V_0} t_{\mathrm{con}}, \tag{3.14}$$

where t_{con} is the time taken for the fluid level to drop from A to B. Crucially, the kinematic viscosity, ν, only depends on parameters that are constant to the viscometer and the time, t_{con}.

U-tube viscometers are generally used to measure the viscosity of oils and other liquids, many of which are immiscible in water. Glycerol is miscible so it was

Table 3.4: Temperature measurements taken from the ambient, first and second lock-boxes. The corresponding sample or batch number is given for each case. For the cases measured, the temperature of the mixture before the u-tube viscometer used, the time for the liquid to drain and the corresponding kinematic viscosity calculated from the u-tube viscometer also given. Finally, the Reynolds number calculated from $Re_{\text{act}} = \sqrt{h_{\text{lock}}^3 g'}/2\nu$ is given.

Case	Temperature (°C)			Sample	Sample Temperature ($°C$)		Sample Time (s)		Measured viscosity (ν, $\times 10^{-5}$) (m^2 s^{-1})	Re_{act}
	Ambient	1^{st}	2^{nd}		1^{st}	2^{nd}	1^{st}	2^{nd}		
RS77	18.4	19.7	N/A	1		N/A		N/A		
	18.5	20.0	N/A	1		N/A		N/A		
	18.5	20.3	N/A	1		N/A		N/A		
RS84	16.9	18.0	N/A	2a	18.3	N/A	105.5	N/A	10.6	202
	17	17.9	N/A	2a		N/A	83.0	N/A	8.30	258
	16.8	17.9	N/A	2b		N/A		N/A		
RS90	17.8	19.0	N/A	4	18.4	N/A	170.0	N/A	17.0	129
	17.9	19.3	N/A	4		N/A		N/A		
	18.0	19.2	N/A	4		N/A		N/A		
RD77-1/2	16.9	18.0	17.7	1		18.2		48.9	4.89	425
	16.9	18.0	17.9	1				49.2	4.92	422
	16.9	17.9	17.8	1	19.3	18.4	47.88	48.2	4.80	433
RD84-1/2	16.8	17.9	17.9	2b	18.2	18.2	108.3	105.2	10.7	200
	16.9	18.0	18.0	2b						
	17.0	18.1	18.1	2b			103.4		10.3	207
RD84-3/8	17.3	18.9	18.7	3		20.2		80.6	8.06	265
	17.9	19.3	19.2	3						
RD84-1/4	17.2	19.4	19.9	3		19.2		76.4	7.64	280
	17.9	19.3	19.2	3						
RD84-1/8	17.3	19.2	19.2	3						
	17.7	19	19	3		19.5		76.3	7.63	280
RD90-1/2	17.5	19.2	19	4		19		188.2	18.8	116
	17.5	19	18.8	4						
RD90-3/8	17.5	19	18.7	4		19		179.3	17.9	122
RD90-1/4	17.5	18.8	19.2	4						
	17.6	19.2	19.5	4						
RD90-1/8	17.5	19.2	19	4						
HSD90-1/2	15.8	17.9	17.9							
	15.8	18	18							
HSD90-3/8	15.8	18	17.9							
	15.8	18	18							
HSD90-1/4	15.7	16.9	17							
	15.7	17.3	17.3							

easily cleaned from the device by repeated rinsing. However, small amounts of water remained within the viscometer, which could not be removed except by evaporation over the period of a few days. This meant that after the first measurement conducted during the week, the results were corrupted by the mixing of the additional water into the mixture. The extent of this was not realised until after the experiments had been conducted.

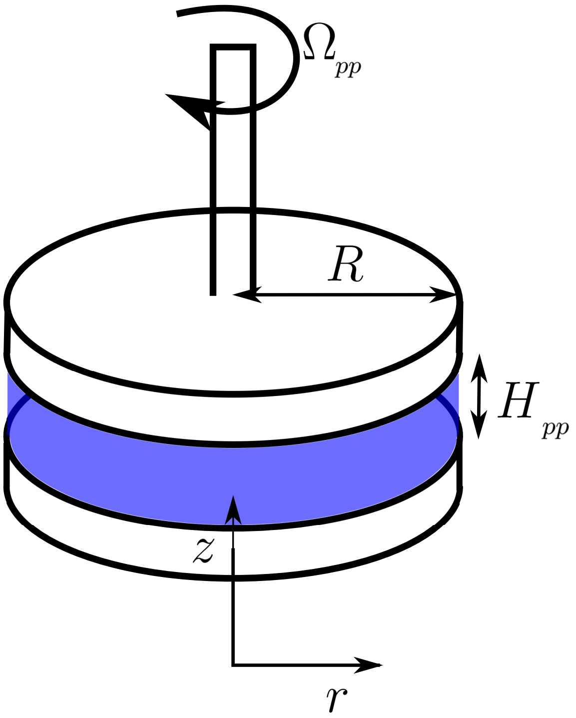

Figure 3.5: Diagram of a parallel-plate rheometer. The plate separation, H, radius of the circular plate R and angular velocity Ω_{pp} are fixed. The viscosity is calculated by measuring the required torque M to maintain a fixed angular velocity, Ω_{pp}. In axisymmetric cylindrical co-ordinates (r, z).

The viscosity of samples from each batch of glycerol/water mixtures used during the first series of experiments was evaluated in a parallel plate rotary rheometer, figure 3.5. This type of rheometer measures the dynamic viscosity, μ, of a liquid from the torque required to maintain two plates rotating at a constant angular velocity, Ω_{pp}. The two plates are separated by a distance, H, and filled with the sample fluid in a configuration similar to a Hele-Shaw cell. Provided the plates are sufficiently close together, Stokes flow may be assumed. The shear strain, $\dot{\gamma}$, at a given radius, r, is $\dot{\gamma}(r) = r\Omega_{pp}/H_{pp}$. The total torque, M, for a Newtonian fluid required to rotate the plate at angular velocity, Ω_{pp}, is

$$M = \int_{0}^{R} 2\pi r^2 \dot{\gamma}\mu \, \mathrm{d}r = \int_{0}^{R} \frac{2\pi r^3 \Omega_{pp}\mu}{H_{pp}} \, \mathrm{d}r = \frac{\pi\mu\Omega_{pp}R^4}{2H_{pp}}. \tag{3.15}$$

Thus, by measuring the torque M for a fixed value of the angular velocity Ω_{pp}, the dynamic viscosity, μ, may be calculated as

$$\mu = \frac{2H_{pp}M}{\pi\Omega_{pp}R^4}. \tag{3.16}$$

For non-Newtonian fluids, varying Ω_{pp} varies the shear rate rate, $\dot{\gamma}$, and the change in μ may be measured. For Newtonian fluids, the viscosity should, obviously, remain constant. In addition to the five samples from the experiments, a further sample of the pure glycerol provided was retained and labelled 'sample 5'. The sample number for each case is included in table 3.4. For each sample, a number of different temperatures, displayed in table 3.5, were selected and the dynamic viscosity, μ, of the mixture was measured using the rotary rheometer over a range of angular velocities, Ω_{pp}, figure 3.6. The rotary rheometer had an inbuilt temperature control that was accurate to two decimal places about the desired temperature. At high values of Ω_{pp}, viscous dissipation raised the temperature by as much as 0.1 °C, but the measured values of dynamic viscosity were already inaccurate from the choice of Ω_{pp}. A suitable range of angular velocities Ω_{pp} was not known a priori and so a range was selected over three to four orders of magnitude with equal spacings of 10 per decade on a log scale. The values of the measured dynamic viscosity presented in table 3.5 are the mean values over the range of Ω_{pp} presented for each case. Significant variations of the measured dynamic viscosity were observed for $\Omega_{pp} \leq 0.1$ ($\log \Omega_{pp} \leq -2.3$) from sample 3, figure 3.6, and these were excluded before calculating the mean. Samples 2a, 2b and 3 correspond to the same glycerol concentration (0.84). The mean value from samples 2a and 2b is relatively close to the target dynamic viscosity, table 3.5, and, as expected, roughly double mean value of sample 1. Samples 3, 4 and 5 measure the dynamic viscosity to be roughly 30 to 40% lower than the target value, table 3.5. Further, although more prevalent for sample 5, all samples, apart from sample 1, exhibit shear-thinning behaviour, figure 3.6. It was unclear what caused this variation in the dynamic viscosity or the discrepancy between the first three and the last three samples. A possible explanation would be that viscous dissipation raised the temperature of the sample reducing its viscosity. However, the internal temperature readings on the rheometer only detected an increase of 0.2 °C for sample 4 and 0.4 °C for sample 5, which would only change the viscosity by 1.6 and 3.17%, respectively.

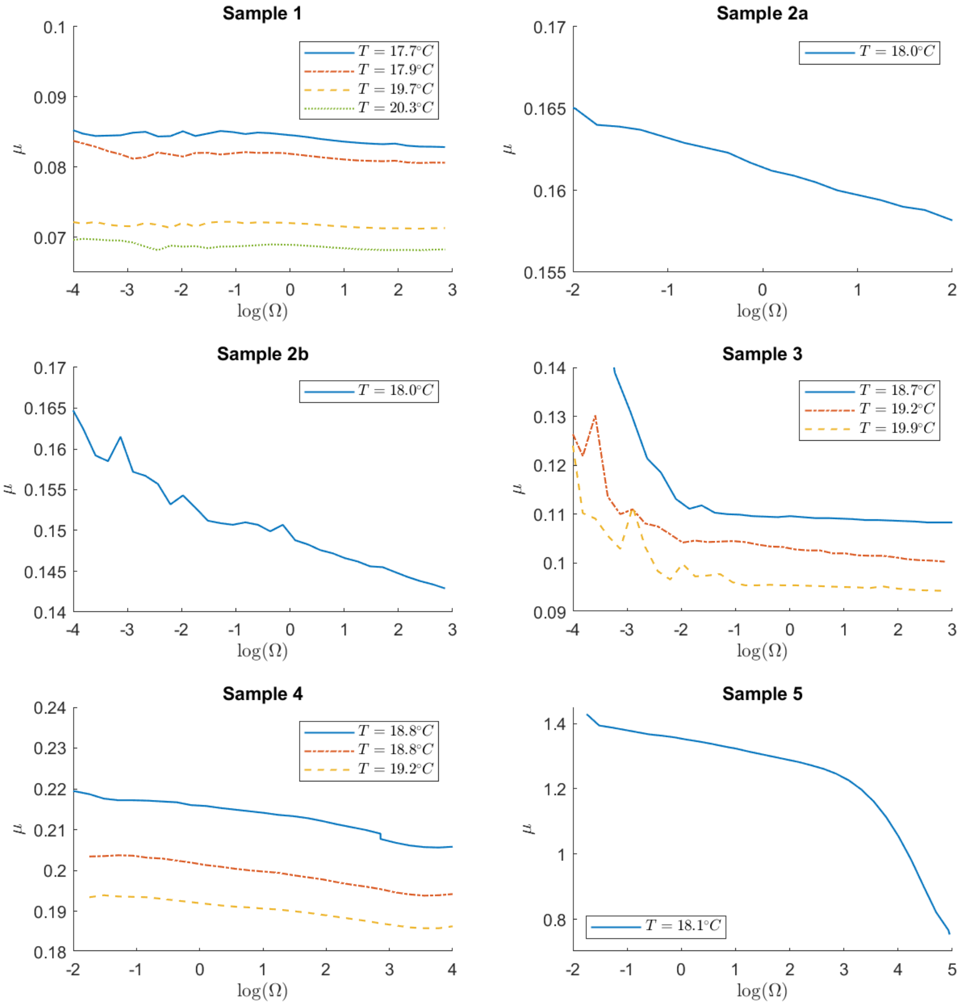

Figure 3.6: Measured dynamic viscosity, μ (kg·m·s^{-s}), from the rotary viscometer against the natural log of the target angular velocity, Ω_{pp} (s^{-1}), for different glycerol concentrations: 0.77 (sample 1); 0.84 (samples 2a, 2b and3); 0.90 (sample 4); and 0.995 (sample 5). Measurements were repeated over a range of temperatures to capture the range of temperatures observed during experiments.

Table 3.5: Table of the measured dynamic viscosities from the rotary rheometer for the six different samples at glycerol concentration α_g. The target dynamic viscosity and the current density, ρ_c, is calculated using the empirical model of Cheng (2008). The viscosity discrepancy is calculated as $|\mu_{\text{measured}} - \mu_{\text{target}}|/\mu_{\text{target}}$. The corresponding Reynolds numbers from the measured viscosity, $Re_{\text{act}} = \sqrt{g' h_{\text{lock}}^3}\rho_c/2\mu$, are given. The measured dynamic viscosity is calculated from the mean value over possible angular velocities, Ω_{pp}, from the data presented in figure 3.5 with the exception of sample three, where the values $\Omega_{pp} \leq 0.1$ ($\log(\Omega_{pp}) \leq -2.3$) are excluded before averaging.

Sample	α_g	T (°C)	Measured dynamic viscosity (μ, kg·m·s^{-1})	Target dynamic viscosity (μ, kg·m·s^{-1})	Viscosity discrepancy (%)	Current density (ρ_c, kg·m^{-3})	Re_{act}
1	0.77	17.7	0.0842	0.0778	8.2	1211.7	299
	0.77	17.9	0.0816	0.0768	6.3	1211.6	309
	0.77	19.7	0.0717	0.0684	4.8	1210.5	350
	0.77	20.3	0.0687	0.0659	4.2	1210.1	365
2a	0.84	18.0	0.1673	0.165	1.4	1227.8	157
2b	0.84	18.0	0.1512	0.165	8.4	1227.8	174
3	0.84	18.7	0.1097	0.157	30.1	1227.4	240
	0.84	19.2	0.1076	0.151	28.7	1227	244
	0.84	19.9	0.0958	0.144	33.5	1226.6	274
4	0.90	18.8	0.2167	0.333	34.9	1240.8	125
	0.90	19.2	0.1982	0.323	38.6	1240.5	137
	0.90	19.5	0.1895	0.315	39.8	1240.3	143
5	1	18.1	1.225	1.689	27.4	1261.9	23

3.3 Image processing

3.3.1 Lens distortion

A pinhole camera is a simple camera without a lens, figure 3.7. Effectively it is a lightproof box with a small opening on one side that is known as an aperture. Light passes through the aperture and creates an inverted image on the back of the box, which is known as the image plane. All light rays travel in straight lines through the aperture producing a near infinite depth of view (the range of distances where the objects are in focus). However, they require long exposure times. The principal axis is defined in the direction normal to the image plane that passes through the aperture.

Lens are transparent objects added to cameras. Simple convex or concave lens bend light rays by an amount proportion to the distance from the central axis of the lens, figure 3.8. Convex lens reduce the field of view (the angle through which the camera can detect light), figure 3.9, and the depth of view, but significantly increase the amount of light from the observed region reaching the image plane when placed in front of the aperture. Thus, they are essential for most situations, in particular those where the objects are moving or in darker environments. The amount that the lens bends light is measured by its focal length, the distance from the lens that parallel rays of light converge, figure 3.8. The focal length, Z_c also determines the magnification of the image that is projected onto the image plane. Short focal lengths provide a wider field of view, whereas long focal lengths are more suitable for viewing objects that are further away. Compound lenses, with variable focal lengths, are constructed from a series of lens along a common axis. Varying the separation of these lens adjusts the focal length of the compound lens. However, the image quality is reduced when compared to a single (or prime) lens.

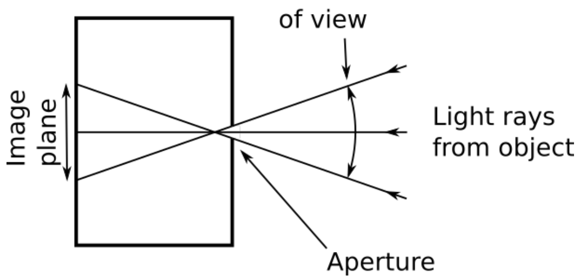

Figure 3.7: Schematic of a pinhole camera. Light from an objects travels in straight lines through the aperture creating an inverted image on the image plane. The field of view is the angle between the the two extreme edges that are displayed on the image plane.

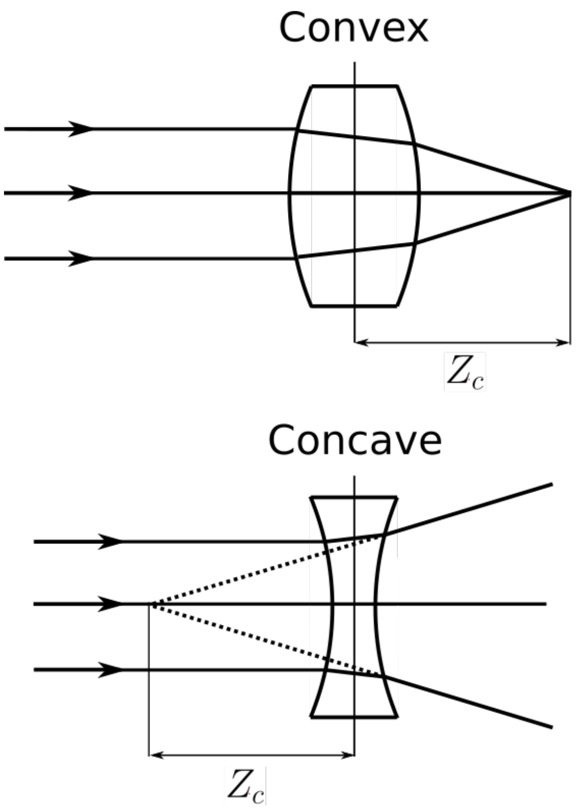

Figure 3.8: The affect on parallel rays of light from a convex (top) and concave (bottom) lens with focal lengths, Z_c and $-Z_c$, respectively. The convex lens bends light rays towards the central axis, whereas the concave lens bends light rays away.

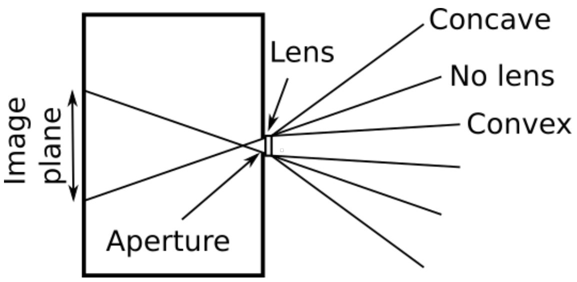

Figure 3.9: The affect of different types of lens on the field of view in a camera. The convex lens has a narrow field of view, but increase the magnification and the amount of light entering from a more distance object. A concave lens has a negative focal length and any object outside of the camera will be out of focus. As such, the concave lens is not useful on its own, but is an essential part of a compound lens.

One of the main drawback of lens is the distortion of images, particularly near the edges of images, that they introduce. This is arises from the inability to construct lens that distort light rays perfectly, as in figure 3.9, and a uniform rate of increase from the optical centre. This leads to radially symmetric distortions. Asymmetric distortions can arise from asymmetry in the lens itself, which is usually negligible relative to the symmetric distortion. Further, distortion can arise if the lens is incorrectly aligned with the image plane. These produce more complex distortion patterns and are known as tangential distortions.

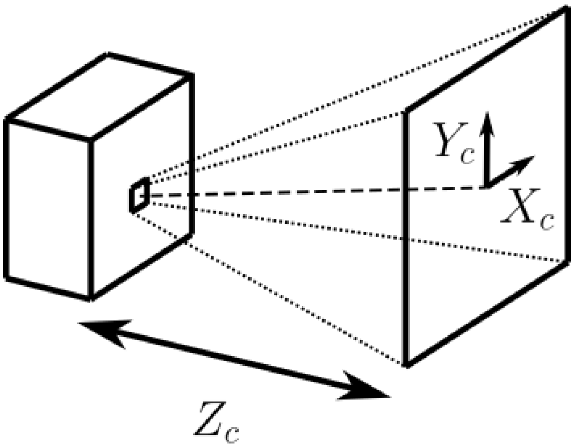

Figure 3.10: The virtual image plane is the observed space capture at distance of the focal length of the camera Z_c with plane co-ordinates (X_c, Y_c) centred about the principal axis (dashed line).

In order to estimate the affect of lens distortion the position of the 3-D object, in world co-ordinates (X, Y, Z), that is being observed needs to be converted onto the virtual image plane defined with normal in the direction of the principal axis and at distance Z_c from the aperture, figure 3.10. The co-ordinates of the virtual image plane are (X_c, Y_c, Z_c). The object can be mapped to the virtual image plane by a rotation matrix R, translation vector $\mathbf{t}$ such that,

$$(X_c, Y_c, Z_c) = R(X, Y, Z) + \mathbf{t}. \tag{3.17}$$

The rotation and translation are the extrinsic (independent of the camera) parameters and represent the location of the camera in 3-D space relative to the object. If the size of the object is known, then the pixel lengths on the virtual image plane, (p_x, p_y) can be determined. The focal length is normalised by these lengths, $(f_x, f_y) = (Z_c/p_x, Z_c/p_y)$. Further, the skew $s = f_x \tan \alpha_s$ can be determine, where α_s is the difference in angle between orthogonal axes and the image axes. Finally, we translate to camera co-ordinates which are centred about the principal point, the centre of the virtual image plane in pixels (c_x, c_y), and normalised by the normalised focal lengths. This is encoded in the intrinsic matrix, K, given by,

$$K = \begin{pmatrix} f_x & 0 & 0 \\ s & f_y & 0 \\ c_x & c_y & 1 \end{pmatrix}. \tag{3.18}$$

The camera co-ordinates (x, y) are then defined

$$(x, y, 1) = K(X_c, Y_c, Z_c) = K\left(R(X, Y, Z) + \mathbf{t}\right). \tag{3.19}$$

The intrinsic (specific to the camera) parameters represent the translation of the observed object onto the image plane of the camera.

Radial distortions can be modelled in the form of a power series in r^2

$$\begin{pmatrix} x_d \\ y_d \end{pmatrix} = \begin{pmatrix} x \\ y \end{pmatrix} \left(1 + k_1 r^2 + k_2 r^4 + \cdots\right), \tag{3.20}$$

(Fitzgibbon, 2001) where $r^2 = x^2 + y^2$ is the distance from the principle point, k_i are the radial distortion coefficients and (x_d, y_d) are the distorted image co-ordinates in the camera co-ordinates. In practice only the first few terms from the series are required to accurately capture most radial lens distortions(De Villiers et al., 2008).

The three common types of radial lens distortions are displayed in figure 3.11. Barrel and pincushion distortions are both quadratic, with opposite signs of the k_1 coefficient. Quartic order radial distortions either look similar to the quadratic distortions (when k_1 and k_2 share the same sign) or produce a blending of the two. When $k_1 < 0$ and $k_2 > 0$ straight lines near the centre curve up near the centre and the opposite way towards the edges creating curves that look like moustaches, figure 3.11d, which are hence known as moustache distortions. When $k_1 > 0$ and $k_2 < 0$ the opposite effect occurs, figure 3.11e. This is not generally observed and so is unnamed.

Tangential distortions arise from the lens and the image place not being completely aligned. Brown (1966) proposed the following model for calculating the undistorted points, (x, y) in the camera co-ordinates

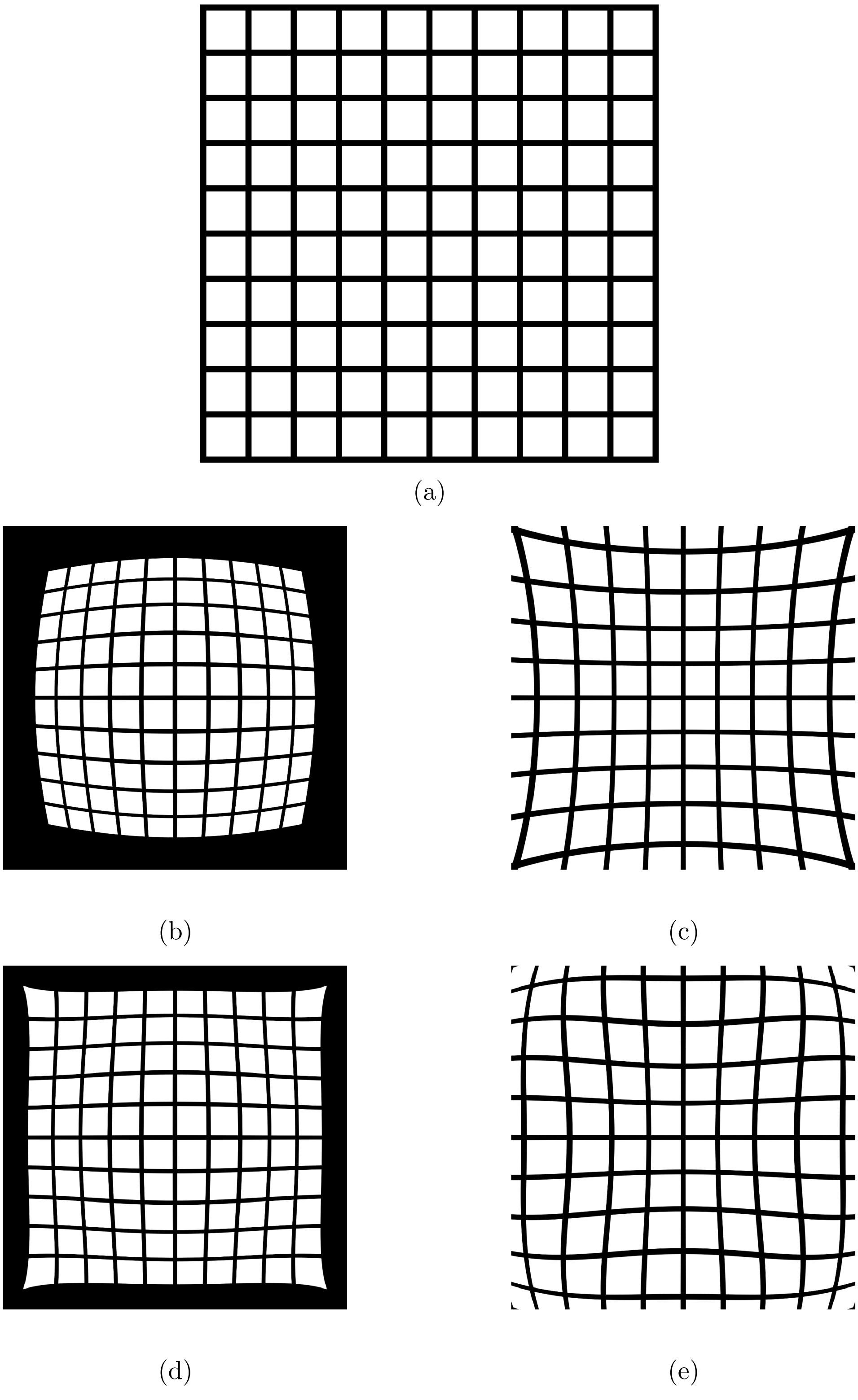

(a)

(b)

(c)

(d)

(e)

Figure 3.11: (a) A mesh grid with no distortion. Types of quadratic (b and c) and quartic (d and e) radial distortions: (a) barrel ($k_1 < 0, k_2 = 0$), (b) pincushion ($k_1 > 0, k_2 = 0$), (c) moustache ($k_1 < 0, k_2 > 0$) and (d) ($k_1 > 0, k_2 < 0$). The names are derived from common objects. The line appear to bulge in the centre of a barrel distortion resembling a barrel. The pincushion pinches at the corners. Lines near the centre curve upwards near the centre and then the other way in a moustache distortion. The final type does not appear in standard lens and, as such, has no name.

Table 3.6: Table of parameters and errors from the camera calibration. Errors for the radial diffusion coefficients, k_i are one standard deviation of the data. The camera co-ordinates of the top right corner of the image is $(x_{\text{max}}, y_{\text{max}})$ and has corresponding distance r_{max} from the principal point. This is approximately equivalent for all four corners of the image. The correction is calculated at the extreme points. Also given is the smallest and largest corrections at one standard deviation from the mean.

k_1	k_2	x_{max}	y_{max}	r^2_{max}	r^4_{max}	x_{cor} (mm)	y_{cor} (mm)
0.0583±0.004	-0.0091±0.0056	0.538	0.359	0.418	0.175	6.5 (5, 9.2)	4.3 (3.4, 6.1)

$$\begin{aligned}\begin{pmatrix} x_d \\ y_d \end{pmatrix} = \begin{pmatrix} x \\ y \end{pmatrix} &\left(1 + k_1 r^2 + k_2 r^4 + \cdots\right) \\ + \begin{pmatrix} 2\mathcal{P}_1 xy + \mathcal{P}_2(r^2 + 2x^2) \\ \mathcal{P}_1(r^2 + 2y^2) + \mathcal{P}_2 xy \end{pmatrix} &\left(1 + \mathcal{P}_3 r^2 + \mathcal{P}_4 R^4 + \cdots\right)\end{aligned} \tag{3.21}$$

A checkerboard pattern with squares of length 33 mm was created and still photographs were taken at numerous angles before each day of filming within the laboratory. By using the detectCheckerboardPoints function in MATLAB. A collection of points in world co-ordinates, of known distances apart, can be identified within each image, figure 3.12. From the multiple orientations, the intrinsic parameters of the camera, the radial and translation errors and the skew can be estimated. For the cameras used in the experiments the error introduced tangential distortion and the skew are negligible compared to those from the radial distortion. The radial coefficients are given in table 3.6 along with a errors at one standard deviation from the mean. Using dimension of known objects in the image (e.g. the checkerboard or the ruler) the size of the image in world units can be determined and from this the maximum radial distortion in mm, table 3.6. The radial correction is computed $r_{\text{cor}} = \sqrt{x^2_{\text{cor}} + y^2_{\text{cor}}}$. Correction by the mean values of the radial distortion coefficients, reduces the radial distortion by 7.8 mm at the corners. At one standard deviation away from the mean values the largest error is 3.2 mm. Ideally the head or pulse of the current is kept in the centre of the image whilst filming. This was true for the majority of experiments. Additionally, the current remains confined vertically near the centre of the camera reducing the effect of lens distortion. Thus, after correction, we do not expect lens distortion to be significant.

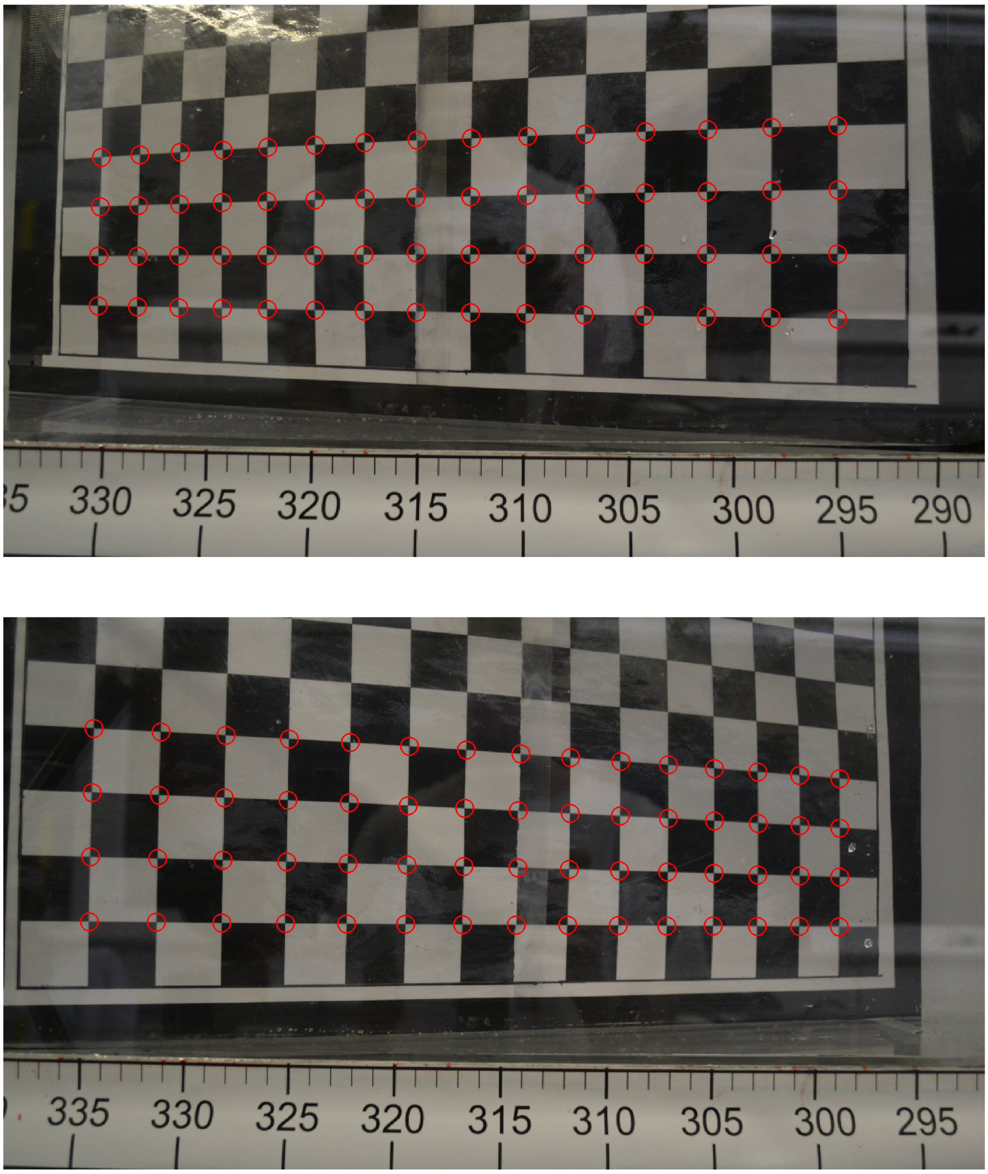

Figure 3.12: Still photos of the checkerboards taken in different orientations. The corners of the square detected using the detectCheckerboardPoints function in MATLAB are shown by red circles. Although not all of the corners are detected, a sufficient number are detected in order to the use the camera calibration.

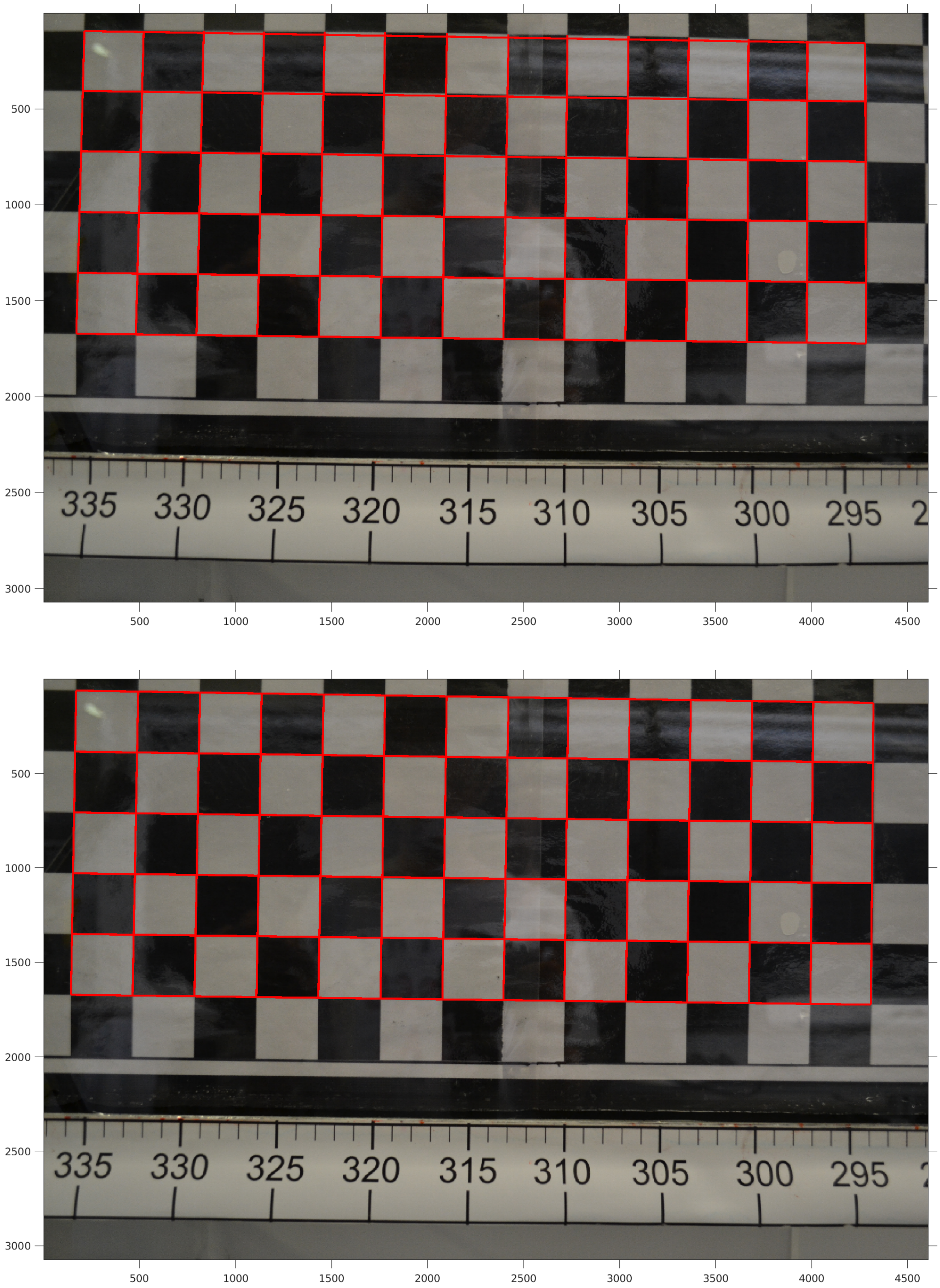

Figure 3.13: Still photos of a front on checkerboard taken before camaera calibration (top) and afterwards(bottom). Straight red lines are drawn between the checkerboard corners to demonstrate the curvature that is removed by lens correction.

3.3.2 Image processing

As a result of the lobe and cleft structures that to formed at the head, together with wall effects, there was noticeable cross-stream variation at the head of the flow, figure 3.14. Further, it was unclear how far from the near side wall the maximum occurred and variations behind it were obstructed. Thus the average values of minimum and maximum observed values over the cross-stream would still be prone to error and for simplicity, the head of the current was defined to be the maximum value (i.e. 1.85 m in figure 3.14).

The position of the pulse in the experiments, X_s, is difficult to quantify exactly for two reasons: First, upon release and during a brief initial transience, the pulse had not formed, figure 3.14. Second, further downstream, the pulse was of the order of 0.1 m long, figure 3.15a. Far downstream, the depth maximum (2.15 m in figure 3.15b) was used. In the early stages, both the local depth maximum (if it existed) and the maximum observable distance of the blue mixture were considered. The maximum of these two values was then chosen as the pulse position.

Both the head and pulse position were measured at a rate of 4 Hz. Explicitly defining how the head and pulse position were captured reduced measurement bias and enabled more consistent measurements across different cases. However, these methods were still subject to some level of interpretation and error. For small t_{re} cases, the pulse depth was less than double the height of the surrounding current, making the depth maximum difficult to interpret. Further, although best effort was made to keep the cameras centred exactly at the position of the head or pulse, this proved impossible and measurements were subject to parallax error, figure 3.15b. The speed of the head, $\dot{X}_N$, and pulse, $\dot{X}_s$, was then calculated from the change in position and the time between frames. There was significantly less cross-stream variation in the pulse and so, the near-wall position was used. This helped minimise parallax error.

The maximum error in measuring the position is assumed to be ± 0.005 m for the head and, as it is significantly harder to identify, ± 0.01 m for the pulse. This yields dimensionless errors (scaled by h_{lock}) of $\pm$ 0.05 for the head and $\pm$ 0.1 for the pulse. The maximum parallax error can be estimated from the image frames by considering the difference between the pulse position on the near and far side walls. For the worst case scenario, where the pulse is at the edge of the image, the difference can be as large as 0.03 m. Thus, the dimensionless errors are ± 0.15. Further, it is assumed that the error in time measurement in between the camera frames is negligible relative to the error in position. Thus, using the smallest velocity scale (as it varies slightly with the density of the current) over the three cases, the maximum error for the speed is ±0.1 for the head and ±0.2 for the pulse.

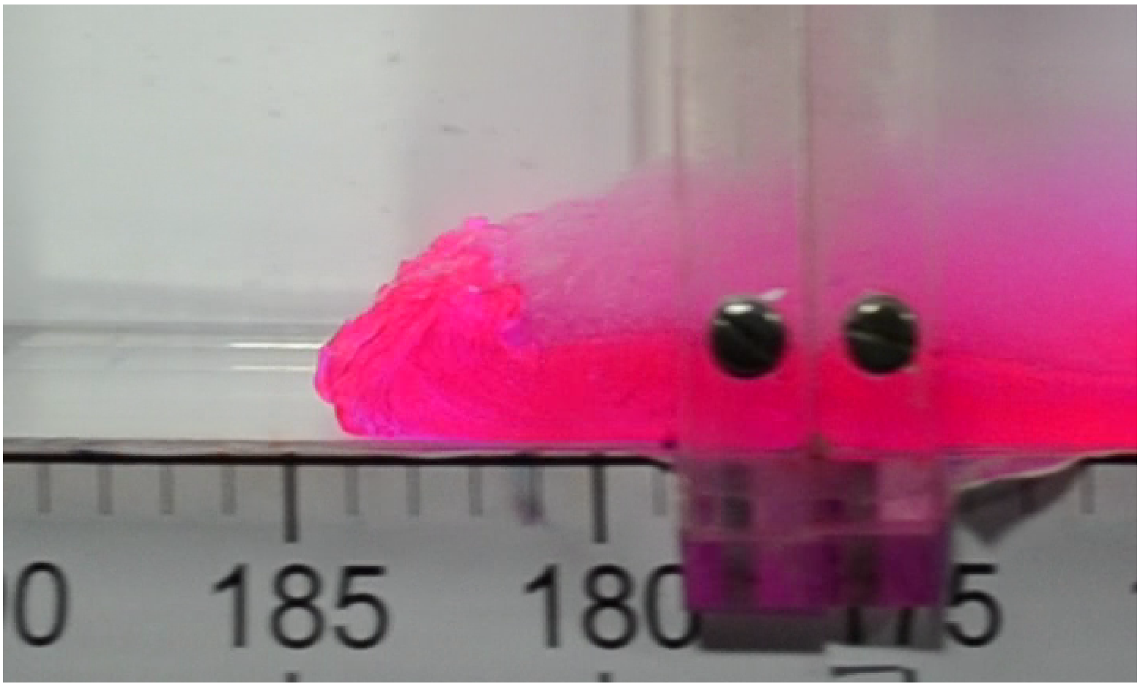

Figure 3.14: Downstream (case: RD90-3/8) image at dimensionless time $t = 9.0$ after release taken from the first camera. The cross-stream variation in head position can be observed. The variations cover the region between 1.84 and 1.85 m. The head position is taken to be the larger of these two values.

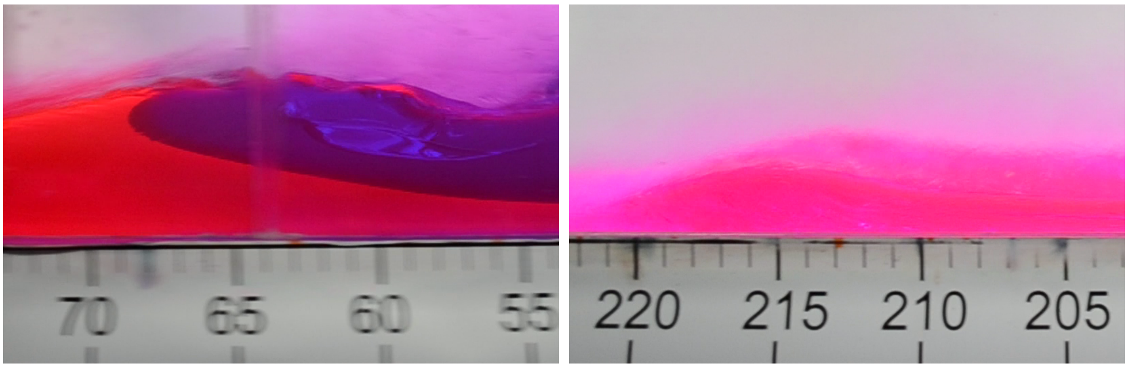

(a) (b)

Figure 3.15: Downstream images (case: RD90-3/8) from the second camera, which tracks the head of the flow: (a) $t = 5.5$ and (b) $t = 10.4$ after initial release. Blurring is observed in (a), as a result of the shutter speed on the camera being too low. Parallax error may be observed in (b), because the camera is centred at 2.03 m.

3.4 Surface tracking

MATLAB was used to extract the free surface position and the interface between the two fluids from individual frames within the videos. The processing algorithm involved the use of several different colour schemes. There are numerous colour schemes available for representing the colour spectrum digitally. Many consist of co-ordinate based systems that closely resemble commonly used co-ordinate bases, such as Cartesian or cylindrical co-ordinate systems. Perhaps the most well known are additive schemes such as RGB, where three values between 0 (no colour) and 1 (full colour) control the strength of three channels of: red, R; green, G; and blue, B, light. Each colour in RGB corresponds to the long, medium and short wavelength receptors in the eye, respectively, red, green, and blue light. Each interval [0,1] is usually discretised into 2^8 or 2^{16} classes, each with a specified intensity. This scheme allows for the largest representation of human colour space to be captured. However, every human eye detects the intensity of wavelengths slightly differently and this is reflected in manufacturers using different values for these three wavelengths.

One of the main drawbacks of the RGB colour scheme is its lack of intuitiveness. Given three values for the channels RGB, it is not immediately obvious what the resulting colour will look like and this is compounded by the fact that the human eye is more sensitive to different wavelengths of light. The HSV (and closely related HSL) is a cylindrical colour system developed during the 1970s to be closer to the way human vision interprets light. In cylindrical co-ordinates (r, θ, z) the angular component, θ, controls the hue, H, and represents a colour wheel going from red (0°), to green (120°), to blue (240°), and back to red (360°). The radial component, r controls the saturation of the colour, with 1 being fully saturated and 0 being shades of grey. The vertical co-ordinate, z, controls the value, where 0 is fully black and 1 is fully white. RGB and HSV produced the most promising results.

A key component to image filtering is the Gaussian filter. The function is a discrete version of the two dimensional Gaussian normal distribution with standard deviation, σ,

$$G(x, y) = \frac{1}{2\pi\sigma^2} \exp\left(-\frac{(x - x_0)^2 + (y - y_0)^2}{2\sigma^2}\right), \tag{3.22}$$

where (x_0, y_0) is the 2 dimensional position of the centre of the pixel being considered. The normal distribution produces a bell shaped peak about the point (x_0, y_0). Weighting factors for a matrix, known as a Gaussian smoothing kernel are produced by averaging $G(x, y)$ over unit-squares in (x, y)-space and centred around (x_0, y_0). For example, the middle element is

$$\int_{-\frac{1}{2}}^{\frac{1}{2}} \int_{-\frac{1}{2}}^{\frac{1}{2}} G(x, y)\, \mathrm{d}x\mathrm{d}y \tag{3.23}$$

In practice, the weighting factors are negligible more than 3σ from the centre and so are neglected. Thus producing a matrix of size $\lceil 6\sigma \rceil \times \lceil 6\sigma \rceil$, where $\lceil\rceil$ is the ceiling or round-up function. Once calculated, this can be applied to each pixel to smooth the image. For pixels that are within 3σ of the boundary the stencil of the matrix will partially lie outside of the image. To correct for this, it is assumed that the image is symmetric about its edges.

3.4.1 Single-release surface tracking

The single-release experiments are considered first, because they are simpler than the double-release. For a single-release, there is only a single colour of dye. Mixing occurred only with the ambient, which diluted, but did not alter the colour of the liquid. Each frame from the videos were imported into MATLAB and converted into RGB values. These were normalised by three times the lightness, $3I = (R+G+B)$, the average of the RGB values of each pixel, figure 3.16a & 3.16c. This procedure removed downstream variations in the brightness of each image, caused by one end of the tank being closer to external light sources. Note that the lightness, I, is different from the value, V, used in the HSV scheme even though they represent the same physical quantity. The resulting images were then converted to HSV, figures 3.16b & 3.16d. The advantage of using both colour schemes is that different parts of the flow are more easily identified in certain channels, figure 3.16. For example, the modified red, R, and blue, B, channels capture the taps with the highest contrast, which need to be removed, whereas in the saturation channel, S, there is the largest distinction between the current and the ambient, figures 3.16b & 3.16d. The aim was to utilise the strengths of the different channels to identify the depth of the current in each frame.

Throughout this section, when a pixel was excluded from further calculation, this means that the RGB and HSV channels were set to values outside the range that were subsequently considered. Thus, they still appear as white or black, or a fixed shade of grey. First, the values of hue, H, greater than 0.65 and less than 0.1 were excluded. Second, regions of saturation, S, less than 0.1 were excluded and

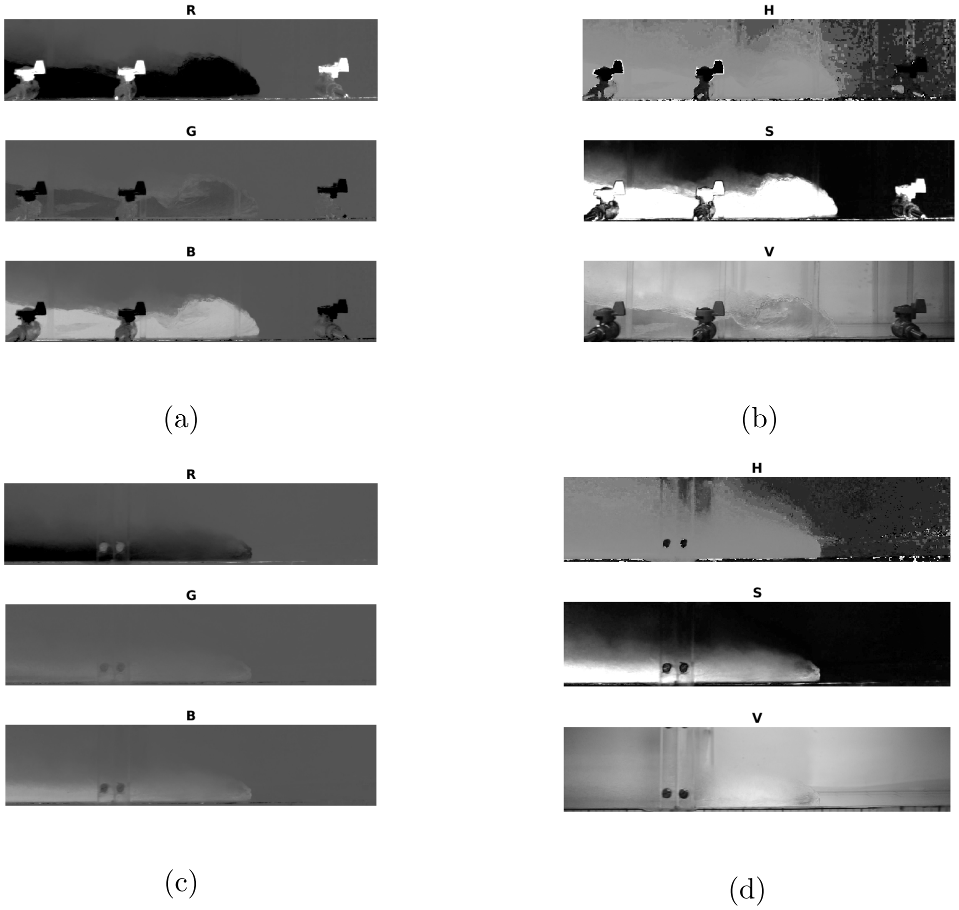

(a) (b)

(c) (d)

Figure 3.16: Single-release (case: RS84) at t =2.4 (a & b) and t =12.8 (c & d): (a & c) - RGB colour channels and (b & d) - HSV colour channels. The RGB channels were normalised by three times the lightness, $3I = (R + G + B)$, before being converted to the HSV channels. Note that value, V, is the maximum value of the three RGB channels and, generally greater than the lightness, I.

finally red, R, less than 0.15. The resulting channels for R, S and H are displayed in figure 3.17. This selection of H, S and R values removed the taps and the bulk of the ambient in the red, R, and saturation, S, channels. Next, a Gaussian filter with standard deviation $\sigma = 4$ (as described earlier) was applied to the saturation channel S, to remove high frequency noise. Finally, for each column, and starting at the top, the first pixel to have saturation S above 0.4, 0.6, or 0.8, was calculated and plotted as the corresponding green, black, and red lines in figure 3.18. All three lines are in close agreement during the early stages of the flow where there had been only a limited amount of mixing and the saturation was larger, figure 3.18a. However, further downstream, mixing with the ambient can be seen to blur the saturation, increasing the separation of the lines, figure 3.18b. The red (0.8 saturation) does not capture the front of the flow, whereas the green line (0.4 saturation) captures too much of the ambient.

Normalising by the light intensity, $3I$, as the initial step provided significant improvement to these results. The main problem arose from the fact the colour of the current approaches that of the ambient as it flows and thus, noise in the colour channels played an increasingly significant role. Further, it is significantly easier for the viewer to recognise the location of the free surface, compared to a computer. Attempts to introduce time varying light intensity modification (e.g. as a function of average lightness of the total frame) did not produce noticeably better results.

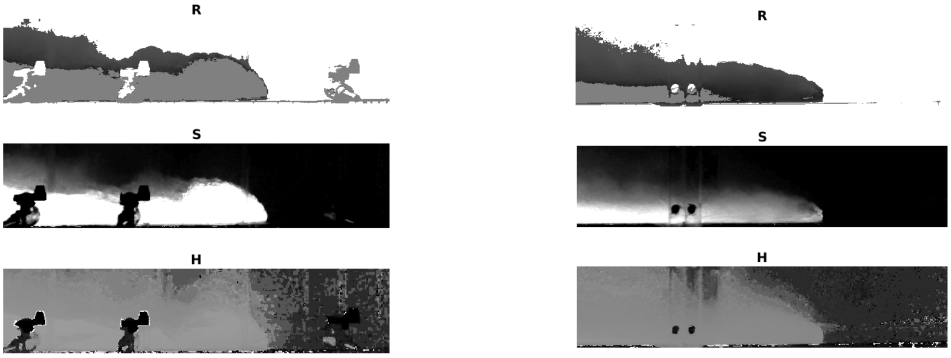

(a) (b)

Figure 3.17: R, S and H channels at $t = 2.4$ (a) and $t = 12.8$ (b) of a RS84 single-release flow. Regions of hue, H, greater than 0.65 and less than 0.1, regions of saturation, S, less than 0.1 and regions of red, R, less that 0.15 have been masked and excluded.

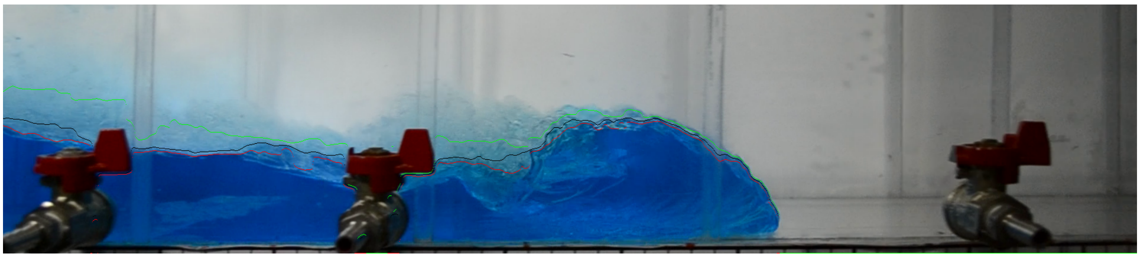

(a)

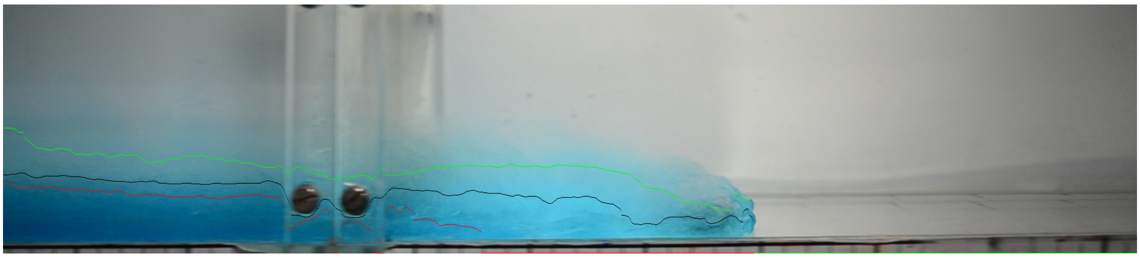

(b)

Figure 3.18: Images at $t = 2.4$ (a) and $t = 12.8$ (b) of a RS84 single-release flow. Coloured lines correspond to the highest vertical value with saturation, S, above: 0.4 (red); 0.6 (black); or 0.8 (green). The position of the current is significantly easier to identify by eye early in the experiments.

3.4.2 Double-release surface tracking

For the double-release experiments, the extraction of the surface profile proved more difficult for numerous reasons: First, the extra colour produced different distributions of the colour channels across the current, and mixing between these two in the wake of the pulse, figures 3.19a & 3.19d, created blurred boundaries between the distinct colours. Second, the red dye proved harder to contrast with ambient than the blue. Third, the red dye was more transparent, resulting in larger variations in average frame lightness.

The process of the single release surface tracking was extended and modified to the double release case. An overview of the steps involved is presented below:

1. Each frame was loaded into MATLAB in RGB format and cropped above the starting height of the lock gate and below the bottom of the tank.

2. The RGB format was converted into HSV. Entries in the value channel, V, were replaced by the frame-average value. This was an improvement from the single-release process to normalise each frame by the light intensity, I, that proved more effective for the double-release.

3. The resulting HSV was converted back into RGB to create R, G and B channels that had been normalised by value, V.

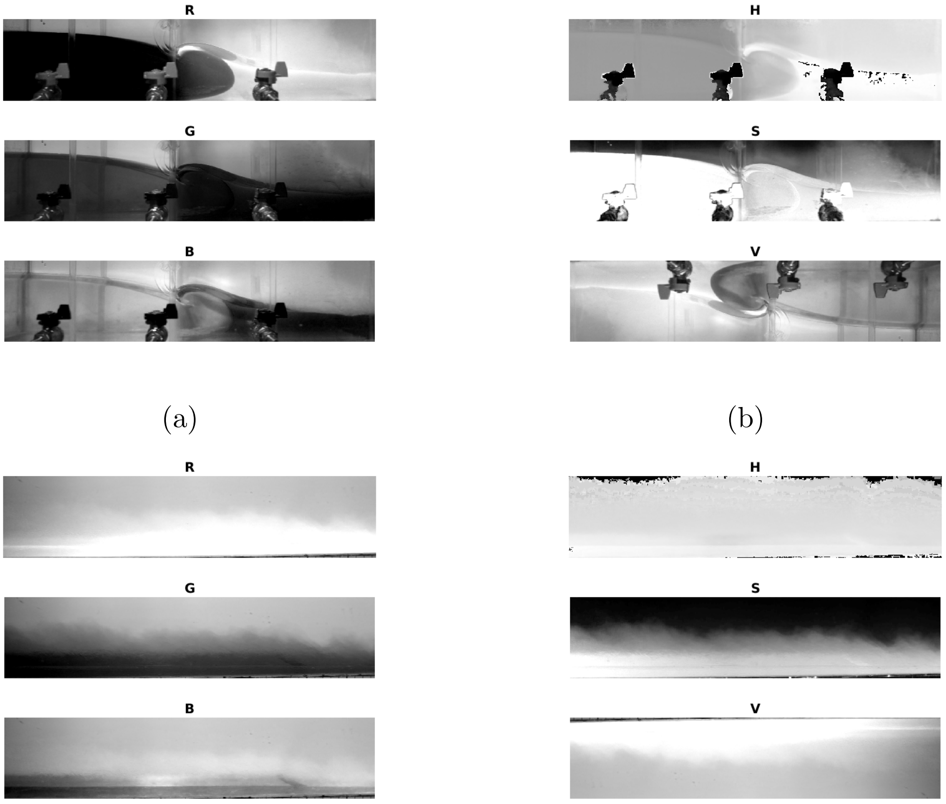

(a) (b)

(c) (d)

Figure 3.19: Colour channels for the double-release case: RD84-1/2 at $t = 3.4$ (a & b) and $t = 18.1$ (c & d). Corresponding channels are: RGB (a & c) and HSV (b & d).

4. Regions of Hue, H, less than 0.2 were excluded from further calculations.

5. The Gaussian filter, with standard deviation $\sigma = 3$, was applied to the saturation, S, and green, G, channels. After which, regions of green, G, greater than 0.5 were excluded. This consisted of the majority of the ambient.

6. Two alternatives were then used to determine the position of the free surface: In each column of an image frame, the largest difference between neighbouring pixels in hue, H, was used; or alternatively, the largest difference in green, G, figure 3.20.

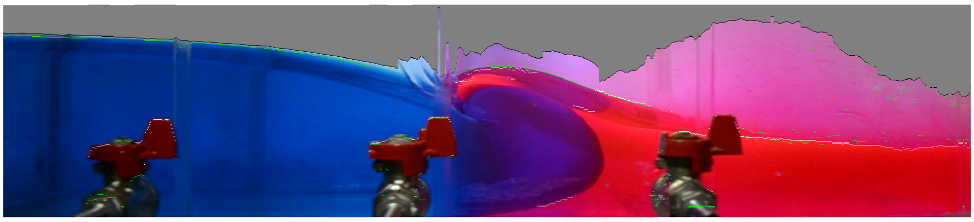

(a)

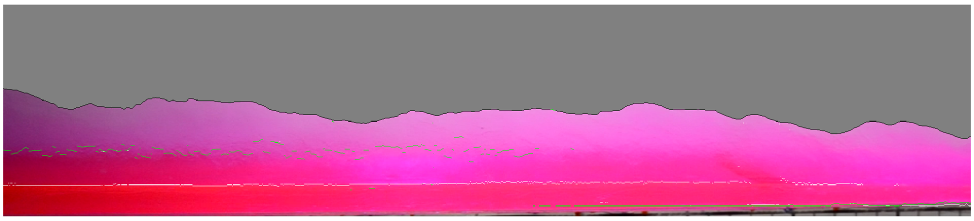

(b)

Figure 3.20: Images for the double-release case RD84-1/2 for the camera tracking the pulse at $t = 3.4$ (a) and $t = 18.1$ (b). The black line indicates the boundary of the pixels that were excluded, the white line represents the points with the largest vertical gradient in hue H and the green line represents the largest vertical gradient in green. The excluded pixels are coloured grey.

Many variations on this method were tried, but none produced improved results. In figure 3.20, the region of the domain excluded before the final step is shown as grey and the edge highlighted with a black line. The lines representing the largest gradient in hue, H, (white line) and green, G, (green line) colour channels do capture some regions of the flow, but others poorly.

3.5 Results and discussion

3.5.1 Repeatability of the experiments

The repeatability of the experiments was assessed by comparing experiments within the same case, figure 3.21. Head position was consistent between runs for each of the three cases, with only a minor deviation at late times for one of the RS90 experiments, figure 3.21. However, there was more variation in the estimated speed, figure 3.21. This variation is within the measurement error discussed in the previous section. Similarly, the position and speed of the head and pulse for three double release cases (RD77-1/2, RD84-1/2 & RD90-1/4) are presented in figure 3.22. Although only three cases are presented, all other cases where multiple runs were conducted showed similarly strong agreement. To reduce experimental costs, later cases consisted of fewer runs, table 3.4, because the experiments were highly repeatable, figures 3.21 & 3.22.

3.5.2 Visualisation

In contrast to the hydraulic jump in the numerical model presented in chapter 2, the disturbance from the second release in the experiments was quickly smoothed out to form a solitary wave, or bore, of order $0.4l$. Initially, the pulse was predominantly contained within the blue current, but it rapidly transitioned into the red current and through towards the front of the flow, figure 3.23. As the pulse propagated towards the head of the flow it became wider and less pronounced.

Figure 3.24 displays stills from the video recorded on the rolling camera following the head of the current for the RD77-1/2 case. The first three images show the pulse as it arrived at the head of the current and the final image when the transition to dilute flow had occurred. In contrast to the preliminary experiments of Ho et al. (2018a,b, 2019), the arrival of the pulse resulted in an increase of dense fluid at the head of the flow. In a single release case, the head transitioned into a dilute flow regime within 10 cm from this point of the flow. However, the additional supply of dense material keeps the head in a relatively dense regime for a further 60 cm. Thus, in this case, it was observed that the pulse inhibited the transition to a dilute current. Slowing down this transition resulted in more of the current being mixed with the ambient and a thicker head in the dilute phase when compared with the single release.

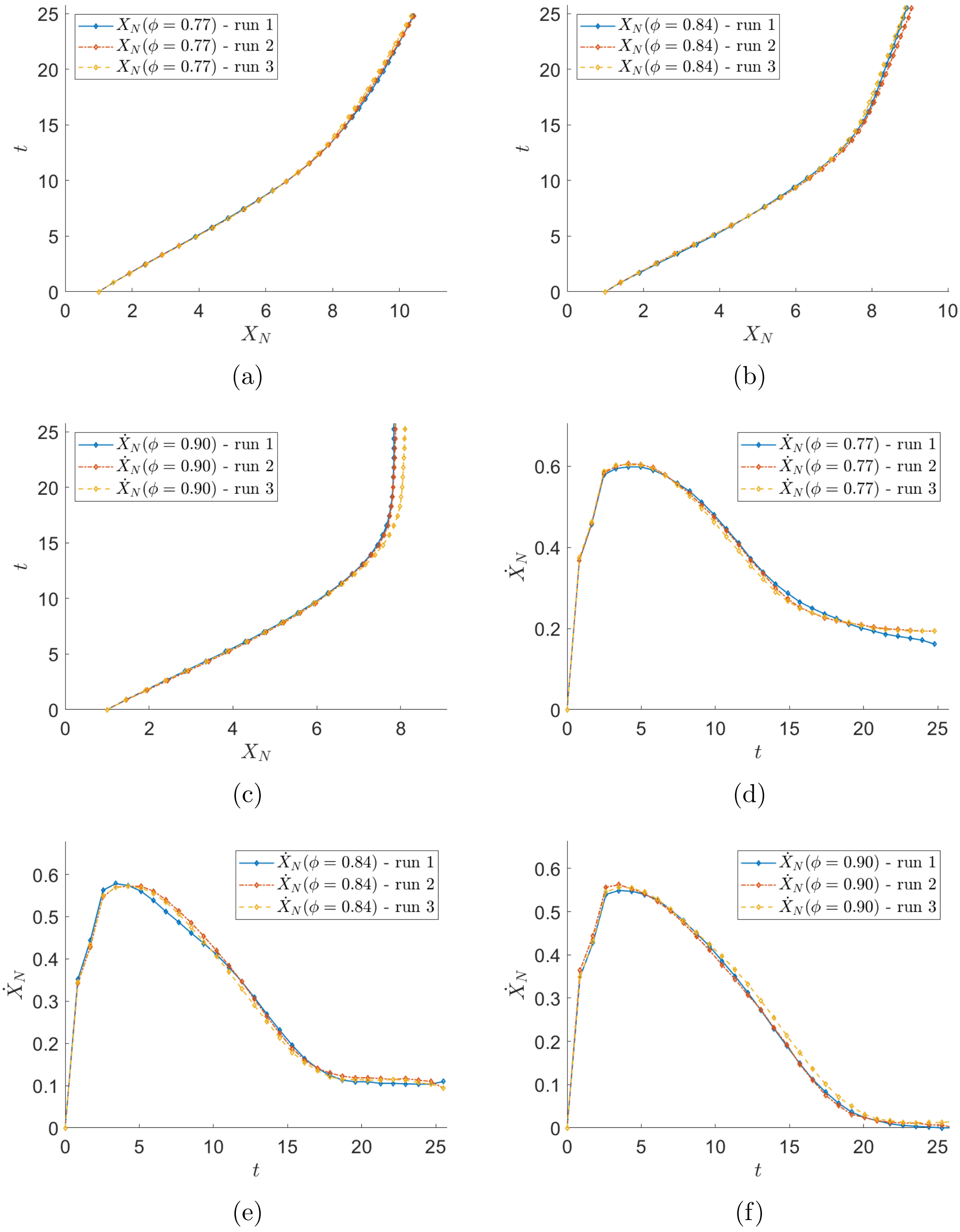

(a) (b)

(c) (d)

(e) (f)

Figure 3.21: Dimensionless head position, X_N (a-c) and speed $\dot{X}_N$ (d-f) for each of the three experiments conducted for each concentration: RS77 (a&d), RS84 (b&e) and RS90 (c&f).

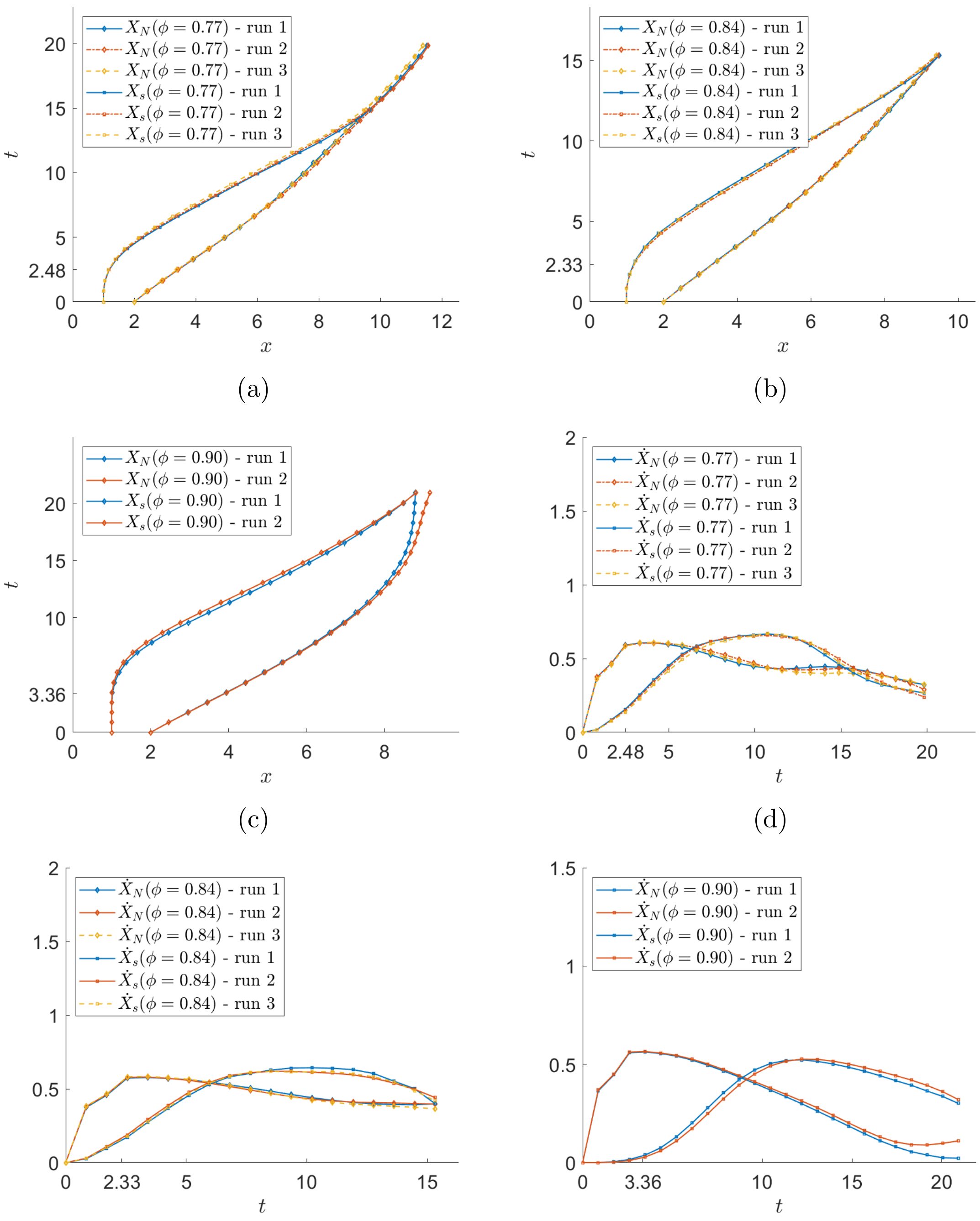

(a) (b)

(c) (d)

(e) (f)

Figure 3.22: Dimensionless position of the head, X_N, and pulse, X_s, (a-c) and speed of the head, $\dot{X}_N$, and pulse, $\dot{X}_s$, (d-f) for all of the experiments conducted for the following cases: RD77-1/2 (a&d), RD84-1/2 (b&e) and RD90-3/8 (c&f). Pulse separation times t_{re} are displayed on the t axis for each case: (a) 2.48, (b) 2.33 and (c) 3.36.

Figure 3.23: Snapshots from the RD90-1/8 case after $t_{\mathrm{re}} = 23.6$. Initially (top left), the pulse is predominantly in the second current (blue or darker fluid). The pulse gradually transitions into the first current (top right) and completely separates from the second current (bottom). Over time the pulse becomes wider and less pronounced.

Similar results to the RD77-1/2 were observed for the RD84-1/2 and RD84-3/8. However, the increased viscosity resulted in less mixing with the ambient and a smaller dilute current after the head of the flow had transitioned. For RD84-1/4 the current diluted before the pulse of denser fluid reached the head of the flow. Upon the arrival of the pulse at the head, a brief transition back into laminar-transitional behaviour was observed before transitioning back into a dilute regime. For the longest release time, RD84-1/8, the pulse itself transitioned to a turbulent behaviour whilst inside the already diluted head of the first current, figure 3.25.

Minimal mixing occurred for the highest glycerol concentration and this led to neither the single- or double-release cases transitioning to dilute turbulent behaviour at the head. For example, images from the videos for the RD90-3/8 case are displayed in figure 3.26. Before and after the pulse arrived the head of the flow remains unmixed. The arrival of the pulse did provide a brief increase to mixing, but it was insufficient to initiate a cascade of mixing, which led to the dilution of the head for the lower concentrations.

In all three cases the pulse increased the amount of mixing that occurred during the flow. However, the amount of this was negligible for the highest glycerol concentration considered. In the lowest two glycerol concentrations considered (0.77 and 0.84) the head of the flow always transitioned to dilute behaviour. However, this either occurred after the pulse reached the head of the flow (RD77-1/2, RD84-1/2 and RD84-3/8), where dilution was delayed by a supply of denser material from the pulse, or before (RD84-1/4 and RD84-1/8). For the latter, the pulse either diluted

Figure 3.24: Pulse arriving at the head for the RD77-1/2 case with release time $t_{\mathrm{re}} = 2.48$. The pulse arrives from the left and reaches the head of the current (top three images corresponding to $t = 10.67$, 12, 13.3). However, the current remains relatively dense until over 2 lock-lengths further downstream (bottom image at $t = 21$). Each image is approximately 35 cm wide.

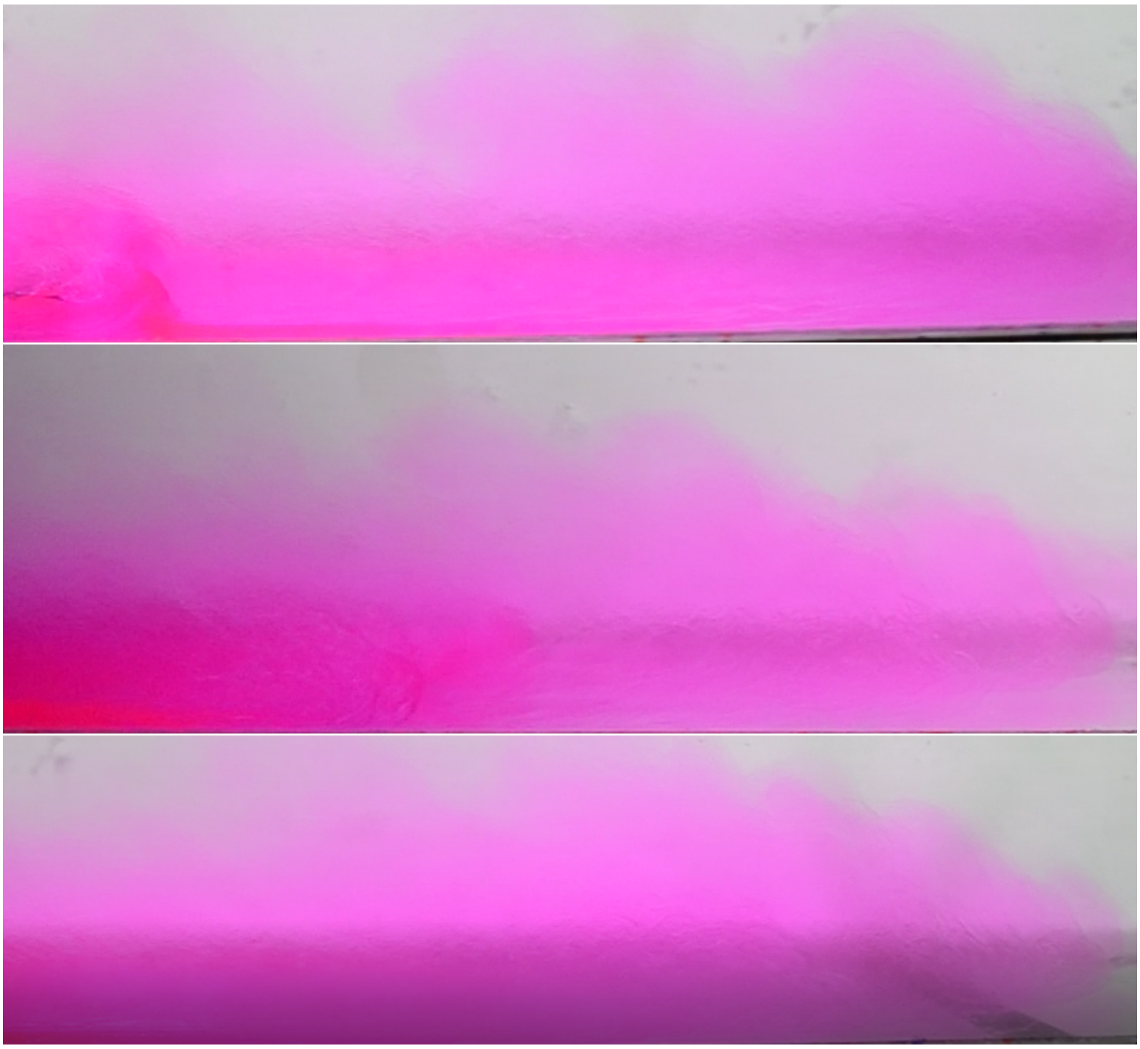

Figure 3.25: Pulse arriving at the head for the RD84-1/8 case with release time $t_{\text{re}} = 8.6$. The pulse arrives from the left and, but becomes indistinguishable from the current before it reaches the head (the three images correspond to $t = 24.1$, 27.5, 31). Each image is approximately 25 cm wide.

within the current or transitioned the flow back into a denser regime for a brief period. The double-lock release experiments conducted by Ho et al. (2018a,b, 2019) at 0.80 glycerol concentration ($Re_t = 280$) is the only case where the cascade of mixing occurred with the arrival of the pulse at the head of the flow. Thus, this behaviour may only occur for a limited range of concentrations and release times and further investigation would be required to quantify this.

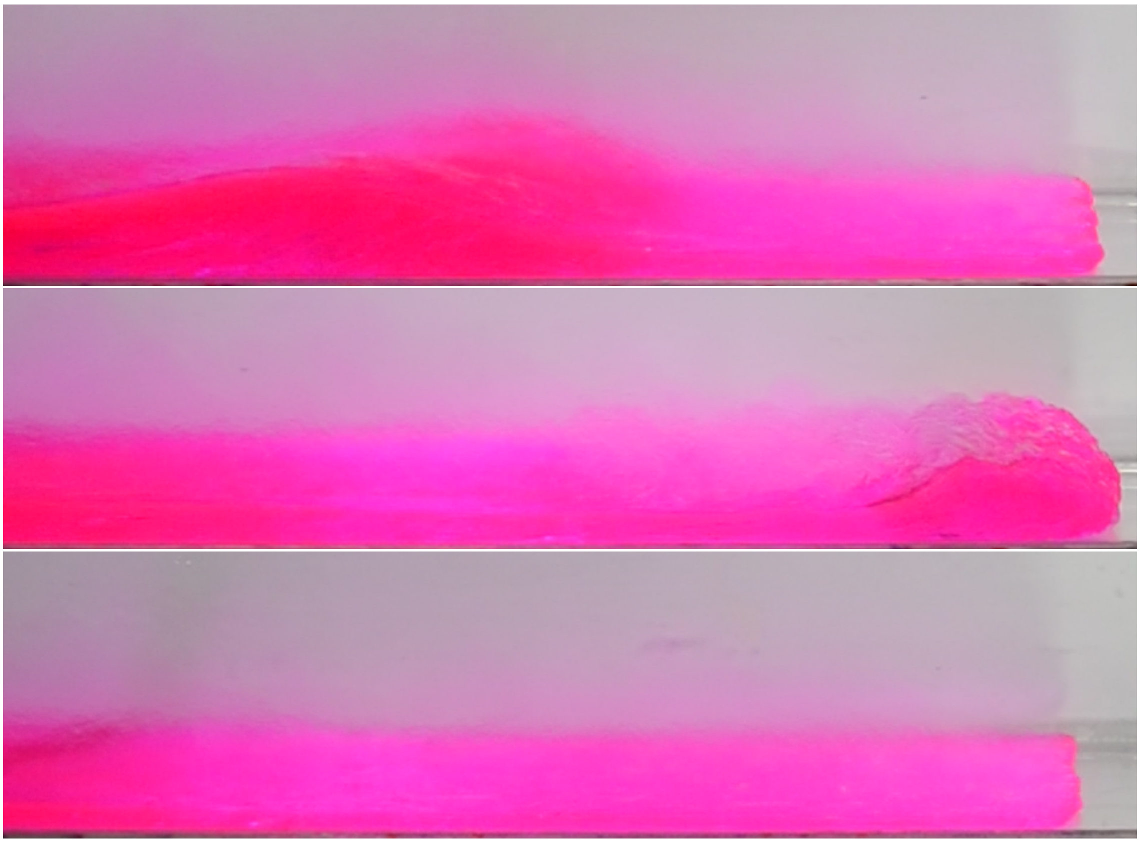

Figure 3.26: Pulse arriving at the head for the RD90-3/8 case with release time $t_{\mathrm{re}} = 3.36$. The pulse arrives from the left and, but becomes indistinguishable from the current before it reaches the head. (three images correspond to $t = 14.9$, 17.5, 20.2). Each image is approximately 25 cm wide.

3.5.3 Validation of shallow-water model

In this section, results from the experimental model are presented and compared to the shallow-water model discussed in chapter 2. The position of the head, X_N, and shock, X_s, were extracted from the footage from the two rolling cameras at 0.5 s intervals, as discussed in section 3.3.2.

In figure 3.27a head position, X_N, up to $t = 15$ for the three concentrations for the single release cases. Time is plotted on the y axis for consistency with the

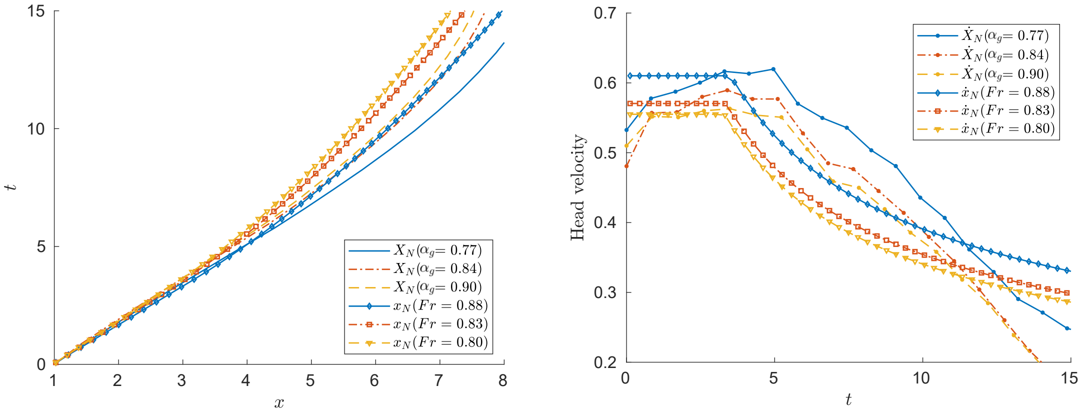

(a) (b)

Figure 3.27: (a) Head position against time and (b) head velocity against time for the single release experiments, x_N, and shallow-water simulations, X_N for concentration, 0.77, 0.84 and 0.90 and Froude numbers, Fr, 0.88, 0.83 and 0.80, respectively. Head position is plotted on the x-axis for comparison with the characteristic diagrams in chapter 2.

characteristic diagrams. Further, the head velocity from the double release experiments up to $t = 15$ is plotted in figure 3.27b. Beyond $t = 15$ the fastest pulse starts interacting with the head. After an initial transience, a period of constant velocity is observed (the slumping phase) before the velocity starts decreasing. The approximately constant value of the velocity was used to estimate the densimetric Froude number $Fr = u_N/\sqrt{h_N}$ of the flow. Simulations were conducted in the single release configuration for the determined values of $Fr = (0.80, 0.83, 0.88)$ corresponding to concentrations $(0.90, 0.84, 0.77)$. Note that these experiments are outside of the Boussinesq regime as the current density is more than 20% larger than the current. Thus our estimates of the Benjamin Froude number are adjusted by the square root of the density ratio to give $Fr_B = (0.89, 0.92, 0.97)$. The strong quantitative agreement between the head position and velocity, figure 3.27b confirms the validity of the constant Fr in the theoretical model.

As discussed in the introductory chapter, the Benjamin Froude number condition (1.25) is an increasing function of the fractional depth of the current $a = h/H$. Thus, the theoretical dimensionless speed of the current increases over time as the current thins and the depth ratio between the ambient and the current H increases. This indicates why a constant velocity region is not observed in the experiments. Further, the slumping distance (distance travelled by the current whilst in the slumping phase of constant head velocity) increases as the depth ratio H decreases. For $H = 2.5$ Ungarish and Zemach (2005) estimate this distance to be approximately 3 using a single-layer (infinitely deep ambient) and 5.5 using a two-layer shallow-water model using a Benjamin head condition. This is confirmed by the experimental and single-layer model results in figure 3.27. The head velocity of the single-layer model is constant until $t = 4$, whereas the experiments show a sharper decrease in head velocity at around $t = 6$. Simple dimensional arguments to calculate the time-scale t_c for inertia, viscosity and buoyancy to all be balanced (Huppert, 1982) produces $t_c \sim$ 3-7 and so unsurprisingly the head velocity in the experiments reduces quickly after the end of the slumping phase.

Figures 3.28 & 3.29 plot the shock position and velocity, respectively, against time for concentrations 0.84 and 0.9. Without the equivalent of a Froude number condition at the pulse, the extra dissipation at the shock is poorly captured by the numerical model, leading to over prediction of the shock velocity. However, the model does correctly predict that shocks with a longer release time t_{re} travel faster. The shock velocity is overestimated by roughly a factor of 2. The overestimate is a consequence of the inviscid assumptions in the shallow water equations and could be feasibly included into the model via a source term into the momentum equation. However, although this may provide a better model of the experiments, an additional parameter would be introduced. Figure 3.30 shows the temporal variation of the ratio between the distance the shock has travelled in both the theoretical model and the experiments. After the initial transience caused by the variable time the shock takes to accelerate between the experiments and the theoretical model, the different concentrations tend to similar ratios, signifying the constant effect of dissipation for a given concentration. Thus, the (Fr, t_{re}) parameter space will qualitatively change for every concentration considered.

Simple two-layer models have been used to describe the propagation speed of a bore into a quiescent ambient (White and Helfrich, 2014). However, these assume the denser fluid and the ambient are both stationary and of constant thickness. Further a variety of closure models, as discussed in White and Helfrich (2014), are required to provide an expression for the pressure drop across the bore. These closure models do not produce ideal agreement with numerical or observational results over the full range of parameters. Critically, the bore propagation is assumed to be steady in its own reference frame. However, as observed in the experiments presented here, the bore is dispersive, figure 3.23. Further, given that the ambient and first current are flowing relative to each other and that the first current is thinning, application of these simplified two-layer bore models is hard to justify.

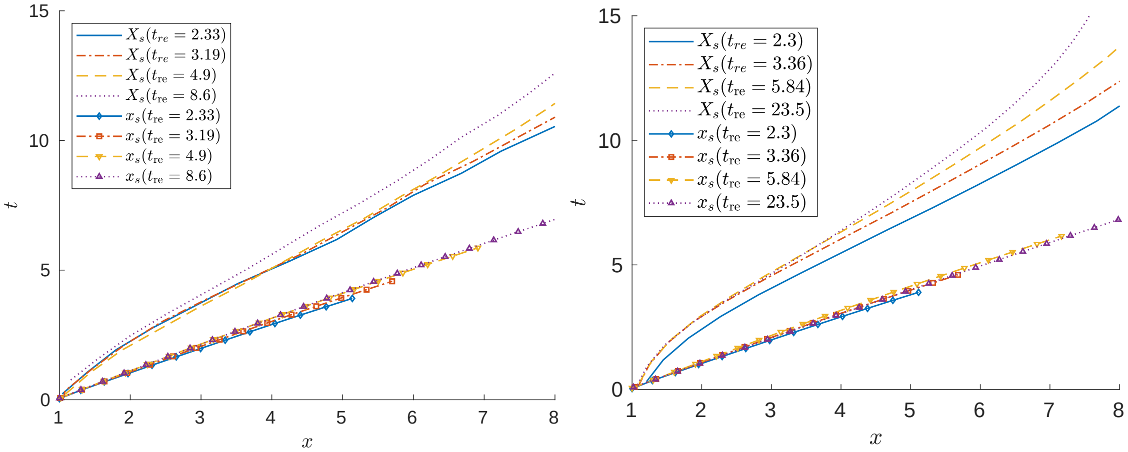

(a) (b)

Figure 3.28: Shock position for the experiments, X_s, and the shallow-water model, x_s, at different gate release separation times, $t_{\rm re}$: (a) concentration 0.84 ($Fr = 0.80$) and (b) concentration 0.90 ($Fr = 0.77$).

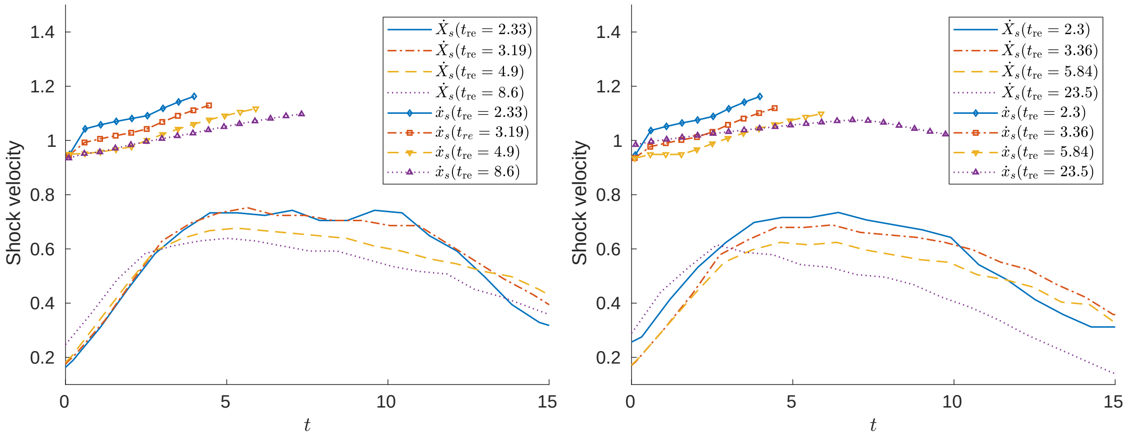

(a) (b)

Figure 3.29: Shock velocity for the experiments, $\dot{X}_s$, and the shallow-water model, $\dot{x}_s$ at different gate release separation times, $t_{\rm re}$: (a) concentration 0.84 ($Fr = 0.80$) and (b) concentration 0.90 ($Fr = 0.77$).

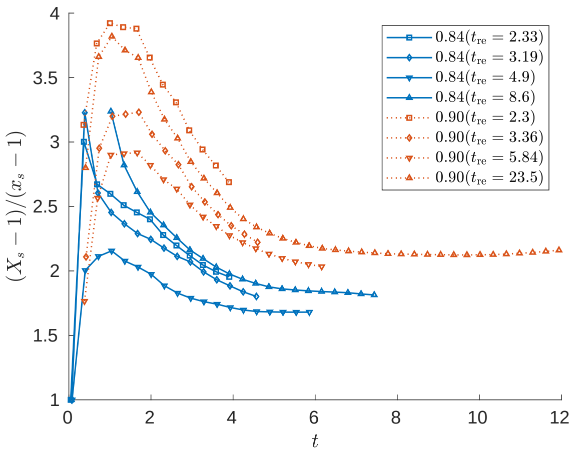

Figure 3.30: Comparison of the ratio of shock displacement from the front of the second lock box between experiments and the shallow-water model at concentrations 0.84 (–) and 0.90 ($\cdots$) for four different gate release separation times, t_{re}.

3.6 Conclusions and further work

In this chapter pulses in gravity currents have studied using an idealised double-lock release problem. The setup was based on the work of Ho et al. (2018a,b, 2019), but an order of magnitude smaller Reynolds numbers were considered. By increasing the viscosity of the current the amount of entrainment and mixing was reduced during the flow. Further, the transition to dilute turbulent behaviour was observed through a cascade of mixing, which was enhanced by large viscosity contrast between glycerol and water and the non-linear relationship between the mixture viscosity and glycerol concentration (Cheng, 2008). However, the increased viscosity led to viscous forces becoming increasingly significant over time.

The second release created a pulse that appeared as a bore that transitioned from the second release into the body of the first current and towards the head of the flow. This pulse transferred energy to the head of the flow and led to an increase in mixing. In contrast, the dilute experiments of Ho et al. (2018a,b, 2019) where an intrusion is formed that transport mass as well energy to head of the flow.

A series of single-release experiments were conducted to determine a suitable Froude number Fr for the head of current at each concentration to enable comparison with the theoretical shallow-water model presented in chapter 2. Excellent agreement with the head and speed over time was observed for the first 10 to 15 time units of the flow. This is before viscous effects start to become important and the head slows down relative to the theoretical model. The numerical model over-predicts the speed of the pulse by a factor of two. This discrepancy arises because of the neglected viscous forces that would act to smooth the shock and energy required to displace the ambient water. At the head of the flow, these are captured by the Froude number condition. However, no such condition exist for the pulse in the numerical model. Thus, a further developed model could impose a similar condition to the constant frontal Froude number at the shock. However, the Froude number condition is determined for a current head propagating into an ambient and not through the body of another gravity current. Further, this would be more difficult to impose numerically as for the flow considered in this chapter, the pulse propagates at a different speed to the surrounding current. This contrasts the head of the first current where the head speed is the same as the fluid velocity there.

Chapter 4

Direct numerical simulation of the lock-exchange problem

4.1 Introduction

4.1.1 Lock-exchange problem

In the experimental chapter, the lock-release problem was studied with large viscosity gradients between the current and the ambient using three glycerol-water mixtures. This chapter will explore the behaviour of gravity driven flows with a large viscosity contrast and categorise how a viscosity contrast affects the flow dynamics, and in particular the mixing. Direct numerical simulation using the spectral-element solver NEK5000 (Fischer et al., 2008) is used to capture the mixing dynamics across the relevant scales. To fully resolve the experiments presented in the previous chapter requires more computational resources than available and therefore, a reduced problem based on the lock-exchange problem of Özgökmen et al. (2009b) is considered, which significantly reduces the required domain size. Further, boundary conditions are chosen to be free-slip or periodic to remove the viscous boundary layers near the wall and simple linear relationships are posed for fluid properties, such as density and viscosity, to reduce the computational cost. These assumptions enable the study of viscosity contrast between the ambient and current of up to an order of magnitude in simulations that are sufficiently resolved. All simulations were conducted on ARC3, part of the High Performance Computing facilities at the University of Leeds. The amount of cores available on this shared system limited the amount of simulations that could be conducted and their resolution.

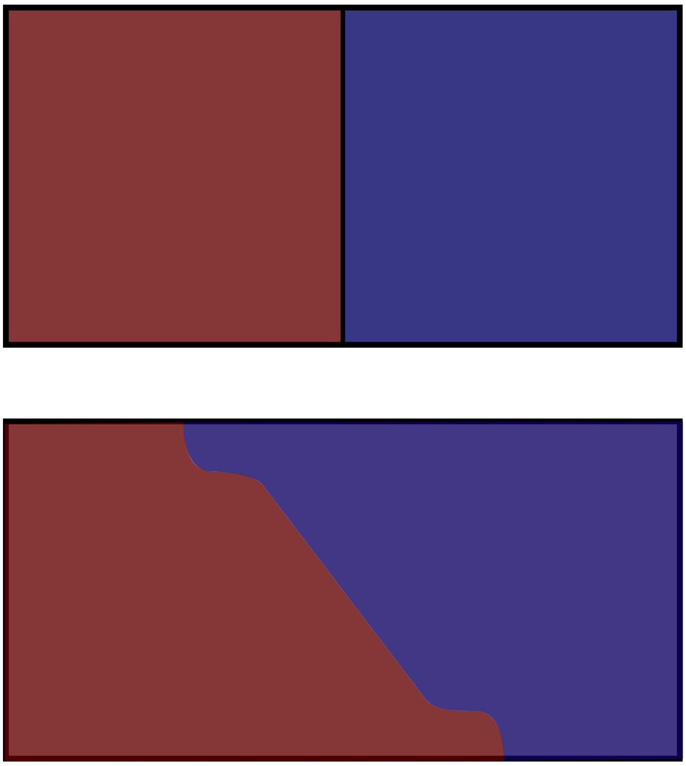

Figure 4.1: Diagram of the lock exchange problem. Initially denser (red) fluid and less dense (blue fluid) is held in place by a vertical gate in the centre of the domain (top). At $t = 0$ the gate is released with the density difference driving the flow outwards (bottom).

The lock-exchange problem considers a lock-release problem where the locked fluids each occupy exactly half of the domain, figure 4.1. Initially denser (red fluid) and less dense (blue fluid) are separated by a vertical gate in the centre of the domain. At $t = 0$ the gate is released and the density difference drives the red fluid to the right along the base and similarly the blue fluid to the left along the top of the domain.

The lock-exchange problem has been used as a bench-mark for studying mixing in stratified flows. This is a fundamental area of research in oceanography because mixing occurs in subsurface flows near equatorial zones (Kantha and Clayson, 2000), overflows (Price and Baringer, 1994) and flows that interact with topographic features (Ledwell et al., 2000). Özgökmen et al. (2009b) extend their previous testing of large-eddy simulation (LES) of the lock-exchange problem (Özgökmen et al., 2007, 2009a) with DNS conducted with NEK5000. They investigated the sensitivity of the LES results with respect to the Reynolds number and use both DNS and LES to explore how the extent of mixing changes for a range of Reynolds numbers. As a result of the available computational power, they limit their DNS to Reynolds numbers between 10^3 and 3×10^4. Pseudo-spectral simulations for a longer domain have also been conducted (Cantero et al., 2006, 2007). The setup considered in this chapter is similar to that of Özgökmen et al. (2009b). However, in additional to a density variation between the two fluids, a viscosity difference is introduced with the viscosity based on the local concentration of each fluid.

4.2 Methodology

Navier-Stokes and advection-diffusion equations

The gravity driven flow of two fluids of different densities and viscosities in a lock-exchange configuration is modelled with the Navier-Stokes equations and single transport equation for the local phase concentration, $\phi = \phi(x, y, z, t)$. The denser fluid, which will form the intruding gravity current along the base is denoted as fluid 2 and the lighter or ambient fluid as fluid 1. Each pure phase has constant density ρ_i and dynamic viscosity μ_i. The phase concentration $\phi \in [0, 1]$ represents the concentration of fluid 2 and thus, $\phi = 1$ or $\phi = 0$ corresponds to points of purely fluid 2 or fluid 1, respectively. This is an adaption of the volume-of-fluid (VOF) method (Scardovelli and Zaleski, 1999), as here the viscosity is also a function of the phase concentration.

By studying the Stokes' equations Moresi et al. (1996) demonstrated that the accuracy of two finite-element-type schemes depended on the viscosity gradients between adjacent cell rather than the contrast across the entire domain. Although this study is for a related problem, it illustrates viscosity gradients are a limiting factor for required resolution. Thus, in order to minimise the computational resources used, linear relationships are assumed for both viscosity and density

$$\rho(\phi) = \phi\rho_2 + (1-\phi)\rho_1 = \left(1 + \frac{\rho_2 - \rho_1}{\rho_1}\phi\right)\rho_1 \tag{4.1}$$

$$\mu(\phi) = \mu^*(\phi)\mu_1 = (1 + \gamma\phi)\mu_1, \tag{4.2}$$

where γ is a constant. A linear relationship provides the smoothest transition between fluid 1 and fluid 2 viscosities and therefore higher viscosity contrasts can be studied. Surface tension and other inter-molecular forces are neglected. The density difference between the two layers is assumed to be small, i.e. $\rho_2/\rho_1 \sim 1$, so that the Boussinesq approximation (Boussinesq, 1897) can be applied. This neglects density variations in all terms that are not multiplied by gravitational acceleration g.

The domain Ω used is a rectilinear box, in three spatial dimensions (x, y, z), of length L, height H, and width, W. Thus $\Omega = \{(x, y, z) \in \mathbb{R}^3 \,|x \in [-L/2, L/2], y \in$

$[0, H], z \in [0, W]\}$, figure 4.2. The aspect ratio L/H is an important parameter of the system. When $L \gg H$, the flow is essentially a two-layer exchange flow with counter-propagating gravity currents with the appearance of Kelvin-Helmholtz rolls (Ilıcak et al., 2009). Mixing occurs predominately by turbulent breakdown and second-instabilities about these rolls in a stably-stratified setting (Özgökmen et al., 2009b). A longer domain would be more representative of the experimental setup discussed in 3, but would significantly increase the computational cost. In a short domain with $L < H$ the gravity currents would rapidly encounter the two end walls at $x = \pm L/2$. An aspect ratio $L/H = 2$ provides regions of the flow when stably-stratified mixing occurs and more complex convection-driven mixing at the ends wall whilst keeping computational cost reasonable and allowing a range of viscosity differences to be studied. The width aspect ratio W/H is fixed at 1, which is the same as the studies of Özgökmen et al. (2009a,b) and similar to value of 1.5 used by (Härtel et al., 2000; Cantero et al., 2006).

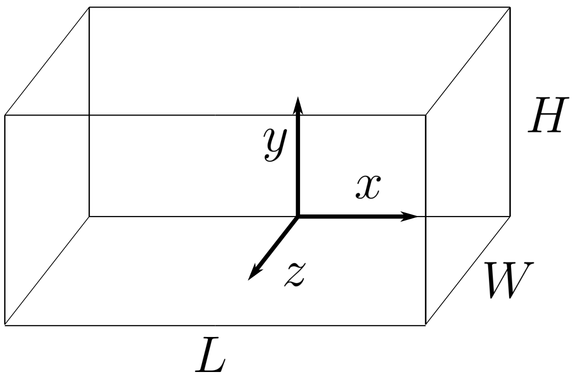

Figure 4.2: Geometry for the lock-exchange problem. A box length L, height H and width W in the x-, y-, and z-directions, respectively. The aspect ratios used in all simulations are $L/H = 2$ and $W/H = 1$.

For spatial co-ordinates aligned with the horizontal, vertical and orthogonal direction, $\mathbf{x} = (x, y, z)$ and time t, the Navier-Stokes equations for an incompressible Boussinesq fluid are, Tritton (2012):

$$\frac{\partial \mathbf{u}}{\partial t} + (\mathbf{u} \cdot \nabla)\, \mathbf{u} = - \nabla p + \nabla \cdot \boldsymbol{\tau} + \frac{\rho(\phi)}{\rho_1}\mathbf{g}, \tag{4.3}$$

$$\nabla \cdot \mathbf{u} = 0, \tag{4.4}$$

where, $\mathbf{u}(\mathbf{x}, t) = (u(\mathbf{x}, t), v(\mathbf{x}, t), w(\mathbf{x}, t))$, is the velocity along the three spatial axes, $\mathbf{g} = (0, -g, 0)$ is the gravitational vector and g is gravitational acceleration. The stress tensor, $\boldsymbol{\tau}$, is expressed

$$\boldsymbol{\tau} = \mu \left[(\nabla \mathbf{u}) + (\nabla \mathbf{u})^T \right], \tag{4.5}$$

Further, an advection-diffusion equation is used to model the transport of dense phase concentration ϕ,

$$\frac{\partial \phi}{\partial t} + \mathbf{u} \cdot \nabla \phi = \nabla \cdot (D \nabla \phi), \tag{4.6}$$

where D is the mass diffusivity. These equations (4.3, 4.4 & 4.6) are non-dimensionalised with length scale, H, velocity scale, U, and the advective time-scale H/U

$$(x, y, z) = H(x^*, y^*, z^*), \quad (u, v, w) = U(u^*, v^*, w^*), \quad \text{and} \quad t = \frac{H}{U} t^*, \tag{4.7}$$

where an asterisk * refers to a dimensionless quantity. The velocity scale $U = \sqrt{g' H/2}$, where $g' = g(\rho_2 - \rho_1)/\rho_1$, is the reduced gravity, is used. Finally, a high-Reynolds number scaling based on the fluid 1 density, ρ_1, was used for the pressure and pressure normalised by $p - \rho_1 g = p^* \rho_1 U^2$. This yields dimensionless equations

$$\begin{aligned}
\frac{D^* \mathbf{u}^*}{D^* t^*} =& - \nabla^* p^* + \frac{1}{Re_1} \nabla \cdot \left(\mu^*(\phi) \left((\nabla^* \mathbf{u}^*) + (\nabla^* \mathbf{u}^*)^T \right) \right) - \frac{\phi}{Fr} (0, 1, 0), && (4.8) \\
\nabla^* \cdot \mathbf{u}^* =& 0, && (4.9) \\
\frac{D^* \phi}{D^* t^*} =& \nabla^* \cdot \left(\frac{1}{Pe} \nabla^* \phi \right), && (4.10)
\end{aligned}$$

where $Fr = U^2/(Hg')$ is the Froude number, $Re_1 = HU/\nu_1 = \rho_1 HU/\mu_1$, is the ambient or fluid 1 Reynolds number and $Pe = HU/D$ is the Péclet number, which is the ratio between advective and diffusive transport rates. With our choice of velocity scale $Fr = 1/2$. The Péclet number is more commonly expressed in terms of the Schmidt number, $Sc = \nu/D$, the ratio of momentum and mass diffusivities, and the Reynolds number,

$$Pe = Re_1 Sc. \tag{4.11}$$

The asterisks * are dropped for convenience, except on the viscosity function $\mu^*(\phi)$, yielding

$$
\begin{aligned}
\frac{D\mathbf{u}}{Dt} &= -\nabla p + \frac{1}{Re_1}\nabla\cdot\left(\mu^*(\phi)\left((\nabla\mathbf{u})+(\nabla\mathbf{u})^T\right)\right) - 2\phi(0,1,0), && (4.12)\\
\nabla\cdot\mathbf{u} &= 0, && (4.13)\\
\frac{D\phi}{Dt} &= \nabla\cdot\left(\frac{1}{Re_1 Sc}\nabla\phi\right), && (4.14)
\end{aligned}
$$

to be solved on the dimensionless domain $\Omega = \{(x,y,z) \in \mathbb{R}^3\,|x \in [-1,1], y \in [0,1], z \in [0,1]\}$. Three dimensionless parameters categorise the flow behaviour: the ambient Reynolds number Re_1, the Froude number Fr and the Schmidt number Sc. The Schmidt number depends only on material properties and the local concentration ϕ and in the limits of pure water diffusing into glycerol and pure glycerol diffusing into water yield 9×10^2 and 5×10^7, respectively. These were calculated by D'Errico et al. (2004) using an extrapolation technique for concentrations of nearly pure water or glycerol at $25\,^\circ C$.

Large Schmidt numbers indicate the mass diffusivity is negligible compared to the vorticity. As the limit tends to infinity this corresponds to immiscible fluids that can only be mixed at macroscopic scales through interface instability and fluid turbulence (Bonometti and Balachandar, 2008). For flows involving (nearly) immiscible fluids, surface tension effects can become important.

In the context of gravity currents, initial studies suggested a Schmidt number Sc similarity for values larger than roughly 1 (Necker et al., 2005) or that the influence of the Schmidt number Sc to be quite small in the range 0.2-5 (Birman et al., 2005). Bonometti and Balachandar (2008) demonstrated that quantitative changes can be observed between gravity currents with high or low Schmidt numbers Sc. A depression that separates the head from the body occurs at high-Sc, which can move up or down the gravity current body. If it reaches the head it can either shrink and disappear or result in an oscillatory behaviour depending on the Reynolds number. Bonometti and Balachandar (2008) observe that at high Reynolds numbers ($Re > 10^4$) the effect of the Schmidt number Sc on the head of a gravity current in small. However, the value of the Schmidt number Sc affects vortex formation within the body.

The linear relationship between concentration and viscosity reduces the sharp jump between viscosity that can occur at the interface between the two fluids. Further, by keeping the Schmidt number Sc limited to 7, there is at least some diffusive thickening of the concentration boundary layers. This increases the amount of mixing that occurs locally at the interface and will act to smooth the sharp density and viscosity gradient there. This contribution to mixing increases over time and therefore will be dominant for large integration times. Thus, fixing the Schmidt number Sc at 7 limits the total integration time the simulations can be conducted for. However, as discussed in section 4.2.2, $Sc = 7$ is sufficient for numerous sloshings to occur without significant diffusive mixing to occur.

Boundary and initial conditions

The boundaries of the domains at $x = -1, x = 1, y = 0, y = 1$ are prescribed as symmetry planes

$$\mathbf{u}(-1, y, z, t) \cdot \mathbf{n} = 0, \quad \mathbf{u}(1, y, z, t) \cdot \mathbf{n} = 0, \quad \mathbf{u}(x, 0, z, t) \cdot \mathbf{n} = 0, \quad \mathbf{u}(x, 1, z, t) \cdot \mathbf{n} = 0, \tag{4.15}$$

where $\mathbf{n}$ is the outward pointing normal on the domain boundary $\partial\,\Omega$ and at the $z = 0$ and $z = 1$ planes a periodic condition is imposed

$$\mathbf{u}(x, y, 0, t) = \mathbf{u}(x, y, 1, t), \quad \phi(x, y, 0, t) = \phi(x, y, 1, t) \tag{4.16}$$

The initial conditions consist of a concentration profile, in which the majority of the fluid is either at $\phi = 0$ or $\phi = 1$. A small sinusoidal perturbation is introduced to the interface in the z direction $\eta(z) = 0.05 \sin(2\pi z)$ and the sharp jump between $\phi = 0$ and $\phi = 1$ is replaced by a linear variation in concentration of a small region of width $2\zeta_0 = 0.01$.

$$\phi(x, y, z, 0) = \begin{cases} 1 & \text{if} \quad x \in [-1, -\zeta_0 - \eta(z)], \\ \frac{1}{2\zeta_0}(\zeta_0 - x - \eta(z)) & \text{if} \quad x \in [-\zeta_0 - \eta(z), \zeta_0 - \eta(z)], \\ 0 & \text{if} \quad x \in [\zeta_0 - \eta(z), 1]. \end{cases} \tag{4.17}$$

The velocity is set to zero everywhere initially, $\mathbf{u}(x, y, z, 0) = \mathbf{0}$. The boundary condition remove the viscous boundary layers that would required significantly more computational resources. Further, limiting the Schmidt number Sc to 7 enables us to study the mixing that occurs in gravity driven flows with a range of viscosity differences between the two layers. As discussed in the introduction chapter, a no-slip boundary condition along the bottom boundary results in the nose of the gravity current rising up from the bed and forcing ambient fluid underneath as it propagates. This leads to entrainment into the body of the current. With a free slip boundary condition the propagating wavefront will not raise up from the boundary and hence no fluid will be entrained through this mixing mechanism.

Numerous studies use simplified boundary conditions to allow better resolution of the mixing dynamics that occur. For example free-slip conditions on the top, bottom, and end walls of the domain and periodic boundary conditions in the cross-stream direction (Härtel et al., 2000; Cantero et al., 2006; Özgökmen et al., 2009a,b). Further studies have been conducted in a two-dimensional domain, but these cannot capture any three-dimensional variations in the flow.

Cases conducted

For the set of simulations conducted, the fluid 1, or ambient, Reynolds number is fixed at 1000. By varying the coefficient γ, the fluid 2 Reynolds number, defined as $Re_2 = Re_1/(1+\gamma)$ can be varied. Six different values of γ are chosen for the simulations conducted, $\gamma = 0, 0.1, 1, 2, 4, 10$. The corresponding dimensionless numbers for each case is presented in table 4.1.

The base case is $\gamma = 0$ where the Reynolds numbers in each layer are the same and provides a source of comparison to the cases where the base layer Reynolds number is increased. Increasing the viscosity contrast, increases the computational cost required to reach suitably resolved solutions, as discussed later in section 4.2.3. The largest value of γ that is feasible in this study is $\gamma = 10$. The remaining cases are chosen to vary the viscosity difference over two orders of magnitude between that of $\gamma = 10$ and the base case, $\gamma = 0$. The total integration time for each case T_{int} is fixed at 13.5 in dimensionless units. As discussed by Özgökmen et al. (2009b) this corresponds to 3.35 times the time for the current to cross one length of the domain and 2.15 times the buoyancy period. Thus, although it is not sufficient for the flow to come to rest, it captures multiple sloshings and is sufficient for the bulk of turbulent mixing to occur (Özgökmen et al., 2009b). Further, the choice of integration time is low enough for the diffuse contribution to mixing to be negligible.

4.2.1 Solver and numerical details

What is NEK5000?

NEK5000 is a computational fluid dynamics code that solves the Navier-Stokes equations by direct numerical simulation (Fischer et al., 2008). It uses the spectral

Table 4.1: Fluid 2 (current) Re_2 and fluid 1 (ambient) Re_1 Reynolds numbers, Schmidt numbers Sc and Péclet numbers Pe corresponding to the cases studied in this chapter.

γ	Re_2	Re_1	Sc	Pe
0	1000	1000	7	7000
0.1	910	1000	7	7000
1	500	1000	7	7000
2	333	1000	7	7000
4	200	1000	7	7000
10	91	1000	7	7000

element method to discretise the spatial domain, which has significant advantages over other schemes when the Reynolds number is large or long time integration is required, because of the minimal numerical dispersion and dissipation that occurs. It is designed for laminar, transitional and turbulent flows with both heat and species transport, and can also be used for incompressible magnetohydrodynamics (MHD) or low-Mach number flows. NEK5000 has been demonstrated to be more computationally efficient for high-fidelity jets when compared with a finite-volume method (FVM) based scheme (Capuano et al., 2019) in the open-source code OpenFOAM (Jasak et al., 2007). NEK5000 provides extremely rapid (exponential) convergence in space and fast-scalable multi-grid solvers making it efficient in terms of parallelisation. NEK5000 has been demonstrated to reach the scaling limits for PDE-based simulations on peta-scale computers with up to 2 billion degrees of freedom (Fischer, 2015; Offermans et al., 2016; Merzari et al., 2020). Weak-scaling results in a fixed computational time if the number of processors and the degrees of freedom to be increased proportionally, whereas strong-scaling allows computational cost to be reduce inversely proportional to the number of processors for a fixed problem size Merzari et al. (2020). Reaching these limits is required for the simulations to be computationally efficient.

Spectral elements methods (SEM) are a class of high-order weighted residual techniques and a subset of finite-element methods (FEM) (Deville et al., 2002) and were developed by Patera (1984). In this computational method the domain is split into E rectilinear elements with basis functions formed from an $\mathcal{N}$-th order tensor product polynomial in each spatial direction. Thus, there are $(\mathcal{N}+1)^d$ degrees of freedom for each element E, where d is the number of spatial dimensions. Spectral elements are optimised for polynomial orders $\mathcal{N}$ between 7 and 15 (Patera, 1984). For a given suitably smooth function $f(\xi, t)$, the spectral element approximation on a reference cube $(\xi_x, \xi_y, \xi_z) \in [-1,1]^3$ is represented as

$$f(\xi, t) \approx \sum_{i,j,k=0}^{\mathcal{N}} f_{ijk}(t)\pi_i(\xi_x)\pi_j(\xi_y)\pi_k(\xi_z). \tag{4.18}$$

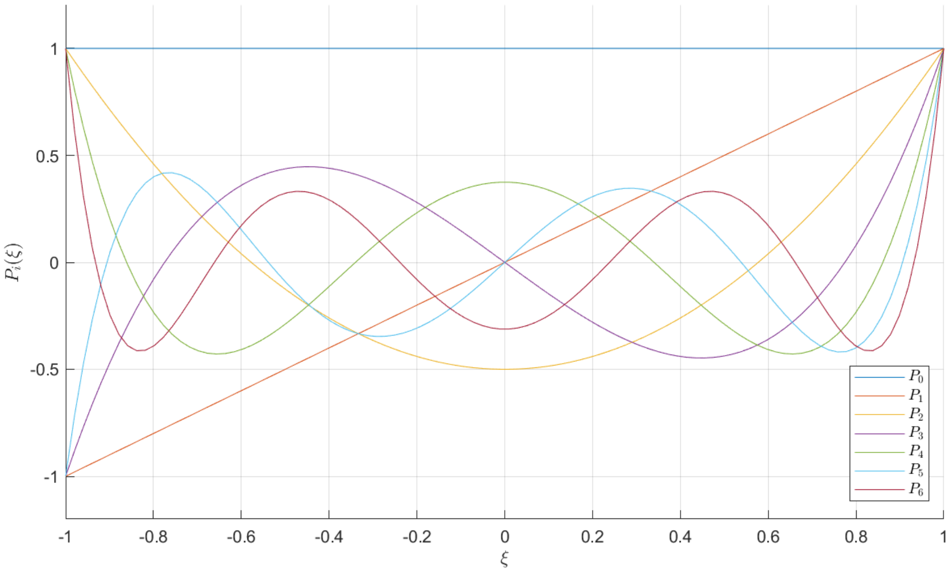

Figure 4.3: the Legendre polynomials P_n up to degree 6. The Legendre polynomials are the unique polynomial solutions to the equation $\langle P_i, P_j \rangle = 2/(2i+1)\delta_{ij}$.

In NEK5000 these basis functions $\pi_i(\xi)$ for SEM, up to degree $\mathcal{N}$, are constructed from the Legendre polynomials, $P_{\mathcal{N}}$, of degree $\mathcal{N}$, which are the unique polynomial solutions to

$$\langle P_i, P_j \rangle = \int_{-1}^{1} P_i P_j \,\mathrm{d}\xi = \frac{2}{2i+1}\delta_{ij}, \tag{4.19}$$

where δ_{ij} is the Kronecker delta. The first few Legendre polynomials are plotted in figure 4.3. The Gauss-Lobatto-Legendre (GLL) points are used as the quadrature nodes for fitting the smooth functions in each element. For a polynomial interpolation of order $\mathcal{N}$, the set of GLL points is defined $\Xi_{\mathcal{N}} = \{\xi_0, \xi_1, \ldots, \xi_{\mathcal{N}}\}$ as the ordered solutions to the equation

$$\left(1-\xi^2\right) P'_{\mathcal{N}}(\xi) = 0, \tag{4.20}$$

where $P'_{\mathcal{N}}$ is the derivative of $P_{\mathcal{N}}$ with respect to its argument. The set basis functions $\{\pi_j\}$ for interpolation can be calculated from the Legendre polynomials. These functions are explicitly given

$$\pi_j(\xi) = \frac{-1}{\mathcal{N}(\mathcal{N}+1)} \frac{(1-\xi^2)\, P'_{\mathcal{N}}(\xi)}{(\xi-\xi_j) P_{\mathcal{N}}(\xi_j)}. \tag{4.21}$$

Crucially the roots of equation (4.20) are distinct and are normalised so that $\pi_j(\xi_k) = \delta_{jk}$, i.e. at the each GLL quadrature point precisely one of the basis functions π_j is non-zero and takes the value 1. For $\mathcal{N} = 6$ the basis functions $\{\pi_j\}$ are plotted along with the GLL points in figure 4.4. A regular mesh is created by posing the number of elements in each of the spatial direction (N_x, N_y, N_z). This gives the total number of elements $\mathcal{E} = N_x N_y N_z$. Each element e then contains $\mathcal{N}^3$ nodes corresponding to relative positions of the GLL points when the element is mapped onto the reference cube. An example mesh with $(N_x, N_y, N_z, \mathcal{N}) = (32, 16, 16, 8)$ is displayed in figure 4.5 corresponding to a total of 8192 elements and approximately 4.2×10^6 nodes. For simplicity, all the results presented in this chapter are first interpolated onto a regular mesh containing the same number of nodes as the simulation mesh. Increasing the number of nodes up to a factor of eight times the number of simulation nodes did not noticeably change any of the results.

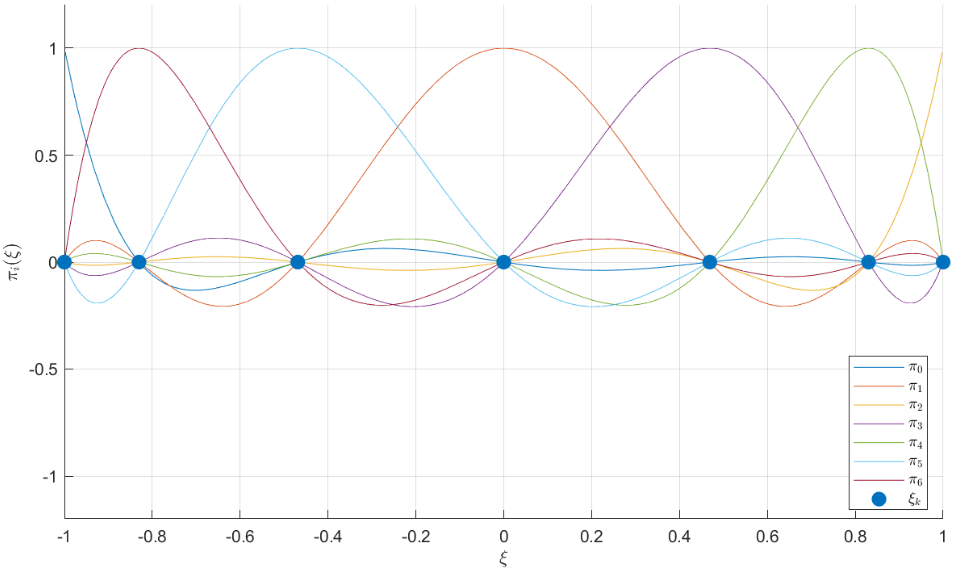

Figure 4.4: The Legendre interpolation basis functions π_j based of the Legendre polynomial of degree $\mathcal{N} = 6$. At the GLL points ξ_k $\pi_j(\xi_k) = \delta_{jk}$.

Time integration

Two expansions are used in time discretisation: a k-th order backwards-difference scheme; and, to reduce some of the complexity of handling the non-linear advection terms, a forward extrapolation to k-th order. Consider a simple first-order in time

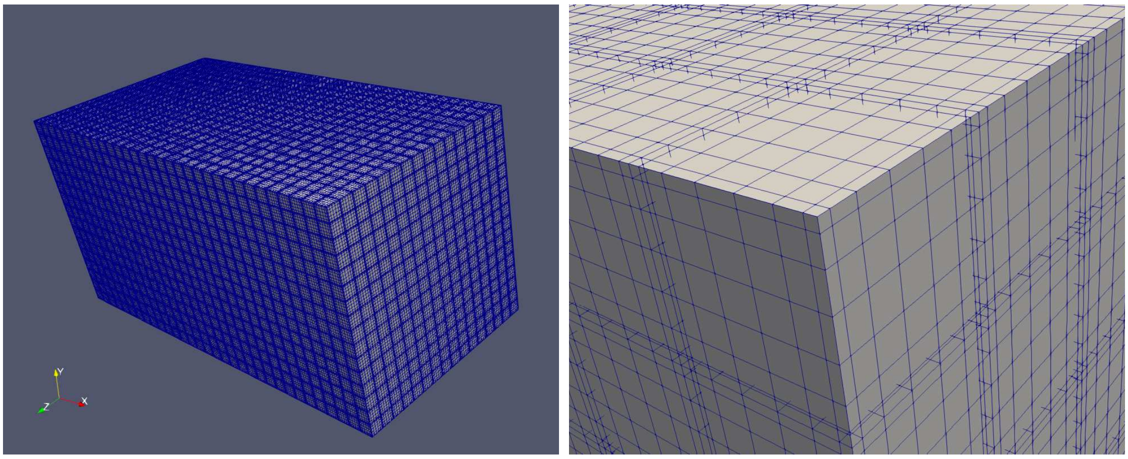

(a) (b)

Figure 4.5: Example spectral element mesh on a $2 \times 1 \times 1$ domain with $32 \times 16 \times 16 = 2^{13}$ elements and $\mathcal{N} = 8$ (a). Close up highlighting the node structure within each element. The total number of nodes in the mesh is $2^{13} \times 8^3 \approx 4.2 \times 10^6$.

PDE of the form

$$\frac{\partial \mathbf{u}}{\partial t} = \mathcal{L}^* \left[\mathbf{u}\right], \tag{4.22}$$

where $\mathcal{L}^*$ is an arbitrary spatial differential operator. The k-th order backwards difference scheme (BDFk), for time steps given by superscript, is

$$\mathcal{L}^*[\mathbf{u}^{n+1}] = \frac{1}{\Delta t} \sum_{i=0}^{k} b_i \mathbf{u}^{n+1-i}, \tag{4.23}$$

where Δt is the time-step. The k-th order extrapolation (EXTk) is

$$\mathcal{L}^*[\mathbf{u}^{n+1}] = \sum_{i=1}^{k} a_i \mathcal{L}^* \left[\mathbf{u}\right]^{n+1-i}. \tag{4.24}$$

The expansion coefficients are given in table 4.2 for the first values of k. By combining both BDFk and EXTk an implicit/explicit (IMEX) scheme can be obtained. For the convection-diffusion equation, BDF3 is used to discretise the time derivatives and EXT3 is used to remove the implicit $(n+1)$ dependence on the convection term $\mathbf{u} \cdot \nabla \phi$. The time-stepping for the Navier-Stokes follows the $\mathbb{P}_{\mathcal{N}} - \mathbb{P}_{\mathcal{N}}$ approach presented in Tomboulides et al. (1997) and Tomboulides and Orzag (1998). The method involves a splitting approach, where first an intermediary velocity is created using EXTk (4.24) to remove the implicit non-linear terms. Then the Laplacian of the pressure is updated from this velocity. Finally, the velocity is updated using the pressure gradient and the viscous source terms. The splitting introduces a small mass error, but provides high temporal accuracy (Tomboulides et al., 1997).

Table 4.2: Coefficients for the k-th order backwards difference scheme (a_i) and the extrapolation scheme (b_i) for $k = 1, 2, 3$.

	Backwards difference coefficients (b_i)				Extrapolation coefficients (a_i)		
k	b_0	b_1	b_2	b_3	a_1	a_2	a_3
1	1	-1	0	0	1	0	0
2	3/2	-2	1/2	0	2	-1	0
3	11/6	-3	3/2	-1/3	3	-3	1

Computational cost

The computational cost for a direct numerical simulation is a function of both the number of mesh points and the number of time steps. The spatial resolution required in each direction can be estimated from the Kolmogorov length scale $l_\nu = (\nu^3/\bar{\epsilon})^{1/4}$, where $\bar{\epsilon}$ is the mean turbulence energy dissipation rate, (Kolmogorov, 1941). The Kolmogorov length scale is an eddy length scale based on inertial and viscous forces being equal in magnitude. Length scales smaller than this will be dominated by viscosity and do not need to be resolved. The mean turbulence energy dissipation rate is proportional to ${u'_{\text{RMS}}}^3/L_E$, where L_E is the largest eddy structure in the flow (bounded above by the domain size) and the root-mean square velocity fluctuation is given by

$$u'_{\text{RMS}} = \sqrt{\frac{\overline{u'^2} + \overline{v'^2} + \overline{w'^2}}{3}} \tag{4.25}$$

and (u', v', w') are the fluctuating velocity components (Lipatnikov, 2012). Thus, the Kolmogorov length scale is $l_\nu = (\nu^3 L_E/u'^3)^{3/4}$. To capture the turbulence at its smallest scales, the grid spacing $\Delta x = L_E/N$ (assuming the worst case scenarios where the largest eddy is the size of the domain) needs to be below the Kolmogorov scale, i.e.,

$$N > \frac{L_E}{\eta} = \left(\frac{u'^3 L_E^3}{\nu^3}\right)^{\frac{1}{4}} = Re^{\frac{3}{4}}. \tag{4.26}$$

For a three dimensional problem the number of cells required N^3 is proportional to $Re^{9/4}$. However, increasing the number of cells also decreases the largest stable time-step that can be used. Kooij et al. (2018) demonstrated that the total cost (in CPU hours) is proportional to the number of cells to the power of 4/3. Thus, the total computational cost for a three dimensional time-dependent problem is proportional to Re^3 (Pope, 2001). So far the effect of the mass diffusivity has not be discussed. The Batchelor length scale, l_b is the diffusion length scale for the problem and can be expressed $l_\nu = Sc^{1/2} l_b$ (Meiburg et al., 2015). For $Sc < 1$ this is larger than the Kolmogorov scale and so the above computational cost estimate is sufficient. However, when $Sc > 1$ this diffusive length scale becomes the smallest and so a problem requires a total number of cells $N^3 \sim Re^{9/4} Sc^{3/2}$ and for a time dependent problem, the total computation cost is proportional to $Re^3 Sc^2$. As a result of this most studies of gravity currents either reduce the value of the Schmidt number to close to unity or do not use sufficient resolution to capture the region of sharp concentration gradients.

Stability and projection

For convection dominated flows, the Galerkin formulation suffers from a well known instability arising from under-resolved boundary layers, for example Brown (1995). This can lead to energy accumulation in high-frequency modes (small spatial scales) that cannot be resolved (Özgökmen et al., 2009b). Although the instability is more common at very large Reynolds numbers, it has been observed at moderate to high Reynolds numbers (10^3-10^4). Filtering attempts to address this behaviour, whilst also preserving the exponential converge rate in space (Fischer and Mullen, 2001; Fischer et al., 2002), and involves multiplying the highest order basis polynomial coefficient by a factor $1 - \beta_f$. Fischer et al. (2002) demonstrate a value $\beta_f = 0.05$ mostly removes the instability for problems such as shear layer roll-up and plane-Poiseuille flow. As such, the value $\beta_f = 0.05$ is used throughout our simulations, which is consistent with other studies in the literature (Özgökmen et al., 2004; Özgökmen and Fischer, 2008; Özgökmen et al., 2009b; Lomperski et al., 2017).

High-frequency oscillations can also lead to instability through an aliasing error. I.e. errors arising from insufficient resolution to capture high frequency oscillations, which can instead appear as spurious low-frequency noise (Kirby and Karniadakis, 2003). Even if the resolution is of the order of the Kolmogorov length scale l_ν, errors can be introduced from the non-linear terms in the Navier-Stokes equations. For a linear equation, the solution for the polynomial coefficients is interpolated exactly (within computational error) with $(\mathcal{N} + 3)/2$ quadrature points when the solution is a polynomial of degree N. However, the convection term in the Navier-Stokes equation is quadratic rather than linear. This leads to a stronger requirement of $3(\mathcal{N} + 1)/2$ quadrature points. Without sufficient GLL points, an aliasing error can arise from this non-linear term (Ohlsson et al., 2011). To correct for this, $\lceil 3(\mathcal{N} + 1)/2 \rceil$ GLL points are used in each direction for the integration of the non-linear term, where $\lceil\,\rceil$ is the ceiling or round-up function. This is similar to 3/2-rule in pseudo-spectral methods (Ohlsson et al., 2011) and is consistent with other studies in the literature (Özgökmen et al., 2004, 2009b). Note, that the aliasing error leads to problems with stability and not accuracy (Özgökmen et al., 2004).

NEK5000 implements an iterative solver to approximate the solutions to the linearised equations equations. By suitable choice of an initial guess to compute the values at the $(n+1)$-th time-step the number of iterations can be greatly reduced and hence the computational time. A simple choice is to use the values at the previous time-step. However, this can be improved by considering a Taylor expansion backwards in time of a set number of time-steps and extrapolating to estimate the values at the current time-step. These extrapolation methods have been used extensively and further details are given by Hageman and Young (1981). Fischer (1998) developed an optimal implementation given a specific basis using a projection scheme with a reduced risk of a poor initial guess, which is implemented into NEK5000. The projection process starts after the 5th time-step and uses data from up to 20 (where available) previous time-steps to compute the initial guess used in the iterative solve. Solver tolerances are expressed in terms of residual error and set to 10^{-5} for the pressure solver and 10^{-7} for the Helmholtz solvers (velocity and scalar-transport equations). These tolerances were chosen to be as large as possible to minimise the computational time without affecting the solution.

4.2.2 Analysis tools

Residual potential energy and energy balance

Upon release, the potential energy stored in the initial distribution of fluid 2 is converted into kinetic energy as it is driven horizontally by the density difference. When the propagating waves reach the end walls at $x = -1$ and $x = 1$ they are driven vertically converting some of the kinetic energy back into potential energy. The potential energy is then converted back into kinetic energy as the density difference drives the flow back the other way. Without mixing or viscous dissipation this exchange between potential and kinetic energy would continue indefinitely. The total kinetic energy $KE(t)$ and potential energy $PE(t)$ are given functions of time (Winters et al., 1995):

$$KE(t) = \frac{1}{2}\int\limits_{\Omega}(u^2 + v^2 + w^2)\,\mathrm{d}V, \tag{4.27}$$

$$PE(t) = \int\limits_{\Omega}\frac{\phi}{Fr}y\,\mathrm{d}V = \int\limits_{\Omega}2\phi y\,\mathrm{d}V, \tag{4.28}$$

As a result of the Boussinesq approximation only the potential energy contains the excess density ϕ. Further, recall that the Froude number $Fr = 1/2$. The total energy of the system at time t therefore satisfies

$$KE(t) + PE(t) + D_v(t) = PE(0) = 1, \tag{4.29}$$

where $D_v(t)$ is the energy converted into heat by viscous dissipation. Thus, by calculating the kinetic energy KE and potential energy PE over time, the viscous dissipation can be obtained from

$$D_v(t) = 1 - PE(t) - KE(t). \tag{4.30}$$

The potential energy $PE(t)$ can be further decomposed into two components: residual potential energy (RPE) and available potential energy (APE). The residual potential energy $RPE(t)$ provides a measure for quantifying the mixing that occurs within a closed system (Winters et al., 1995). At fixed time t the RPE represents the minimum potential energy that can be obtained through adiabatic redistribution of the fluid within the domain, to a stratified state with the most dense fluid at the bottom and is no density variation across the length or width of the flow. RPE is monotonically (but not strictly) increasing over time and measures how much potential energy has been irreversibly lost to mixing. The available potential energy $APE(t) = PE(t) - RPE(t)$ is the maximum amount of potential energy that can be converted into kinetic energy $KE(t)$ (Lorenz, 1955). Thus the total in the system can be expressed

$$PE(0) = KE(t) + RPE(t) + APE(t) + D_v(t) \tag{4.31}$$

The dense phase concentration ϕ is equivalent to the excess density in the system (4.12-4.14) and is used to determine the RPE. Following the method of Tseng and Ferziger (2001), the first step is compute the density distribution function $P(\phi)$ for the concentration $\phi \in [0, 1]$. From the density distribution function, the height of fluid, of concentration ϕ in the minimum potential energy state $Y_r(\phi)$ is given by

$$Y_r(\phi) = \int\limits_{\phi}^{1} P(\tilde{\phi})\,\mathrm{d}\tilde{\phi}. \tag{4.32}$$

Given the depth of the concentration in the minimal energy state, the residual potential energy is then

$$RPE = 4\int\limits_{0}^{1} \phi Y_r(\phi)\mathrm{d}Y_r, \tag{4.33}$$

where the factor of four arises from the cross-sectional area of the domain in the x, z plane and the reciprocal Froude number $1/Fr = 2$. By definition, the height of the fluid, at concentration ϕ in the minimum potential energy state is monotonic function and so invertible. Thus, the residual potential energy RPE can be expressed

$$RPE = 4\int\limits_{0}^{1} \phi(Y_r)Y_r\mathrm{d}Y_r. \tag{4.34}$$

Given the discrete data obtained from the simulations, the probability density function $P(\phi)$ is approximated using the 'histcounts' function in MATLAB (MathWorks, 2018a). A total of N_{bins} equally spaced bins that form a partition of concentrations in the interval $[0,1]$ are created. The ith bin corresponds to concentrations $[(i-1)/N_{\text{bins}}, i/N_{\text{bins}}]$. The total number of nodes that have concentration within the i-th bin is denoted n_i, such that

$$n = \sum_{i=1}^{N_{\text{bins}}} n_i. \tag{4.35}$$

Thus, the thickness of each layer corresponding to the ith bin is $h_i = n_i/n$. The concentration is each cell is approximated by its mid-value $\phi_i = (i+1/2)/N_{\text{bins}}$. The height of the fluid in the ith cell is then approximated

$$Y_r(\phi_i) \approx Y_{ri} = \begin{cases} \frac{h_1}{2} & \text{if} \quad i = 1, \\ \frac{h_1}{2} + \sum_{l=2}^{i}\left(\frac{h_i + h_{i-1}}{2}\right) & \text{if} \quad i > 1. \end{cases} \tag{4.36}$$

Thus, the residual potential energy can be approximated

$$RPE = 4\int\limits_{0}^{1} \phi(Y_r)Y_r\,\mathrm{d}Y_r \approx 4\sum_{i=1}^{N_{\text{bins}}} h_i\phi_i Y_{ri} \tag{4.37}$$

The values of RPE over time are computed in intervals of 0.5 dimensionless time and normalised by the initial state $RPE(0)$. The completely mixed state, where $\phi = 1/2$ throughout the entire domain, corresponds to

$$RPE_{\max} = 4 \int_0^1 \frac{Y_r}{2} \, \mathrm{d}Y_r = 1. \tag{4.38}$$

The normalised residual potential energy $NRPE(t)$ is defined

$$NRPE(t) = \frac{RPE(t) - RPE(0)}{RPE_{\max} - RPE(0)} \tag{4.39}$$

This is distinct from the definition of Winters et al. (1995) who instead define

$$NRPE(t) = \frac{RPE(t) - RPE(0)}{RPE(0)}. \tag{4.40}$$

However, as $2RPE(0) \approx RPE_{\max}$ in our setup both methods give similar results, but the definition (4.39) takes values between 0 and 1. The fully mixed stated, i.e. $\phi = 1/2$ everywhere, yields $NRPE(t) = 1$. The normalised residual potential energy $NRPE$ will be used to classify the amount of mixing that occurs in the flow over time.

Mixing volume fraction

A second measure based on the volume fraction of the fluid that has been mixed is also used to measure the mixing in the flow. For a parameter β_v, the volume fraction in the domain that is within concentration $[\beta_v, 1 - \beta_v]$ is

$$\theta(t; \beta_v) = \frac{1}{2} \int_{\Omega} \mathcal{F}(\phi; \beta_v) \, \mathrm{d}V, \tag{4.41}$$

where $\mathcal{F}(\phi; \beta_v)$ is the box filter function defined as

$$\mathcal{F}(\phi; \beta_v) = \begin{cases} 1 & \text{if} \quad \phi \in [\beta_v, 1 - \beta_v], \\ 0 & \quad \text{otherwise}. \end{cases} \tag{4.42}$$

This method is similar to that of Bonometti and Balachandar (2008). However, they normalised the integral by a volume based on the depth H and the distance the protruding fronts have travelled. In our case, as the flow reaches the end walls at

$x = -1$ and $x = 1$ within a fraction of the total integral time T_{int}, the total volume

$$\int_{\Omega} \mathrm{d}V = 2 \tag{4.43}$$

is used instead. The parameter β_v is set to 0.01 throughout. Similarly to the residual potential energy, the mixing volume fraction $\theta(t)$ is scaled using its initial and maximum, $\theta_{\max} = 1$, value

$$N\theta(t) = \frac{\theta(t) - \theta(0)}{\theta_{\max} - \theta(0)} \tag{4.44}$$

Thus the values $N\theta(t) = 0$ and $N\theta(t) = 1$ correspond respectively to no mixing of the initial state and to mixing having occurred everywhere (i.e. $\phi \in [\beta, 1-\beta]\, \forall (x, y, z) \in \Omega$). The statistics $N\theta$ and normalised residual potential energy $NRPE$ provide two different methods for computing the amount of mixing that has occurred in the flow. For sharp initial conditions $N\theta(t) \geq NRPE(t)$, with equality only if $\phi(x, y, z, t) \in \{0, 0.5, 1\}\, \forall (x, y, z) \in \Omega$. Note that as a result of the linear concentration gradient over a region of thickness $2\zeta_0 = 0.01$ it is possible for $N\theta(t) < NRPE(t)$. However, the difference would be close to zero.

Normalised mixing volume $N\theta$ provides a more global picture of the mixing, whereas, $NRPE$ includes effects from local mixing across concentration gradients. For example, if a small amount of diffusion occurs and convection redistributes changes in concentration ϕ over the domain, so that a relatively sharp transition is maintained, but most regions of the flow have concentration $\phi \in [\beta, 1-\beta]$. Then $N\theta$ will increase rapidly compared to $NRPE$. Conversely, if the interface itself is smoothed, but the majority of the flow has concentration $\phi \notin [\beta, 1-\beta]$. Then $NRPE$ will increase at a rate similar to $N\theta$. Thus distinctions between the rates that $N\theta$ and $NRPE$ increase can be used to indicate the relative importance of local mixing near the interface.

Diffusive contribution to mixing

Diffusion of the concentration will lead to a slow rate of mixing in the fluid at a rate that depends on the inverse of the Peclet number $1/Pe$ or, since $Pe = ReSc$, Schmidt number Sc. In the limit $Sc \to \infty$ no mixing occurs as the fluids are immiscible. However, as discussed earlier large Schmidt numbers require increased computational resources to accurately resolve the solution. Given the initial conditions used for the lock-exchange problem (4.17), a lower bound of pure diffusive mixing can be obtained from the system of equations (4.12–4.14) with $\mathbf{u} = \mathbf{0}$ everywhere. This reduces to the diffusion equation

$$\frac{\partial \phi}{\partial t} = \frac{1}{Re_1 Sc} \nabla^2 \phi. \tag{4.45}$$

Instead of considering the full three-dimensional solution to the diffusion equation, a reduced one-dimensional (in the x-direction) problem is considered with the following initial conditions

$$\phi(x, y, z, 0) = \phi_0(x) = \begin{cases} 1 & \text{if} \quad x \in [-\infty, -\zeta_0], \\ \frac{1}{2\zeta_0}(\zeta_0 - x) & \text{if} \quad x \in [-\zeta_0, \zeta_0], \\ 0 & \text{if} \quad x \in [\zeta_0, \infty], \end{cases} \tag{4.46}$$

where $2\zeta_0 = 0.01$ as before and the flow boundaries at $x = \pm 1$ are replaced by boundaries at infinity. This removes the slight variation in the z direction and reduces the problem to solving a one-dimensional diffusion equation

$$\frac{\partial \phi}{\partial t} = \frac{1}{Re_1 Sc} \frac{\partial^2 \phi}{\partial x^2}. \tag{4.47}$$

for each fixed y and z. Further, using an infinite domain removes negligible contribution from the boundary conditions and enables the general solution to be expressed as

$$\phi(x, t) = \int_{-\infty}^{\infty} S\,(x - y, t)\, \phi_0(y)\, \mathrm{d}y, \tag{4.48}$$

$$= \int_{-\infty}^{-\zeta_0} S\,(x - y, t)\ \mathrm{d}y + \int_{-\zeta_0}^{\zeta_0} S\,(x - y, t)\, \frac{\zeta_0 - y}{2\zeta_0}\, \mathrm{d}y, \tag{4.49}$$

where

$$S\,(x, t) = \sqrt{\frac{Re_1 Sc}{4\pi t}} \exp\left(-\frac{Re_1 Sc x^2}{4t}\right) \tag{4.50}$$

(Evans, 2010). These integrals were solved numerically in MATLAB (MathWorks, 2018a) on a spatial grid containing 3000 points at time intervals of $t = 0.5$ up to the total integration time $T_{\text{int}} = 13.5$. The lower limit of the first integral was replaces with -10^4. These choices of spatial resolution and lower limit were checked for convergence. The concentration profile subject to diffusion at the total integration time $T_{\text{int}} = 13.5$ with $Pe = 1/(Re_1 Sc) = 7000$ is presented in figure 4.6. Noticeable diffusion can be observed, but localised around $x = 0$.

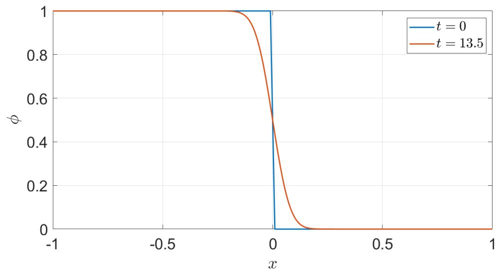

Figure 4.6: Concentration profiles ϕ for a one-dimensional pure diffusion problem at $t = 0$ and $t = 13.5$. The Péclet number Pe is fixed at 7000.

With this profile, the three-dimension equivalent can be reconstructed based on the initial conditions without z variation (4.46). Pseudo-colour plots are presented in figure 4.7 at $t = 0$ and $t = 13.5$ demonstrating the change in concentration profiles arising from pure diffusion in the (x, z)-plane, in which deep red corresponding to fluid 2 ($\phi = 1$) and deep blue corresponding to fluid 1 ($\phi = 0$). Further, the change in $NRPE$ and $N\theta$ over time is displayed in figure 4.8. An approximately linear increase in $NRPE$ over time can be observed, whereas $N\theta$ increases proportionally to $\sqrt{t}$, as locally the solution is self-similar with $\xi_0 = x/\sqrt{t}$, has a decreasing gradient as the interface grows diffusively.

By assuming no variation in the z direction, the initial surface area of the region of the flow where $\phi(x, y, z, 0) = 0.5$ is reduced and the amount of mixing is underestimated. However, the surface area ratio ψ_0 between the curved initial conditions and the $x = 0$ plane is the same as the ratio of arc lengths or sinuosity of the z-variation

$$\psi_0 = \frac{\int_0^1 \sqrt{1 + \eta'^2}\, \mathrm{d}z}{\int_0^1 \mathrm{d}z}, \tag{4.51}$$

where $\eta' = \mathrm{d}\eta/\mathrm{d}z = 0.1\cos(2\pi z)$. This integral can be reduced to a complete elliptic integral of the second kind, to which no closed form solution exists (Carlson, 1995). However, numerical approximations can be obtained, again using MATLAB (MathWorks, 2018a), providing $\psi_0 \approx 1.024$. Thus the error for neglecting the z-variation of the initial conditions is negligible. Further, the initial values of residual

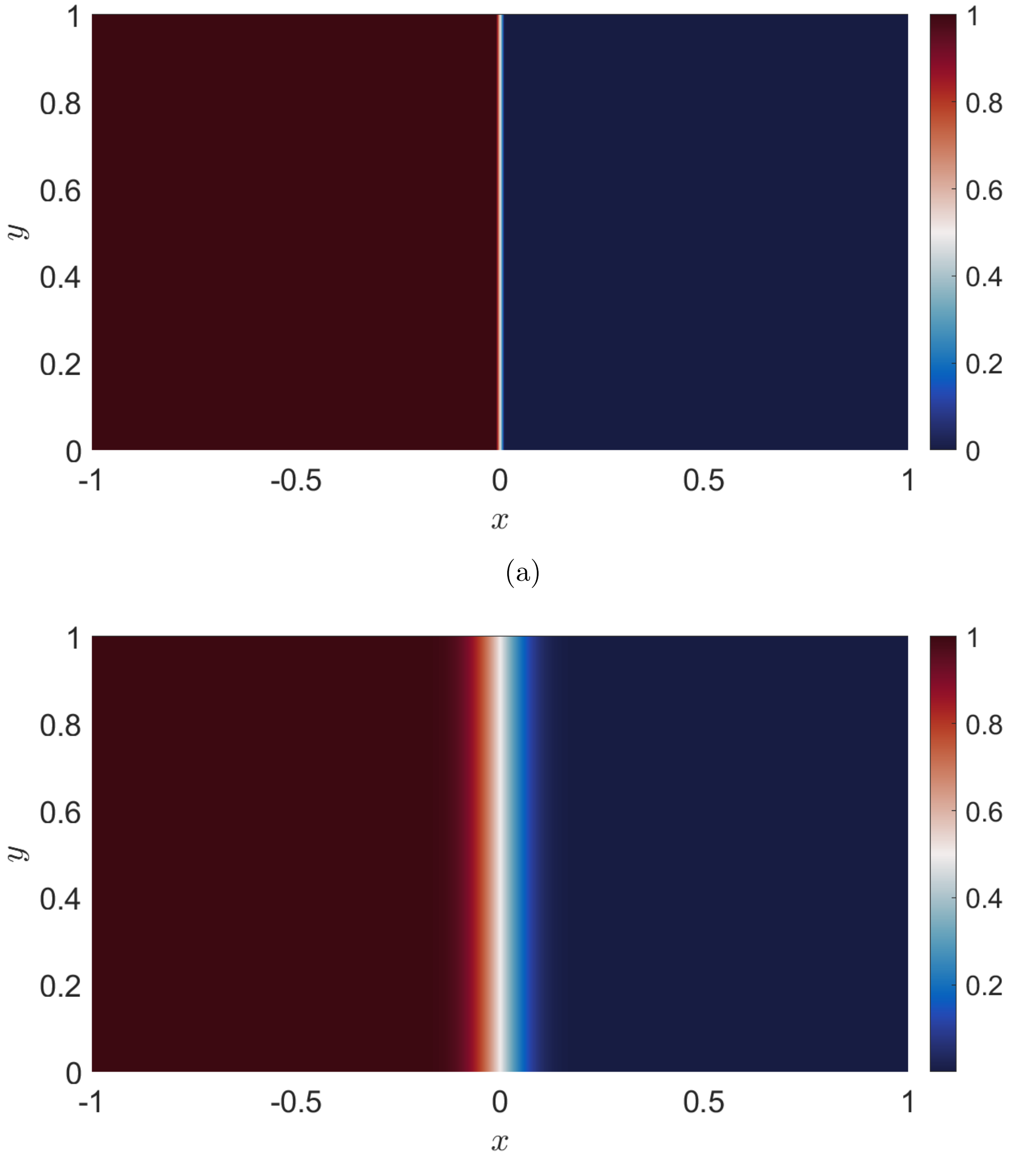

(a)

(b)

Figure 4.7: Distribution of concentration ϕ in the (x, y)-plane at $t = 0$ (a) and $t = 13.5$ (b) for the pure diffusion problem.

potential energy $RPE(0)$ and $\theta(0)$ can be expressed in terms of ψ_0

$$RPE(0) = \int\limits_{0}^{1/2-0.005\psi_0} y\,\mathrm{d}y + \int\limits_{1/2-0.005\psi_0}^{1/2+0.005\psi_0} \frac{1}{0.01\psi_0}\left(1 + 0.005\psi_0 - y\right) y\,\mathrm{d}y \approx 0.5002, \tag{4.52}$$

$$\theta(0) = 0.0098\psi_0 \approx 0.01004. \tag{4.53}$$

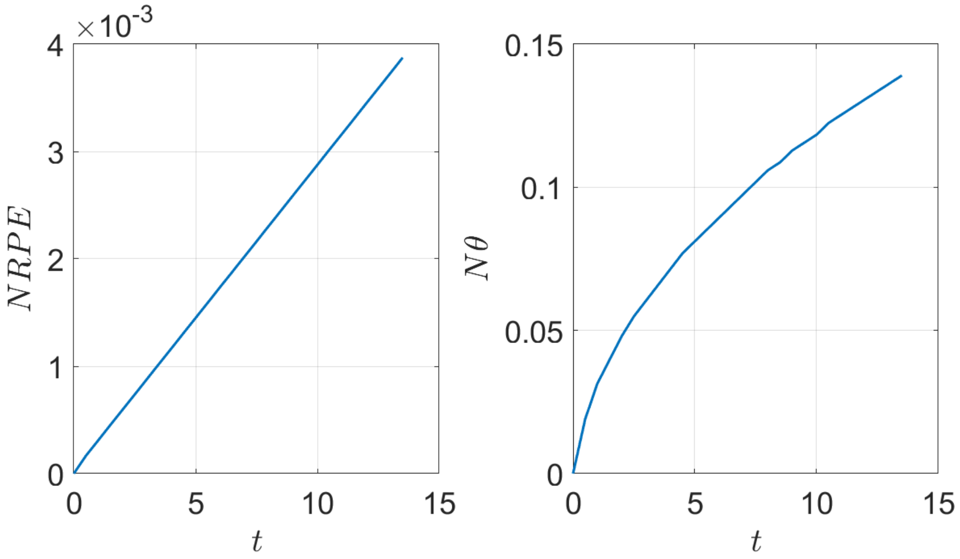

Figure 4.8: Normalised residual potential energy ($NRPE$, left) and Normalised θ ($N\theta$, right) over time for the pure diffusion problem.

Free surface and depth averaged properties

As mixing and diffusion occur within the flow, the interface between the two fluids becomes blurred over time. An approximate position of it can be defined in multiple ways. The first method used is the depth integration of the concentration

$$h_{\text{int}}(x,z,t) = \int_0^1 \phi(x,y,z,t)\,\mathrm{d}y. \tag{4.54}$$

This produces a single depth of the fluid at each point in the (x,z)-plane. An alternative is to define the interface, where the concentration is 0.5. However, this leads to a multi-valued function. For example if eddies that result from a Kelvin-Helmholtz instability lead to fluid fluid overturning. The depth integration of concentration can be averaged over the cross-stream (z-direction) as well to produce an averaged depth along the horizontal extent of the domain

$$\bar{h}_{\text{int}}(x,t) = \int_0^1 h_{\text{int}}(x,z,t)\,\mathrm{d}z. \tag{4.55}$$

Further alternatives that avoid multi-valued functions can be used by taking the maximum or minimum y-value for which $\phi = 0.5$

$$h_{\max}(x,z,t) = \sup\{y \in [0,1] \,|\, \phi(x,y,z,t) \geq 0.5\}, \tag{4.56}$$

$$h_{\min}(x,z,t) = \inf\{y \in [0,1] \,|\, \phi(x,y,z,t) \leq 0.5\}. \tag{4.57}$$

These too can be computed based on cross-stream-averaged data

$$\bar{h}_{\max}(x,t) = \sup\left\{ y \in [0,1] \,\middle|\, \int_0^1 \phi(x,y,z,t)\,\mathrm{d}z \geq 0.5 \right\}, \tag{4.58}$$

$$\bar{h}_{\min}(x,t) = \inf\left\{ y \in [0,1] \,\middle|\, \int_0^1 \phi(x,y,z,t)\,\mathrm{d}z \leq 0.5 \right\}. \tag{4.59}$$

In regions where the flow overturns the depths based of the extremal values $h_{\min}$ and $h_{\max}$ can result in large differences. Further, the maximum value may include regions of the flow with zero, or close to, concentration which corresponds to fluid 1. Thus, the average of these two $h_{\text{ave}}(x,z,t)$ will also be considered

$$h_{\text{ave}}(x,z,t) = \frac{h_{\max}(x,z,t) + h_{\min}(x,z,t)}{2}. \tag{4.60}$$

In regions of the flow without overturning $h_{\min}$ and $h_{\max}$ produce the same result. With the corresponding definition of the free surface, the depth-averaged velocity of fluid 2 is defined as

$$\mathbf{u}_f(x,z,t) = \frac{1}{h_f} \int_0^{h_f} \phi(x,y,z,t)\mathbf{u}(x,y,z,t)\,\mathrm{d}y, \tag{4.61}$$

$$\bar{\mathbf{u}}_f(x,t) = \frac{1}{h_f} \int_0^{h_f} \int_0^1 \phi(x,y,z,t)\mathbf{u}(x,y,z,t)\,\mathrm{d}z\mathrm{d}y, \tag{4.62}$$

where $f \in \{\max, \min, \text{ave}\}$ or

$$\mathbf{u}_{\text{int}}(x,z,t) = \frac{1}{h_{\text{int}}} \int_0^{1} \phi(x,y,z,t)\mathbf{u}(x,y,z,t)\,\mathrm{d}y, \tag{4.63}$$

$$\bar{\mathbf{u}}_{\text{int}}(x,t) = \frac{1}{h_{\text{int}}} \int_0^{1} \int_0^1 \phi(x,y,z,t)\mathbf{u}(x,y,z,t)\,\mathrm{d}z\mathrm{d}y, \tag{4.64}$$

4.2.3 Resolution

Five meshes, labelled A, B, C, D, and E are used to perform a grid (or mesh) independence study. Mesh independence studies are used to demonstrate that the solution to a numerical computational does not depend on the grid sized used for the mesh (Klein, 1999). The total number of nodes in the mesh n, and other mesh statistics, are presented in table 4.3. The number of elements in each spatial direction (N_x, N_y, N_z) are chosen to provide equal resolution in each spatial dimension, i.e. $N_x = 2N_y = 2N_z$. The number of GLL points $\mathcal{N}$ is chosen to be within the optimal range of 7 to 15 (Patera, 1984). Each simulation is conducted with a Courant number $Cr = 0.1$ in our resolution study. The corresponding computation cost in terms of core hours (simulation time times the number of cores used) and the total number of cores used for each simulation is presented in table 4.4. All simulations were conducted on the ARC3, part of the High Performance Computing facilities at the University of Leeds, UK. Each compute node consisted of 24 Broadwell E5-2650v4 CPUs with a base frequency of 2.2 GHz. Note that the variable viscosity cases take significantly longer even when the viscosities are similar ($\gamma = 0.1$, for example) because the full discretisation of the stress tensor is required.

Table 4.3: Characteristics of the meshes presented in this chapter. The number of elements in each spatial direction (x, y, z) is (N_x, N_y, N_z). The total number of elements in the domain is $\mathcal{E} = N_x N_y N_z$. Each element contains $\mathcal{N}$ GLL points in each spatial direction giving the total number of nodes $n = \mathcal{E}\mathcal{N}^3$.

Mesh	N_x	N_y	N_z	E	$\mathcal{N}$	n
A	32	16	16	8192	8	4194304
B	48	24	24	27648	9	20155392
C	60	30	30	54000	9	39366000
D	72	36	36	93312	9	68024448
E	84	42	42	148176	9	108020304

Table 4.4: Computational time in core hours (number of computational cores times the clock time) for each case and mesh. The number of cores used for each simulation is shown in brackets. Dashed indicate that a lower resolution mesh was deemed sufficiently resolved and hence not conducted.

Mesh	$\gamma = 0$	$\gamma = 0.1$	$\gamma = 1$	$\gamma = 10$
A	213 (48)	424 (48)	394 (48)	463 (48)
B	2361 (96)	4303 (120)	3999 (120)	3592 (120)
C	5890 (192)	14244 (216)	10700 (216)	9118 (216)
D	-	-	-	20152 (432)
E	-	-	-	37828 (480)

To reduce the physical memory restraints of saving the results from each simulations, the data at each node n is exported every 0.5 dimensionless time units. The mixing and energy variables introduced in section 4.2.2 are interpolated between these points using a piece-wise cubic spline that matches the values and gradients at the known time steps. This creates a smoothed fit for the variables in between the known values at 0.5 intervals.

In figure 4.9 the normalised residual potential energy $NRPE$ is plotted each case and each mesh used. For $\gamma = 0$ and $\gamma = 0.1$ similar results are obtained for all the meshes considered indicating that the meshes are sufficiently resolved. As the viscosity difference between the layers increases ($\gamma = 1$ and $\gamma = 10$), higher resolution is required to produce a mesh-independent solution. In particular, the $NRPE$ on mesh B is not sufficient for $\gamma = 1$, as it deviates after approximately $t = 9$. A distinct difference between the $NRPE$ for all four meshes for $\gamma = 10$ can be observed. A higher resolution mesh would be required for $\gamma = 10$ to confirm that the mesh E, $\gamma = 10$ solution is sufficiently resolved. However, this was not possible given the computational resources available and thus mesh E will be used assuming that it is sufficiently resolved. Further, mesh D will be used for cases $\gamma = 2$ and $\gamma = 4$.

In addition to $NRPE$, $N\theta$ for $\gamma = 0$ and $\gamma = 10$ with their corresponding meshes is plotted against time in figure 4.10. Finally, the distributions of potential energy PE, kinetic energy KE, available potential energy APE and dissipated energy D_v for $\gamma = 10$ are displayed in figure 4.11. Apart for the solutions obtained using mesh A, all the results for $N\theta$ and the energy distributions are nearly coincident. The agreement between meshes appears better for the energy distributions when compared to $NRPE$, but arises because the total variation is smaller for $NRPE$. Finally, for $\gamma = 0$ on mesh C, normalised residual potential energy $NRPE$ and normalised theta $N\theta$ are plotted for three different Courant numbers Cr (0.5, 0.25, 0.1) in figure 4.12. Decreasing the Courant number decreases the time-step used and similarly to decreasing the spatial resolution, both $NRPE$ and $N\theta$ produce similar result for $Cr = 0.1$ and $Cr = 0.25$. Although the $NRPE$ is not coincident for $Cr = 0.1$ and $Cr = 0.25$ it is for the remaining energy distributions, figure 4.13. Thus, a Courant number of 0.1 is deemed to be sufficient for all simulations.

4.3 Results and discussion

In this section the results from all cases are reported on the mesh with the highest resolution used in the mesh independence study. I.e., mesh C for $\gamma = 0$, $\gamma = 0.1$,

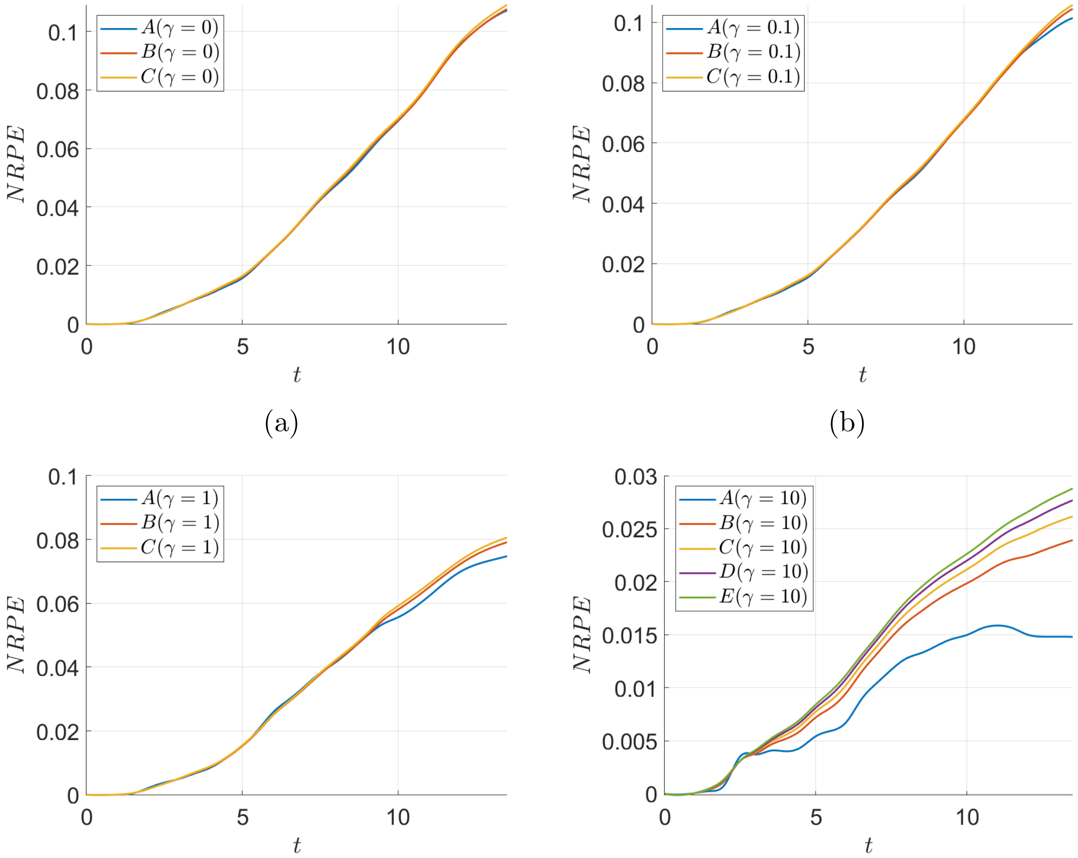

(a) (b)

(c) (d)

Figure 4.9: Normalised residual potential energy $NRPE$ against time for different meshes: (a) - $\gamma = 0$, (b) - $\gamma = 0.1$, (c) - $\gamma = 1$, and (d) - $\gamma = 10$

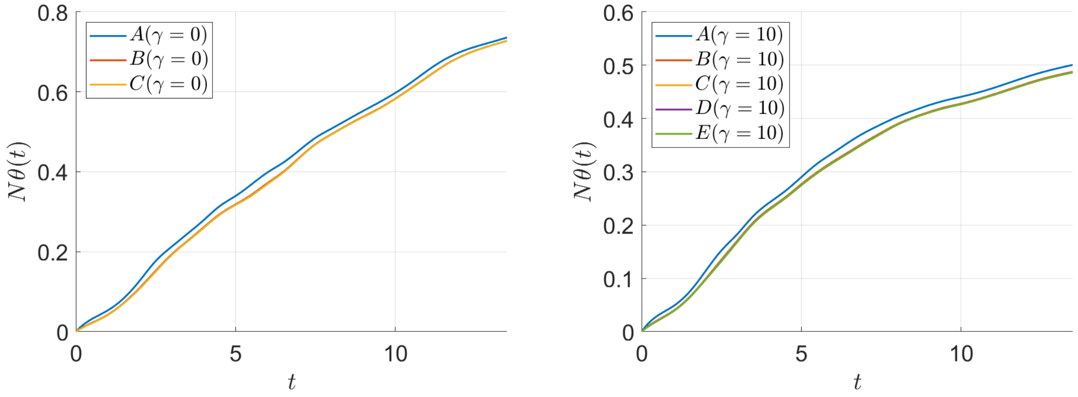

(a) (b)

Figure 4.10: Normalised volume fraction of mixed fluid $N\theta(t)$ against time for the four meshes A, B, C and D. The curves for B and C for $\gamma = 0$ and B, C, and D for $\gamma = 10$ are coincident.

$\gamma = 1$ and E for $\gamma = 10$. Mesh D is used for cases $\gamma = 2$ and $\gamma = 4$. Further, every simulation is conducted with a Courant number of 0.1.

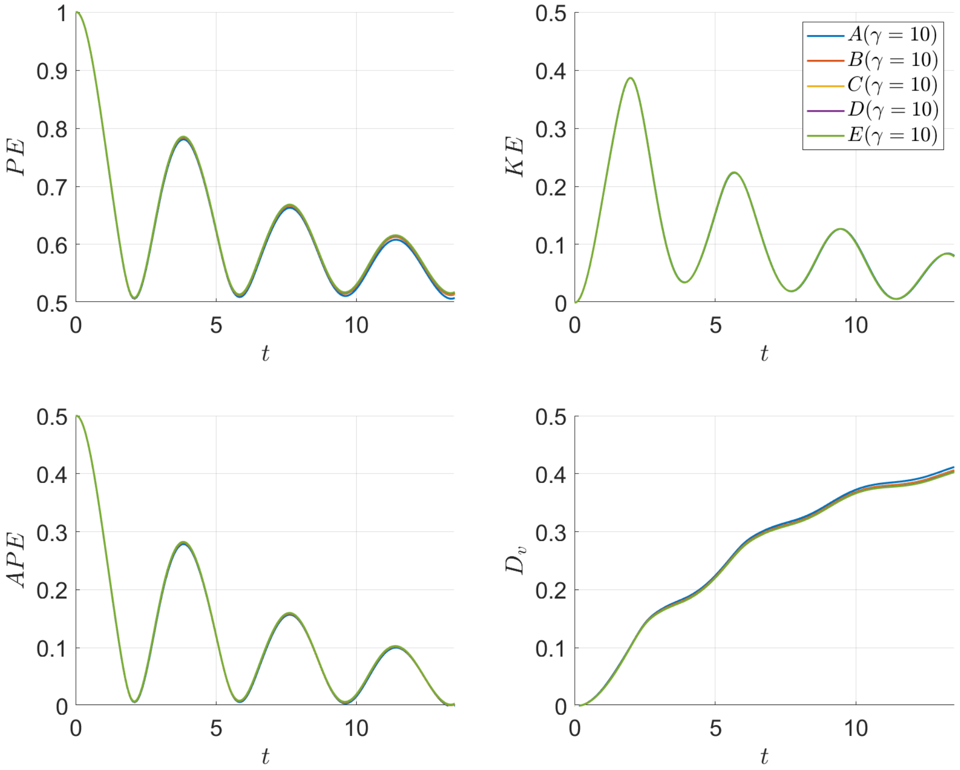

Figure 4.11: Potential energy PE, Kinetic energy KE, Available potential energy APE and dissipated energy D for $\gamma = 10$ simulations with the meshes used. The curves for B, C, D and E are coincident.

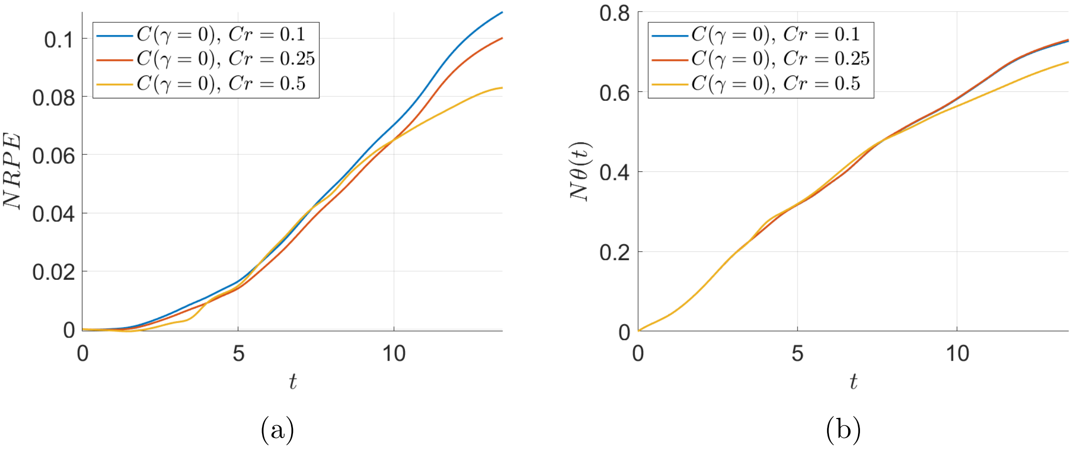

Figure 4.12: Normalised residual potential energy $NRPE$ (a) and Normalised volume fraction of mixed fluid $N\theta$ (b) against time for mesh C and $\gamma = 0$ simulations at different Courant numbers

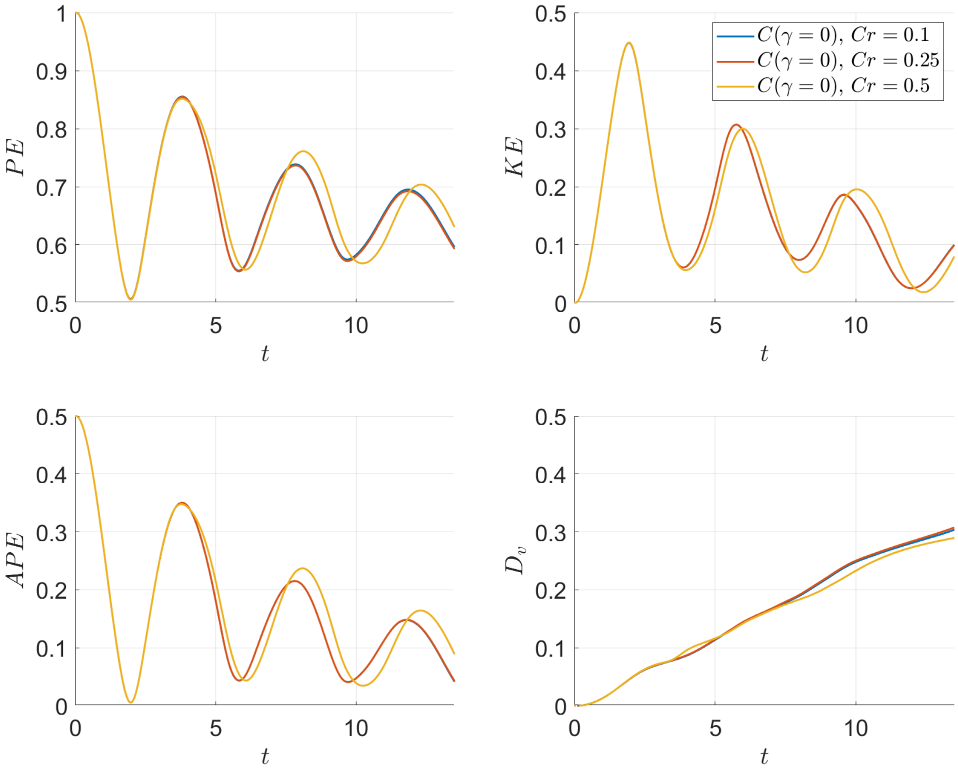

Figure 4.13: Potential energy PE, Kinetic energy KE, Available potential energy APE and dissipated energy D_v for $\gamma = 0$ on mesh C with Courant numbers of 0.1, 0.25 and 0.5.

4.3.1 Visualisations

Pseudo-colour plots of fluid 2 concentration ϕ on the centre-plane $z = 1/2$ at 0.5 time intervals are displayed in figure 4.14 for the case of equal viscosity, i.e. $\gamma = 0$. The concentration ϕ is used to colour the plane with $\phi = 1$ corresponding to a deep red and $\phi = 0$ corresponding to deep blue. Intermediate values are coloured from red to white to blue as concentration decreases, thus highlighting regions of the flow that have mixed. Over the first few times steps a symmetric profile of concentration can be observed as the density difference drives fluid 2 to the right and fluid 1 to the left. Just before the wave fronts hit the side walls at $x = -1$ and $x = 1$, Kelvin-Helmholtz-like rolls start to form behind the propagating wavefronts. These rolls are absorbed into the wavefronts as they travel back towards the centre. The rolls start to diffuse into the surrounding fluid becoming less clearly defined by the time the two wave fronts intersect in the middle, at $t = 4$. After this, a large mixed region can be observed behind each wavefront. After $t = 8.5$ a clearly defined wavefront can no longer be seen because of the increase is mixing and dissipation within the flow. Towards the end of the simulation only a thin region near $y = 0$

and $y = 1$ remains completely unmixed. The symmetry of the flow is maintained throughout. This is to be expected due to the equal viscosities of the two fluids, but its preservation demonstrates that the simulation is properly resolved.

At nine different time-steps pseudo-colour plots of concentration are presented for $\gamma = 0$, $\gamma = 1$ and $\gamma = 10$ in figure 4.15. At $t = 1$ the flows appear similarly, but by $t = 2$, the increasing viscosity in the base layer inhibits the formation of the Kelvin-Helmholtz rolls that start to form. The intermediate viscosity ($\gamma = 1$) produces Kelvin-Helmholtz rolls, but less fluid is exchanged between the bulk of each layer. Asymmetry in the flow is clearly observed at later times for $\gamma = 1$ and $\gamma = 10$ at $t = 3$. The Kelvin-Helmholtz roll entrains more fluid in $x > 0$ than the corresponding roll in $x < 0$ for $\gamma = 1$. The returning wavefront in $x < 0$ for $\gamma = 10$ appears in a similar shape to $\gamma = 0$ and $\gamma = 10$ without the Kelvin-Helmholtz roll, but a constant gradient is observed in $x > 0$, which has increased mixing across the fluid interface. At $t = 5$ significantly more of fluid 2 is entrained by the right-travelling head of fluid 1 for $\gamma = 1$ when compared to $\gamma = 0$. Although, less actual mixing appears to occur. As the simulation time increases towards $t = 13.5$, significantly more unmixed regions can be observed as the viscosity of fluid 2 increases. Further, the sloshing speed appears to be affected by the viscosity with $\gamma = 1$ having significantly more fluid 2 in $x > 0$ when compared to the other two cases. The effect of viscosity on the mixing and sloshing speed will be characterised later in this section.

In order to visualise the full three-dimensional variation in the concentration ϕ, isosurface plots are displayed for $\gamma = 0$ and $\gamma = 10$ in figure 4.16 at different time steps. Isosurfaces represent surfaces of constant concentration ($\phi = 0.05, 0.25, 0.5, 0.75, 0.95$ for these cases) and are a natural extension to two-dimensional contour plots. Each of the five surfaces is coloured from blue to green to red with increasing fluid 2 concentration. The Kelvin-Helmholtz rolls observed in $\gamma = 0$ propagate over the cross-stream (z-direction) of the flow. However, after the reflected wavefronts cross at $t = 5.5$ the flow starts to become more chaotic, figure 4.17. The cross-stream variation of the extreme isosurfaces ($\phi = 0.05$ and $\phi = 0.95$) extends over much of the domain by $t = 9.5$ for $\gamma = 0$. In contrast $\gamma = 10$ shows only slightly cross-stream variation all the way through to $t = 9.5$ signifying the effect of increasing viscosity on the flow. However, from $t = 2.5$ onwards, the variation in the flow across $\phi = 0.5$ is apparent with the formation of a smaller Kelvin-Helmholtz roll only in fluid 1.

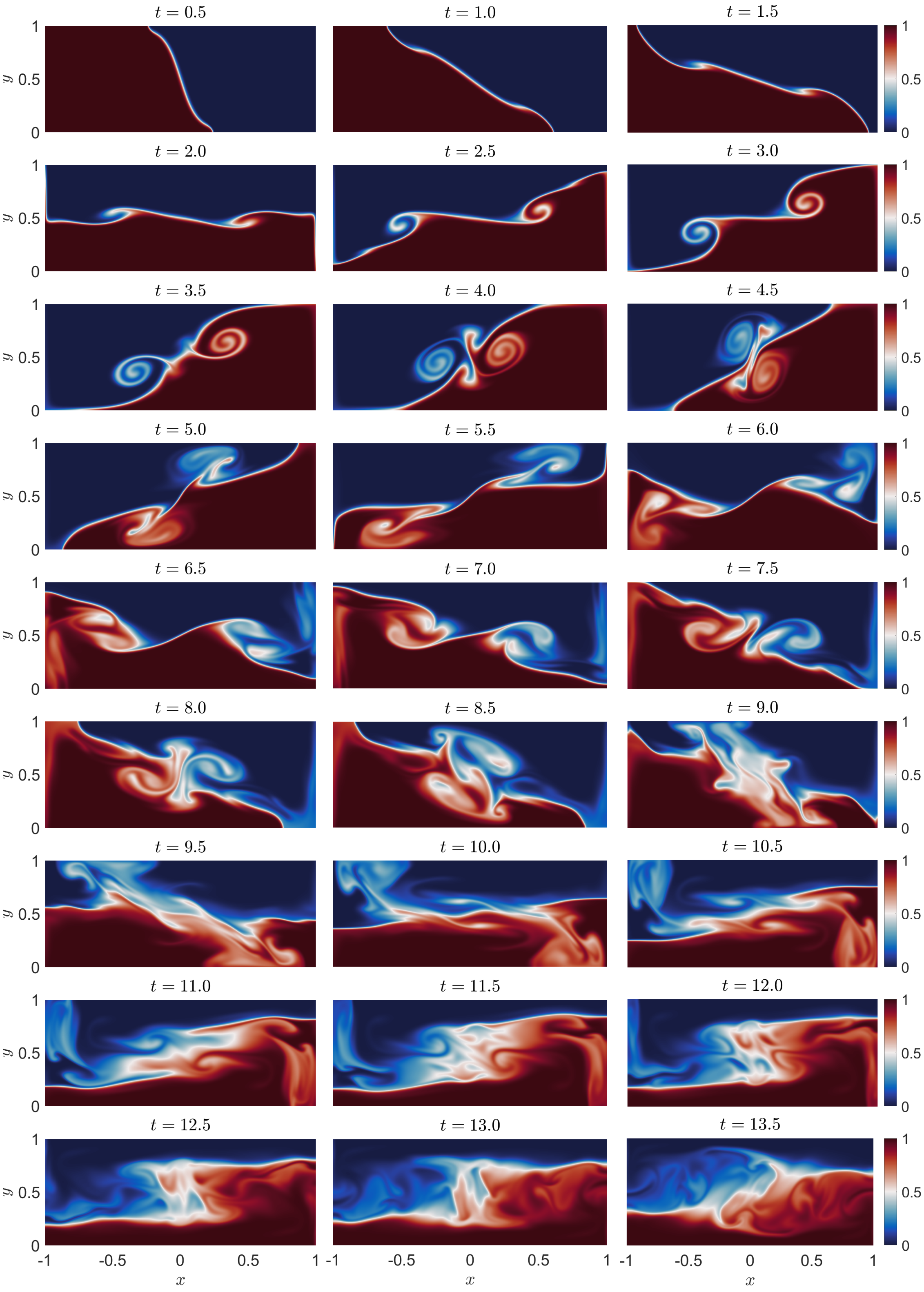

Figure 4.14: Pseudo-colour plots of concentration ϕ on the centre plane $z = 1/2$ over $t = 0.5$ time steps for the $\gamma = 0$ ($Re_1 = Re_2 = 1000$). Deep red corresponds to the denser fluid 2 and deep blue corresponds to fluid 1.

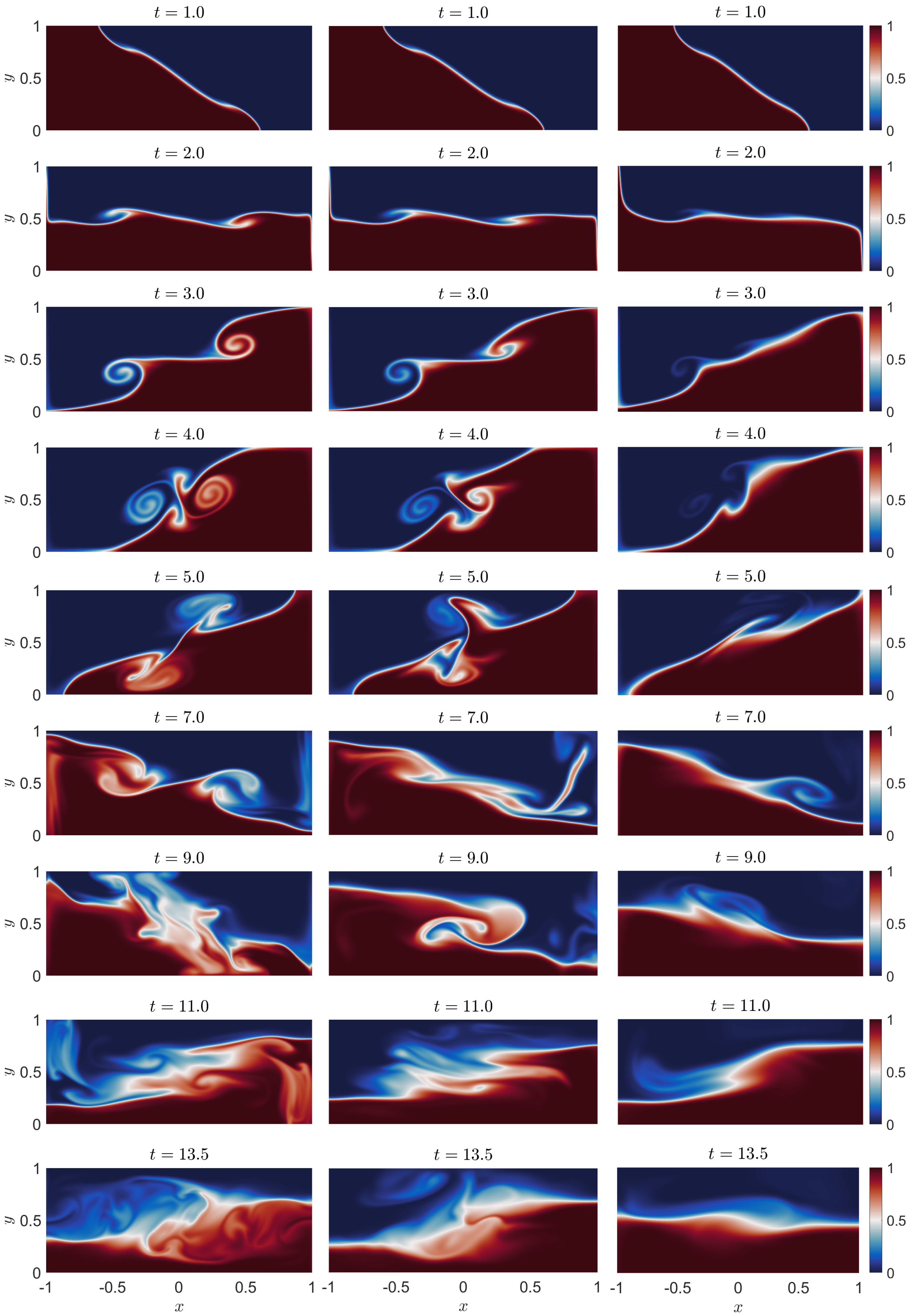

Figure 4.15: Pseudo-colour plots of concentration ϕ on the centre plane $z = 1/2$ for three different cases: $\gamma = 0$ (left), $\gamma = 1$ (middle) and $\gamma = 10$ (right). These correspond to layer two Reynolds numbers $Re_2 = (1000, 500, 91)$, respectively. Deep red corresponds to the denser fluid 2 and deep blue corresponds to fluid 1.

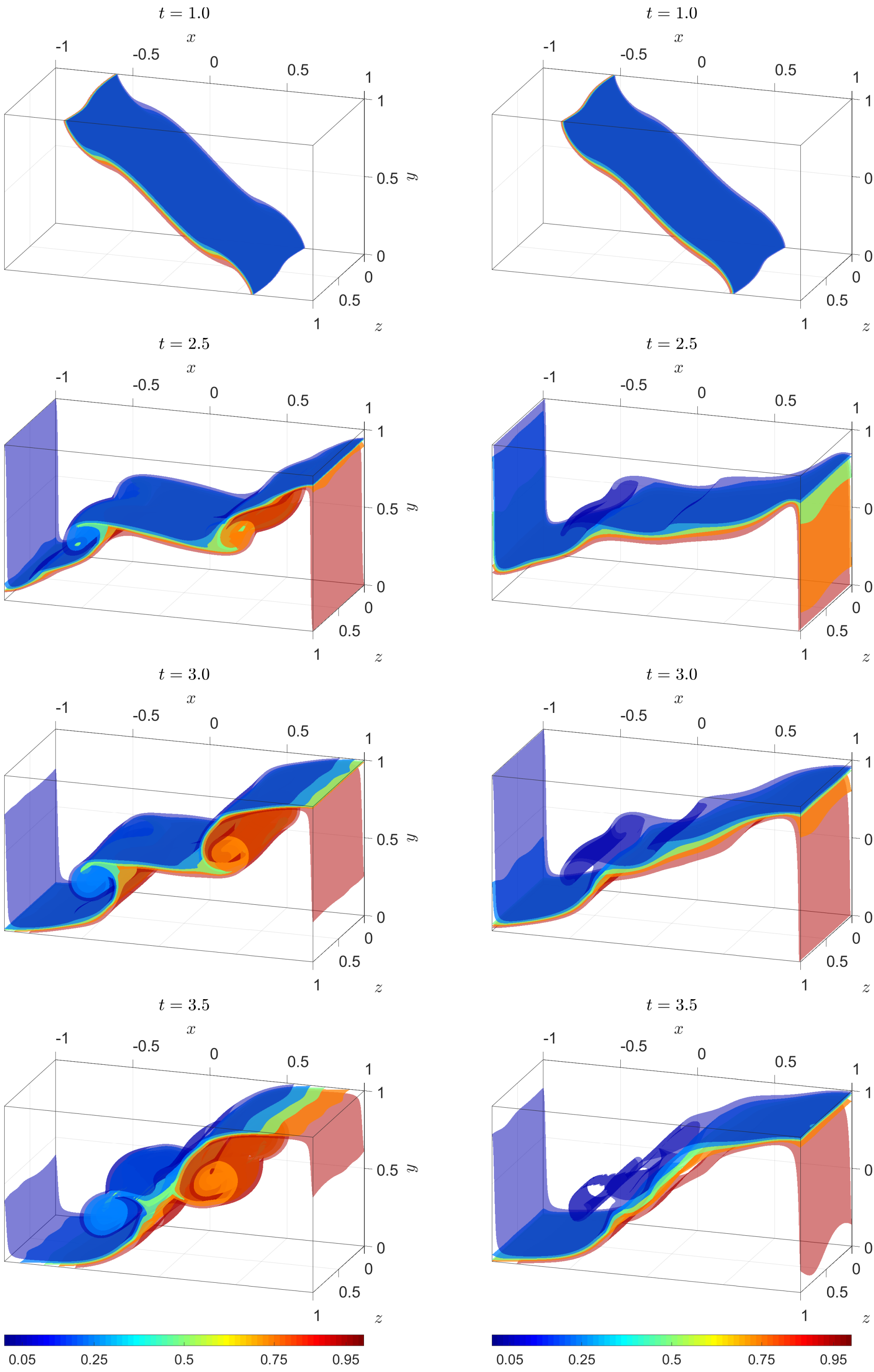

Figure 4.16: Isosurface plots of concentration ϕ for $\gamma = 0$ (left) and $\gamma = 10$ (right). Each coloured surface corresponds to concentrations $\phi = (0.05, 0.25, 0.5, 0.75, 0.95)$ ranging from deep blue ($\phi = 0.05$) to deep red $\phi = 0.95$.

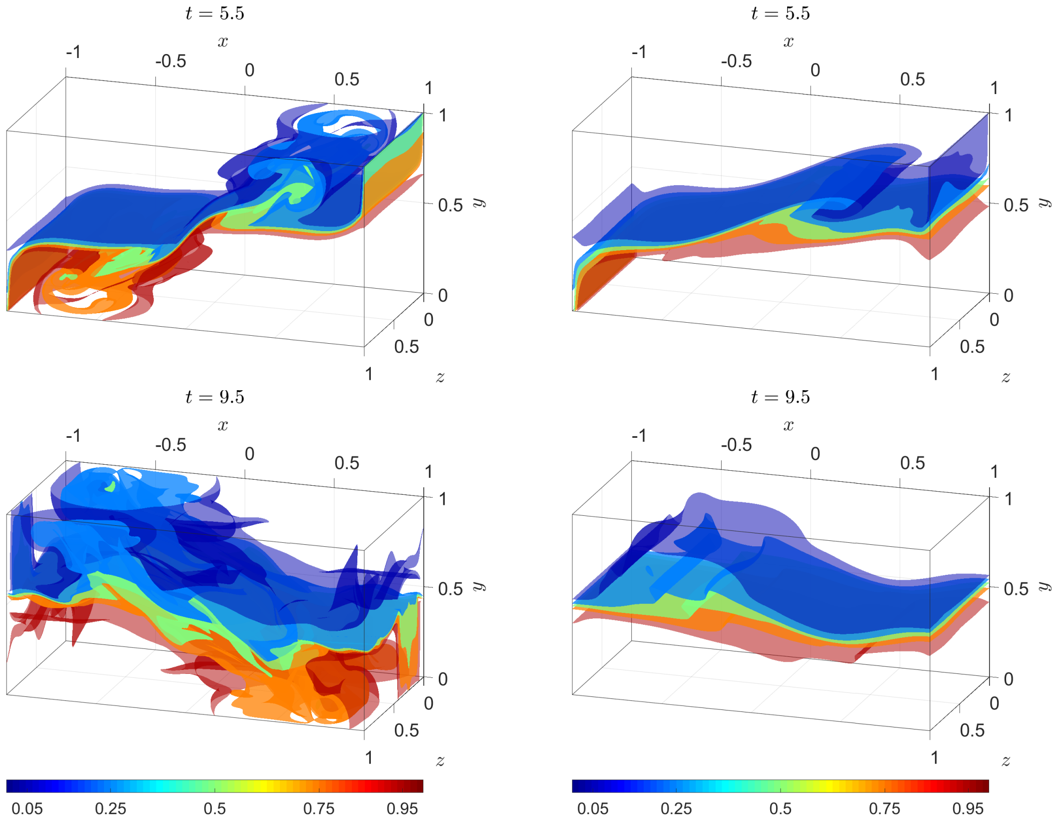

Figure 4.17: Isosurface plots of concentration ϕ for $\gamma = 0$ (left) and $\gamma = 10$ (right). Each coloured surface corresponds to concentrations $\phi = (0.05, 0.25, 0.5, 0.75, 0.95)$ ranging from deep blue ($\phi = 0.05$) to deep red $\phi = 0.95$.

4.3.2 Depth averaging

In this section the different ways of defining the depth of the flow discussed in section 4.2.2 are compared to the DNS results. For data on the centre plane $z = 1/2$, $h_{\text{int}}(x, z, t)$, $h_{\text{max}}(x, z, t)$ $h_{\text{min}}(x, z, t)$ and $h_{\text{ave}}(x, z, t)$ are overlaid onto pseudo-colour plots of concentration for $\gamma = 0$ and $\gamma = 10$, figure 4.18. The increased viscosity of $\gamma = 10$ inhibits the free surface deformation and therefore the depth of the flows defined with the four defined depths all producing similar results. During the later stages of the flow, when the interface starts to diffuse, h_{int} deviates away from h_{min}, h_{max} and h_{ave}. This arises because h_{int} considers contributions from concentrations $\phi < 0.5$ that are spread over the entire depth. However, in $\gamma = 0$, where mixing is significantly larger, no method is able to capture the overturning regions accurately. h_{int} and h_{ave} provide smoother transitions in the overturning regions of the flow. Similar results are obtained if the z averaged fluid 2 depths are used instead. In the rest of this section the depth of fluid 2 used is defined by h_{ave}. This captures the regions of the flow where there is limited mixing and provides a smoother transition in the overturning regions than h_{max} or h_{min} individually.

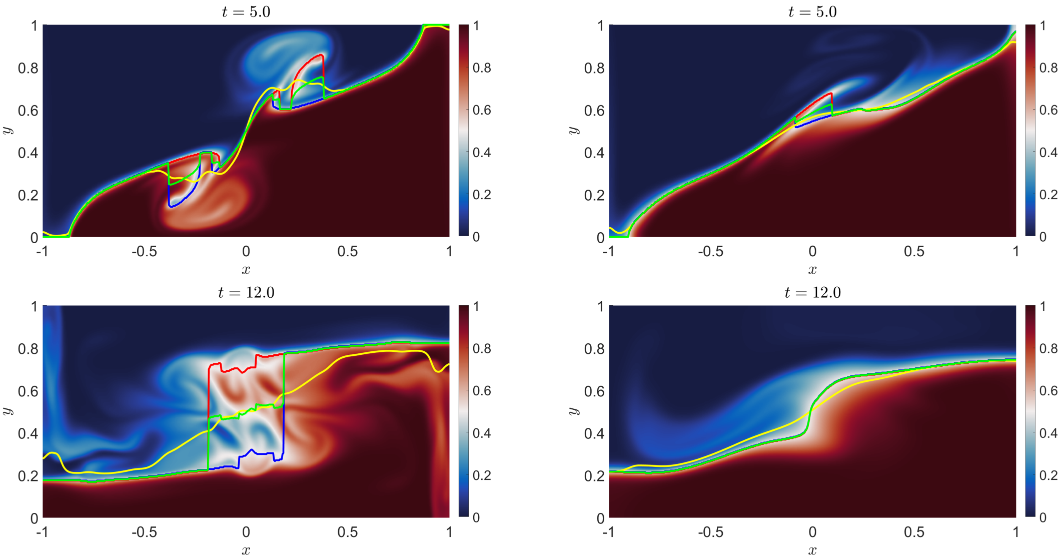

Figure 4.18: Pseudo-colour plots of concentration for $\gamma = 0$ (left) and $\gamma = 10$ (right) overlaid with depth averaged profiles calculated on the centre plane $z = 1/2$: $h_{\text{int}}(x, z, t)$ (yellow); $h_{\text{max}}(x, z, t)$ (red); $h_{\text{min}}(x, z, t)$ (blue); and $h_{\text{ave}}(x, z, t) = (h_{\text{max}}(x, z, t) + h_{\text{min}}(x, z, t))/2$ (green).

Using the averaged depth definition h_{ave}, the depth of the flow and x and y components of velocity (u_{ave},v_{ave}) are compared for the four cases in figure 4.19. At $t = 1$ the depth profiles reveal that the distance the wavefronts propagate over the first time unit decreases as γ increases. Further, both components of velocity are smaller in magnitude for the highest viscosity case, $\gamma = 10$. By $t = 2$ small changes in the profiles can be observed between $\gamma = 1$ when compared to $\gamma = 0$ and $\gamma = 0.1$ indicating that the increased viscosity is starting to affect the flow. For all cases the maximum and minimum of vertical velocity is close to 1 and -1, respectively, but it is localised near the side walls at $x = \pm 1$.

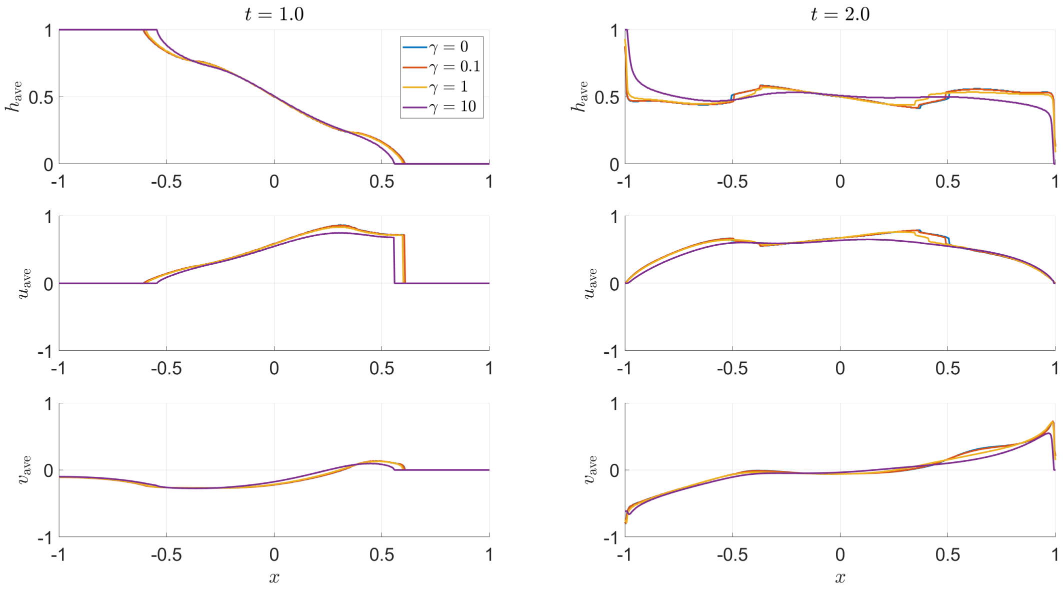

Figure 4.19: Centre-plane depth of the flow $h_{\mathrm{ave}}(x, 1/2, t)$ for the cases $\gamma = 0, 0.1, 1, 10$.

Pseudo-colour plots of u and v components of velocity on the centre-plane $z = 1/2$ overlaid with depth are displayed in figure 4.20 for $\gamma = 0$ and figure 4.21 for $\gamma = 10$. Similar to the depth-averaged profiles presented in figure 4.19, the flow is predominantly horizontal except in a region localised near the flow boundaries at $x = \pm 1$. The largest vertical velocities are observed at $t = 2$ when the wave fronts are reflecting off these side walls. As expected, $\gamma = 10$, with the higher fluid 2 viscosity, produces much smoother velocity gradients in both components over the domain.

4.3.3 Mixing and energy distribution

For the cases considered normalised residual potential energy $NRPE$ and normalised-mixing fraction $N\theta$ over time is displayed in figure 4.22. Similar trends can be observed with both mixing measures. As time increases, the amount of mixing increases. However, the amount of mixing decreases with increasing fluid 2 viscosity. $\gamma = 0$, $\gamma = 0.1$ and $\gamma = 1$ all exhibit similar levels of mixing up to $t = 6$ for both $NRPE$ and $N\theta$. Curiously, this continues up to $t = 9$ for normalised mixing fraction $N\theta$. Thus, the initial impact of increasing the viscosity is to reduce the local

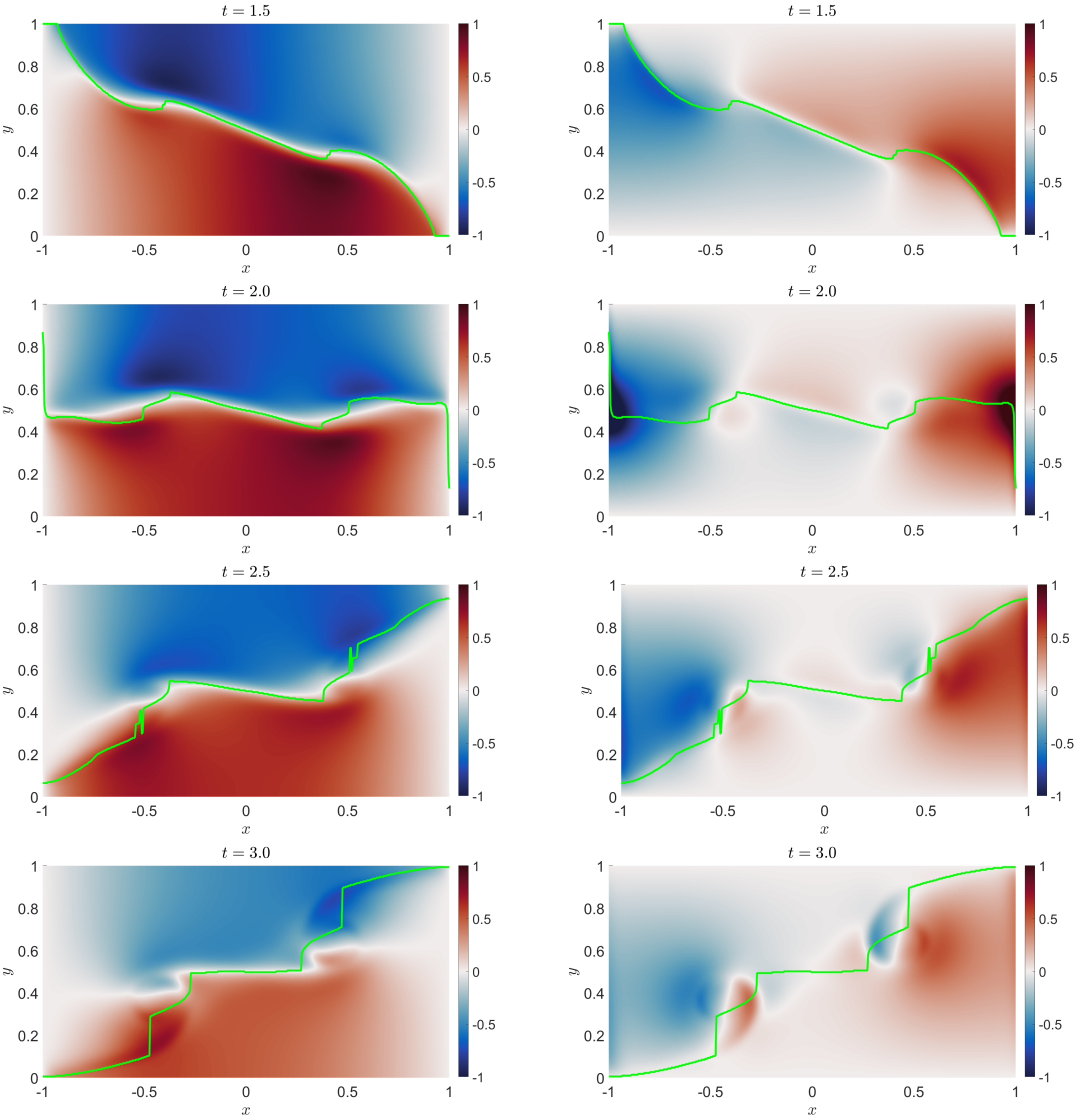

Figure 4.20: Pseudo-colour plots of u and v on the centre plane $z = 1/2$ for $\gamma = 0$. The lines overlaid are $h_{\text{ave}}(x, 1/2, t)$ (green).

mixing at the sharp concentration gradient. For $\gamma = 10$ the increased viscosity of fluid 2 creates significantly less mixing after the wavefronts reflect of the end walls, $x = \pm 1$, at $t = 1.5$. Similarly to $\gamma = 1$, $NRPE$ increases at a reduced rate before $N\theta$ for $\gamma = 10$ indicating that the increase is viscosity first acts to reduce the local mixing near the interface and then the larger-scale free surface deformation. This can also been seen in figure 4.15.

In figure 4.23 potential energy PE, kinetic energy KE, available potential energy APE and energy dissipated D_v are plotted against time for the four cases. As the flow sloshes back and forth the exchange between potential and kinetic energy can be observed. For $\gamma = 10$, with the highest viscosity in the current, the rate of dissipation increases sharply during the periods of the flow between the reflections of the wavefronts off the side walls, i.e., when the kinetic energy is largest.

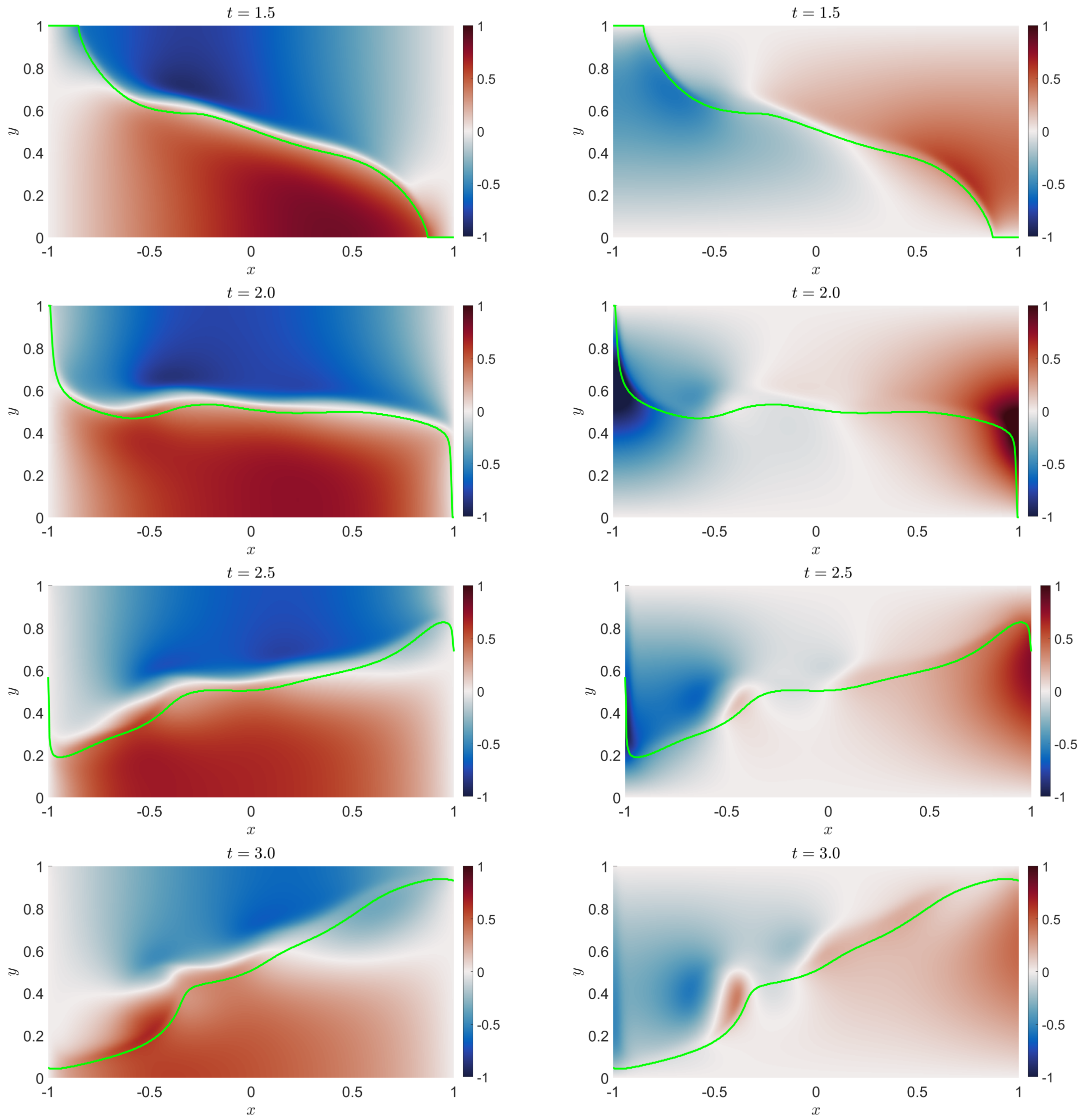

Figure 4.21: Pseudo-colour plots of u and v on the centre plane $z = 1/2$ for $\gamma = 10$. The lines overlaid are $h_{\text{ave}}(x, 1/2, t)$ (green).

Up until $t = 6$ $\gamma = 1$ exhibits similar behaviour to $\gamma = 0$ and $\gamma = 0.1$. However, after $t = 6$ two key differences can be observed: first, the local extremal values of the potential energy PE and kinetic energy KE do not decrease as quickly; second, the time between the extrema increases. This indicates that more of the available potential energy APE in converted to kinetic energy KE and that the sloshing speed slows down for $\gamma = 1$ and vice versa. The extra dissipation in $\gamma = 10$ reduces the total energy in the system and hence the maximum value of the extrema of potential energy PE and kinetic energy KE. Further, the exchange between potential energy PE and kinetic energy KE occurs more quickly after $t = 6$ for $\gamma = 10$. These changing speeds are consistent with the centre-plane concentration profiles in figure 4.15. At $t = 13.5$, $\gamma = 10$ is closest to the lowest potential energy state, with $\gamma = 0$ and $\gamma = 1$ both showing fluid 2 concentration distributions before

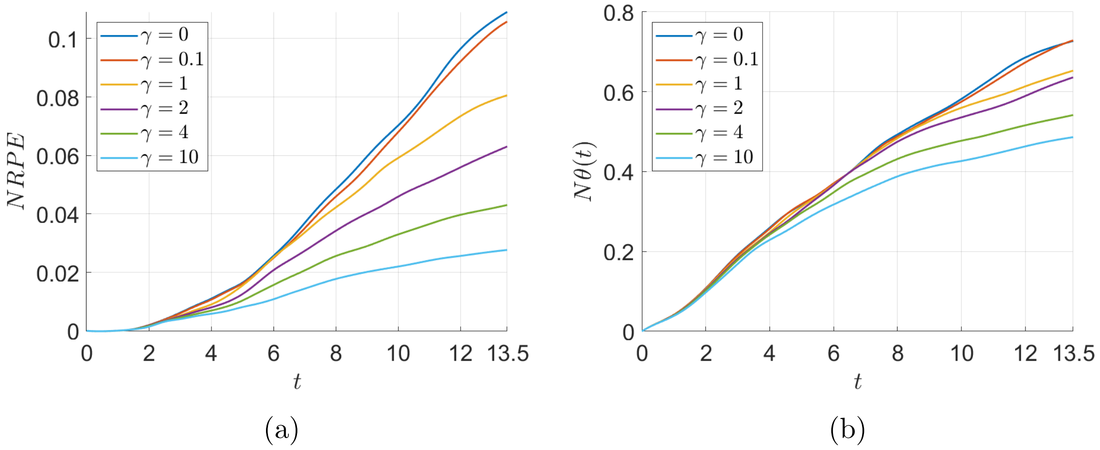

(a) (b)

Figure 4.22: Normalised residual potential energy $NRPE$ (a) and normalised-θ $N\theta$ for the cases $\gamma = 0, 0.1, 1, 2, 4, 10$.

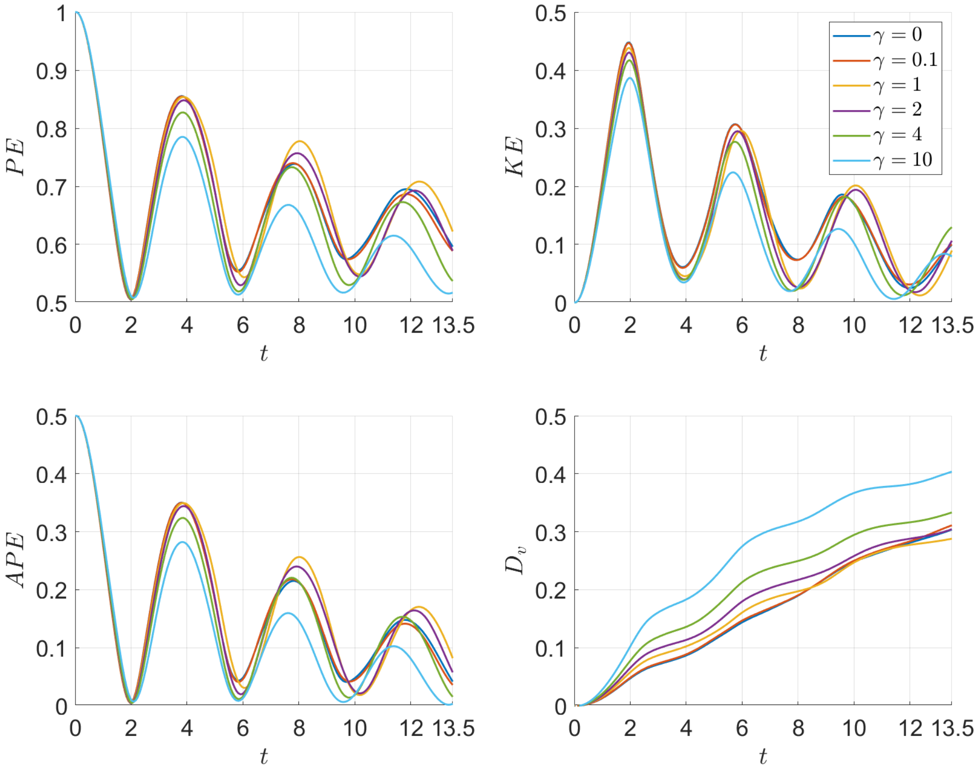

Figure 4.23: Energy distribution for the cases $\gamma = 0, 0.1, 1, 2, 4, 10$: potential energy PE (top-left), kinetic energy KE (top-right), available potential energy APE (bottom-left) and energy dissipated D (bottom-right).

this state.

To explore the energy loss from the system further, the change in residual

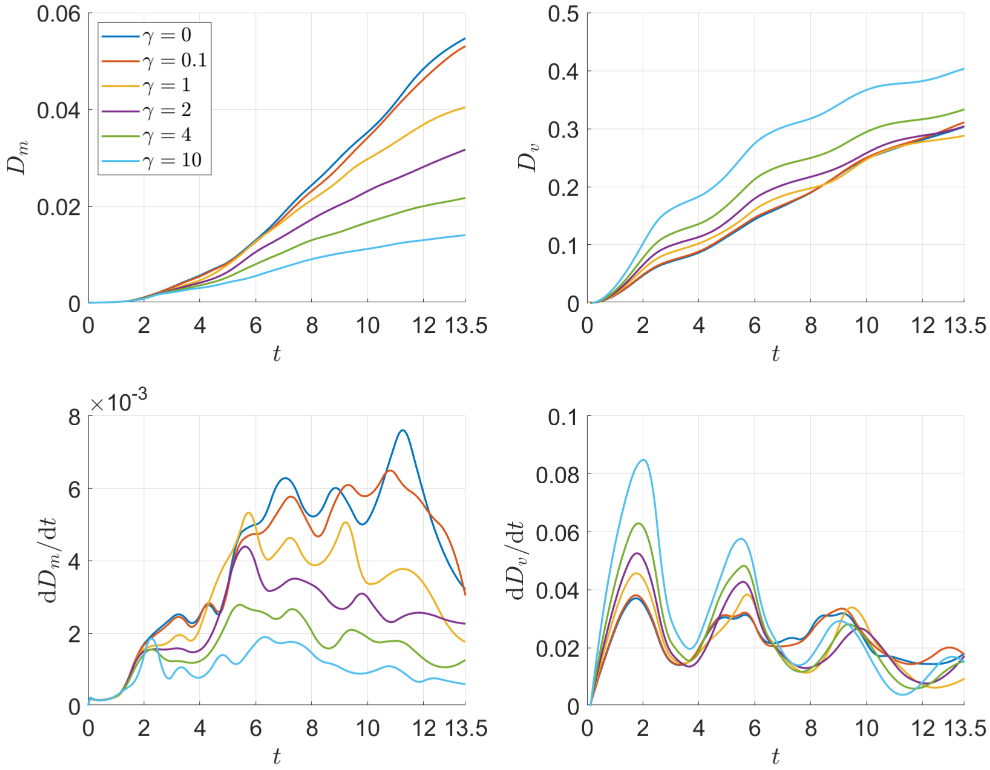

Figure 4.24: For the cases $\gamma = 0, 0.1, 1, 2, 410$: Gain in residual potential energy $D_m = RPE(t) - RPE(0)$ (top-left); energy lost to viscous dissipation D_v (top-right); rate of change of residual potential energy $\mathrm{d}D_m/\mathrm{d}t$ (bottom-left); and rate of change of viscous dissipation $\mathrm{d}D_v/\mathrm{d}t$ (bottom-right).

potential energy over time D_m is introduced

$$D_m(t) = RPE(t) - RPE(0). \tag{4.65}$$

This measures the increase in amount of energy that can no longer be converted into kinetic energy within the flow. The change in residual potential energy over time D_m, total viscous dissipation D_v and the rate of change of both quantities over time, $\mathrm{d}D_m/\mathrm{d}t$ and $\mathrm{d}D_v/\mathrm{d}t$, is presented in figure 4.24. The gradients of D_m and the energy dissipated to viscous diffusion D_v are calculated using a forward difference scheme and a total of 200 points equally spaced and interpolated from the piece-wise cubic spline for each variable. At $t = 0$ these gradients are assumed to be 0. As expected, all cases exhibit local maxima of viscous dissipation rate when the kinetic energy is largest. Initially, the rate of mixing is the same for all cases reaching a global maximum during the simulation. The time this global maximum occurs reduces as the fluid 2 viscosity is increased. further, the rate of viscous dissipation $\gamma = 10$ although initially taking the largest values decreases at a rate much faster than the other cases and has slower rates of viscous diffusion at the extrema near

$t = 9$ and $t = 11.5$.

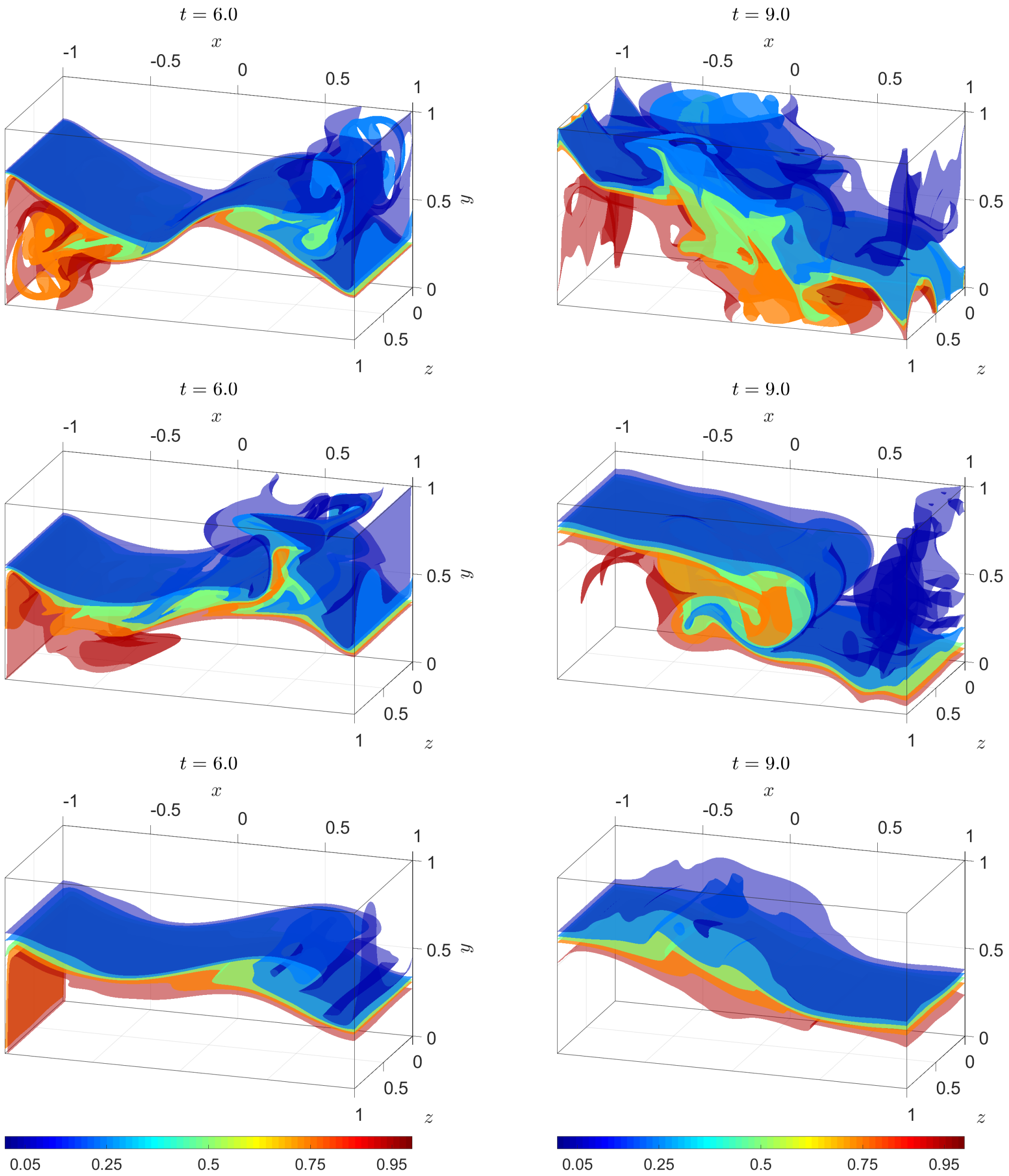

Figure 4.25: Isosurface plots of concentration ϕ for $\gamma = 0$ (top), $\gamma = 1$ (middle) and $\gamma = 10$ (right) cases and at times $t = 6$ (left) and $t = 9$ (right). Each coloured surface corresponds to concentrations $\phi = (0.05, 0.25, 0.5, 0.75, 0.95)$ ranging from deep blue ($\phi = 0.05$) to deep red $\phi = 0.95$.

Isosurface plots of the concentrations $\gamma = 0$, $\gamma = 1$ and $\gamma = 10$ at times $t = 6$ and $t = 9$ are presented in figure 4.25. At $t = 6$ the wave fronts have just reflected off the boundaries $x = \pm 1$ with fluid 2 travelling back towards the right (positive x) and fluid 1 towards the left. These wave fronts reflect back off end walls at $x = \pm 1$ and cross again just before $t = 9$. Increasing the viscosity initially acts to decrease the mixing locally near the interface. This can be observed by the reduced visibility of the 0.25 and 0.75 isosurfaces in $\gamma = 1$ when compared with $\gamma = 0$.

However, the 0.5 isosurfaces remain similarly perturbed in both cases. In $\gamma = 10$ and at $t = 6$ the deformation of the free surface is significantly reduced. By $t = 9$, the mixing in $\gamma = 0$ is affecting the majority of the flow and all isosurfaces are more distorted. In $\gamma = 1$ and $\gamma = 10$ the isosurfaces remain closer together indicating less mixing across the fluid interface. The 0.05 isosurface for $\gamma = 1$ is significantly more broken up near $x = 1$ compared to the 0.95 isosurface near $x = -1$. This highlights noticeable asymmetry in the flow and demonstrates that the increased viscosity in fluid 2 is inhibiting the mixing into that fluid. $\gamma = 10$ again exhibits significantly reduce free surface deformation.

The total surface area of the 0.5 isosurface $A_{0.5}(t)$ is used to measure the surface area of the fluid 1-fluid 2 interface. Initially, the interface surface area increases in size as the flow spreads out laterally, figure 4.26. The rate of increase decreases with increasing fluid 2 viscosity. After $t = 2$ for the cases $\gamma = 0$, $\gamma = 0.1$ and $\gamma = 10$ a decrease in surface area is observed. The decrease for $\gamma = 10$ the decrease is marginal and remains fairly constant after the initial phase of becoming horizontal. This corresponds to the wavefronts reflecting of the side walls and the flows becoming more horizontally stratified. $\gamma = 1$, however, does not exhibit this noticeable decrease, but still increases at a similar rate afterwards. Thus, during the first three oscillations the fluid 2 viscosity increase predominantly affects the surface-destruction rather than surface-creation mechanisms. Large scale flow shear (when the wave fronts at crossing) increases the surface area. Interface-scale mixing and diffusion then reduces it.

Oscillatory behaviour can be observed with local maxima of $A_{0.5}(t)$ coinciding with the maximal kinetic energy configuration, i.e. when the wave fronts cross and the flow is in the lowest potential energy state. $\gamma = 1$ exhibits the largest surface area between $t = 3$ and $t = 11$ before rapidly decreasing at the end of the flow. $\gamma = 10$ still exhibits the sharp increase of interface size as the flow spreads horizontally from release, but decays in a oscillatory behaviour thereafter. Clearly, viscosity has a significant affect on the flow during the first few time units by dissipating the energy required for significant interface deformation.

$\gamma = 1$ appears as an intermediary case in which, the increase in fluid 2 viscosity is not sufficiently large to inhibit the shear and interface creation on the system scale, but is sufficient to inhibit local interface-scale mixing. The increase in maximum available potential energy APE for $\gamma = 1$ at $t = 8$ and $t = 12$ arises because of the decreased mixing in the flow, which is aided by the increase viscosity. However, increasing the viscosity further, i.e. $\gamma = 10$, inhibits the initial surface deformation and dissipates considerably more energy in the system.

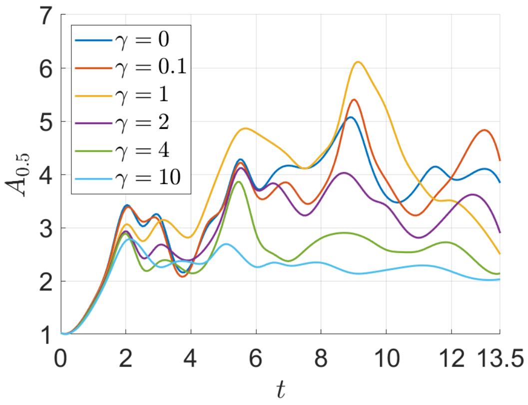

Figure 4.26: Surface area of the 0.5 isosurface $A_{0.5}$ against time for the cases $\gamma = 0, 0.1, 1, 2, 4, 10$

In order to explore this behaviour further, two additional simulations are conducted with $\gamma = 2$ and $\gamma = 4$ on mesh D. As the viscosity increases, the $NRPE$ decreases away from the equal viscosity case ($\gamma = 0$) more quickly, figure 4.22. Further, the normalised mixing fraction $N\theta$ stays coincident with $\gamma = 0$, but for less time (8 for $\gamma = 2$ and 5 for $\gamma = 4$). Increasing the viscosity also decreases the phase difference between the extrema of kinetic and potential energy, figure 4.23. Similar time differences can be observed for $\gamma = 2$, but $\gamma = 4$ shows phase difference similar to the equal viscosity case again. Further, the maximal and minimal values become more extreme. Although the total dissipation increases, the rate of change of dissipation decreases towards the total integration time $T_{\text{int}} = 13.5$, figure 4.24. The total dissipation might decrease below that of $\gamma = 0$ if the total integration time was increased. Finally, similar behaviour in terms of the total surface area $A_{0.5}$ is observed initially. However, by $t = 6$ $\gamma = 4$ transitions into a state more similar to $\gamma = 10$ and remains fairly constant. For $\gamma = 2$ a reduced surface area is observed, but oscillatory behaviour is still present. These two additional cases behave similarly to $\gamma = 1$, but as time increase (in particular for $\gamma = 4$) behaviour more similar to $\gamma = 10$ is observed. This further indicates that increasing the viscosity initially impacts the local interface mixing and enhances the exchange of energy between kinetic and potential energy and as the viscosity is increased further, viscous dissipation within the body of the flow starts to dominate.

4.4 Conclusions and future work

This chapter explored the lock-exchange problem with a variable viscosity for the denser fluid over transitional to moderate Reynolds numbers. The ambient or fluid

1 Reynolds number Re_1 was kept fixed at 10^3 throughout. A linear relationship was posed for the mixture viscosity as a function of fluid 2 concentration ϕ with the fluid 2 Reynolds number varying between 91 and 10^3. This linear relationship and the simple choice of domain and boundary conditions enabled the study of excess viscosity over two orders of magnitude. Direct numerical simulation was conducted using the spectral element solver NEK5000.

A small increase in the viscosity of fluid 2 by 10% produced similar results to those obtained for equal viscosities. However, when the fluid 2 viscosity was double that of the ambient ($\gamma = 1$) the viscosity gradients at interface act to suppress local mixing. Preservation of the viscosity gradient across the fluid interface lead to an enhanced ability of the flow to transfer energy between available potential energy APE and kinetic energy KE. Further, the total energy dissipated to viscosity was lower for this case than the lower viscosity cases ($\gamma = 0$ and $\gamma = 0.1$) and an increased sloshing period was observed. However, when the fluid 2 viscosity was increased further to 11 times that of the ambient ($\gamma = 10$) viscous dissipation was significantly higher resulting in a decreased sloshing time.

The available computational resources limited the cases studied and therefore there are many possibilities for extension to the results presented here, which were unfortunately beyond the scope of this chapter. First, the domain could be extended to that of the lock-release problem to see if similar traits are observed as the viscosity is increased. Second, a large range of viscosity differences and different functions for the viscosity could be studied, such as the empirical relationship developed by Cheng (2008) for the viscosity of glycerol/water mixtures rather than rather than a linear mixing law. Further, for the glycerol concentration experiments the viscosity ratio was as large as 300. Finally, although a Schmidt number Sc of 7 limited the amount of diffusion, studying larger Schmidt numbers would allow the characterisation of the effect of this assumption.

Chapter 5

Two-layer model for the lock-exchange problem

5.1 Introduction

In the previous chapter, the lock-exchange problem with different viscosities for the denser fluid (fluid 1) was investigated using direct numerical simulation (DNS) of the Navier-Stokes equations. The fully resolved DNS captured all the scales of motion down to the limit of viscosity. However, this required significant computational cost that increases with the excess viscosity ratio γ. The two fluids remained relatively unmixed over the total integration time T and exhibited predominantly horizontal flow. Further, the horizontal velocity profile was approximately uniform over the depth of the flow.

Depth-averaged models are capable of capturing some of the key flow dynamics at significantly reduced computational costs as discussed in the chapters 1 and 2. However, in contrast to the lock-release model in Chapter 2, the ratio of the locked fluid to the ambient is now 1, which is below the critical value of 2 for quantitative differences in the solution to be observed (Ungarish, 2009). Thus a two-layer model, which includes the ambient flow, is required. Two-layer shallow-water models have been used to study the lock-exchange problem before (for example Rottman and Simpson (1983); Bonnecaze et al. (1993); Hogg et al. (2000); Hallworth et al. (1998)). However, in this chapter, the equations are extended by the inclusion of a source term representing the viscous strain in each layer. The equations are solved using a linearised finite-volume scheme (LeVeque, 2002) for the hyperbolic equations and then the source terms contributions are included using a 4th-order Runge-Kutta

(Süli and Mayers, 2003).

This chapter explores whether a depth-averaged model can capture the affects of changing the denser fluid viscosity on the flow dynamics. Further, the significantly reduced computational cost (of order 10^4) enables the study of more cases and, in particular, varying an equal viscosity for both layers is investigated. Finally, a comparison between the depth-averaged results from the DNS discussed in the previous chapter and the two-layer shallow-water model is conducted for model validation. In particular, what structure and features can be captured by the theoretical model.

5.2 Methodology

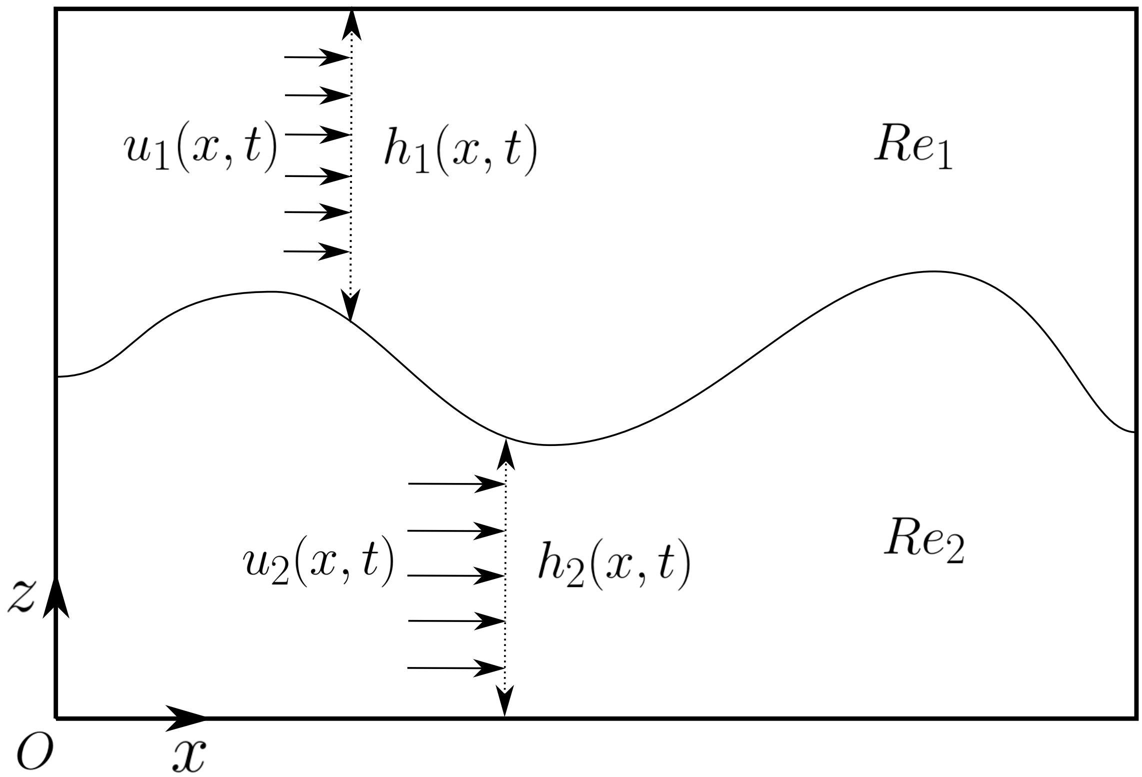

Figure 5.1: Schematic of the two-layer shallow-water model for the lock-exchange problem. Each layer has depth h_i, depth-averaged velocity u_i and Reynolds number $Re_i = \sqrt{g'H^3/2\nu_i^2}$, where ν_i is the kinematic viscosity of layer i and $g' = g(\rho_1 - \rho_2)/\rho_2)$ is the reduced gravity. The total depth is fixed, so that $h_1 + h_2 = H$

Similar to the previous chapter, the lock-exchange problem with two incompressible fluids of density ρ_i and dynamic viscosity μ_i is considered. The density difference between the fluids is assumed to be small so that the Boussinesq approximation can be applied. The results from the DNS demonstrate that the flow has negligible cross-stream velocity and therefore, a two-dimensional problem in the (x, y) plane is considered. Thus, the problem domain Ω reduces to $\Omega = \{(x, y) \in \mathbb{R}\,|x \in [-L/2, L/2], y \in [0, H]\}$, where $L/H = 2$. The depth of the domain remains fixed, and so

$$H = h_1(x,t) + h_2(x,t), \tag{5.1}$$

where $h_i(x,t)$ is the thickness of each layer and the interface between the two fluids is at $y = h_1(x,t)$. In this chapter it is assumed that the fluids are immiscible, so that the concentration of fluid 2 ϕ can only take the values 0 or 1. This assumption requires that no mixing or entrainment occurs within the flow. Further, the flow is assumed to remain stratified at all times with the denser fluid (fluid 2) beneath the less dense fluid (fluid 1). Apart from near $x = -L$ and $x = L$, when the wavefronts reflect off the end wall, the flow direction is predominantly horizontal as demonstrated in the previous chapter. Therefore, it is assumed that the velocity in each fluid can be described by its depth-averaged quantity

$$u_1(x,t) = \int_0^{h_1} u(x,y,t)\,\mathrm{d}y \tag{5.2}$$

and by conservation of mass the depth-averaged velocity in fluid 2 as $u_2 = -h_1 u_1/h_2$. These assumptions allow us to apply the two-layer shallow water equations to the problem as discussed in chapter 1.

In order to incorporate the effects of differing viscosity in each layer into the shallow-water model the further assumption that the layer i Reynolds number $Re_i = \sqrt{g' H^3/2\nu_i^2}$ is large for both layers. This is required for the horizontal velocity profile to be uniform (Dorrell et al., 2014) and hence the shape factor β takes the value 1. Neglecting basal drag as considered in the DNS study, the effects of viscosity on the flow are included via a viscous source term in the two-layer shallow-water model. This appears on the right-hand side of the layer 1 and layer 2 momentum equations:

$$\frac{\partial h_1}{\partial t} + \frac{\partial}{\partial x}\left(h_1 u_1\right) = 0, \tag{5.3}$$

$$\frac{\partial}{\partial t}\left(h_1 u_1\right) + \frac{\partial}{\partial x}\left(h_1 {u_1}^2\right) + h_1 \frac{\partial P_i}{\partial x} = \nu_1 h_1 \frac{\partial^2 u_1}{\partial x^2}, \tag{5.4}$$

$$\frac{\partial h_2}{\partial t} + \frac{\partial}{\partial x}\left(h_2 u_2\right) = 0, \tag{5.5}$$

$$\frac{\partial}{\partial t}\left(h_2 u_2\right) + \frac{\partial}{\partial x}\left(h_2 {u_2}^2 + \frac{g'}{2}{h_2}^2\right) + h_2 \frac{\partial P_i}{\partial x} = \nu_2 h_2 \frac{\partial^2 u_2}{\partial x^2}, \tag{5.6}$$

and is of the form considered by Higuera (1994); Dasgupta and Govindarajan (2010); Kanayama and Dan (2013). Although direct depth-averaging of the Navier-Stokes equations yields a viscous source term of the form (Gustafsson and Sundström, 1978):

$$\nu_i \frac{\partial}{\partial x}\left(h_i \frac{\partial u_i}{\partial x}\right) = \nu_i h_i \frac{\partial^2 u_i}{\partial x^2} + \nu_i \frac{\partial h_i}{\partial x}\frac{\partial u_i}{\partial x}. \tag{5.7}$$

This form does not reproduce the same symmetries as the momentum dissipation in the Navier-Stokes equations (Gent, 1993; Schär and Smith, 1993) and Schär and Smith (1993) propose a new form of the dissipation in attempt to address this. However, the additional term in dissipation term (5.7) is only large near the head of the flow where the shallow-water approximation also breaks down. Critically interfacial drag terms are neglected in the model. An estimate of the size of these terms is $\sim \mu |u_2 - u_1| / h_{\text{layer}}$, where h_{layer} is an estimated thickness of the velocity transition region. These terms are likely to be of similar order, and may even been larger, to the momentum diffusion terms and therefore the regime with only momentum diffusion may not be realistic.

The depth of each layer is scaled by H, and the same spatial, time, and velocity scales are used as in the DNS

$$h_i = H h_i^*, \quad x = H x^*, \quad u_i = \sqrt{\frac{g' H}{2}} u_i^*, \quad t = \sqrt{\frac{2H}{g'}} t^*, \tag{5.8}$$

where $g' = g(\rho_2 - \rho_1)/\rho_2$ is the reduced gravity and g is gravitational acceleration. In dimensionless form the two-layer shallow water model (5.3-5.6) is

$$\frac{\partial h_1}{\partial t} + \frac{\partial}{\partial x}\left(h_1 u_1\right) = 0, \tag{5.9}$$

$$\frac{\partial}{\partial t}\left(h_1 u_1\right) + \frac{\partial}{\partial x}\left(h_1 {u_1}^2\right) + h_1 \frac{\partial P_i}{\partial x} = \frac{1}{Re_1} h_1 \frac{\partial^2 u_1}{\partial x^2}, \tag{5.10}$$

$$\frac{\partial h_2}{\partial t} + \frac{\partial}{\partial x}\left(h_2 u_2\right) = 0, \tag{5.11}$$

$$\frac{\partial}{\partial t}\left(h_2 u_2\right) + \frac{\partial}{\partial x}\left(h_2 {u_2}^2 + {h_2}^2\right) + h_2 \frac{\partial P_i}{\partial x} = \frac{1}{Re_2} h_2 \frac{\partial^2 u_2}{\partial x^2}, \tag{5.12}$$

where P_i^* is the dimensionless interfacial pressure. The interfacial pressure P_i^* term is left implicit, and can be eliminated from the momentum equations (5.10) and (5.12) to yield a single momentum conservation equation for both layers in terms of just h_2 and u_2, where for brevity the asterisks * are neglected

$$\frac{\partial}{\partial t}\left(h_2 u_2\right) + \left(1 - h_2\right) \frac{\partial}{\partial x}\left(h_2 u_2^2 + h_2^2\right) - h_2 \frac{\partial}{\partial x}\left(\frac{h_2^2 u_2^2}{1 - h_2}\right) = \psi(x,t), \tag{5.13}$$

where $\psi(x,t)$ are the viscous source terms given by

$$\psi(x,t) \equiv \left(1 - h_2\right) h_2 \frac{\partial^2}{\partial x^2}\left(u_2\left(\frac{1}{Re_2} + \frac{1}{Re_1}\frac{h_2}{1 - h_2}\right)\right). \tag{5.14}$$

Note, that the definition $h_1 + h_2 = 1$ has been used to simply these expressions. With our mass conservation for the basal layer (5.11), this gives two equations for the two unknowns h_2 and u_2. Zero flux boundary conditions are imposed at the ends of the domain for all cases

$$u_2(-1,t) = 0 \quad \text{and} \quad u_2(1,t) = 0. \tag{5.15}$$

The momentum conservation equation (5.13) contains second order spatial derivatives of h and m and therefore two additional boundary conditions are required. At the boundaries $x = \pm 1$, the momentum equation combined with the zero flux boundary conditions (5.15) reduces to

$$\left(1 - h_2\right) 2 h_2 \frac{\partial h_2}{\partial x} = \psi \quad \text{at} \quad x = \pm 1 \tag{5.16}$$

As with the single-layer shallow-water equation when the viscous source terms are zero, this reduces $\partial h_2 / \partial x(\pm 1, t) = 0$ and will be used later when applying the fractional step method. When the viscous sources terms are not in general zero in the bulk of the flow, zero boundary conditions will be imposed on $\psi(\pm 1, t) = 0$. This is equivalent to

$$\frac{\partial h_2}{\partial x}(-1,t) = 0 \quad \text{and} \quad \frac{\partial h_2}{\partial x}(1,t) = 0 \tag{5.17}$$

by considering equation (5.16). The initial conditions are prescribed functions of x

$$u_2(x,0) = u_0(x), \tag{5.18}$$

$$h_2(x,0) = h_0(x). \tag{5.19}$$

In contrast to the single-layer model discussed in chapter 2, no Froude number condition is imposed. In the DNS simulations presented in the previous chapter, a clearly defined gravity current head is not observed during the later stages of the flow ($t > \geq 9$) or during the phases of the flow where it is interacting with the end walls at $x = \pm 1$.

5.2.1 Numerical scheme

Henceforth, the following variables used $h = h_2$ and $m = h_2 u_2$ for simplicity. The mass (5.11) and momentum equations (5.13) for the basal layer can be written in matrix form

$$\frac{\partial \mathbf{q}}{\partial t} + \mathcal{A}\frac{\partial \mathbf{q}}{\partial x} = \mathbf{\Psi}, \tag{5.20}$$

where

$$\mathbf{q} = \begin{pmatrix} h_2 \\ h_2 u_2 \end{pmatrix} = \begin{pmatrix} h \\ m \end{pmatrix}, \tag{5.21}$$

$$\mathcal{A} = \begin{pmatrix} 0 & 1 \\ \mathcal{P}(h,m) & \mathcal{Q}(h,m) \end{pmatrix}, \tag{5.22}$$

$$\mathbf{\Psi} = \begin{pmatrix} 0 \\ \psi(h,m) \end{pmatrix}, \tag{5.23}$$

$$\mathcal{P}(h,m) = (1-h)\left(2h - \frac{m^2}{h^2}\right) - \frac{hm^2}{(1-h)^2}, \tag{5.24}$$

$$\mathcal{Q}(h,m) = \frac{2m(1-2h)}{h(1-h)}, \tag{5.25}$$

$$\psi(h,m) = h(1-h)\frac{\partial^2}{\partial x^2}\left(\frac{m}{(1-h)Re_1} + \frac{m}{hRe_2}\right). \tag{5.26}$$

The eigenvalues of the Jacobian matrix $\mathcal{A}$ are required to be real and distinct for the system to be hyperbolic. These eigenvalues are given by

$$\lambda_\pm = \frac{\mathcal{Q} \pm \sqrt{\mathcal{Q}^2 + 4\mathcal{P}}}{2}, \tag{5.27}$$

and are real and distinct provided the discriminant $\mathcal{Q}^2 + 4\mathcal{P}$ is positive. Numerical calculations are used to evaluate the regions where the eigenvalues, (5.27) are real, figure 5.2. As the depth of the flow becomes dominated by one of the layers ($h \to 0$ or $h \to 1$), the momentum must tend to zero as well, figure 5.2a. This however, is not true for the velocity in each layer, figure 5.2b. The velocity in the layer can increase provided the momentum itself tends to zero as $h \to 0$. When $h > 0.5$, the velocity magnitude is larger in the top layer than the basal, because $u_1 = -u_2 h/(1-h)$. For the two-layer shallow water without fixed depth, loss of hyperbolicity corresponds to the formation of Kelvin-Helmholtz instabilities forming at the interface (Castro et al., 2001; Audusse, 2005; Kim and LeVeque, 2008). These instabilities arise when small perturbations to the interface grow in time with the growth (or decay) rate determined by a balance between shearing force and buoyancy and leads to mixing as a source to dissipate energy. The eigenvalues becoming complex signifies that the no-entrainment/mixing assumption in the model breaking down and therefore, the solver is restricted to the case where the equations remain hyperbolic.

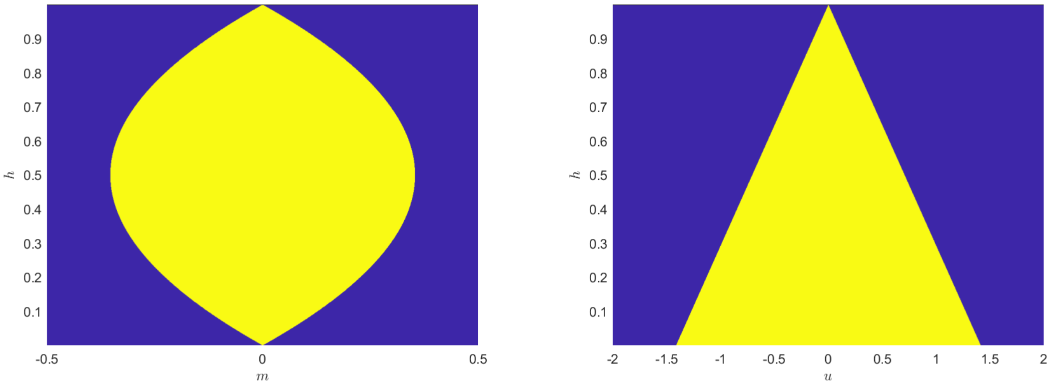

(a) (b)

Figure 5.2: Regions in (h, m)-space (a) and (h, u)-space (b), where the system of equations are hyperbolic, shown in yellow. Outside of these ranges, shown in purple, the finite-volume schemes cannot be applied. Critically, as $h \to 1$, the equations become elliptic for all finite values of the velocity u. Thus an arbitrarily thin wetting layer in the overlying fluid is not compatible with a finite-volume scheme.

Fractional step method

Provided the eigenvalues of the matrix $\mathcal{A}$ remain distinct, the balance law, here a conservation equation with a second-order source term, (5.20) can be solved using finite-volume schemes (LeVeque, 2002). A standard approach for solving such problems are the fractional step methods, or operator splitting (LeVeque, 2002). The balance law (5.20) is split into two simpler problems that are solved independently

$$\frac{\partial \mathbf{q}}{\partial t} + \mathcal{A}\frac{\partial \mathbf{q}}{\partial x} = 0, \tag{5.28}$$

$$\frac{\partial \mathbf{q}}{\partial t} - \mathbf{\Psi} = 0. \tag{5.29}$$

At each time-step first the homogeneous hyperbolic equation (5.28) is solved to produce an intermediate solution, $\mathbf{q}^*$, which is then used as the initial state for the source term correction (5.29). Although this introduces an additional source of error into the numerical method, it enables the use of standard schemes for solving these individual problems. A linearised finite-volume scheme, detailed below, is used to solve the hyperbolic equation (5.28). A 4th-order Runge-Kutta method is used to solve separately for the ODE corresponding to the source terms (5.29). Note, that Riemann invariants exists for the reduced hyperbolic problem (5.28) as stated in Bonnecaze et al. (1993).

Finite-volume scheme

This section details how the first part of the fractional step method (5.28) is solved using a scheme for non-conservative non-linear hyperbolic equations. Although, the system of PDEs (5.28) is not hyperbolic for all values of h and m, it is for a range of physically realistic variables. Thus, in this section it is assumed that the problem is hyperbolic. I.e., the matrix $\mathcal{A}$ has two, real and distinct eigenvalues, $\lambda^1 = \lambda_+$ and $\lambda^2 = \lambda_-$, given by (5.27) with corresponding eigenvectors

$$\mathbf{r}^1 = \begin{pmatrix} 1 \\ \lambda^1 \end{pmatrix} \quad \text{and} \quad \mathbf{r}^2 = \begin{pmatrix} 1 \\ \lambda_2 \end{pmatrix}. \tag{5.30}$$

Thus the Jacobian matrix, $\mathcal{A}$, can be decomposed

$$\mathcal{A} = B\Lambda B^{-1} = \begin{pmatrix} 1 & 1 \\ \lambda^1 & \lambda^2 \end{pmatrix} \begin{pmatrix} \lambda^1 & 0 \\ 0 & \lambda^2 \end{pmatrix} \begin{pmatrix} 1 & 1 \\ \lambda^1 & \lambda^2 \end{pmatrix}^{-1}. \tag{5.31}$$

The significance of the equation being hyperbolic is that the solution of the Riemann problem for the equation decouples into two independent linear equations in the directions $\mathbf{r}_i$ with speeds λ_i and, provided the waves from neighbouring cell interfaces do not interact, the flux through each cell interface can be calculated. The sign of the eigenvalue determines whether each wave is left (negative) or right (positive) propagating. The Jacobian matrix can be decomposed into its left $\mathcal{A}^-$ and right-propagating $\mathcal{A}^+$ components

$$\mathcal{A}^{\pm} = B \begin{pmatrix} (\lambda^1)^{\pm} & 0 \\ 0 & (\lambda^2)^{\pm} \end{pmatrix} B^{-1}. \tag{5.32}$$

The domain, $x \in [-1, 1]$, is split into N_x equally spaced cells of width $\Delta x = 2/N_x$ and so that the i-th cell is the region $[x_{i-1/2}, x_{i+1/2}]$ and centred at x_i, where $x_i = -1 + (i - 1/2)\Delta x$. The initial depth h_0 and momentum $m_0 = h_0 U_0$ profiles are integrated over each cell, denoted by subscript i, and divided by the cell width Δx to produce the cell-averaged quantities

$$\mathbf{Q}_i^0 = \int_{x_{i-1/2}}^{x_{i+1/2}} \mathbf{q}(x, 0)\,\mathrm{d}x. \tag{5.33}$$

To compute the flux between cells, and hence the cell-averaged quantities at the next time step, superscript $(n+1)$, the solution of the Riemann problem (or approximation of it) needs to be obtained. Eigenvalues and eigenvectors of the Jacobian matrix $\mathcal{A}$ are required at the cell interfaces. However, the values of h and m are only stored at the cell centres, not the interfaces. The values at the interfaces are computed as an average of the values from the neighbouring cells thus approximating the solution. Various different averaging methods have been proposed (e.g. Roe's method (Roe, 1981), but in general closed forms of these averages do not exist in general). For the two-layer model considered here closed form of the Roe averages could not be obtained and so the arithmetic average

$$h_{i-1/2} = \frac{h_i + h_{i-1}}{2} \quad \text{and} \quad m_{i-1/2} = \frac{m_i + m_{i-1}}{2} \tag{5.34}$$

is instead used. The eigenvalues and eigenvectors at each interface are then calculated from these values

$$\lambda^1_{i-1/2} = \frac{\mathcal{Q}_{i-1/2} + \sqrt{(\mathcal{Q}_{i-1/2})^2 + 4\mathcal{P}_{i-1/2}}}{2}, \tag{5.35}$$

$$\lambda^2_{i-1/2} = \frac{\mathcal{Q}_{i-1/2} - \sqrt{(\mathcal{Q}_{i-1/2})^2 + 4\mathcal{P}_{i-1/2}}}{2}, \tag{5.36}$$

$$\mathbf{r}^1_{i-1/2} = \begin{pmatrix} -\lambda^2_{i-1/2} \\ 1 \end{pmatrix}, \tag{5.37}$$

$$\mathbf{r}^2_{i-1/2} = \begin{pmatrix} -\lambda^1_{i-1/2} \\ 1 \end{pmatrix}, \tag{5.38}$$

where

$$\mathcal{P}_{i-1/2} = \left(1 - h_{i-1/2}\right)\left(2h_{i-1/2} - \left(\frac{m_{i-1/2}}{h_{i-1/2}}\right)^2\right) - \frac{h_{i-1/2}\left(m_{i-1/2}\right)^2}{\left(1 - h_{i-1/2}\right)^2}, \tag{5.39}$$

$$\mathcal{Q}_{i-1/2} = \frac{2m_{i-1/2}\left(1 - 2h_{i-1/2}\right)}{h_{i-1/2}\left(1 - h_{i-1/2}\right)}. \tag{5.40}$$

The approximate eigenvalues and eigenvectors are used to define the local approximation to the non-linear problem (5.28)

$$\frac{\partial \mathbf{q}}{\partial t} - \mathcal{A}_{i-1/2}\frac{\partial \mathbf{q}}{\partial x} = 0 \tag{5.41}$$

at each cell interface. The difference in $\mathbf{Q}$ between neighbouring cells at the $i - 1/2$ interface is computed

$$\Delta\mathbf{Q}^n_{i-1/2} = \mathbf{Q}^n_i - \mathbf{Q}^n_{i-1}. \tag{5.42}$$

When the solution is smooth, $\Delta\mathbf{Q}^n_{i-1/2} = \mathcal{O}(\Delta x)$ and the Jacobian matrix is nearly constant (LeVeque, 2002) and the linearised Riemann solver provides an accurate approximation of the true Riemann solution. However, near shocks $\Delta\mathbf{Q}^n_{i-1/2}$ can be large and the application of a linearised method is harder to justify. This can result in the solution near shocks being inaccurately captured. Note, that Roe averaged interface variables are chosen to ensure the correct behaviour near a shock captured (Roe, 1981). The inclusion of viscous diffusion acts to smooth the solution near regions where the velocity gradients are large and suppress the formation of shocks that can occur in an inviscid case.

As the eigenvectors of $\mathcal{A}_{i-1/2}$ form a basis, the difference $\Delta\mathbf{Q}^n_{i-1/2}$ may be expressed as a linear combination, with coefficients $\gamma^p_{i-1/2}$ of the two eigenvectors

$$\sum_{p=1}^{2} \gamma^p_{i-1/2} \mathbf{r}^p_{i-1/2} = \Delta \mathbf{Q}^n_{i-1/2}. \tag{5.43}$$

The coefficients $\gamma^p_{i-1/2}$ are given by

$$\begin{pmatrix} \gamma^1_{i-1/2} \\ \gamma^2_{i-1/2} \end{pmatrix} = B^{-1} \Delta \mathbf{Q}^n_{i-1/2}. \tag{5.44}$$

The waves are then split into left- and right-fluctuations

$$\mathcal{A}^- \Delta \mathbf{Q}_{i-1/2} = \sum_{p=1}^{2} \left(\lambda^p_{i-1/2}\right)^- \gamma^p_{i-1/2} \mathbf{r}^p_{i-1/2} = \sum_{p=1}^{2} \left(\lambda^p_{i-1/2}\right)^- \mathcal{W}^p_{i-1/2}, \tag{5.45}$$

$$\mathcal{A}^+ \Delta \mathbf{Q}_{i-1/2} = \sum_{p=1}^{2} \left(\lambda^p_{i-1/2}\right)^+ \gamma^p_{i-1/2} \mathbf{r}^p_{i-1/2} = \sum_{p=1}^{2} \left(\lambda^p_{i-1/2}\right)^+ \mathcal{W}^p_{i-1/2}, \tag{5.46}$$

where $(x)^+ = \max(0, x)$ and $(x)^- = \min(0, x)$. These represent the right- and left-going fluctuations in the flux of m and h and correspond to waves $\mathcal{W}^p_{i-1/2}$ travelling at speed $\lambda^p_{i-1/2}$ Finally, the solution of the hyperbolic equation in each cell at the next time step is computed

$$\mathbf{Q}^{*n}_i = \mathbf{Q}^n_i - \frac{\Delta t}{\Delta x} \left(\mathcal{A}^+ \Delta \mathbf{Q}_{i-1/2} + \mathcal{A}^- \Delta \mathbf{Q}_{i+1/2}\right). \tag{5.47}$$

This intermediate solution, $\mathbf{Q}^{*n}_i$, is now used as the initial data for the the source-term part of the fractional step method (5.29). This intermediate solution in each cell is calculated from the cell's values at the previous time step and those from the adjacent cells. This is known as a three-point stencil. For the first and last cells (those with interfaces at the boundary) additional 'ghost' cells are required at $i = 0$ and $i = N_x + 1$ to impose the boundary conditions $u(-1, t) = u(1, t) = 0$. For the homogenous hyperbolic equation (5.28), these boundary conditions are equivalent to symmetry conditions, i.e.

$$\frac{\partial h}{\partial x}(-1, t) = \frac{\partial h}{\partial x}(1, t) = 0. \tag{5.48}$$

When computing the eigenvalue and eigenvectors at these boundary values, the discretised boundary conditions provide $m_{1/2} = m_{N_x+1/2} = 0$ and

$$\frac{h_0 + h_1}{\Delta x} = 0 \implies h_{1/2} = h_1, \tag{5.49}$$

$$\frac{h_{N_x} + h_{N_x+1}}{\Delta x} = 0 \implies h_{N_x+1/2} = h_{N_x}, \tag{5.50}$$

$$\tag{5.51}$$

Entropy violating shocks

By linearising the Jacobian matrix, $\mathcal{A}$, the system of PDEs is essentially reduced to two linearly-independent problems, which are solved separately with each corresponding to an advection equation with speed λ_p in the direction $\mathbf{r}^p$ in (h, m)-space (LeVeque, 2002). The main disadvantage of linearised Riemann solvers is that the solutions to the Riemann problem can only consist of discontinuities (shocks), whereas for non-linear conservation laws can result in rarefaction waves (LeVeque, 2002). For a scalar conservation law with flux function $f(q)$, i.e. $\partial q / \partial t + \partial(f(q)) / \partial x = 0$, which is assumed to be concave (or convex), i.e. $f''(q)$ does not change sign over the region of interest, there are five possible choices for exact solutions, $Q^{\downarrow}_{i-1/2} = q^{\downarrow}(Q^n_{i-1}, Q^n_i)$ to the Riemann problem along the interface $x = x_{i-1/2}$, figure 5.3. When both the left, λ^p_{i-1}, and right λ^p_i eigenvalues are negative, figure 5.3 a&c, the solution is $Q^{\downarrow}_{i-1/2} = Q_i$ and when both are positive, figure 5.3 b&d, the solution is $Q^{\downarrow}_{i-1/2} = Q_{i-1}$. However, when the eigenvalues change sign from negative to positive across the cell interface, figure 5.3e, the rarefaction wave spreads both to the left and to the right of the interface. This has exact solution $Q^{\downarrow}_{i-1/2} = q_s$, where q_s is the unique value satisfying $f'(q_s) = 0$. Crucially the weak solutions to conservation laws are not necessarily unique and in general an additional condition, for example based on entropy, is required (Goodman and LeVeque, 1988).

In a linearised solver, the only time the correct solution is not selected is when the transonic rarefaction exists (LeVeque, 2002). To address this, the Harten-Hyman entropy fix developed by Harten and Hyman (1983) is used when a transonic rarefaction exists, with the exact formulation slightly modified by LeVeque (1990). When a transonic rarefaction exists, the averaged eigenvalue at the cell interface ${\lambda^p}_{i-1/2}$ is split into left- and right-propagating components via

$$(\lambda^p)^-_{i-1/2} = \Gamma^p \lambda^p_{i-1} \quad \text{and} \quad (\lambda^p)^+_{i-1/2} = \Gamma^p \lambda^p_i, \tag{5.52}$$

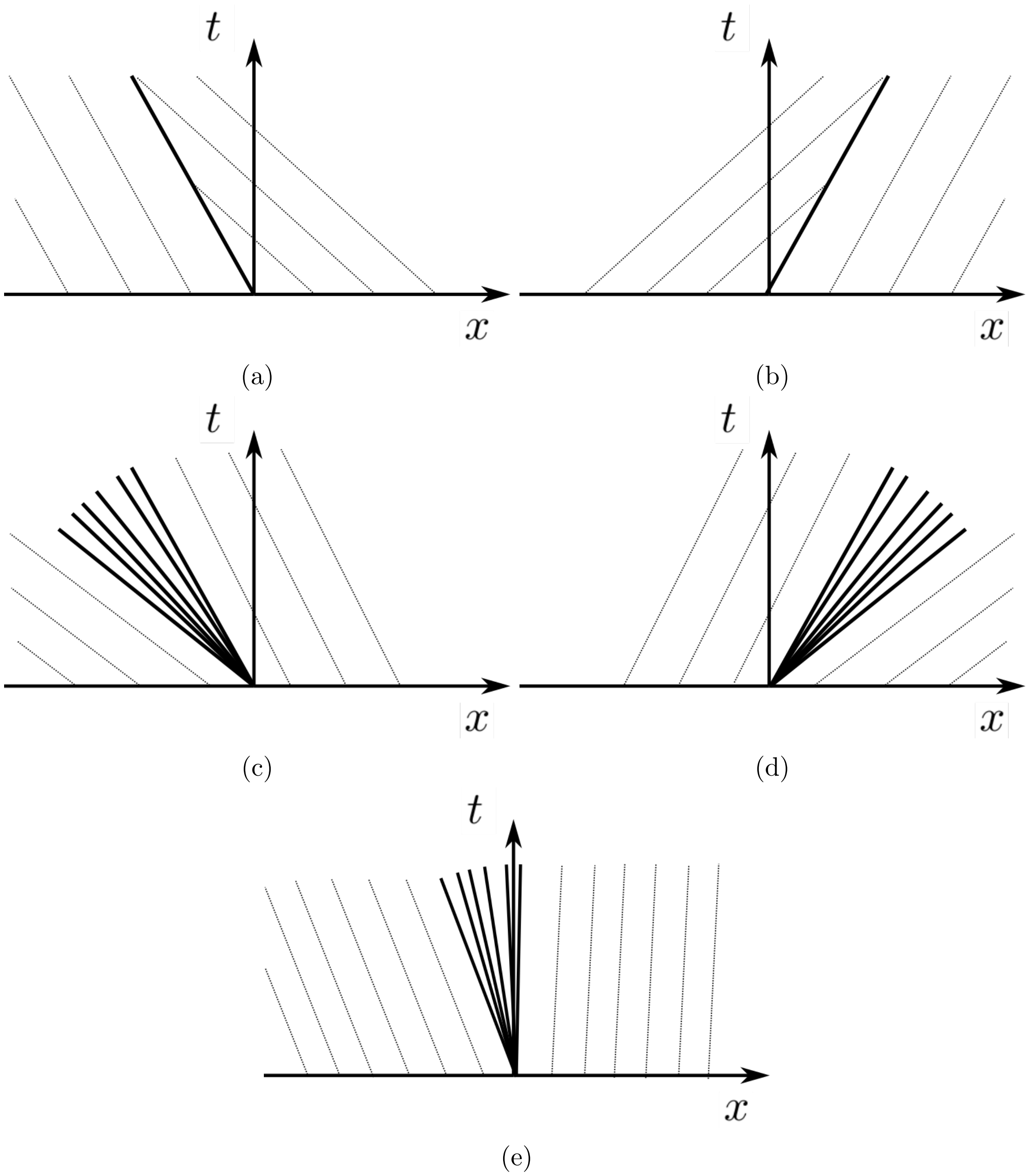

(a) (b) (c) (d) (e)

Figure 5.3: The five possible solutions to a linearised scalar conservation equation for the Riemann problem. Solid lines represent shocks (a and b) in the Riemann solution or expansion fan regions (c,d and e). Dotted lines represent characteristic curves. They are characterised by the values of the eigenvalues to the left (λ_l^p and right (λ_r^p of the cell interface located at the position of the t axis: (a) ($\lambda_r^p < \lambda_l^p < 0$) - left going shock, (b) ($0 < \lambda_r^p < \lambda_l^p$ - right going shock, (c) ($\lambda_l^p < \lambda_r^p < 0$) left going rarefaction wave, (d) ($0 < \lambda_l^p < \lambda_r^p$) - right going rarefaction wave and (e) ($\lambda_l^p < 0 < \lambda_r^p$) transonic rarefaction wave.

where

$$\Gamma^p = \frac{{\lambda^p}_i - {\lambda^p}_{i-1/2}}{{\lambda^p}_i - {\lambda^p}_{i-1}}. \tag{5.53}$$

These modified eigenvalues are then used in the calculation of the fluxes with both a left and right going contribution from the p-th wave.

High-resolution scheme

The approximate Riemann solver presented earlier is only first order accurate and introduces significant numerical diffusion, which acts to smooth out the solution. This is particularly noticeable for solutions that require a long-time integration (LeVeque, 2002). High-resolution schemes, which include second-order-accurate correction terms, remove a lot of the numerical diffusion, but can lead to oscillations near discontinuities. The introduction of limiters, which act to suppress, or even negate, the second-order correction terms near shocks provide a scheme that is second-order accurate wherever possible that does not introduce spurious and non-physical oscillations. Further, LeVeque (2002) demonstrated that second-order methods when used in conjunction with the entropy fix, provide significantly more accurate results in the presence of transonic rarefactions waves compared with the entropy fix alone.

The approximate Riemann solver is extended to a high-resolution scheme with the addition of correction terms, $\mathcal{F}_{i+1/2}$, to yield the following

$$\mathbf{Q}^{*n}_i = \mathbf{Q}^n_i - \frac{\Delta t}{\Delta x}\left(\mathcal{A}^+\Delta\mathbf{Q}_{i-1/2} + \mathcal{A}^-\Delta\mathbf{Q}_{i+1/2}\right) - \frac{\Delta t}{\Delta x}\left(\mathcal{F}_{i+1/2} - \mathcal{F}_{i-1/2}\right) \tag{5.54}$$

(LeVeque, 2002). The high-resolution corrections are computed from the wave speeds

$$\mathcal{F}_{i-1/2} = \frac{1}{2}\sum_{p=1}^{2} |s^p_{i-1/2}| \left(1 - \frac{\Delta t}{\Delta x}|s^p_{i-1/2}|\right) \tilde{\mathcal{W}}^p_{i-1/2}, \tag{5.55}$$

where $\tilde{\mathcal{W}}^p_{i-1/2}$ is the limited wave speed. The limited wave speed is obtained by comparing $\mathcal{W}^p_{i-1/2}$ to its upwind value, $\mathcal{W}^p_{I-1/2}$, where

$$I = \begin{cases} i-1 & \text{if} \quad s^p_{i-1/2} > 0, \\ i+1 & \text{if} \quad s^p_{i-1/2} < 0. \end{cases} \tag{5.56}$$

This increased the stencil from three to five grid-points and thus an additional ghost cell is required at each boundary. For example, the waves at the left boundary $\mathcal{W}^p_{1/2}$ can be compared to $\mathcal{W}^p_{-1/2}$, which is computed from cells 0 and -1.

The limited wave, $\tilde{\mathcal{W}}^p_{i-1/2}$, is computed from a flux limiter function ϕ,

$$\tilde{\mathcal{W}}^p_{i-1/2} = \phi(\theta_{i-1/2})\mathcal{W}^p_{i-1/2}, \tag{5.57}$$

where its argument, $\theta^p_{i-1/2}$, is determined from the projection of $\mathcal{W}^p_{I-1/2}$ onto $\mathcal{W}^p_{i-1/2}$,

$$\theta^p_{i-1/2} = \frac{\mathcal{W}^p_{I-1/2} \cdot \mathcal{W}^p_{i-1/2}}{\mathcal{W}^p_{i-1/2} \cdot \mathcal{W}^p_{i-1/2}}. \tag{5.58}$$

A variety of different choices exist for the flux limiter, ϕ, which all produce similar, but slightly different, behaviour. Zhang et al. (2015) provide a thorough review of ten different flux limiters. One of the simplest to impose is the minmod (Roe, 1986) function

$$\phi(\theta) = \text{minmod}(1, \theta) = \max(0, \min(1, \theta)), \tag{5.59}$$

and was chosen as the flux limiter for this high-resolution scheme. A comparison between three simulations using the minmod, superbee (Roe, 1986; Kemm, 2011) and the monotonized central (Van Leer, 1974) flux limiters revealed no noticeable change in the solution. When the solution is relative smooth $\mathcal{W}^p_{I-1/2} \sim \mathcal{W}^p_{i-1/2}$, giving $\theta \sim 1$ and $\tilde{\mathcal{W}}^p_{I-1/2} \sim \mathcal{W}^p_{i-1/2}$. Conversely, when there is a rapid change in the solution near the interface, either θ is large, in which ϕ takes the value 1 and $\tilde{\mathcal{W}}^p_{I-1/2} \sim \mathcal{W}^p_{i-1/2}$ or θ is close to 0 and thus the correction term is as well. Thus, producing the required limiter behaviour.

Runge-Kutta 4th order method for the source term correction

A 4th-order Runge-Kutta scheme was used to solve the system of ODEs (5.29) representing the viscous source terms. Note that as the first component of ψ is zero, this reduces to a scalar ODE. The Runge-Kutta method is an iterative process that defines coefficients $\mathbf{k}_i$ (Süli and Mayers, 2003) as follows:

$$\mathbf{k}_1 = \Delta t \boldsymbol{\Psi}\left(\mathbf{Q}^{*n}_{i}\right); \tag{5.60}$$

$$\mathbf{k}_2 = \Delta t \boldsymbol{\Psi}\left(\mathbf{Q}^{*n}_{i} + \mathbf{k}_1/2\right); \tag{5.61}$$

$$\mathbf{k}_3 = \Delta t \boldsymbol{\Psi}\left(\mathbf{Q}^{*n}_{i} + \mathbf{k}_2/2\right); \tag{5.62}$$

$$\mathbf{k}_4 = \Delta t \boldsymbol{\Psi}\left(\mathbf{Q}^{*n}_{i} + \mathbf{k}_3\right), \tag{5.63}$$

where

$$\boldsymbol{\Psi}(\mathbf{Q}^{*n}_{i}) = \begin{pmatrix} 0 \\ \frac{h^n_i\left(1-h^n_i\right)}{\Delta x^2}\left[\xi^n_{i+1} - 2\xi^n_i + \xi^n_{i-1}\right] \end{pmatrix}, \tag{5.64}$$

$$\xi^n_i = m^n_i\left[\frac{1}{(1-h^n_i)Re_1} + \frac{1}{h^n_i Re_2}\right] \tag{5.65}$$

and for simplicity we have dropped the * from the intermediate variables. The 4th-order Runge-Kutta method is then used to compute the values of h^{n+1}_i and m^{n+1}_i at the next time step

$$\mathbf{Q}^{n+1}_{i} = \mathbf{Q}^{*n}_{i} + \frac{1}{6}\left(\mathbf{k}_1 + 2\mathbf{k}_2 + 2\mathbf{k}_3 + \mathbf{k}_4\right). \tag{5.66}$$

Although an explicit method, the 4th-order Runge-Kutta scheme produces $\mathcal{O}\left(\Delta t^5\right)$ error (Süli and Mayers, 2003). This was compared to a Crank-Nicholson semi-implicit method, which produced near-identical results.

CFL-condition

A necessary, but not sufficient, condition for the stability is the CFL-condition (Courant et al., 1928), which states “A numerical method can be convergent only if its numerical domain of dependence contains the true domain of dependence of the PDE, at least in the limit as Δt and Δx go to zero.” (LeVeque, 2002, p. 69). The Courant number Cr is defined as a maximum over all cells i and eigenvalues p

$$Cr = \frac{\Delta t}{\Delta x}\max_{i,p}|\lambda^p_i| \tag{5.67}$$

This represents the number of cells travelled by the fastest travelling wave in a single time step. For a three-point scheme, In order for the domain of dependence of the numerical scheme to contain the domain of dependence of the PDE, it is required that the waves do not interact with the solution in neighbouring cells. This is equivalent to $Cr < 1$. Further, if $Cr < 1/2$ then the fastest forwards-travelling and backwards- travelling waves do not interact. A five-point scheme provides a less restrictive condition than a three-point scheme (Laney, 1998), but the flux limiters may produce a three-point scheme in certain regions of the flow. However, $Cr < 1$ is only a necessary, not sufficient. Therefore, there may be stricter conditions on the time-step size and often, smaller values are used. To keep the ratio, $\Delta t/\Delta x$, fixed, the Courant number is imposed across the simulation and thus the time-step

$$\Delta t = \frac{Cr\Delta x}{\max\limits_{i,p} |\lambda_i^p|} \tag{5.68}$$

is determined from it. By imposing the Courant number Cr rather than fixing the time-step enables larger time-steps to be used in periods where the maximum wave speeds are smaller.

Linear stability analysis

The particular form of the combined momentum diffusion term in the two-layer shallow water model can further restrict the range depth h and momentum m which produce stable solutions. To explore this further, linear stability analysis is conducted on the system of equations (5.20). First, it is noted that the constant solution $\mathbf{q}_0 = (h_0, m_0)$ satisfies the system of equations for all $h_0 \in (0, 1)$ and $m_0 \in \mathbb{R}$. Next a perturbation $\mathbf{q}' = (h', m')$ is introduce, where $|h'|, |m'| \ll 1$ and it is assumed that $h_0 + h' \in (0, 1)$. To study linear stability analysis, consider $\mathbf{q} = \mathbf{q}_0 + \mathbf{q}'$. Substituting into the system of equations (5.20) yields

$$\frac{\partial\, \mathbf{q}'}{\partial\, t} + \mathcal{A}(\mathbf{q}_0)\frac{\partial\, \mathbf{q}'}{\partial\, x} = \begin{pmatrix} 0 \\ \psi(\mathbf{q}) \end{pmatrix} + \mathcal{O}(h'^2, m'h', m'^2), \tag{5.69}$$

where

$$\psi(\mathbf{q}) = \frac{1-h_0}{Re_2}\left(m'_{xx} - \frac{m_0 h'_{xx}}{h_0}\right) + \frac{h_0}{Re_1}\left(\frac{m_0 h'_{xx}}{(1-h_0)} + m'_{xx}\right) + \mathcal{O}(h'^2, m'h', m'^2). \tag{5.70}$$

To study linear stability consider the following forms for h' and m'

$$h' = A\exp(ikx + \omega t), \tag{5.71}$$

$$m' = B\exp(ikx + \omega t), \tag{5.72}$$

for some constants $A, B \in \mathbb{R}$. Note that the wavenumber k and growth rate ω can be chosen as the same for both h' and m' without loss of generality from the mass conservation equation. With this form, the diffusive term $\psi(\mathbf{q})$ can be expressed

$$\begin{aligned}\psi(\mathbf{q}) =& -k^2\left(\frac{m_0h_0}{(1-h_0)Re_1}-\frac{m_0(1-h_0)}{h_0Re_2}\right)h' - k^2\left(\frac{1-h_0}{Re_2}+\frac{h_0}{Re_1}\right)m' && (5.73)\\ \equiv& -k^2\psi_h h' - k^2\psi_m m', && (5.74)\end{aligned}$$

where quadratically small terms are neglected. Combining this with the left-hand side of (5.69) yields the following system of equations for the coefficients A and B

$$\begin{pmatrix} \omega & ik \\ ik\mathcal{P}(\mathbf{q}_0)+\psi_h & ik\mathcal{Q}(\mathbf{q}_0)+\psi_m+\omega \end{pmatrix}\begin{pmatrix} A \\ B\end{pmatrix} = \begin{pmatrix} 0 \\ 0\end{pmatrix}, \qquad (5.75)$$

in which the following expressions have been used to simplify

$$\begin{aligned}\frac{\partial h'}{\partial x} &= ikh', && (5.76)\\ \frac{\partial h'}{\partial t} &= \omega h', && (5.77)\\ \frac{\partial m'}{\partial x} &= ikm', && (5.78)\\ \frac{\partial m'}{\partial t} &= \omega m'. && (5.79)\end{aligned}$$

The system of equations (5.75) can only yield non-trivial solutions if the determinant of the matrix is zero. Thus, the growth rate ω is the solutions of the following quadratic equation

$$\omega^2 + (ik\mathcal{Q}(\mathbf{q}_0)+\psi_m)\omega - ik\psi_h + k^2\mathcal{P}(\mathbf{q}_0) = 0 \qquad (5.80)$$

For a given Re_1, Re_2, h_0, m_0 and k this equation yields two complex roots for the growth rate ω with the stability of the solution determined by the real part of each root. If both of the real parts of these two roots are less than zero, then the constant solution to the system of equations is linearly stable. If one is positive then the system of equations is linearly unstable for the given Re_1, Re_2, h_0, m_0 and k. Note than in the inviscid limit $Re_1, Re_2 \to \infty$, this reduces to

$$\omega = \pm\frac{k}{2}\sqrt{-\mathcal{Q}(\mathbf{q}_0)^2 - 4\mathcal{P}(\mathbf{q}_0)}, \qquad (5.81)$$

which gives the following condition for the equation to be linearly unstable

$$-\mathcal{Q}(\mathbf{q}_0)^2 - 4\mathcal{P}(\mathbf{q}_0) > 0. \qquad (5.82)$$

This is identical to the condition for the eigenvalues of the conservative part of the system of equations (5.27) to be no longer be real and distinct (i.e., for the system to no longer be hyperbolic). The growth rate equation (5.81) is solved numerically in MATLAB for a range of conditions Re_1, Re_2, h_0, m_0 and k. Two key simplifications are observed: First, the stability of a solution is independent on the magnitude of Re_1, Re_2, and only their relative magnitude contributes to whether a solution is stable or not. With equal Reynolds numbers, $Re_1 = Re_2$, the same stability as the inviscid case is produced. Second, the stability of a solution is independent of the wavenumber k. However, the magnitude of the growth is dependent on both the Reynolds numbers and wavenumber k. Thus the studyis restricted to a limited number of Reynolds number ratios $Re_1/Re_2 = 1, 2, 4, 11, 41, 100$ to illustrate how the stability changes over a range of h_0 and m_0.

The linearly stability for a given pair (h_0, m_0) is displayed in figure 5.4. Similarly to the hyperbolicity plots, figure 5.2, the stability is also plotted in (h_0, u_0)-space, where $u_0 = m_0/h_0$. The coloured regions correspond to the lowest value of the Reynolds number ratio for which the solution is linearly unstable. For example dark blue regions are only linearly unstable for $Re_1/Re_2 = 1$ and yellow regions are linearly unstable for all ratios considered. White regions are stable for all the Reynolds number ratios considered. As the Reynolds number ratio is increased, significantly more regions of (h_0, m_0) space become unstable. During the early stages of the flow, where the flow depth is greater than 1 and the momentum is large solutions may become unstable. Finally, we note that if this analysis is repeated with Re_2 fixed and Re_2/Re_1 varied a similar pattern is observed, but with the stability plots reflected about $h_0 = 0.5$. This arrives naturally from the symmetry of the problem discussed earlier.

Critically, this analysis reveals that when the Reynolds numbers in each layer are distinct, the simulations can be unstable to a viscous-driven instability as small perturbations growing in time. Even though there is a small amount of numerical diffusion present in the finite volumes scheme small perturbations to h and m can grow in time for a suitably large viscosity ratio, which would be damped out for an equation Reynolds number case. This was observed in the highest Reynolds number ratios studied in this chapter and in order to counteract this, a small amount of mass diffusion was introduced into the model. This provides an additional stabilising affect to the small perturbations and acts to smooth them out before they grow too large. As demonstrated later in the chapter, the mass diffusion has negligible effect on the solution provided the diffusion coefficient is chosen to be small enough.

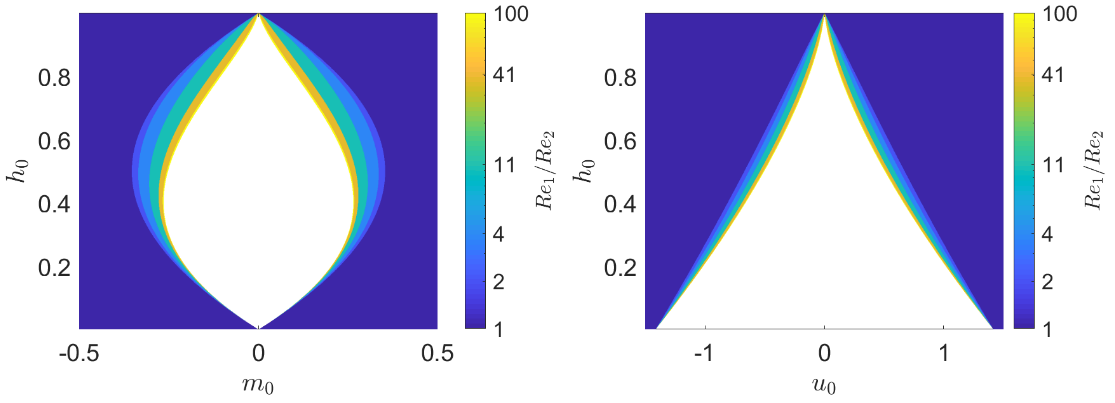

(a) (b)

Figure 5.4: Stability of linearly perturbed solution in: (a) (h_0, m_0)-space and (b) (h_0, u_0)-space. Dark blue represents the region that is linearly unstable for $Re_1/Re_2 = 1$. Each subsequent colour (up to yellow, where $Re_1/Re_2 = 100$) represents the additional region that becomes unstable as the Reynolds number ratio is increased. The region coloured white is stable for all Reynolds number ratios considered. As discussed in the text, the stability is independent on magnitude of the Reynolds numbers (only their relative magnitude) and the wavenumber k.

The conservation of mass is adjusted to include this diffusion term as follows

$$\frac{\partial h}{\partial t} + \frac{\partial m}{\partial x} = D_1 \frac{\partial^2 h}{\partial x^2}, \tag{5.83}$$

where D_1, the diffusion coefficient, is constant. Similar to viscous source terms, this contribution is solved during the Runge-Kutta step by adjusting the source vector $\mathbf{\Psi}$ to be

$$\mathbf{\Psi}(\mathbf{Q}^{*n}_{i}) = \begin{pmatrix} D_1 \frac{h^n_{i+1} - 2h^n_i + h^n_{i-1}}{\Delta x^2} \\ \frac{h^n_i (1 - h^n_i)}{\Delta x^2} \left[\xi^n_{i+1} - 2\xi^n_i + \xi^n_{i-1}\right] \end{pmatrix}, \tag{5.84}$$

Inclusion of the mass diffusion term is difficult to justify as it breaks mass conservation. Further, the mass conservation is used to simplify the momentum equation, which further impacts the validity of the model. However, inclusion of the mass diffusion term stabilises the equations and allows for a larger range of Reynolds number ratios to be studied. The instability that caused by the anti-diffusion is shear-related. In a physical system small perturbations to the surface would rupture the surface and lead to dispersion or entrainment allowing them to dissipate. However, no such mechanism is present in our system without the inclusion of the mass diffusion term.

5.2.2 Verification

To explore grid resolution and the effect of other parameter values on the numerical scheme, a series of tests were performed varying each parameter individually for the two-layer shallow-water problem with the following initial conditions

$$h_0(x) = \varepsilon_0 + \frac{1 - 2\varepsilon_0}{2}(1 - \tanh(\zeta_0 x)) \tag{5.85}$$

$$u_0(x) = 0, \tag{5.86}$$

where ε_0 and ζ_0 are constants. This provides similar conditions to the dam break provided ε_0 is small, but imposes that the depth is non-zero in both layers, which would lead to the problem no longer being hyperbolic. As discussed in section 5.2.1, the linearised scheme may not accurately capture the solution near the presence of shocks. Thus, the step function used for the DNS simulations is replaced by a tanh profile to smooth the initial condition. The constant $\zeta_0 = 10$ is chosen and motivated in section 5.2.2.

Assuming that these constants are fixed, the only physical parameters that can be varied in the model are the Reynolds number of each layer, Re_i. The parameter of a numerical model that can be varied are the number of cells N_x, the Courant number, Cr, and the mass diffusion parameter D_1.

Visualisation

For $\varepsilon_0 = 0.01$, depth and momentum profiles evolving in time, with $Nx = 1600, Cr = 0.02, D1 = 1/1000, Re_1 = 1000$ and $Re_2 = 1000$, are presented in figure 5.5. Initially, a right-propagating wave in the basal layer and a left-propagating wave in the above fluid can be observed as the density difference drives the denser fluid to the right. These waves reflected off the side walls and back towards the centre numerous times during the duration. As expected, the depth profile remains rotationally symmetric about $x = 0, y = 0.5$ and the momentum symmetric about $x = 0$.

Resolution

Grid resolution was studied by varying N_x with all other parameters fixed. Depth h and momentum m profiles are plotted in figure 5.6 for various values of N_x at $t = 13.5$. For the lowest values of N_x considered, significant numerical diffusion is present. As N_x decreases, the profiles sharpen and appear to converge towards a

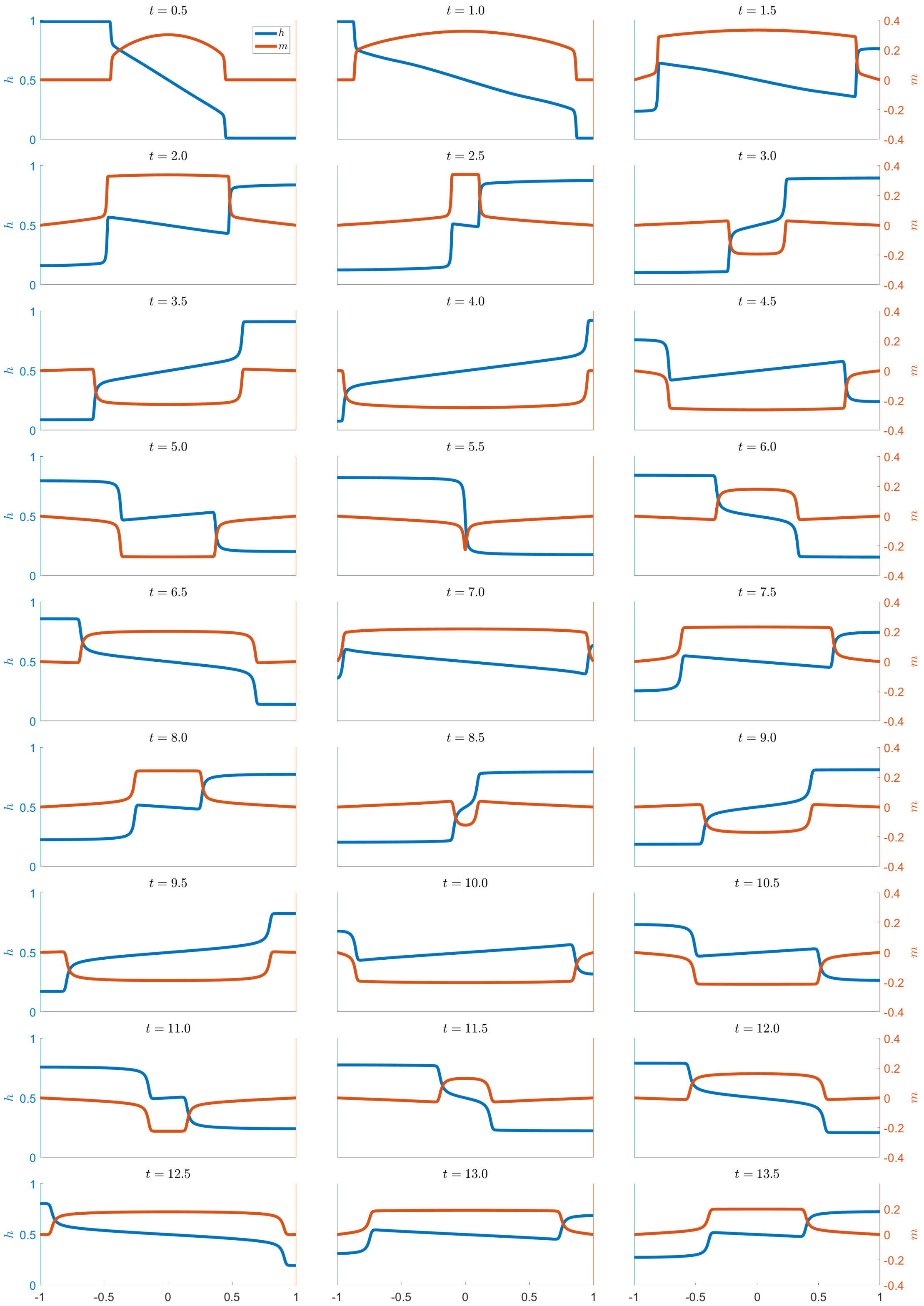

Figure 5.5: Evolution of the depth, h, and momentum over time with the following parameters: $N_x = 1600, Cr = 0.02, D_1 = 10^{-3}, Re_1 = 1000, Re_2 = 1000$.

fixed value. A similar study, with fixed $N_x = 1600$ and varying the Courant number Cr, revealed that the variations in time-step (which is inversely proportional to the Courant number, are negligible. Finally, in figure 5.7, the convergence of the ℓ_1-error defined in chapter 2 for the two variables with either fixed spatial resolution or fixed Courant number Cr is presented, also at $t = 13.5$. The analytical solution for this problem is not known, so instead the error are calculated relative to $Nx = 6400$ and $Cr = 0.02$ for the spatial error and $N_x = 1600$ and $Cr = 0.0025$ for the temporal error. Gradients of these lines provide the scaling of the error in terms of Δx and Δt. The error for both variables scales approximately as Δx and Δt.

All simulations conducted henceforth in this chapter use $Nx = 1600$ and $Cr = 0.02$. The choice of spacial resolution was chosen as the highest value, which still had a reasonable run time of order a couple of hours. A low Courant number was required for stability at the lowest Reynolds numbers considered. Using a step profile required an order of magnitude larger number of spatial cells to provide converged solutions. Further, the majority of the error arises during the early stages of the flow $t < 0.5$ signifying that sharp initial conditions required significantly more cells. The error still decreases proportional to Δx and Δt, but a reduced number of cells is required to provide a sufficiently resolved solution. As a balance between computational time and capturing the initial conditions of the DNS motivates the choice $\zeta_0 = 10$ and $N_x = 1600$.

Mass diffusion

Finally, the affect of the mass diffusion parameter D_1 on the simulations is demonstrated in figure 5.8. At time $t = 12.5$, the solutions are coincident for $D_1 \leq 10^{-4}$ and within a similar accuracy to the spatial error for $D_1 = 10^{-3}$. The highest value of diffusion considered $D_1 = 10^{-2}$ smooths the solution considerably and is too large to use.

5.3 Results and Discussion

Two studies are conducted using the model presented in this chapter. First, the ratio of the Reynolds number is kept fixed at unity and the Reynolds number in both layers is varied at the same time. Second, the Reynolds number of the top layer is fixed at $Re_1 = 1000$ and the basal layer Reynolds number is varied. In this section, unless otherwise stated, all simulations were conducted with the following parameters: $N_x = 1600$, $Cr = 0.02$, $D_1 = 10^{-3}$, $\varepsilon_0 = 10^{-2}$. Smaller values of the wetted layer ε_0 lead to stable solutions when the Reynolds number in each layer were equal (or similar). However, for all but the lowest Reynolds number considered, the

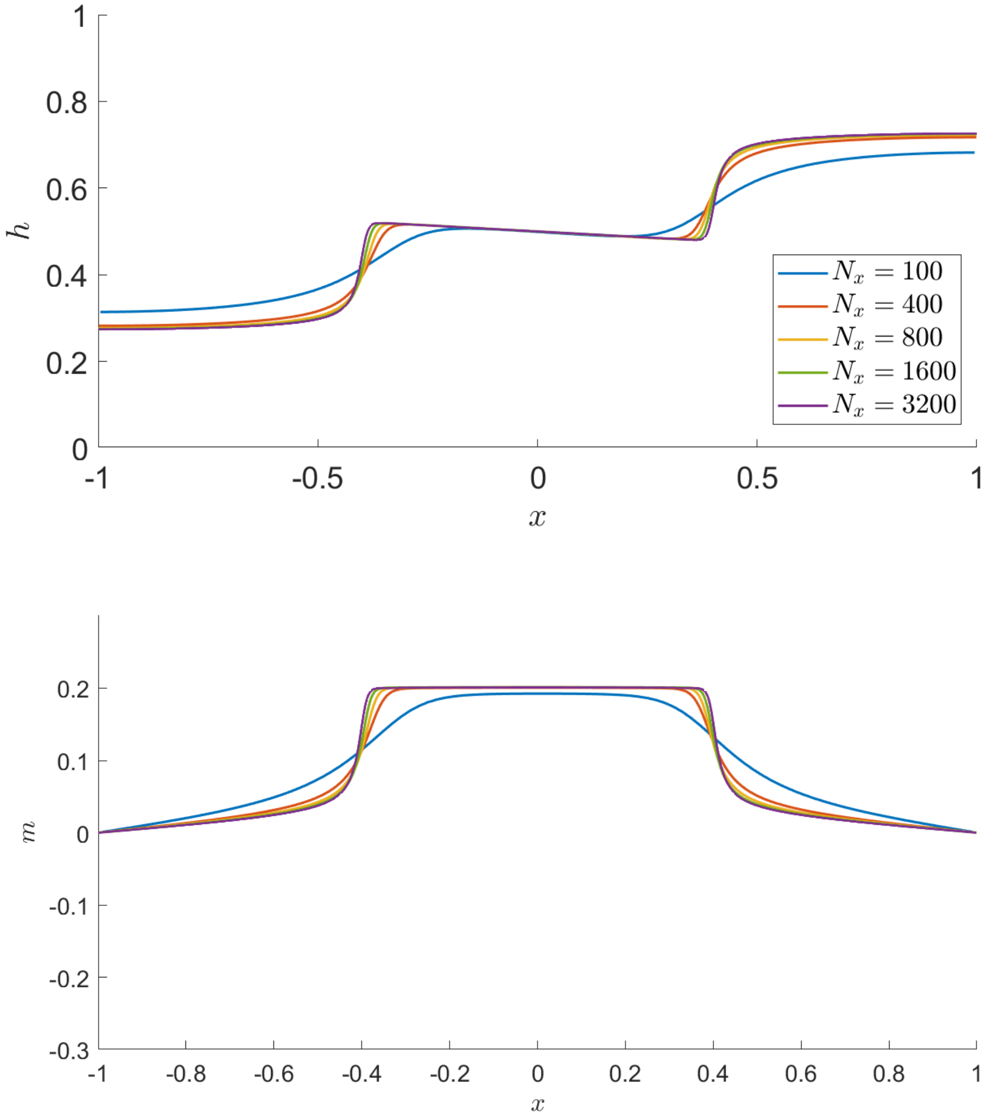

Figure 5.6: Depth h (top) and momentum m (bottom) profiles at $t = 12.5$ for various values of N_x. Other parameters are: $Cr = 0.02, D_1 = 0, Re_1 = 1000, Re_2 = 1000$. As N_x increases, the profiles converge towards a value. For low values of N_x significant numerical diffusion can be observed.

solutions contained regions with velocities greater than one, and as high as 1.3 for the inviscid case, when $\varepsilon_0 = 10^{-4}$. This could result in a viscosity driven instability and divergence of the solution when the Reynolds number ratio is large. A wetting layer thickness $\varepsilon_0 = 10^{-2}$ produced peak velocities less than 0.9 for an inviscid case. The mass diffusion $D_1 = 10^{-3}$ was only required to make the highest two viscosity ratios stable. Further, when the viscosity ratio was fixed, stability was still achieved without mass diffusion. The values of D_1 and ε_0 will quantitatively change the

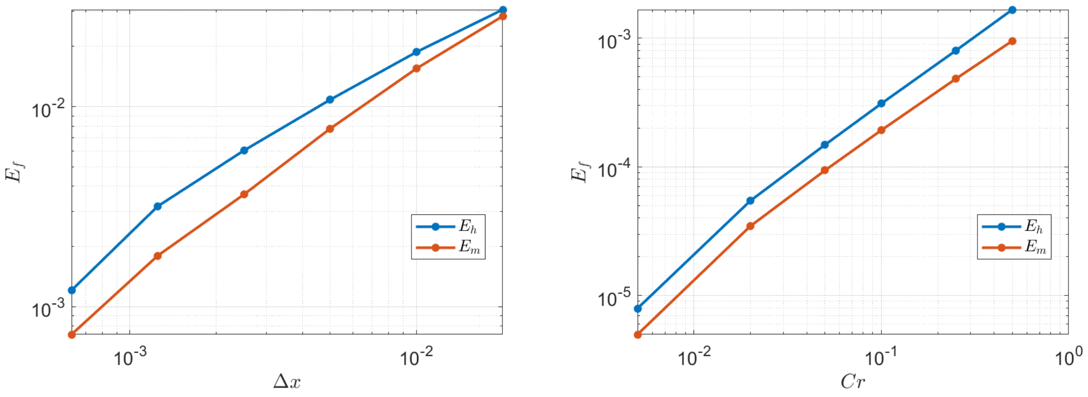

(a) (b)

Figure 5.7: ℓ_1-error for depth E_h and momentum E_m at: (a) fixed Courant number $Cr = 0.02$ (a) and $N_x = (100, 200, 400, 800, 1600, 3200)$ and (b) fixed $N_x = 1600$ and $Cr = (0.5, 0.25, 0.1, 0.05, 0.02, 0.005)$. Other parameters for these graphs are $D_1 = 1/1000$, $Re_1 = 1000$ and $Re_2 = 1000$. The gradient of the lines (computed using the end points) provide the convergence rate of the scheme. $E_h \sim \Delta x^{0.93}$, $E_m \sim \Delta x^{1.06}$, $E_h \sim \Delta t^{1.01}$, $E_m \sim \Delta t^{0.99}$.

solutions by a small amount, but they are required to study the highest viscosity ratios considered here. Keeping these values consistent across all simulations enabled a consistent comparison between each case considered.

In the early stages of the flow, before the waves have reflected off the $x = -1$ and $x = 1$ boundaries, the positions of wavefronts heads are defined

$$x_L = \min_{x \in (-1,0)} \left(\frac{\partial h}{\partial x} \right), \tag{5.87}$$

$$x_R = \min_{x \in (0,1)} \left(\frac{\partial h}{\partial x} \right). \tag{5.88}$$

Defining the head positions based on a depth threshold proved less effective because the high variance in head position as the threshold value changed for the lowest Reynolds number cases.

Varying Reynolds number in both layers

First, the effect of varying the Reynolds number in both layers simultaneously, whilst keeping the ratio fixed at unity, i.e. $Re_1 = Re_2$ is studied. At $t = 0.5$ a significant effect on the flow profiles can be observed even for the highest Reynolds number (1000), when compared to an inviscid case ($Re_i = \infty$), figure 5.9a. Decreasing the Reynolds number decreased the propagation speed of both wavefronts and smoothed out the momentum profiles. Although reducing the Reynolds number in both layers

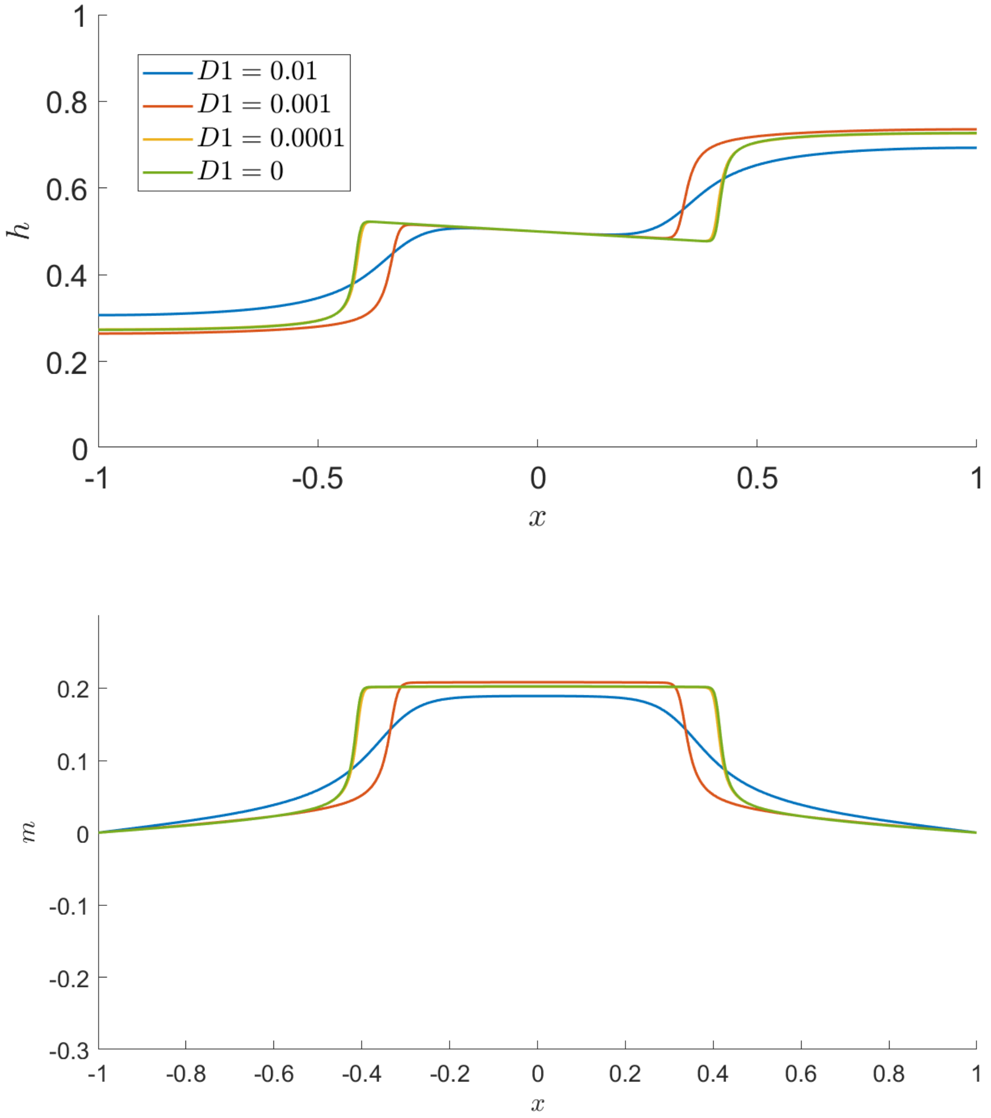

Figure 5.8: Depth h (top) and momentum m (bottom) profiles at $t = 12.5$ for four different values of D_1. Other parameters are: $N_x = 1600, Cr = 0.02, Re_1 = 1000, Re_2 = 1000$.

reduces the maximum momentum value, the change is less noticeable. In particular, the depth and momentum values for the inviscid case and highest Reynolds number cases are coincident except for the regions near the head. Thus viscosity is only non-negligible when the flow gradients are large.

The symmetric momentum profile of the $Re_1 = Re_2 = 1000$ case leads to a velocity profile that is increasing up to a maximum value just before the head of the flow at around $x = 0.4$, figure 5.11. Conversely, the velocity in the upper layer takes its most negative value at around $x = -0.4$. When the Reynolds number of each layer are equal, the smoothing displays a symmetric pattern between the two layers, figure 5.11a&b. The maximum value of the velocity initially decreases with increasing viscosity, but below $Re_i = 200$ this value does not change. Similarly to when only the bottom layer Reynold number is decreased, as both Reynolds number are decreased the propagation of the speed of the wavefronts is reduced. Near $x = 0.4$ for the basal layer and $x = -0.4$ for the top layer, the two highest viscosity cases ($Re_i = 15, 25$) show a highly smoothed behaviour near the wavefronts of the flow and it appears as though these flows are travelling faster. However, the momentum in these regions is still negligible, figure 5.9a. This arises from the viscous diffusion providing a small amount of momentum to travel into the thin wetting layer ahead of the wavefront. Similarly to the depth and momentum profiles, the velocity continues to smooth out as time increases.

Just before the reflected wavefronts cross, further viscous diffusion can be observed, figure 5.9b. The wavefronts remain clearly visible for the highest three Reynolds numbers as the sharp jump in depth just to the left and right of $x = 0$. The front position of the reflected wave becomes harder or even impossible to identify by eye for the three lower Reynolds numbers. Just after the third and fourth times the wave fronts cross, figure 5.9c and figure 5.9d, respectively, all profiles can be seen to be smoothed, but the highest three Reynolds number still maintain a clearly defined wave front. In particular, the highest two cases the smoothing is likely to be a result of the grid resolution rather than the viscosity (recall the spatial resolution study, figure 5.6). Critically, the separation of the wave fronts appears to remain roughly constant for the later stages of the flow indicating that viscosity plays a significant role on the wavefront speed only during the initial stages of the flow when the gradients are large.

Varying basal layer Reynolds number

To study the effects of varying the Reynolds number ratio, only one Reynolds number needed to be varied. This is because the problem is invariant under the transform h to $1 - h$, x to $-x$ and Re_1 to Re_2. This produces the momentum profiles that were symmetric about $x = 1$ when the Reynolds number of each layer was equal and forces $h(1, t) = 1/2 \ \forall t$. The top layer Reynolds number was fixed to be 1000 and four decreasing values of the base layer Reynolds number were chosen along with $Re_2 = 1000$ for comparison. The depth and momentum profiles at four times are displayed in figure 5.10.

At $t = 0.5$, just after the release, the asymmetry of the flow is clear,

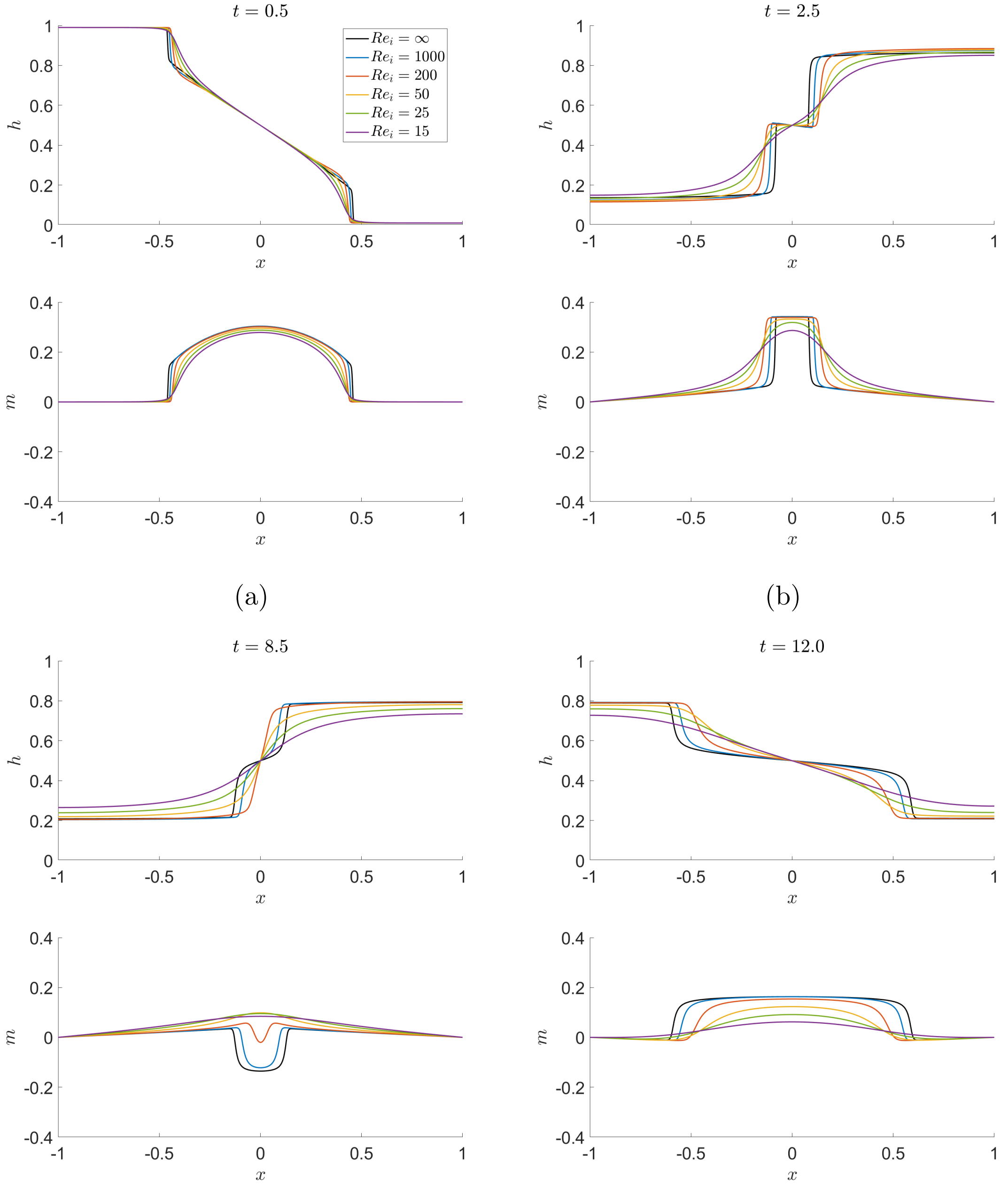

(a) (b)

(c) (d)

Figure 5.9: Depth (top of each pair) and momentum (bottom of each pair) profiles for the lock exchange problem with both layers having the same Reynolds number compared to the inviscid case $Re = \infty$. Profiles are at times: (a) 0.5, (b) 2.5, (c) 8.5 and (d) 12.

figure 5.10a. The right propagating wavefront of the lower layer travels at reduced speed with decreasing Reynolds number, similar to when the Reynolds number in both layers are increased. Further, the depth at $x = 0$ no longer takes the value 1/2. Predominately, the viscosity acts to prevent the flow in the basal layer from travelling to the right. This can be seen clearly in the asymmetric momentum profiles.

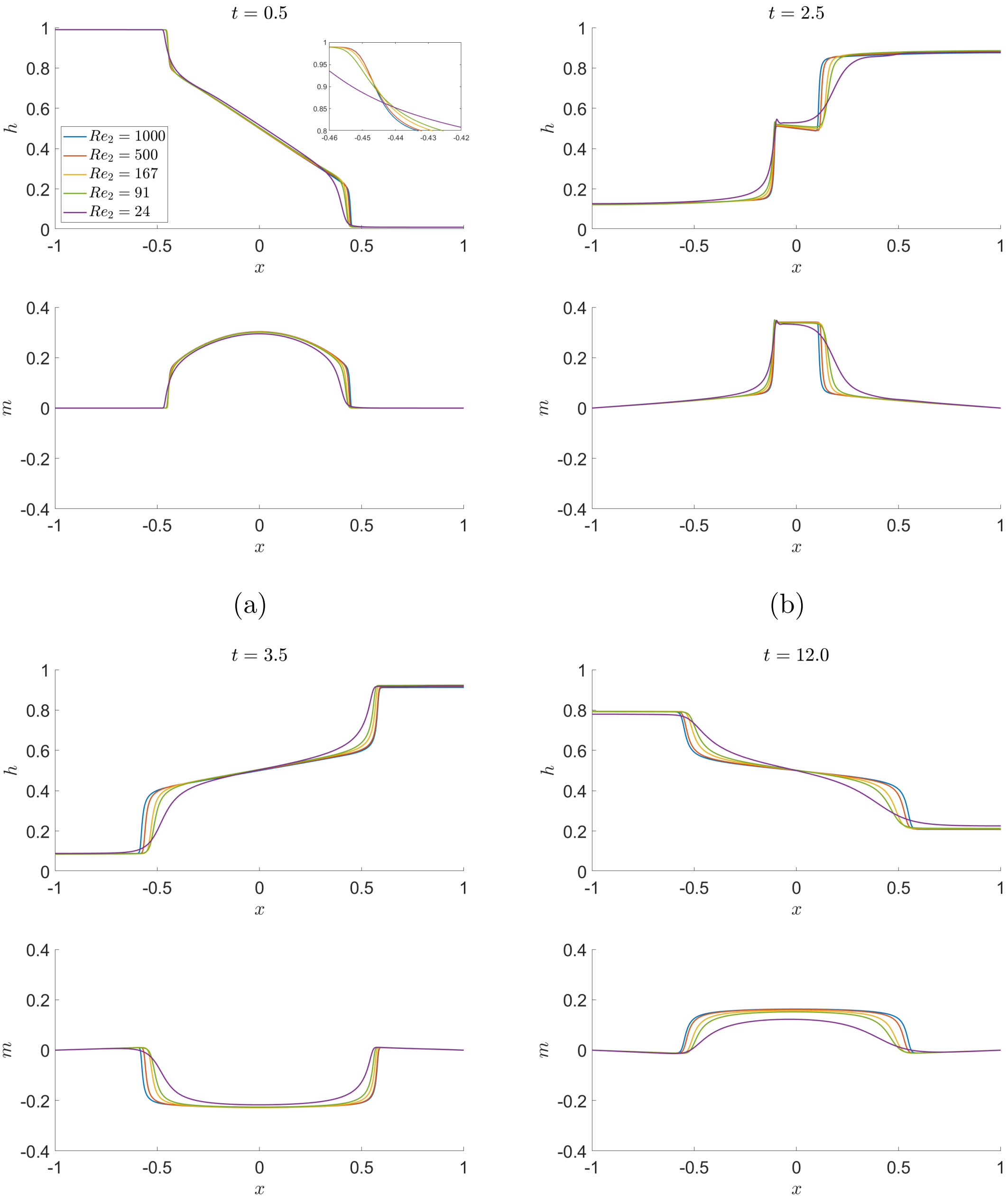

(a) (b)

(c) (d)

Figure 5.10: Depth (top of each pair) and momentum (bottom of each pair) profiles for the lock exchange problem with both layers having the same Reynolds number compared to the inviscid case $Re = \infty$. Profiles are at times: (a) 0.5, (b) 2.5, (c) 3.5 and (d) 12. Inset in (a) shows the head of the left propagation wavefront.

Varying the viscosity in just the basal layer has a significantly different effect on both top and basal layer velocity profiles, figure 5.11c&d. In contrast to varying the Reynolds number in both layers, the velocity maximum in the basal layer decreases with decreasing Reynolds number and the top layer maximum velocity only shows minimal variation. The variation in the top layer is less pronounced and focused in the region where it is thickest, $x > 0$. Later in time, when the wave fronts

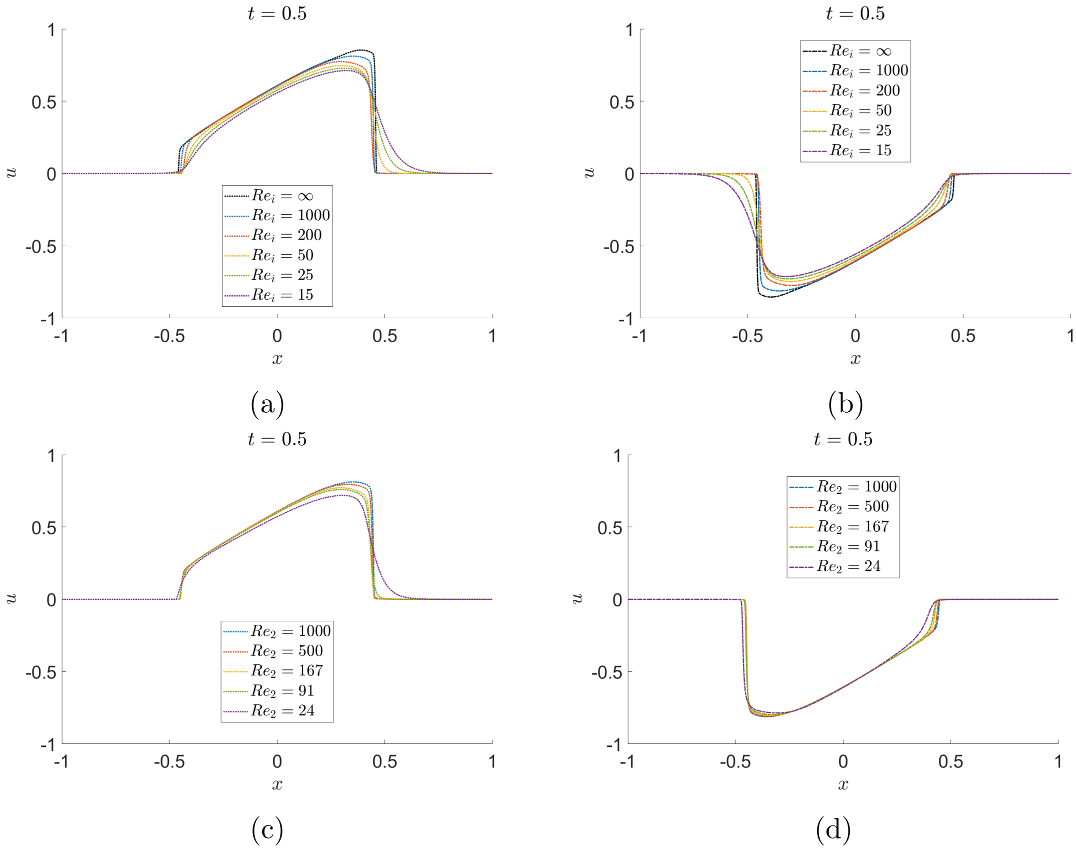

(a) (b)

(c) (d)

Figure 5.11: Velocity profiles for the top (a&c) and bottom (b&d) at $t = 0.5$. The top two graphs (a&b) vary the Reynolds number in both layers, whereas the bottom two graphs (c&d) fix the top layer Reynolds number ($Re_1 = 1000$) and vary the basal layers Reynolds number Re_2. Top layer velocity is computed $u_1 = -m/(1-h)$ and basal layer $u_2 = m/h$.

have reflected off the side walls and the deepest part of the flow now occurs in $x > 0$, the viscosity provides a strong affect in these regions. Thus, the resulting profiles look more similar to those where both Reynolds numbers are varied. Finally, the sharpening affect of the viscous source term can be observed in figure 5.11d. As the viscosity of the basal layer increases, there is an increased resistance to flow to the right of $x = 0$ as a result of the basal layer being thinner there. This acts to sharpen the velocity profile near $x = 0$.

Contributions to viscous diffusion

The viscous diffusion term ψ is dominant near the waves fronts of the flow as the momentum gradients change most rapidly there. In order to study this diffusion term and the effect on the propagating wave fronts travelling co-ordinates with each

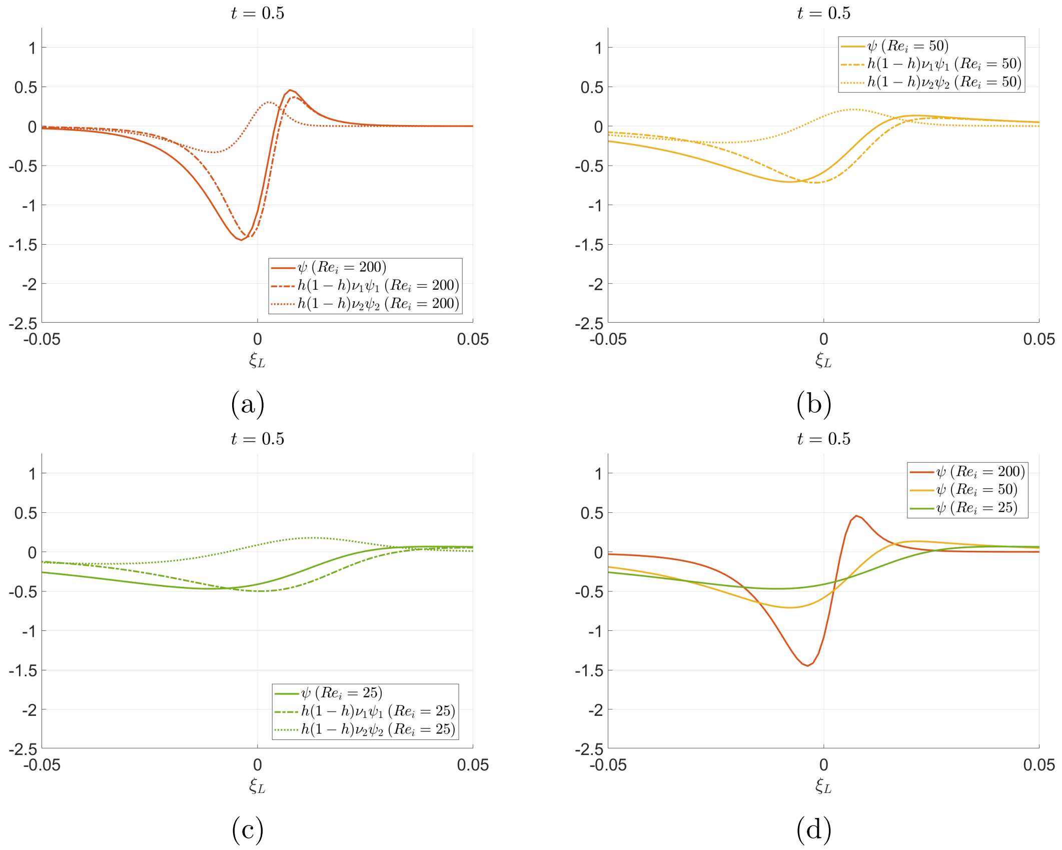

(a) (b)

(c) (d)

Figure 5.12: Total viscous diffusion ψ $(——)$ and the contribution from each layer $h(1-h)\psi_1/Re_1$ $(-\cdot)$ and $h(1-h)\psi_2/Re_2$ $(\cdots)$ at $t = 0.5$ for the left-travelling wavefront, when the viscosity in both layers are equal. (a), (b), and (c) corresponds to the Reynolds number in both layers being 200, 50, and 25, respectively. (d) compares the total viscous diffusion for these three cases. Co-ordinates in the frame of the left travelling wavefront ξ_L are used.

wavefront are introduced:

$$(\xi_L, \tau_L) = (x_L - x, t), \tag{5.89}$$

$$(\xi_R, \tau_R) = (x - x_R, t), \tag{5.90}$$

where x_L (5.87) and x_R (5.88) are the positions of the left- and right-travelling wavefronts, respectively. This allows a more straightforward comparison when comparing layers of different Reynolds number because, positive values of ξ_L or ξ_R both correspond to values ahead of the wavefront.

The contributions to the total viscous diffusion

$$\psi(h, m) = h(1-h)\left(\psi_1/Re_1 + \psi_2/Re_2\right), \tag{5.91}$$

where

$$\psi_1 = \partial^2 \,/\, \partial\, x^2 (m/(1-h)) \quad \text{and} \quad \psi_2 = \partial^2 \,/\, \partial\, x^2 (m/h), \tag{5.92}$$

are plotted for variations of the Reynolds number in both layers, figure 5.12 for the left-propagating wave. When the Reynolds number in each layer is equal, the total viscous diffusion is dominated by the thinner layer of the flow, figure 5.12 a, b, and c, 5.14 a and 5.13 a, but with diminishing effect as the Reynolds number is decreased. Specifically, the dominant contribution comes from layer 1 for the left-propagating wavefront, figure 5.14a, and from layer two for the right-propagating wavefront, figure 5.13a. This is to be expected as the velocity is proportional to $1/h$ or $1/(1-h)$ for the top and basal layers, respectively. The contribution from the thicker layer is not completely negligible and predominately acts to add a slight phase difference between the thinner layer and the total contribution. The size of the phase difference increases with viscosity and acts to push the peak viscous diffusion further behind the head of the flow, figure 5.12. The maximum amount of viscous diffusion occurs in the $Re_i = 200$ case when the layers have equal viscosity at $t = 0.5$. This is because viscous diffusion is a lot stronger in the early stages of the flow for the higher viscosity cases and thus the profiles are already smoothed considerably by $t = 0.5$.

By increasing the viscosity in the basal layer, this symmetry in clearly broken, figure 5.10. At the right-propagating wave, figure 5.13, the total diffusion is dominated by the basal layer diffusion. For both cases ($Re_2 = 167$ and $Re_2 = 24$) the contribution to the total viscous diffusion from the top layer decreases. This is a result of the increased overall diffusion of the flow. For the left-propagating wave, figure 5.14, the dominant contribution to viscosity now comes from the basal layer rather than the top (thinner layer). This results in a phase difference that now pushes the peak of viscous diffusion further to the right (positive ξ_L). Thus, relative to the equal Reynolds number cases, the viscous source term acts to push the velocity peak towards the front of the left-propagating wavefront and increase the overall propagation speed.

Validation against DNS

In this section simulations from the two-layer shallow-water model are compared to the DNS simulations in the previous chapter. As discussed earlier, the two-layer shallow-water model requires a smoothed initial conditions in the form of a tanh profile rather than the sharp interface used in the DNS. To address this, when comparing to the DNS results, the simulations are initialised at $t = 0.5$ with the depth h_{ave} and momentum m_{ave} profiles obtained by depth averaging the DNS simulations at $t = 0.5$. For flow depths less than the wetting layer thickness, $h < \epsilon_0$ and $h > 1 - \varepsilon_0$, are set to ε_0 and $1 - \varepsilon_0$, respectively. Depth and momentum profiles

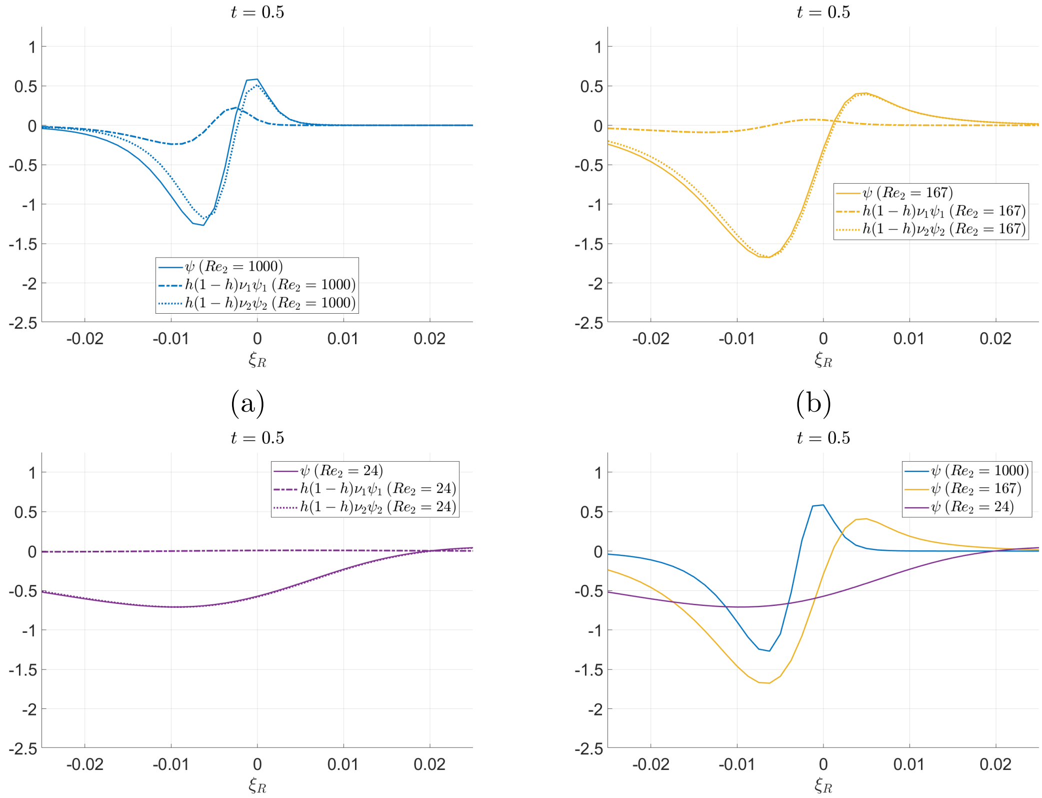

(a) (b)

(c) (d)

Figure 5.13: Total viscous diffusion ψ (——) and the contribution from each layer $h(1-h)\psi_1/Re_1$ ($-\cdot$) and $h(1-h)\psi_2/Re_2$ ($\cdots$) at $t = 0.5$ for the right-travelling wavefront, when the viscosity in the top layer is fixed at $Re_1 = 1000$. (a), (b) and (c) corresponds to the Reynolds number in the basal layers being 1000, 167 and 24, respectively. (d) compares the total viscous diffusion for these three cases. Co-ordinates in the frame of the right travelling wavefront ξ_R are used.

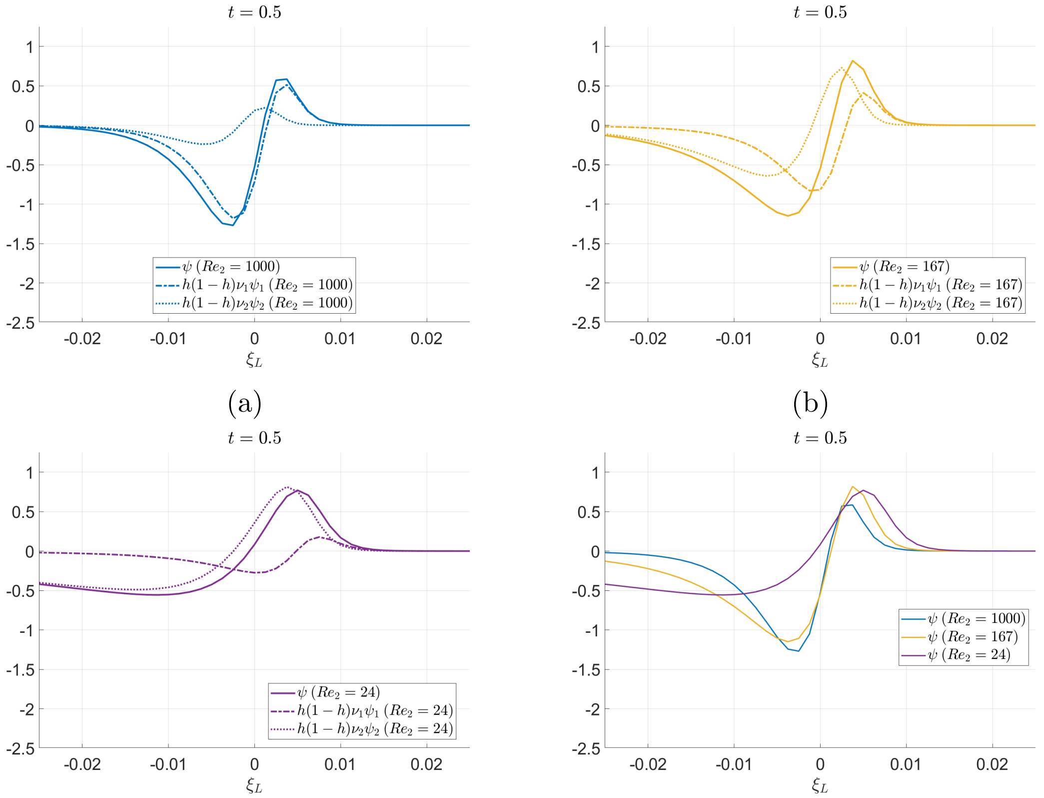

(a) (b)

(c) (d)

Figure 5.14: Total viscous diffusion ψ (——) and the contribution from each layer $h(1-h)\psi_1/Re_1$ (−·) and $h(1-h)\psi_2/Re_2$ ($\cdots$) at $t = 0.5$ for the left-travelling wavefront, when the viscosity in the top layer is fixed at $Re_1 = 1000$. (a), (b) and (c) corresponds to the Reynolds number in the basal layers being 1000, 167 and 24, respectively. (d) compares the total viscous diffusion for these three cases. Co-ordinates in the frame of the left travelling wavefront ξ_L are used.

are displayed in figure 5.15 for three cases corresponding to a basal layer Reynolds numbers $Re_2 = 1000, 500$ and 91 over and for five times including the initial state. The two-layer simulation for $Re_2 = 91$ becomes unstable before reaching $t = 3$ and so further comparison for all three of these cases is not possible.

From the identical initial conditions the shallow-water model predicts as faster propagation speed of the wavefronts and higher momentum at $t = 1$. By $t = 2.5$ the reflected waves front are near $x = \pm 1$ for the DNS simulations, whereas for the shallow-water model they have travelled further reaching $x = \pm 0.5$. The maximum observed value of momentum is similar between the models and nearly exact before the wavefronts reflect of the side walls. Increasing the viscosity in the basal layers produces similar features in both flows: The head speed is reduced; the maximum value of momentum is reduced (although this is less obvious in the shallow-water simulations); and the momentum profile is smoother. This is partly as result of the increased mixing and turbulence that is present when the fluid 1 and fluid 2 viscosities are similar. In particular for $Re_2 = 1000$, the depth and momentum profiles exhibit high-frequency disturbances as a result of the depth-averaging process near $x = \pm 0.5$ at $t = 2.5$. The correct trend is, in general, still reproduced with the highest viscosity case producing the smoothest profile over the length of the flow.

The flow in the DNS is significantly more diffusive indicating that three-dimensional structures and, mixing and entrainment affect the flow dynamics. This can be seen in the depth and momentum profiles after reflection; the DNS remain smooth whereas the two-layer shallow-water model predicts a sharper jump. The mixing and entrainment act to smooth out the profiles. This is further enhanced by the interaction of the flow with the end walls at $x = \pm 1$, which create three-dimensional structures and mixing that the two-layer shallow-water model cannot capture.

5.4 Conclusions and future work

In this chapter, the lock-exchange problem with variable viscosity was studied using the two-layer shallow-water model presented in Hogg et al. (2000) with the inclusion of source term to account for viscous momentum dissipation. The system of two equations was solved using a fractional step method with a high-resolution finite-volume scheme for the conservative part and a fourth-order Runge-Kutta for the source terms. Linear stability analysis revealed that increasing the Reynolds number

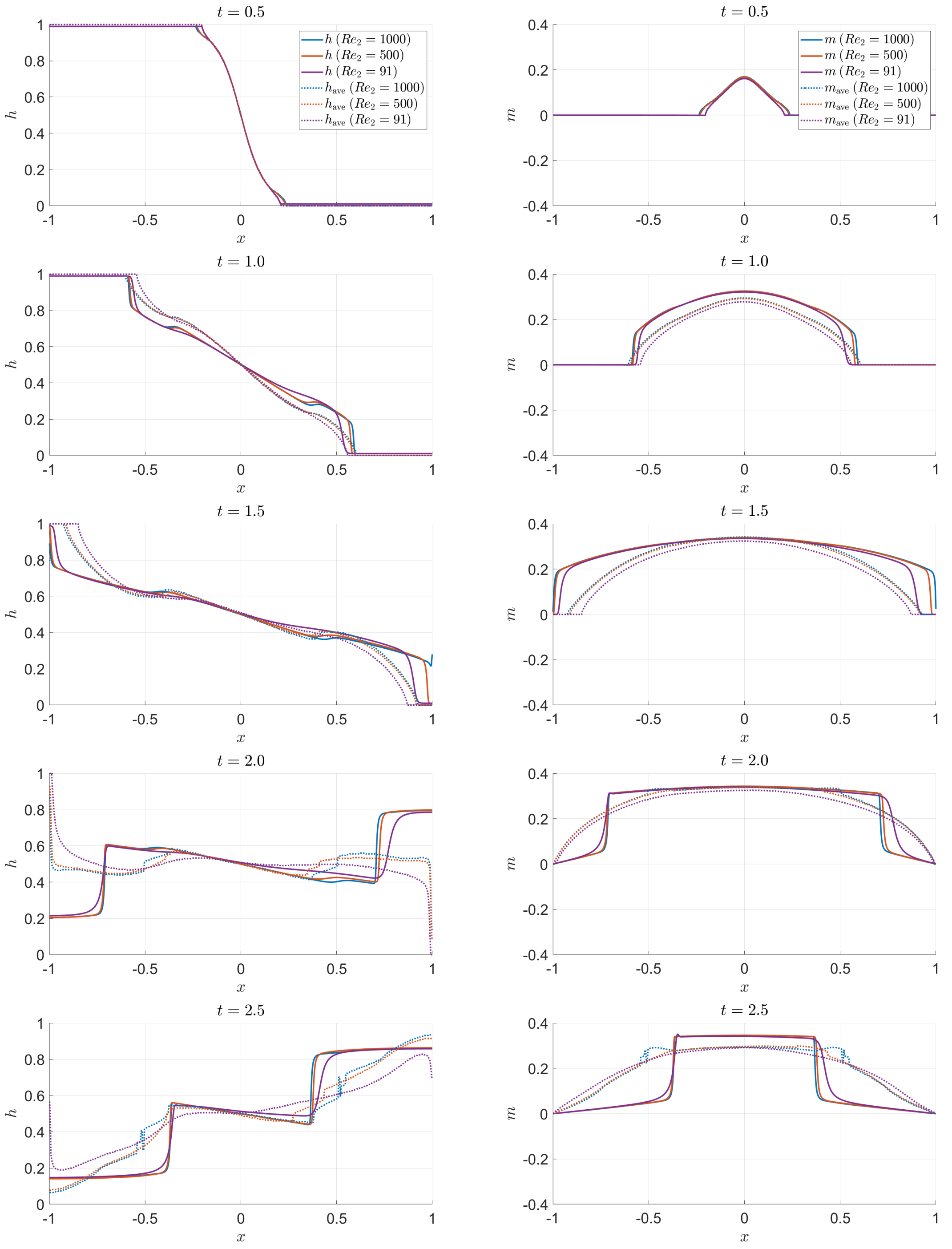

Figure 5.15: Depth-averaged concentration h_{ave} and fluid 2 momentum m_{ave} from the DNS and fluid 2 depth h and momentum m from the two-layer shallow model at five different times. The two-layer shallow water model uses the profiles of h_{ave} and m_{ave} at $t = 0.5$ as initial conditions.

ratio increases the region of the (h_0, m_0) parameter space where the solution is unstable.

When the ratio of the Reynolds numbers was kept fixed, decreasing the Reynolds number smooth the depth and momentum profiles whilst maintaining the symmetry between the two layers. With a fixed ambient Reynolds number, decreasing the basal layer Reynolds number results in an increased asymmetry between the two layers. Further, the right-propagating wavefront reduced whereas the left-propagating wavefront increased in speed. This arose as the ratio of the Reynolds numbers increases because of the phase difference between the contributions from each layer. Comparison with the DNS simulations presented in the previous chapter demonstrated that the two-layer shallow-water model can qualitatively capture some of the key features of the flow, such as the smoothing of depth and momentum profiles and the maximum value of momentum. However, the two-layer shallow-water model over-predicted the propagation speed of the wavefronts.

The model presented here neglects entrainment, which is observed in the DNS simulations presented in the previous chapter. Entrainment could be included by the introduction of a third transition-layer in between the two fluids, for example Hogg et al. (2005). Further, as discussed in the methodology, multiple forms of the viscous diffusion have been used previously; each with their advantages and disadvantages. Studying these various forms and comparison with the DNS would indicate which is most suitable for the variable viscosity lock-exchange flow. Finally, the neglecting interfacial drag terms are likely to be significant and their inclusion would be a important to develop the model further.

Chapter 6

Conclusions and outlook

Motivated by the enigmatic transition mechanics observed between sub-aqueous debris flows and turbidity currents, this thesis considered two different problems: the phased lock-release and the variable viscosity lock-exchange. Pulses in flow occur regularly in gravity currents and can arise from flow instabilities, the combining of flows downstream or a variable supply of material. Further, preliminary experiments of Ho et al. (2018a,b, 2019) indicate that a pulse can cause a cascade of mixing and a rapid transition to dilute behaviour for compositional gravity currents when there is a significant viscosity difference between the current and the ambient. This motivated the study of lock-release flows with currents of different viscosities. Varying the viscosity in the current enabled the mixing dynamics that occur in a gravity-driven flow to be studied.

In chapter 2 pulses in gravity were explored using a depth-averaged shallow-water model to study the double lock-release problem. The phased release of the two lock-gates created a pulse that propagated as a shock through to the head of the current. The shallow-water model was solved using a Lax-Wendroff finite difference scheme based on the method presented by Bonnecaze et al. (1993). By extending the characteristic method used by Hogg (2006) for the single release, we showed that the solutions changed qualitatively depending on the interaction of three critical curves, $x_{\mathrm{fan}}, x_{\mathrm{fin}}$ and x_{ref}, the head of the flow x_N and the position of the shock x_s. The critical curves being the three characteristic curves and their subsequent reflection. the flow is fully characterised by two parameters: The dimensionless head speed or Froude number Fr; and a dimensionless lock-gate release time t_{re}. For $Fr \in (0, 2)$ and $t_{\mathrm{re}} \in (1, 21)$ the qualitatively different solutions were classified. Critically, this demonstrated that pulses were either non-decelerating or accelerate for a time and then decelerate thereafter.

Chapter 3 presented an experimental study of the double lock-release for three glycerol/water mixtures at different concentrations (77%, 84% and 90%) released into a water ambient. This work was motivated by the rapid transition from concentrated to dilute behaviour observed in a preliminary experiment conducted by Ho et al. (2018a,b, 2019) and to provide validation for the shallow-water model presented in chapter 2. Four different release times t_{re} were chosen based on the remaining fraction of fluid in the first lock gate. In these experiments the pulse propagated as a bore rather than a shock that transitioned from the second current into the first and towards the head of the flow.

At the highest glycerol concentration (0.90) transition to a dilute flow was not observed and the total amount of mixing was negligible. Significantly more mixing was observed for the other glycerol concentrations (0.77 and 0.84) At the lowest concentration (0.77), where only one release time was studied, the extra supply of dense material delayed the onset to dilute behaviour by as much as two lock-lengths. Three qualitatively different behaviours were observed for the intermediate glycerol concentration (0.84) depending on the release time t_{re}. The lowest two release times behaved qualitatively similar to the lowest glycerol concentration (0.77). The second-longest release time produced a brief transition back into concentrated flow with the arrival of the pulse at the head of the current. For the longest release time, the pulse diluted within the body of the second current.

The shallow-water model presented in chapter 2 neglected the effects of entrainment, bed drag and viscous dissipation of the flow. Despite these simplifications, the head propagation speed was captured by the shallow-water model up until the latter stages of the flow where viscous forces became increasingly significant. However, the pulse speed was over-estimated. This likely arose from the viscous smoothing of the sharp shock in the shallow water model to a bore in the experiments and the absence of a term equivalent to the Froude number condition imposed at the head.

The changing dynamics observed in chapter 3 in the high-viscosity contrast experiments motivated the study of the variable-viscosity lock-exchange problem considered in the next two chapters of the thesis. In chapter 4, direct numerical simulations of the variable viscosity lock-exchange problem were conducted in the spectral element code NEK5000. The use of the lock-exchange problem with simplified boundary conditions enabled fully resolved results for current to ambient excess viscosity ratios γ as large as 10. Although less than the viscosity ratio of the experiments, this range of viscosity ratios does reveal the change in the mixing dynamics from cases where the current and ambient are of similar viscosity.

Increasing the viscosity of the current decreases the total energy irretrievably lost through mixing. When compared to the equal viscosity case, $\gamma = 0$, when the excess viscosity of the current is increased to $\gamma = 1$ or $\gamma = 2$ an increase in sloshing time and a more efficient transfer between kinetic and potential energy. Further, the total energy lost to viscous diffusion decreased. This arose because of the intermediate increase in viscosity suppressing the small scale mixing that occurred near the interface, which acted to preserve the concentration gradient. As the viscosity ratio was further increased viscous diffusion effects become more significant and the sloshing time decreased. For $\gamma = 10$, it was faster than the equal viscosity case. Further for both $\gamma = 4$ and $\gamma = 10$ the total energy lost increased when compared to the equal viscosity case.

Finally, in chapter 5, the lock-exchange problem with variable viscosity was modelled with a two-layer shallow-water model, where effects of viscous diffusion were included as a source term. This chapter assessed whether a depth-averaged model could capture the flow dynamics observed in chapter 4 and further, to explore more cases with the reduced computational cost. The equations were solved using a fractional step method with a finite-volume scheme for the conservative part and a fourth-order Runge-Kutta for the viscous source terms. When the ambient viscosity was kept fixed, increasing the current viscosity led to viscous diffusion becoming dominant in the current. The contribution to viscous diffusion for each layer was out of phase and this resulted in different propagation speeds of the head and an increased asymmetry of the flow. With the viscosity of each layer the same, increasing the viscosity smoothed out the flow features, but symmetry was maintained. A qualitative agreement can be observed with the DNS results, but the wavefronts propagate at a faster rate in the two-layer model.

6.1 Implications

We can now reflect on the implications of our findings on the geophysical events discussed in chapter 1. For particle-driven flows, the particle size distribution is the dominant control on when erosion and deposition rates are in balance (Dorrell et al., 2018). For dilute flows, this equilibrium point defines a particle concentration above or below which the flow is erosional or depositional, respectively. The models discussed in Dorrell et al. (2018) have increasing functions of the shear velocity at the bed u_*, which can be empirically modelled as proportional to, or related to a positive power of the depth-averaged velocity $u = m/h$ (Soares-Frazão and Zech, 2011; Simpson and Castelltort, 2006; Yang et al., 2019). Thus, in regions where the flow speed is increasing it is more erosional and conversely for regions where the flow speed is decreasing it is more depositional. When the particle concentration is large, for example, lahars and landslides, the particles are in constant contact and suspended by matrix strength rather than the fluid. Therefore there is no simple relationship between erosion and deposition rates and the acceleration of the flow for these flows. Instead, erosion and deposition are controlled by a stress balance at the bed (Iverson and Ouyang, 2015).

The hazard assessments conducted for the Soufriére Hills Volcano, Montserrat assume a continuous steady release of material from the lava dome during the 1997 eruption creating a pyroclastic surge flow (Loughlin et al., 2002). However, at the 1997 eruption, the dome failed retrogressively producing a continuous release with three distinct peaks in volume flux identified as individual pulses. Sedimentation from pyroclastic surges can create a complex flow structure with a dense, basal pyroclastic flow component with high-particle concentration, which is overlain by and an upper, less dense pyroclastic surge. In the 1997 event, 1.4 km downstream from the source the third pyroclastic flow associated with the third pulse overspilled the drainage channel and went on to hit the villages of Streatham and Windy Hill. Despite the bend coinciding with a constriction in the channel cross-sectional area, these villages were not considered at risk. However, the previous two pulses had left significant deposits thus increasing the risk of surge detachment and overspilling.

The pulsed nature of this flow affected its run-out and the inundation zone of this flow when compared to a continuous release of the same size (Loughlin et al., 2002). The shallow-water model discussed in chapter 2 suggests that the separation time between the pulses may have a crucial effect on whether the pulses were erosional or depositional at a particular location. Pulses that are close together (case N) are non-decelerating and may entrain more material downstream increasing the depth of the channel or increase the velocity/momentum of the flow. For large separation times, the pulses may transition from erosional to depositional downstream filling in the channel and making it more susceptible to future flows overspilling.

Although the experiments conducted in chapter 3 were not able to replicate the rapid transition to dilute behaviour observed by Ho et al. (2018a,b, 2019), the gravity current was composed of Newtonian fluid with no yield strength. In a pulsed debris flow, the yield strength may prevent it from transforming until the pulse reaches the head of the flow and increasing the range of parameters of which transformation with the arrival of the pulse can occur.

6.2 Outlook

Although each chapter has natural extensions that are discussed in each, here we discuss directions future work could take from the material presented in this thesis. Throughout, compositional flows, where the density difference is assumed to be caused by a dissolved solute or the two fluids are distinct, have been considered. Critically, these have been assumed to be evenly distributed. For highly turbulent flows, the small scale eddies provide sufficient mixing for the particles to be evenly distributed over the depth of the current. However, particle-driven flows commonly exist with insufficient energy to distribute the particles evenly over the current depth resulting in stratification and may deposit or entrain particles as discussed in the section above. Thus, a natural extension to the work conducted in this thesis would be to explore the differences between these flows and particle-driven flows. This would elucidate debris to turbidity current transformation mechanisms and the effect of pulses on other significant geophysical flows.

Our work has been confined to two-dimensional geometries with a horizontal bed, whereas in nature these currents often fan out or are partially- (Kelly et al., 2019) or fully-constrained by topography (Loughlin et al., 2002). For example the 1997 eruption of the Soufriére Hills Volcano, Montserrat, where the pulsed-pyroclastic flow was mostly confined to a drainage channel. Further, bed slope affects gravity current run out lengths and the mechanisms that control debris flow to turbidity current transition (Sohn, 2000). Thus the effects of topography and bed slope could be included into the models to provide a better understanding of real-world gravity currents.

At high particle volume fractions, particulate driven gravity currents will exhibit non-Newtonian rheology. Constitutive laws exist for dry granular flows (Pouliquen, 1999; Jop et al., 2006). However, when the density and viscosity of the ambient are significant, two-phase models are required. For example, an underwater granular avalanche was studied using a two-phase depth-averaged model by Pailha and Pouliquen (2009). Further, the non-Newtonian behaviour can be enhanced by the cohesive strength of materials such as clay (Talling et al., 2012). Incorporating these non-Newtonian effects into depth-averaged models could provide further insight into debris flow to turbidity current transition mechanisms.

References

Citing pages are listed after each entry.

Abad, J. D., Sequeiros, O. E., Spinewine, B., et al. 2011. Secondary current of saline underflow in a highly meandering channel: experiments and theory. *Journal of Sedimentary Research.* **81**(11), pp. 787–813. Cited on p. 12.

Abbott, M. B. 1961. On the spreading of one fluid over another: part 2. *La Houille Blanche.* **6**, pp. 827–836. Cited on p. 13.

Allen, J. R. L. 1971. Mixing at turbidity current heads, and its geological implications. *Journal of Sedimentary Research.* **41**(1), pp. 97–113. Cited on p. 2.

Amy, L. A. and Talling, P. J. 2006. Anatomy of turbidites and linked debrites based on long distance (120× 30 km) bed correlation, Marnoso Arenacea Formation, Northern Apennines, Italy. *Sedimentology.* **53**(1), pp. 161–212. Cited on p. 2.

Ancey, C. 2001. 21 debris flows and related phenomena. In: *Geomorphological fluid mechanics.* Springer, pp. 528–547. Cited on p. 12.

Audusse, E. 2005. A multilayer Saint-Venant model: derivation and numerical validation. *Discrete Contin. Dyn. Syst. Ser. B.* **5**(2), pp. 189–214. Cited on p. 147.

Barley, B. 1999. Deepwater problems around the world. *The Leading Edge.* **18**(4), pp. 488–493. Cited on p. 4.

Benjamin, T. B. 1968. Gravity currents and related phenomena. *Journal of Fluid Mechanics.* **31**(2), pp. 209–248. Cited on pp. 14 and 25.

Birman, V. K., Martin, J. E., and Meiburg, E. 2005. The non-Boussinesq lock-exchange problem. part 2. high-resolution simulations. *Journal of Fluid Mechanics.* **537**, pp. 125–144. Cited on p. 102.

Blight, G. E. and Fourie, A. B. A review of catastrophic flow failures of deposits of mine waste and municipal refuse. In: *International Workshop on occurrence and mechanisms of flow in natural slopes and earthfills*, 2003. Cited on p. 5.

Bonnecaze, R. T., Huppert, H. E., and Lister, J. R. 1993. Particle-driven gravity currents. *Journal of Fluid Mechanics.* **250**, pp. 339–369. Cited on pp. 6, 15, 24, 32, 34, 47, 141, 148, and 179.

Bonometti, T. and Balachandar, S. 2008. Effect of Schmidt number on the structure and propagation of density currents. *Theoretical and Computational Fluid Dynamics.* **22**(5), pp. 341. Cited on pp. 102 and 114.

Borden, Z. and Meiburg, E. 2013. Circulation based models for Boussinesq gravity currents. *Physics of Fluids.* **25**(10), pp. 101301. Cited on p. 14.

Bouguet, J. Y. 2004. Camera calibration toolbox for matlab. *http://www.vision.caltech. edu/bouguetj/calib_doc/index.html.* Cited on p. 51.

Boussinesq, J. 1897. *Théorie de l'écoulement tourbillonnant et tumultueux des liquides dans les lits rectilignes a grande section.*, volume 1. Gauthier-Villars. Cited on p. 99.

Breard, E. C. P. and Lube, G. 2017. Inside pyroclastic density currents–uncovering the enigmatic flow structure and transport behaviour in large-scale experiments. *Earth and Planetary Science Letters.* **458**, pp. 22–36. Cited on p. 1.

Britter, R. E. 1979. The spread of a negatively buoyant plume in a calm environment. *Atmospheric Environment.* **13**(9), pp. 1241–1247. Cited on p. 8.

Brown, D. C. 1966. Decentering distortion of lenses. *Photogrammetric Engineering and Remote Sensing.* Cited on p. 70.

Brown, D. L. 1995. Performance of under-resolved two-dimensional incompressible flow simulations. *Journal of Computational Physics.* **122**(1), pp. 165–183. Cited on p. 110.

Burchard, H., Janssen, F., Bolding, K., Umlauf, L., and Rennau, H. 2009. Model simulations of dense bottom currents in the Western Baltic Sea. *Continental Shelf Research.* **29**(1), pp. 205–220. Cited on p. 19.

Cantero, M. I., Balachandar, S., García, M. H., and Ferry, J. P. 2006. Direct numerical simulations of planar and cylindrical density currents. *Journal of Applied Mechanics.* **73**(6), pp. 923–930. Cited on pp. 98, 100, and 104.

Cantero, M. I., Lee, J. R., Balachandar, S., and Garcia, M. H. 2007. On the front velocity of gravity currents. *Journal of Fluid Mechanics.* **586**, pp. 1–39. Cited on pp. 20 and 98.

Cantero, M. I., Balachandar, S., García, M. H., and Bock, D. 2008. Turbulent structures in planar gravity currents and their influence on the flow dynamics. *Journal of Geophysical Research: Oceans.* **113**(C8). Cited on p. 8.

Capuano, F., Palumbo, A., and de Luca, L. 2019. Comparative study of spectral-element and finite-volume solvers for direct numerical simulation of synthetic jets. *Computers & Fluids.* **179**, pp. 228–237. Cited on p. 105.

Carlson, B. C. 1995. Numerical computation of real or complex elliptic integrals. *Numerical Algorithms.* **10**(1), pp. 13–26. Cited on p. 117.

Carter, L., Burnett, D., Drew, S., et al. 2009. Submarine cables and the oceans: connecting the world: United Nations Environment Programme. *World Conservation Monitoring Center (UNEP-WCMC) Biodiversity Series.* **31**. Cited on p. 4.

Castro, M., Macías, J., and Parés, C. 2001. A Q-scheme for a class of systems of coupled conservation laws with source term. application to a two-layer 1-d shallow water system. *ESAIM: Mathematical Modelling and Numerical Analysis.* **35**(1), pp. 107–127. Cited on p. 147.

Castro-Díaz, M. J., Fernández-Nieto, E. D., Morales de Luna, T., Narbona-Reina, G., and Parés, C. 2013. A HLLC scheme for nonconservative hyperbolic problems. application to turbidity currents with sediment transport. *ESAIM: Mathematical Modelling and Numerical Analysis-Modélisation Mathématique et Analyse Numérique.* **47**(1), pp. 1–32. Cited on p. 12.

Cheng, N. S. 2008. Formula for the viscosity of a glycerol- water mixture. *Industrial & Engineering Chemistry Research.* **47**(9), pp. 3285–3288. Cited on pp. xix, xx, 50, 54, 55, 56, 66, 94, and 140.

Chenlo, F., Moreira, R., Pereira, G., and Bello, B. 2004. Kinematic viscosity and water activity of aqueous solutions of glycerol and sodium chloride. *European food research and technology.* **219**(4), pp. 403–408. Cited on pp. 55 and 56.

Chorin, A. J. 1968. Numerical solution of the Navier-Stokes equations. *Mathematics of computation.* **22**(104), pp. 745–762. Cited on p. 20.

Christoph, R., Schmidt, B., Steinberner, U., Dilla, W., and Karinen, R. *Glycerol.* American Cancer Society., 2006. ISBN 9783527306732. Cited on pp. xix, 53, and 54.

Courant, R., Friedrichs, K., and Lewy, H. 1928. Über die partiellen differenzengleichungen der mathematischen physik. *Mathematische annalen.* **100**(1), pp. 32–74. Cited on p. 156.

Dade, W. B. and Huppert, H. E. 1995. A box model for non-entraining, suspension-driven gravity surges on horizontal surfaces. *Sedimentology.* **42**(3), pp. 453–470. Cited on p. 15.

Dasgupta, R. and Govindarajan, R. 2010. Nonsimilar solutions of the viscous shallow water equations governing weak hydraulic jumps. *Physics of Fluids.* **22** (11), pp. 112108. Cited on p. 144.

De Blasio, F. V., Breien, H., and Elverhøi, A. 2011. Modelling a cohesive-frictional debris flow: an experimental, theoretical, and field-based study. *Earth Surface Processes and Landforms.* **36**(6), pp. 753–766. Cited on pp. vii, 2, and 3.

De Villiers, J. P., Leuschner, F. W., and Geldenhuys, R. Centi-pixel accurate real-time inverse distortion correction. In: *Optomechatronic Technologies 2008*, volume 7266, pp. 1–8. International Society for Optics and Photonics, 2008. Cited on p. 70.

Dengler, A. T., Wilde, P., Noda, E. K., and Normark, W. R. 1984. Turbidity currents generated by hurricane Iwa. *Geo-Marine Letters.* **4**(1), pp. 5–11. Cited on p. 4.

D'Errico, G., Ortona, O., Capuano, F., and Vitagliano, V. 2004. Diffusion coefficients for the binary system glycerol+ water at 25 C. a velocity correlation study. *Journal of Chemical & Engineering Data.* **49**(6), pp. 1665–1670. Cited on p. 102.

Deville, M. O., Fischer, P. F., Mund, E. H., et al. 2002. *High-order methods for incompressible fluid flow.*, volume 9. Cambridge university press. Cited on p. 105.

Didden, N. and Maxworthy, T. 1982. The viscous spreading of plane and axisymmetric gravity currents. *Journal of Fluid Mechanics.* **121**, pp. 27–42. Cited on pp. 8 and 13.

Dorrell, R. M., Darby, S. E., Peakall, J., et al. 2014. The critical role of stratification in submarine channels: Implications for channelization and long runout of flows. *Journal of Geophysical Research: Oceans.* **119**(4), pp. 2620–2641. Cited on pp. 12, 13, and 143.

Dorrell, R. M., Amy, L. A., Peakall, J., and McCaffrey, W. D. 2018. Particle size distribution controls the threshold between net sediment erosion and deposition in suspended load dominated flows. *Geophysical Research Letters.* **45**(3), pp. 1443–1452. Cited on pp. 5 and 181.

Dorrell, R. M., Peakall, J., Darby, S. E., et al. 2019. Self-sharpening induces jet-like structure in seafloor gravity currents. *Nature communications.* **10**(1), pp. 1–10. Cited on p. 12.

Doyle, E. E., Hogg, A. J., Mader, H. M., and Sparks, R. S. J. 2010. A two-layer model for the evolution and propagation of dense and dilute regions of pyroclastic currents. *Journal of Volcanology and Geothermal Research.* **190**(3), pp. 365–378. Cited on pp. 1 and 6.

Ellison, T. H. and Turner, J. S. 1959. Turbulent entrainment in stratified flows. *Journal of Fluid Mechanics.* **6**(03), pp. 423–448. Cited on p. 13.

Embley, R. W. 1976. New evidence for occurrence of debris flow deposits in the deep sea. *Geology.* **4**(6), pp. 371–374. Cited on p. 4.

Espath, L. F. R., Pinto, L. C., Laizet, S., and Silvestrini, J. H. 2014. Two-and three-dimensional direct numerical simulation of particle-laden gravity currents. *Computers & geosciences.* **63**, pp. 9–16. Cited on p. 20.

Evans, L. 2010. *Partial different equations.* American Mathematical Society. Cited on p. 116.

Fallgatter, C., Kneller, B., Paim, P. S. G., and Milana, J. P. 2017. Transformation, partitioning and flow–deposit interactions during the run-out of megaflows. *Sedimentology.* **64**(2), pp. 359–387. Cited on pp. vii and 3.

Fay, J. A. 1971. Physical processes in the spread of oil on a water surface. *International Oil Spill Conference Proceedings.* **1971**(1), pp. 463–467. Cited on p. 14.

Felix, M. and Peakall, J. 2006. Transformation of debris flows into turbidity currents: mechanisms inferred from laboratory experiments. *Sedimentology.* **53**(1), pp. 107–123. Cited on p. 2.

Felix, M., Leszczyński, S., Ślaczka, A., et al. 2009. Field expressions of the transformation of debris flows into turbidity currents, with examples from the polish carpathians and the french maritime alps. *Marine and Petroleum Geology.* **26** (10), pp. 2011–2020. Cited on p. 4.

Fischer, P. F. 1998. Projection techniques for iterative solution of ax= b with successive right-hand sides. *Computer methods in applied mechanics and engineering.* **163**(1-4), pp. 193–204. Cited on p. 111.

Fischer, P. F. 2015. Scaling limits for pde-based simulation (invited). *22nd AIAA Computational Fluid Dynamics Conference.* Cited on p. 105.

Fischer, P. F. and Mullen, J. 2001. Filter-based stabilization of spectral element methods. *Comptes Rendus de l'Academie des Sciences Series I Mathematics.* **332** (3), pp. 265–270. Cited on p. 110.

Fischer, P. F., Kruse, G. W., and Loth, F. 2002. Spectral element methods for transitional flows in complex geometries. *Journal of Scientific Computing.* **17** (1-4), pp. 81–98. Cited on p. 110.

Fischer, P. F., Lottes, J. W., Kerkemeier, S. G., et al. 2008. nek5000 web page:. *https:// nek5000.mcs.anl.gov/.* Cited on pp. 20, 97, and 104.

Fitzgibbon, A. W. Simultaneous linear estimation of multiple view geometry and lens distortion. In: *Proceedings of the 2001 IEEE Computer Society Conference on Computer Vision and Pattern Recognition. CVPR 2001*, volume 1, pp. I–I. IEEE, 2001. Cited on p. 70.

Fourie, A. B., Blight, G. E., and Papageorgiou, G. 2001. Static liquefaction as a possible explanation for the Merriespruit tailings dam failure. *Canadian Geotechnical Journal.* **38**(4), pp. 707–719. Cited on pp. vii and 5.

Fragoso, A. T., Patterson, M. D., and Wettlaufer, J. S. 2013. Mixing in gravity currents. *Journal of Fluid Mechanics.* **734**. Cited on p. 18.

Francisco, E. P., Espath, L. F. R., and Silvestrini, J. H. 2017. Direct numerical simulation of bi-disperse particle-laden gravity currents in the channel configuration. *Applied Mathematical Modelling.* **49**, pp. 739–752. Cited on p. 20.

Gent, P. R. 1993. The energetically consistent shallow-water equations. *Journal of the Atmospheric Sciences.* **50**(9), pp. 1323–1325. Cited on p. 144.

Giorgio Serchi, F., Peakall, J., Ingham, D. B., and Burns, A. D. 2011. A unifying computational fluid dynamics investigation on the river-like to river-reversed secondary circulation in submarine channel bends. *Journal of Geophysical Research: Oceans.* **116**(C6). Cited on pp. 52 and 53.

Goldfinger, C., Galer, S., Beeson, J., et al. 2017. The importance of site selection, sediment supply, and hydrodynamics: A case study of submarine paleoseismology on the Northern Cascadia margin, Washington USA. *Marine Geology.* **384**, pp. 4–46. Cited on pp. 4, 5, and 23.

Gonzalez-Juez, E., Meiburg, E., and Constantinescu, G. 2009. Gravity currents impinging on bottom-mounted square cylinders: flow fields and associated forces. *Journal of Fluid Mechanics.* **631**, pp. 65–102. Cited on p. 4.

Goodman, J. B. and LeVeque, R. J. 1988. A geometric approach to high resolution TVD schemes. *SIAM journal on numerical analysis.* **25**(2), pp. 268–284. Cited on p. 152.

Gustafsson, B. and Sundström, A. 1978. Incompletely parabolic problems in fluid dynamics. *SIAM Journal on Applied Mathematics.* **35**(2), pp. 343–357. Cited on p. 144.

Hacker, J., Linden, P. F., and Dalziel, S. B. 1996. Mixing in lock-release gravity currents. *Dynamics of Atmospheres and Oceans.* **24**(1-4), pp. 183–195. Cited on p. 18.

Hageman, L. and Young, M. 1981. *Applied Iterative Methods Academic.* Cited on p. 111.

Hallworth, M. A., Phillips, J. C., Huppert, H. E., and Sparks, R. S. J. 1993. Entrainment in turbulent gravity currents. *Nature.* **362**(6423), pp. 829–831. Cited on p. 18.

Hallworth, M. A., Huppert, H. E., Phillips, J. C., and Sparks, R. S. J. 1996. Entrainment into two-dimensional and axisymmetric turbulent gravity currents. *Journal of Fluid Mechanics.* **308**, pp. 289–311. Cited on pp. 8 and 18.

Hallworth, M. A., Hogg, A. J., and Huppert, H. E. 1998. Effects of external flow on compositional and particle gravity currents. *Journal of Fluid Mechanics.* **359**, pp. 109–142. Cited on p. 141.

Hampton, M. A. 1972. The role of subaqueous debris flow in generating turbidity currents. *Journal of Sedimentary Research.* **42**(4), pp. 775–793. Cited on p. 3.

Härtel, C., Kleiser, L., Michaud, M., and Stein, C. F. 1997. A direct numerical simulation approach to the study of intrusion fronts. *Journal of engineering mathematics.* **32**(2-3), pp. 103–120. Cited on p. 20.

Härtel, C., Meiburg, E., and Necker, F. 2000. Analysis and direct numerical simulation of the flow at a gravity-current head. part 1. flow topology and front speed for slip and no-slip boundaries. *Journal of Fluid Mechanics.* **418**, pp. 189–212. Cited on pp. 18, 20, 100, and 104.

Harten, A. and Hyman, J. M. 1983. Self adjusting grid methods for one-dimensional hyperbolic conservation laws. *Journal of computational Physics.* **50**(2), pp. 235–269. Cited on p. 152.

Haughton, P. D. W. 1994. Deposits of deflected and ponded turbidity currents, Sorbas Basin, southeast Spain. *Journal of Sedimentary Research.* **64**(2a), pp. 233–246. Cited on p. 5.

Haynes, W. M. 2014. *CRC handbook of chemistry and physics.* CRC press. Cited on p. 58.

Heezen, B. C. and Ewing, M. 1952. Turbidity currents and submarine slumps, and the 1929 grand banks earthquake. *American Journal of Science.* **250**(12), pp. 849–873. Cited on p. 4.

Higuera, F. J. 1994. The hydraulic jump in a viscous laminar flow. *Journal of fluid Mechanics.* **274**, pp. 69–92. Cited on p. 144.

Ho, V. L., Dorrell, R. M., Keevil, G. M., Burns, A. D., and McCaffrey, W. D. 2018a. Pulse propagation in turbidity currents. *Sedimentology.* **65**(2), pp. 620–637. Cited on pp. x, 6, 7, 21, 49, 50, 51, 59, 84, 90, 94, 179, 180, and 182.

Ho, V. L., Dorrell, R. M., Keevil, G. M., Burns, A. D., and McCaffrey, W. D. 2018b. Scaling analysis of multipulsed turbidity current evolution with application to turbidite interpretation. *Journal of Geophysical Research: Oceans.* **123**(5), pp. 3668–3684. Cited on pp. x, 4, 6, 7, 21, 49, 50, 51, 59, 84, 90, 94, 179, 180, and 182.

Ho, V. L., Dorrell, R. M., Keevil, G. M., et al. 2019. Dynamics and deposition of sediment-bearing multi-pulsed flows and geological implication. *Journal of Sedimentary Research.* **89**(11), pp. 1127–1139. Cited on pp. 6, 7, 21, 49, 50, 84, 90, 94, 179, 180, and 182.

Hodgson, K. A. and Manville, V. R. 1999. Sedimentology and flow behavior of a rain-triggered lahar, Mangatoetoenui Stream, Ruapehu volcano, New Zealand. *Geological Society of America Bulletin.* **111**(5), pp. 743–754. Cited on p. 6.

Hogg, A. J. 2006. Lock-release gravity currents and dam-break flows. *Journal of Fluid Mechanics.* **569**, pp. 61–87. Cited on pp. 9, 14, 21, 23, 24, 26, 29, 34, 46, 47, and 179.

Hogg, A. J. and Pritchard, D. 2004. The effects of hydraulic resistance on dam-break and other shallow inertial flows. *Journal of Fluid Mechanics.* **501**, pp. 179–212. Cited on p. 12.

Hogg, A. J. and Woods, A. W. 2001. The transition from inertia-to bottom-drag-dominated motion of turbulent gravity currents. *Journal of Fluid Mechanics*. **449**, pp. 201. Cited on p. 15.

Hogg, A. J., Ungarish, M., and Huppert, H. E. 2000. Particle-driven gravity currents: asymptotic and box model solutions. *European Journal of Mechanics-B/Fluids*. **19**(1), pp. 139–165. Cited on pp. 16, 17, 141, and 175.

Hogg, A. J., Hallworth, M. A., and Huppert, H. E. 2005. On gravity currents driven by constant fluxes of saline and particle-laden fluid in the presence of a uniform flow. *Journal of Fluid Mechanics*. **539**, pp. 349–385. Cited on pp. 14 and 177.

Hoult, D. P. 1972. Oil spreading on the sea. *Annual Review of Fluid Mechanics*. **4** (1), pp. 341–368. Cited on pp. 7 and 14.

Hu, P., Cao, Z., Pender, G., and Tan, G. 2012. Numerical modelling of turbidity currents in the Xiaolangdi reservoir, Yellow River, China. *Journal of Hydrology*. **464**, pp. 41–53. Cited on p. 12.

Hughes, G. O. 2016. Inside the head and tail of a turbulent gravity current. *Journal of Fluid Mechanics*. **790**, pp. 1–4. Cited on p. 49.

Hungr, O. 2000. Analysis of debris flow surges using the theory of uniformly progressive flow. *Earth Surface Processes and Landforms*. **25**(5), pp. 483–495. Cited on p. 4.

Huppert, H. E. 1982. The propagation of two-dimensional and axisymmetric viscous gravity currents over a rigid horizontal surface. *Journal of Fluid Mechanics*. **121**, pp. 43–58. Cited on pp. 7, 14, 15, 54, and 92.

Huppert, H. E. 1986. Intrusion of fluid mechanics into geology. *Journal of Fluid Mechanics*. **173**, pp. 557–94. Cited on p. 15.

Huppert, H. E. 2006. Gravity currents: a personal perspective. *Journal of Fluid Mechanics*. **554**, pp. 299. Cited on pp. vii, 2, and 10.

Huppert, H. E. and Simpson, J. E. 1980. The slumping of gravity currents. *Journal of Fluid Mechanics*. **99**(04), pp. 785–799. Cited on pp. 7, 14, and 15.

Ilıcak, M., Özgökmen, T. M., Peters, H., Baumert, H. Z., and Iskandarani, M. 2008. Performance of two-equation turbulence closures in three-dimensional simulations of the Red Sea overflow. *Ocean Modelling*. **24**(3-4), pp. 122–139. Cited on p. 19.

Ilıcak, M., Özgökmen, T. M., Özsoy, E., and Fischer, P. F. 2009. Non-hydrostatic modeling of exchange flows across complex geometries. *Ocean Modelling.* **29**(3), pp. 159–175. Cited on pp. 20 and 100.

Imran, J., Kassem, A., and Khan, S. M. 2004. Three-dimensional modeling of density current. i. flow in straight confined and unconfined channels. *Journal of Hydraulic Research.* **42**(6), pp. 578–590. Cited on p. 19.

Islam, M. A. and Imran, J. 2010. Vertical structure of continuous release saline and turbidity currents. *Journal of Geophysical Research: Oceans.* **115**(C8). Cited on p. 12.

Iverson, R. M. 1997. The physics of debris flows. *Reviews of geophysics.* **35**(3), pp. 245–296. Cited on p. 12.

Iverson, R. M. and Denlinger, R. P. 2001. Flow of variably fluidized granular masses across three-dimensional terrain: 1. Coulomb mixture theory. *Journal of Geophysical Research: Solid Earth.* **106**(B1), pp. 537–552. Cited on p. 12.

Iverson, R. M. and Ouyang, C. 2015. Entrainment of bed material by Earth-surface mass flows: Review and reformulation of depth-integrated theory. *Reviews of Geophysics.* **53**(1), pp. 27–58. Cited on p. 182.

Jasak, H., Jemcov, A., Tukovic, Z., et al. OpenFOAM: A C++ library for complex physics simulations. In: *International workshop on coupled methods in numerical dynamics*, volume 1000, pp. 1–20. IUC Dubrovnik Croatia, 2007. Cited on p. 105.

Johnson, C. G. and Hogg, A. J. 2013. Entraining gravity currents. *Journal of Fluid Mechanics.* **731**, pp. 477–508. Cited on pp. 18 and 19.

Johnson, C. G., Hogg, A. J., Huppert, H. E., et al. 2015. Modelling intrusions through quiescent and moving ambients. *Journal of Fluid Mechanics.* **771**, pp. 370–406. Cited on p. 15.

Jop, P., Forterre, Y., and Pouliquen, O. 2006. A constitutive law for dense granular flows. *Nature.* **441**(7094), pp. 727. Cited on p. 183.

Kanayama, H. and Dan, H. 2013. A tsunami simulation of Hakata Bay using the viscous shallow-water equations. *Japan Journal of Industrial and Applied Mathematics.* **30**(3), pp. 605–624. Cited on p. 144.

Kantha, L. and Clayson, C. 2000. *Small scale processes in geophysical fluid flows.* Elsevier. Cited on p. 98.

Kassem, A. and Imran, J. 2004. Three-dimensional modeling of density current. ii. flow in sinuous confined and uncontined channels. *Journal of Hydraulic Research.* **42**(6), pp. 591–602. Cited on p. 19.

Kelly, R. W., Dorrell, R. M., Burns, A. D., and McCaffrey, W. D. 2019. The structure and entrainment characteristics of partially confined gravity currents. *Journal of Geophysical Research: Oceans.* **124**(3), pp. 2110–2125. Cited on p. 183.

Kemm, F. 2011. A comparative study of TVD-limiters—well-known limiters and an introduction of new ones. *International Journal for Numerical Methods in Fluids.* **67**(4), pp. 404–440. Cited on p. 155.

Keppie, J. D., Boyle, R. W., and Haynes, S. J. 1986. *Turbidite-hosted gold deposits.*, volume 32. St. John's, Nfld., Canada: Geological Association of Canada. Cited on p. 4.

Kim, J. and LeVeque, R. J. 2008. Two-layer shallow water system and its applications. **52**(96), pp. 102. Cited on p. 147.

Kirby, R. M. and Karniadakis, G. E. 2003. De-aliasing on non-uniform grids: algorithms and applications. *Journal of Computational Physics.* **191**(1), pp. 249–264. Cited on p. 110.

Klein, R. I. 1999. Star formation with 3-d adaptive mesh refinement: the collapse and fragmentation of molecular clouds. *Journal of Computational and Applied Mathematics.* **109**(1-2), pp. 123–152. Cited on p. 121.

Kneller, B., Nasr-Azadani, M. M., Radhakrishnan, S., and Meiburg, E. 2016. Long-range sediment transport in the world's oceans by stably stratified turbidity currents. *Journal of Geophysical Research: Oceans.* **121**(12), pp. 8608–8620. Cited on p. 20.

Kolmogorov, A. N. 1941. The local structure of turbulence in incompressible viscous fluid for very large reynolds numbers. *Cr Acad. Sci. URSS.* **30**, pp. 301–305. Cited on pp. 20 and 109.

Konopliv, N. A., Llewellyn Smith, S. G., McElwaine, J. N., and Meiburg, E. 2016. Modelling gravity currents without an energy closure. *Journal of Fluid Mechanics.* **789**, pp. 806–829. Cited on p. 14.

Kooij, G. L., Botchev, M. A., Frederix, E. M. A., et al. 2018. Comparison of computational codes for direct numerical simulations of turbulent Rayleigh–Bénard convection. *Computers & Fluids.* **166**, pp. 1–8. Cited on p. 109.

Kuenen, P. H. and Migliorini, C. I. 1950. Turbidity currents as a cause of graded bedding. *The Journal of Geology.* pp. 91–127. Cited on p. 2.

Laney, C. B. 1998. *Computational gasdynamics.* Cambridge university press. Cited on p. 157.

Lascelles, D. F. 2007. Black smokers and density currents: a uniformitarian model for the genesis of banded iron-formations. *Ore Geology Reviews.* **32**(1), pp. 381–411. Cited on p. 4.

Ledwell, J. R., Montgomery, E. T., Polzin, K. L., et al. 2000. Evidence for enhanced mixing over rough topography in the abyssal ocean. *Nature.* **403**(6766), pp. 179–182. Cited on p. 98.

LeVeque, R. J. 1990. Hyperbolic conservation laws and numerical methods. *VCFDy.* **1**, pp. 1–42. Cited on p. 152.

LeVeque, R. J. 2002. *Finite volume methods for hyperbolic problems.*, volume 31. Cambridge University Press. Cited on pp. 141, 148, 150, 152, 154, and 156.

Lipatnikov, A. 2012. *Fundamentals of premixed turbulent combustion.* CRC Press. Cited on p. 109.

Lomperski, S., Obabko, A., Merzari, E., Fischer, P., and Pointer, W. D. 2017. Jet stability and wall impingement flow field in a thermal striping experiment. *International Journal of Heat and Mass Transfer.* **115**, pp. 1125–1136. Cited on p. 110.

Lorenz, E. 1955. Available potential energy and the maintenance of the general circulation. *Tellus.* **7**(2), pp. 157–167. Cited on p. 112.

Loughlin, S. C., Calder, E. S., Clarke, A., et al. 2002. Pyroclastic flows and surges generated by the 25 June 1997 dome collapse, Soufrière Hills Volcano, Montserrat. *Geological Society, London, Memoirs.* **21**(1), pp. 191–209. Cited on pp. 6, 182, and 183.

Lowe, R. J., Rottman, J. W., and Linden, P. F. 2005. The non-Boussinesq lock-exchange problem. Part 1. Theory and experiments. *Journal of Fluid Mechanics.* **537**, pp. 101–124. Cited on p. 7.

Manville, V. 2004. Palaeohydraulic analysis of the 1953 Tangiwai lahar; New Zealand's worst volcanic disaster. *Acta Vulcanologica.* **16**(1/2), pp. 1000–1015. Cited on p. 6.

Marino, B. M., Thomas, L. P., and Linden, P. F. 2005. The front condition for gravity currents. *Journal of Fluid Mechanics.* **536**, pp. 49–78. Cited on pp. 18 and 19.

Massey, C. I., Manville, V., Hancox, G. H., et al. 2010. Out-burst flood (lahar) triggered by retrogressive landsliding, 18 march 2007 at Mt ruapehu, New Zealand—a successful early warning. *Landslides.* **7**(3), pp. 303–315. Cited on p. 6.

MathWorks, I. 2018a. *MATLAB: the language of technical computing. Desktop tools and development environment, version 7.*, volume 9. MathWorks. Cited on pp. 113, 116, and 117.

Meiburg, E. and Kneller, B. 2010. Turbidity currents and their deposits. *Annual Review of Fluid Mechanics.* **42**, pp. 135–156. Cited on pp. 1 and 19.

Meiburg, E., Radhakrishnan, S., and Nasr-Azadani, M. M. 2015. Modeling gravity and turbidity currents: computational approaches and challenges. *Applied Mechanics Reviews.* **67**(4). Cited on p. 110.

Mellor, G. L. and Yamada, T. 1982. Development of a turbulence closure model for geophysical fluid problems. *Reviews of Geophysics.* **20**(4), pp. 851–875. Cited on p. 19.

Merzari, E., Fischer, P., Min, M., et al. 2020. Toward exascale: overview of large eddy simulations and direct numerical simulations of nuclear reactor flows with the spectral element method in Nek5000. *Nuclear Technology.* **206**(9), pp. 1308–1324. Cited on p. 105.

Milliman, J. D. and Syvitski, J. P. M. 1992. Geomorphic/tectonic control of sediment discharge to the ocean: the importance of small mountainous rivers. *The journal of Geology.* **100**(5), pp. 525–544. Cited on p. 2.

Moresi, L., Zhong, S., and Gurnis, M. 1996. The accuracy of finite element solutions of Stokes's flow with strongly varying viscosity. *Physics of the Earth and Planetary Interiors.* **97**(1-4), pp. 83–94. Cited on p. 99.

Morgenstern, N. R. 1967. Submarine slumping and the initiation of turbidity currents. *Marine geotechnique.* pp. 189–220. Cited on p. 3.

Morton, B. R., Taylor, G. I., and Turner, J. S. 1956. Turbulent gravitational convection from maintained and instantaneous sources. *Proceedings of the Royal Society of London. Series A. Mathematical and Physical Sciences.* **234**(1196), pp. 1–23. Cited on p. 18.

Mulder, T. and Alexander, J. 2001. The physical character of subaqueous sedimentary density flows and their deposits. *Sedimentology.* **48**(2), pp. 269–299. Cited on pp. 4, 5, and 23.

Nakajima, T. and Kanai, Y. 2000. Sedimentary features of seismoturbidites triggered by the 1983 and older historical earthquakes in the eastern margin of the Japan Sea. *Sedimentary Geology.* **135**(1), pp. 1–19. Cited on pp. 5 and 23.

Nasr-Azadani, M. M. and Meiburg, E. 2011. Turbins: an immersed boundary, Navier–Stokes code for the simulation of gravity and turbidity currents interacting with complex topographies. *Computers & Fluids.* **45**(1), pp. 14–28. Cited on p. 20.

Necker, F., Härtel, C., Kleiser, L., and Meiburg, E. 2002. High-resolution simulations of particle-driven gravity currents. *International Journal of Multiphase Flow.* **28** (2), pp. 279–300. Cited on p. 20.

Necker, F., Härtel, C., Kleiser, L., and Meiburg, E. 2005. Mixing and dissipation in particle-driven gravity currents. *Journal of Fluid Mechanics.* **545**, pp. 339–372. Cited on pp. 20 and 102.

Norem, H., Locat, J., and Schieldrop, B. 1990. An approach to the physics and the modeling of submarine flowslides. *Marine Georesources & Geotechnology.* **9**(2), pp. 93–111. Cited on p. 4.

Offermans, N., Marin, O., Schanen, M., et al. On the strong scaling of the spectral element solver NEK5000 on petascale systems. In: *Proceedings of the Exascale Applications and Software Conference 2016*, pp. 1–10, 2016. Cited on p. 105.

Ohlsson, J., Schlatter, P., Fischer, P. F., and Henningson, D. S. 2011. Stabilization of the spectral-element method in turbulent flow simulations. In: *Spectral and High Order Methods for Partial Differential Equations.* Springer, pp. 449–458. Cited on pp. 110 and 111.

O'Shea, B. E. 1954. Ruapehu and the Tangiwai disaster. *NZJ Sci Technol B.* **36**, pp. 174–189. Cited on p. 6.

Özgökmen, T. M. and Chassignet, E. P. 2002. Dynamics of two-dimensional turbulent bottom gravity currents. *Journal of Physical Oceanography.* **32**(5), pp. 1460–1478. Cited on p. 20.

Özgökmen, T. M. and Fischer, P. F. 2008. On the role of bottom roughness in overflows. *Ocean Modelling.* **20**(4), pp. 336–361. Cited on p. 110.

Özgökmen, T. M., Fischer, P. F., Duan, J., and Iliescu, T. 2004. Three-dimensional turbulent bottom density currents from a high-order nonhydrostatic spectral element model. *Journal of Physical Oceanography.* **34**(9), pp. 2006–2026. Cited on pp. 20, 110, and 111.

Özgökmen, T. M., Fischer, P. F., and Johns, W. E. 2006. Product water mass formation by turbulent density currents from a high-order nonhydrostatic spectral element model. *Ocean Modelling.* **12**(3-4), pp. 237–267. Cited on p. 21.

Özgökmen, T. M., Iliescu, T., Fischer, P. F., Srinivasan, A., and Duan, J. 2007. Large eddy simulation of stratified mixing in two-dimensional dam-break problem in a rectangular enclosed domain. *Ocean Modelling.* **16**(1-2), pp. 106–140. Cited on p. 98.

Özgökmen, T. M., Iliescu, T., and Fischer, P. F. 2009a. Large eddy simulation of stratified mixing in a three-dimensional lock-exchange system. *Ocean Modelling.* **26**(3-4), pp. 134–155. Cited on pp. 20, 98, 100, and 104.

Özgökmen, T. M., Iliescu, T., and Fischer, P. F. 2009b. Reynolds number dependence of mixing in a lock-exchange system from direct numerical and large eddy simulations. *Ocean Modelling.* **30**(2-3), pp. 190–206. Cited on pp. 20, 97, 98, 99, 100, 104, 110, and 111.

Pailha, M. and Pouliquen, O. 2009. A two-phase flow description of the initiation of underwater granular avalanches. *Journal of Fluid Mechanics.* **633**, pp. 115–135. Cited on p. 183.

Parsons, J. D., Friedrichs, C. T., Traykovski, P. A., et al. 2009. The mechanics of marine sediment gravity flows. *Continental margin sedimentation: from sediment transport to sequence stratigraphy.* **37**, pp. 275–334. Cited on p. 12.

Patera, A. T. 1984. A spectral element method for fluid dynamics: laminar flow in a channel expansion. *Journal of computational Physics.* **54**(3), pp. 468–488. Cited on pp. 105 and 121.

Piau, J. M. 1996. Flow of a yield stress fluid in a long domain. application to flow on an inclined plane. *Journal of Rheology.* **40**(4), pp. 711–723. Cited on p. 12.

Piper, D. J. W., Cochonat, P., and Morrison, M. L. 1999. The sequence of events around the epicentre of the 1929 Grand Banks earthquake: initiation of debris flows and turbidity current inferred from sidescan sonar. *Sedimentology.* **46**(1), pp. 79–97. Cited on pp. 2 and 4.

Pope, S. B. 2001. *Turbulent flows.* IOP Publishing. Cited on p. 109.

Pouliquen, O. 1999. Scaling laws in granular flows down rough inclined planes. *Physics of fluids.* **11**(3), pp. 542–548. Cited on p. 183.

Prandtl, L. 1952. *Essentials of Fluid Dynamics, with Application to Hydraulics, Aeronautics, Meteorology and Other Subjects.* Blackie. Cited on p. 18.

Price, J. F. and Baringer, M. O. 1994. Outflows and deep water production by marginal seas. *Progress in Oceanography.* **33**(3), pp. 161–200. Cited on p. 98.

Roche, O., Buesch, D. C., and Valentine, G. A. 2016. Slow-moving and far-travelled dense pyroclastic flows during the Peach Spring super-eruption. *Nature communications.* **7**(1), pp. 1–8. Cited on p. 1.

Roe, P. L. 1981. Approximate Riemann solvers, parameter vectors, and difference schemes. *Journal of Computational Physics.* **43**(2), pp. 357–372. Cited on pp. 149 and 150.

Roe, P. L. 1986. Characteristic-based schemes for the Euler equations. *Annual review of fluid mechanics.* **18**(1), pp. 337–365. Cited on p. 155.

Rottman, J. W. and Simpson, J. E. 1983. Gravity currents produced by instantaneous releases of a heavy fluid in a rectangular channel. *Journal of Fluid Mechanics.* **135**, pp. 95–110. Cited on pp. 9, 13, and 141.

Sagaut, P. 2006. *Large eddy simulation for incompressible flows: an introduction.* Springer Science & Business Media. Cited on p. 20.

Scardovelli, R. and Zaleski, S. 1999. Direct numerical simulation of free-surface and interfacial flow. *Annual review of fluid mechanics.* **31**(1), pp. 567–603. Cited on p. 99.

Schär, C. and Smith, R. B. 1993. Shallow-water flow past isolated topography. part i: Vorticity production and wake formation. *Journal of the atmospheric sciences.* **50**(10), pp. 1373–1400. Cited on p. 144.

Schwarz, H. U. 1982. Subaqueous slope failures, experiments and modern occurrences. *Contributions to Sedimentology.* Cited on p. 2.

Segur, J. B. and Oberstar, H. E. 1951. Viscosity of glycerol and its aqueous solutions. *Industrial & Engineering Chemistry.* **43**(9), pp. 2117–2120. Cited on pp. 55 and 56.

Sequeiros, O. E., Spinewine, B., Beaubouef, R. T., et al. 2010. Characteristics of velocity and excess density profiles of saline underflows and turbidity currents flowing over a mobile bed. *Journal of Hydraulic Engineering.* **136**(7), pp. 412–433. Cited on pp. vii, 3, and 12.

Shankar, P. N. and Kumar, M. 1994. Experimental determination of the kinematic viscosity of glycerol-water mixtures. *Proceedings of the Royal Society of London. Series A: Mathematical and Physical Sciences.* **444**(1922), pp. 573–581. Cited on pp. 55 and 56.

Sher, D. and Woods, A. W. 2015. Gravity currents: entrainment, stratification and self-similarity. *Journal of Fluid Mechanics.* **784**, pp. 130–162. Cited on pp. 18, 19, and 49.

Shin, J. O., Dalziel, S. B., and Linden, P. F. 2004. Gravity currents produced by lock exchange. *Journal of Fluid Mechanics.* **521**, pp. 1–34. Cited on p. 7.

Simpson, G. and Castelltort, S. 2006. Coupled model of surface water flow, sediment transport and morphological evolution. *Computers & Geosciences.* **32**(10), pp. 1600–1614. Cited on p. 181.

Simpson, J. E. 1997. *Gravity Currents: In the Environment and the Laboratory.* Cambridge University Press. Cited on p. 1.

Simpson, J. E. and Britter, R. E. 1979. The dynamics of the head of a gravity current advancing over a horizontal surface. *Journal of Fluid Mechanics.* **94**(3), pp. 477–495. Cited on p. 14.

Soares-Frazão, S. and Zech, Y. 2011. HLLC scheme with novel wave-speed estimators appropriate for two-dimensional shallow-water flow on erodible bed. *International journal for numerical methods in fluids.* **66**(8), pp. 1019–1036. Cited on p. 181.

Sohn, Y. K. 2000. Depositional processes of submarine debris flows in the miocene fan deltas, pohang basin, SE Korea with special reference to flow transformation. *Journal of Sedimentary Research.* **70**(3), pp. 491–503. Cited on p. 183.

Stansby, P. K., Chegini, A., and Barnes, T. C. D. 1998. The initial stages of dam-break flow. *Journal of Fluid Mechanics.* **374**, pp. 407–424. Cited on p. 10.

Süli, E. and Mayers, D. F. 2003. *An introduction to numerical analysis.* Cambridge university press. Cited on pp. 142, 155, and 156.

Talling, P. J., Peakall, J., Sparks, R. S. J., et al. 2002. Experimental constraints on shear mixing rates and processes: implications for the dilution of submarine debris flows. *Geological Society, London, Special Publications.* **203**(1), pp. 89–103. Cited on p. 4.

Talling, P. J., Masson, D. G., Sumner, E. J., and Malgesini, G. 2012. Subaqueous sediment density flows: depositional processes and deposit types. *Sedimentology.* **59**(7), pp. 1937–2003. Cited on pp. 2 and 183.

Tomboulides, A. G. and Orzag, S. A. 1998. A quasi-two-dimensional benchmark problem for low Mach number compressible codes. *Journal of Computational Physics.* **146**(2), pp. 691–706. Cited on p. 108.

Tomboulides, A. G., Lee, J. C. Y., and Orszag, S. A. 1997. Numerical simulation of low Mach number reactive flows. *Journal of Scientific Computing.* **12**(2), pp. 139–167. Cited on pp. 108 and 109.

Tritton, D. J. 2012. *Physical fluid dynamics.* Springer Science & Business Media. Cited on pp. 9 and 100.

Tseng, Y. and Ferziger, J. H. 2001. Mixing and available potential energy in stratified flows. *Physics of Fluids.* **13**(5), pp. 1281–1293. Cited on p. 112.

Turner, J. S. 1979. *Buoyancy effects in fluids.* Cambridge university press. Cited on p. 1.

Turner, J. S. 1986. Turbulent entrainment: the development of the entrainment assumption, and its application to geophysical flows. *Journal of Fluid Mechanics.* **173**, pp. 431–471. Cited on p. 18.

Ubbelohde, L. Viscosimeter, July 21 1936. US Patent 2,048,305. Cited on pp. x, 59, and 60.

Ungarish, M. 2005. Intrusive gravity currents in a stratified ambient: shallow-water theory and numerical results. *Journal of Fluid Mechanics.* **535**, pp. 287–323. Cited on p. 14.

Ungarish, M. 2007. A shallow-water model for high-Reynolds-number gravity currents for a wide range of density differences and fractional depths. *Journal of Fluid Mechanics.* **579**, pp. 373–382. Cited on p. 10.

Ungarish, M. 2009. *An introduction to gravity currents and intrusions.* Chapman and Hall/CRC. Cited on pp. 1, 7, 8, 10, 13, 16, 25, 52, and 141.

Ungarish, M. 2012. A general solution of Benjamin-type gravity current in a channel of non-rectangular cross-section. *Environmental Fluid Mechanics.* **12**(3), pp. 251–263. Cited on p. 14.

Ungarish, M. and Hogg, A. J. 2018. Models of internal jumps and the fronts of gravity currents: unifying two-layer theories and deriving new results. *Journal of Fluid Mechanics.* **846**, pp. 654–685. Cited on p. 14.

Ungarish, M. and Zemach, T. 2005. On the slumping of high reynolds number gravity currents in two-dimensional and axisymmetric configurations. *European Journal of Mechanics-B/Fluids.* **24**(1), pp. 71–90. Cited on p. 91.

van Andel, T. H. and Komar, P. D. 1969. Ponded sediments of the Mid-Atlantic ridge between 22 and 23 north latitude. *Geological Society of America Bulletin.* **80**(7), pp. 1163–1190. Cited on p. 3.

Van Leer, B. 1974. Towards the ultimate conservative difference scheme. ii. monotonicity and conservation combined in a second-order scheme. *Journal of computational physics.* **14**(4), pp. 361–370. Cited on p. 155.

Volk, A. and Kähler, C. J. 2018. Density model for aqueous glycerol solutions. *Experiments in Fluids.* **59**(5), pp. 75. Cited on p. 55.

von Kármán, T. 1940. The engineer grapples with nonlinear problems. *Bulletin of the American Mathematical Society.* **46**(8), pp. 615–683. Cited on p. 14.

Wagener, F. v. M., Craig, H. J., Blight, G., et al. The Merriespruit tailings dam failure-a review. In: *Proceedings of the Conference on Tailings and Mine Waste '98, Colorado State University, Fort Collins*, pp. 925–952, 1998. Cited on p. 5.

Wang, B., Vardon, P. J., and Hicks, M. A. 2016. Investigation of retrogressive and progressive slope failure mechanisms using the material point method. *Computers and Geotechnics.* **78**, pp. 88–98. Cited on p. 5.

Weimer, P., Slatt, R. M., and Bouroullec, R. 2007. *Introduction to the Petroleum Geology of Deep-water Settings.*, volume 57. AAPG. Cited on p. 4.

White, B. and Helfrich, K. 2014. A model for internal bores in continuous stratification. *J. Fluid Mech.* **761**, pp. 282–304. Cited on p. 92.

Whitham, G. B. 2011. *Linear and nonlinear waves.* John Wiley & Sons. Cited on pp. 10, 14, 26, and 31.

Wilson, L. 1976. Explosive volcanic eruptions—III. Plinian eruption columns. *Geophysical Journal International.* **45**(3), pp. 543–556. Cited on p. 6.

Winters, K. B., Lombard, P. N., Riley, J. J., and D'Asaro, E. A. 1995. Available potential energy and mixing in density-stratified fluids. *Journal of Fluid Mechanics.* **289**, pp. 115–128. Cited on pp. 111, 112, and 114.

Woods, A. W. 2010. Turbulent plumes in nature. *Annual Review of Fluid Mechanics.* **42**, pp. 391–412. Cited on p. 1.

Yang, S., An, Y., and Liu, Q. 2019. A two-dimensional layer-averaged numerical model for turbidity currents. *Geological Society, London, Special Publications.* **477**(1), pp. 439–454. Cited on p. 181.

Zhang, D., Jiang, C., Liang, D., and Cheng, L. 2015. A review on TVD schemes and a refined flux-limiter for steady-state calculations. *Journal of Computational Physics.* **302**, pp. 114–154. Cited on p. 155.